Reconfigurable Origami Structures

Mateusz Andrzej Portka

Magdalen College

University of Oxford

A thesis submitted for the degree of

Doctor of Philosophy in Engineering Science

Hilary Term, 2022

ABSTRACT

Reconfigurable Origami Structures

Mateusz Andrzej Portka, Magdalen College, University of Oxford

A thesis submitted for the degree of Doctor of Philosophy in Engineering Science,
Hilary Term, 2022.

This dissertation focuses on the kinematics of origami mechanisms and converting single degree of freedom (DOF) patterns into reconfigurable structures with two DOFs.

The presented kirigami method assumes introducing slits along creases of rigidly-foldable zero-thickness patterns. Before cutting, they usually have one motion driven by a single DOF that leads to only one final form. It makes such shapes a good choice for easily-controlled deployable systems. However, the lack of alternative motions is unfavourable for multifunctional applications requiring reconfigurability. The presented cutting of origami hinges equals removing kinematic joints. Such modifications may bring extra DOFs allowing reconfigurability. The fundamental building blocks used to construct the reconfigurable patterns are two-DOF spatial 8R linkages resulting from two-crease-long slits.

First, the thesis assumes regular multiplication of such slits inside rigid origami version of Miura-ori. As a result, it produces rigid kirigami variants of the pattern that are reconfigurable. They can exhibit new motions paths and numerous alternative shapes and folded forms. During particular reconfigurations, the assembly even displays metamorphic and kinematotropic behaviour, which increases available shapes. However, the above is possible with multiple DOFs, whose number increases as the pattern gets large, making its control challenging.

Therefore, in its second part, the thesis uses an alternative approach to multiplying the slits that includes a step-wise kinematic analysis to control the final DOF number. A target value of two DOFs is assumed, which provides a reasonable balance between reconfiguration choices and simple manipulation by only two inputs. As a result, a two-DOF rigid kirigami Miura-ori is obtained with an orderly symmetric slit layout. It retains the traditional in-plane folding and additionally can reconfigure into bent-like shapes with out-of-plane curvatures. Previously, such forms were impossible without deforming facets or redesigning the crease pattern.

Finally, the third part applies the identified slit arrangements to other one-DOF rigid origami, i.e. Eggbox, Anisotropic Miura, Arc-Miura and Arc patterns. Their reconfigurable two-DOF versions are found, and their models manufactured. Moreover, many intriguing research directions emerge throughout the project. Nevertheless, the identified kirigami structures already provide an exciting platform for novel reconfigurable applications in various fields.

Keywords: rigid origami, kinematics, linkage analysis, degrees of freedom, cutting, reconfigurable mechanism, kirigami structure.

To My Close Ones.

Acknowledgements

I would like to thank the UK Research and Innovation, the Engineering and Physical Sciences Research Council, the University of Oxford's Department of Engineering Science, Magdalen College, and everyone involved in making this research project possible via the Engineering Science EPSRC DTP Studentship.

Firstly, I would like to gratefully acknowledge the guidance of my supervisor, Prof. Zhong You. His passion for the subject and the encouragement to challenge our project were essential for its success. I would also like to thank my departmental assessors, Prof. Manolis Chatzis and Prof. Sinan Acikgoz, a former member of our group, Dr Martin Walker, and other academic and non-academic members of the Engineering Science Department for accurate and stimulating questions during seminars, valuable advice after formal evaluations, as well as general help and advice. I also appreciate the companionship of fellow students both at the department and at my college.

Moreover, I would also like to express my gratitude to the entire Magdalen College community, my college advisor Prof. John Gregg, Mr Rory Maw, and Mr Mark Blandford-Baker, for creating a welcoming environment and supporting my extracurricular projects. I want to also thank the team from Oxford Space Systems, especially Dr Juan Reveles and Mr Vincent Fraux, for being always welcoming, supportive, and understanding during our collaboration period. I also want to thank Prof. David A. Barnhart and his students from the USC Viterbi School of Engineering for their enthusiasm about my research and stimulating conversations about its possible applications. Both collaborations allowed me to see deployable structures from new perspectives.

Finally, I am grateful for my friends' presence and support, especially the ones from the department, college, and the Oxford University Polish Society. Thanks to you, my studies were much more enjoyable. I also want to express my gratitude to my family back in Poland. They were always there for me and always understood my absence. Lastly, but most importantly, I want to thank Rina Komorowska for her unconditional support during our time in Oxford. Without you, this project would not be possible. Thank you.

Contents

List of Figures

Chapter 1
Introduction

1.1 Reconfigurability of rigid origami and kirigami

Origami continues to be a source of inspiring ideas for shape-changing structures and applications. One particular origami type, known as rigid origami, happens to be very useful for engineers and researchers. They resort to it when dealing with materials much less deformable compared with flexible paper, like metal sheets (Zhang et al. 2019), plastics with embedded electronic circuits (Belke and Paik 2017), or fibre-reinforced composites (Saito et al. 2018). Rigid origami assumes such panels to be non-deformable and the creases between them to act as hinges (Chen et al. 2015) (Abel et al. 2016). Such an approach is also helpful when in origami's sub-elements deformations are unwelcome, e.g. in solar sails (Underwood et al. 2019), space membranes with attached devices (Ikeya et al. 2020), or façade glazing (Elghazi and Mahmoud 2016) (Schultz and Katz 2018). It allows designers to focus on complex and ingenious geometries that avoid deformations while disregarding material properties, at least initially.

As a result, rigid origami's folding depends entirely on the geometric arrangement of joints between the rigid bodies. Such a geometric puzzle usually produces assemblies with a single degree of freedom (DOF), i.e. requiring only one external input to decide their shape

(Tachi 2010a) (Klett et al. 2017) (Pratapa et al. 2021). While such one-DOF kinematics sometimes proves challenging to solve, having a motion driven by a single input makes assemblies' control simpler, which is often appreciated by researchers (Tachi 2011) (Chen et al. 2016) (Wang et al. 2018) (Liu and Chen 2018). However, such origami patterns have the disadvantage of limited alternative configurations and shapes they can exhibit. For the significant majority of tessellations, one DOF means only one particular motion that ends in only a single available compact form. While one DOF is efficient for straightforward deployable structures, it is often unsatisfactory for applications assuming reconfiguration between different states, e.g. in origami robotics (Kotikian et al. 2019) (Baek et al 2020) (Wu et al. 2021b), or mechanical computing (Yasuda et al. 2021).

Researchers have been actively exploring reconfigurable origami that could experience various alternative forms due to a potential for increasing applications' functionality. One way to obtain such assemblies is to base the design on mechanical instabilities like buckling (Overvelde et al. 2012) (Rafsanjani et al. 2019) (An et al. 2020), so-called snap-through effects (Silverberg et al. 2014) (Liu et al. 2019, 2021), or other bistable and bimodal behaviour (Silverberg et al. 2015) (Udani and Arrieta 2021) (Wu et al. 2021a). Unfortunately, such solutions often require soft materials to experience bending deformations and facet flexing.

Moreover, some origami patterns have been found to successfully exhibit bistability under rigid origami assumptions, i.e. without relying on material deformation and panel buckling (Yasuda and Yang 2015) (Chen et al. 2016) (Filipov et al. 2016, 2019) (Liu and Chen 2018) (Pratapa et al. 2021). However, not every rigid origami mechanism includes such phenomena, and researchers often must look for alternative means. For example, Liu and Paulino (2017), and Chudoba and Brakhage (2018) added bending rotations to rigid facets, i.e. assumed panels of finite stiffness to allow them to deform enough to transit to otherwise unavailable bifurcated states. Others (Zhu et al. 2020) (McClintock et al. 2021) (Melancon et al. 2021) manufactured elastic hinge regions by fabricating wide enough hinges out of flexible materials to accommodate the required deformation in this region instead of relying on bending the panels.

Reconfigurability is a property much sought-after. Successful attempts to achieve it have been made even by using controlled magnetic forces (Cui et al. 2019), pressurized air (Jin et al. 2020), or liquids (Poon and Hopkins 2019) (Li et al. 2021). Others introduced bi and multistabilities via extra rolling-contact elements (Shaw et al. 2018), stretchable composite laminae (Kim et al. 2019), linear-elastic springs (Li and Pellegrino 2020), or intentional geometrical incompatibilities (Arnouts et al. 2018, 2020a, 2020b). Such shape-shifting structures can inspire exciting applications, e.g. in non-invasive medicine, robotics or active materials. In this thesis, we present a more general and versatile approach for obtaining reconfigurable structures. It is inspired by a jigsaw toy called Rubik's Magic, and it assumes introducing extra DOFs to an assembly to provide freedom to change its shape.

Rubik's Magic is a plate consisting of eight square tiles arranged in a two-by-four rectangle, with hinges between them, allowing the panels to be folded onto each other and unfolded again in two perpendicular directions Fig. 1.1. In fact, with its rigid tiles and joints between them, the toy resembles rigid origami. However, Rubik's Magic can fold into many alternative configurations from its flat state, Fig. 1.1(a), two of which are shown in Fig. 1.1(b)

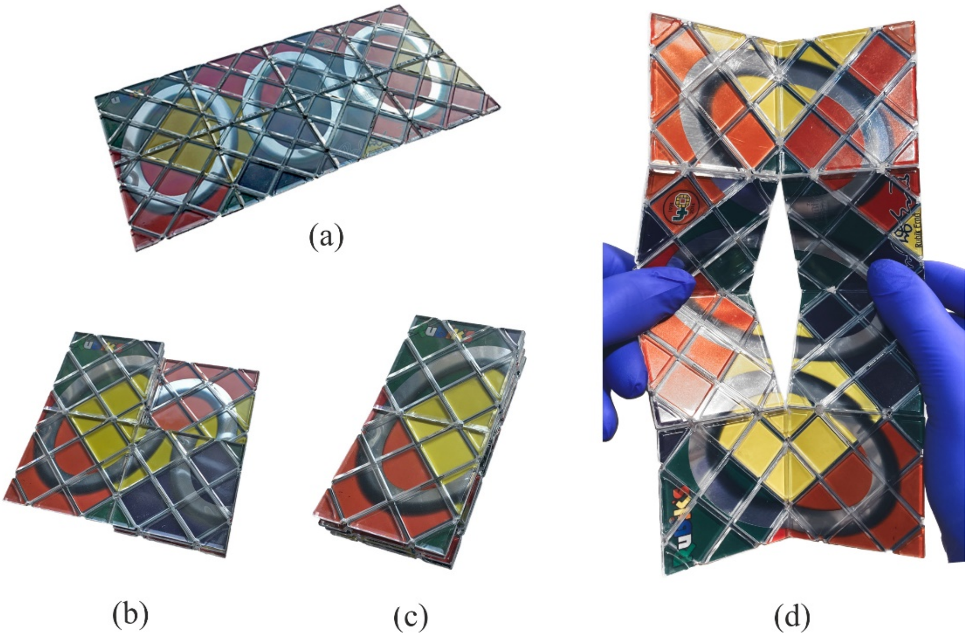

Fig. 1.1 (a) A Rubik's Magic toy in its starting flat form; (b) and (c) are two alternative folded configurations; (d) presents a slit in the toy’s centre; (Rubik’s Brand Limited: www.rubiks.com).

and (c). This is because the toy has a slit inside, Fig. 1.1(d). Kinematically, Rubik’s Magic is a closed kinematic chain of eight rigid bodies connected by revolutes, and thus, it has at least two DOFs. As a result, we can use more than one input to decide on the reconfiguration.

This inspires a method of obtaining reconfigurable structures by making similar inner cuts to typical rigid origami and creating what would actually be rigid kirigami, with Japanese *kiri* meaning *cut*. Such patterns, consisting of rigid panels, hinges between them, and slits, would belong to the so-called *fold* + *cut* kirigami type (Sun et al. 2021). In this project, by cutting origami hinges between the rigid facets, we destroy some of the joints and expect that such a kinematically relaxed pattern will experience an increase in available DOFs. Thus, more inputs available may make reconfiguration into alternative shapes possible.

Such an approach, however, has its challenges. By making an arbitrary number of slits, we remove some of the joints what means decreasing the number of kinematic constraints. Fewer of them may increase the DOF number, but many cuts may result in a significant rise in freedom. While appreciated from the perspective of alternative reconfiguration choices and thus new forms, such extra inputs required make the assembly's control complex. This can be especially problematic in places with limited access, e.g. in space (Morgan et al. 2016) or underwater (Yang et al. 2021). Many new DOFs may also lead to unexpected global panel collisions or costlier and more time-demanding computations (Tachi 2013) (Chen et al. 2016, 2018) (Pratapa et al. 2018). Furthermore, multi-DOF solutions may require figuring out the synchronisation of many actuators, which are often expensive and contribute to the assembly's weight (Okuya et al. 2018).

Many approaches have been investigated to keep the DOF number low and ensure straightforward control. For example, researchers often use overconstrained linkages with one DOF when designing transformable structures (Chen et al. 2016, 2018) (Liu and Chen 2018). Others employ techniques like bar-hinge models (Pratapa et al. 2018), fixing (removing) creases (Hayakawa and Ohsaki 2021), or vertex-splitting, i.e. redesigning the crease pattern to turn a higher-degree vertex into a few lower-degree ones. For example, Zhang and Chen (2019) used an extra crease to separate folds of a six-crease vertex, known to use three DOFs, into two connected four-crease vertices, which require only one input.

For that reason, the challenge this research project tackles is not only identifying what cuts will create new DOFs and allow rigid zero-thick origami to obtain new forms. The introduced slits should simultaneously allow keeping the DOF number as small as possible to help maintain the assembly control relatively simple, not much more complex than single-DOF origami motions. An overall DOF number equal to two would provide a reasonable balance between having more choices when reconfiguring a pattern and keeping only a few independent inputs to manipulate the structure conveniently.

1.2 Research objectives

This research aims to investigate if cutting rigid origami, i.e. creating rigid kirigami, is an efficient way of obtaining new reconfigurable structures out of traditional patterns. It focuses purely on investigating such assemblies' kinematics and does not evaluate resulting patterns' mechanical properties, for example, their capacity for energy absorption, elastic moduli, or Poisson's ratios. The research objectives revolving around rigid origami modified by slit introduction can be further divided into the following questions.

- Can making slits in rigid zero-thickness origami bring extra DOFs allowing new motions leading to alternative configurations and folded forms?
- Can the number of DOFs be kept low, ideally equal to two, so that the folding and subsequent reconfiguration can be controlled easily?
- Can such kirigami patterns be extended into larger versions, comprising more panels and maintaining the identified properties while keeping the number of DOFs finite?

We expect the research to answer also several secondary research questions.

- How do various cuts or their groups, arranged differently, affect the available configurations?

- How do kinematic models, pattern mobility, and motion paths change compared to the uncut versions?
- Can similar cut arrangements be applied to different origami patterns? What distinct functionalities this may bring?

If the objectives above are met, especially the primary ones, new rigid kirigami versions of traditional tessellations may be suggested. Choi et al. (2021) showed that kirigami could be not only a folding enabler but also a reconfigurability source, allowing alternative compact forms. They reported different rectangular and circular folded forms of the same deployed pattern. Such extra reconfiguration of initially only foldable patterns would bring further advantages. Apart from keeping origami's packaging efficiency, modularity and scalability, slits could also bring multifunctionality. For example, structures could be packaged for transport and then deployed into a particular form to complete a defined goal. After the task, they could reconfigure to serve another long-term purpose. An example could be an origami satellite sent into orbit to gather debris. It would deploy to capture and handle the leftovers, and then, it could reshape into a form most suited to collect solar energy and stay in orbit long-term. Another earthbound use case could be reconfigurable search-and-rescue robots. Compactly folded during the search phrase, they could deploy and shapeshift to facilitate the rescue phase via adjusting to various environmental conditions and emergency circumstances.

Reconfigurable kirigami structures could not only serve more than one purpose but also have the final functionality modifiable. For example, they could inspire a new family of tunable metamaterials, which would change their geometry and form periodic structures with distinct mechanical and physical properties (Overvelde et al. 2016, 2017) (Yang and You 2018). They would not have to fold compactly but could stay unfolded and shift between different forms and thus operational modes available. Alternative applications could be space-based telescopes or reflectarray antennas (Wei and Pellegrino 2017) (Arya et al. 2019) (Ikeya et al. 2020). When deployed, the ability to switch geometry, e.g. the panels' inclination angle, would allow sending electromagnetic waves or reflecting solar rays in/from various directions. On Earth, reconfigurable structures could suggest agricultural harvesters. While enclosing volume, i.e. having a particular storage capacity, such machinery could adjust its geometry for the one most suitable for the harvested crop. Such innovative applications inspired this research project.

1.3 Thesis outline

This dissertation is composed of eight chapters.

After the introduction, chapter 2 reviews fundamental concepts around origami and kirigami, i.a. rigid-foldability, linkage mobility, and overconstrained mechanisms. It also explains the kinematic analysis methods used throughout the thesis, the Kutzbach formulas and the matrix method. Finally, it provides an example of how the tools are used by analysing the kinematics of an uncut rigid-panel version of the traditional Miura-ori pattern.

Next, chapter 3 briefly introduces various cut types that can be made to rigid origami. It shows how different slit lengths affect kinematics and how various resulting geometries can influence each other. Simultaneously, the examples in the chapter explain the particular step-wise approach we take to using mobility formulas for initial freedom estimations.

The following chapters 4 and 5 present the first attempt to build a reconfigurable version of Miura-ori. They assume regular slit arrangements to avoid complex crease and slit patterns. Chapters 4 and 5 investigate the regular use of two-crease-long vertical and diagonal slits, respectively. Only after the cuts are made, the patterns' kinematics is verified to learn that the resulting structures are highly reconfigurable but have multiple DOFs, whose number increases as they grow large.

Next, after evaluating the previous results, chapter 6 takes a different approach to obtaining a reconfigurable rigid Miura-ori. This time, the priority is to build a rigid kirigami pattern while maintaining a finite mobility value of two, even if it means sacrificing the slit layout regularity. Nevertheless, the cutting arrangement is later successfully simplified while keeping the two DOFs. Such a kinematic result means finally achieving the main research objective, i.e. a macro-scale two-DOF reconfigurability.

After meeting the principal research goals, chapter 7 applies the findings from previous chapters to other four-crease-vertex origami tessellations, which in their rigid-panel versions also have only one DOF. It uses the slit arrangements identified for Miura-ori on Eggbox, Anisotropic Miura, Arc-Miura and Arc patterns to find their reconfigurable two-DOF rigid-panel counterparts. Additionally, it reports on limitations resulting from particular geometries.

Finally, chapter 8 concludes the research project. It summarises the main findings from each part and suggests their potential applications. Moreover, it highlights some possible future work directions.

Chapter 2

Literature review

This chapter reviews the fundamental origami concepts that are applied and referred to throughout the thesis. It also presents the commonly used methods for origami analysis. Moreover, it employs them to provide an explanatory kinematic study that simultaneously introduces one of the most landmark origami patterns – Miura-ori.

The first section introduces rigid origami, kirigami, and the concept of foldability of such geometries. It explains the fundamental assumptions that this thesis follows and gives requirements for the analysed origami patterns. The second section familiarises us with mechanical linkages, often used to describe origami, and provides insight into formulas that allow estimating their freedom to move. It also explains what overconstrained mechanisms are. The third section discusses the matrix method of kinematic analysis that uses Denavit and Hartenberg’s notation and allows obtaining detailed insight into origami motions. Finally, the last section uses the matrix method’s results to describe the kinematics of a repetitive Miura-ori piece, which serves as an example of how this thesis uses motion equations to determine linkages’ kinematics.

2.1 Rigid origami, kirigami, and foldability

When origami is put in the context of engineering use, it is crucial to evaluate from what its constituent elements are made. Most of the sheet materials used in physical applications are relatively rigid compared to thin and flexible traditionally-used paper. Some of the origami-inspired applications require difficult to bend much stiffer components, e.g. metal sheets (Schenk et al. 2014), aluminium bars (De Temmerman et al.2007), or even impact-resistant composites (Seymour et al. 2018). Moreover, some unique elements, like solar panels (Jasim and Taherin 2018) or space mirrors (Irion 2010) often used in space, will have precision devices mounted upon so any bending or stretching is not permitted to avoid damage to the expensive materials.

In the face of such challenges, attention has been drawn to rigid origami, a subset of origami often used when panel deformations are unwelcome or when designers focus on the ability to change a structure's shape without relying on material strain what limits the possible material choices. As mentioned earlier, rigid origami assumes flat facets to be infinitely rigid, i.e. undeformable, and folds to be ideal revolute joints. Such an approach permits motions only by the pre-assumed joints, without twisting or stretching the panels. As a result, origami's kinematic behaviour is governed solely by the geometric arrangement of revolutes between rigid facets. This allows origami to be readily manufactured from modern materials such as plastic, metal, or carbon-fibre sheets, producing sufficiently strong and durable panels suitable for use in large-scale engineering applications.

So far, rigid origami has been helpful for applications at various scales in numerous fields. For example, it regularly inspires architectural designs that play with form and functionality. An early example is spatial enclosures out of rigid panels with hinges, serving as children playhouses (Hoberman 1988). Others are mobile foldable shelter systems (De Temmerman et al. 2007) (Mira et al. 2014), rigidly-adaptable pavilions (van Knippenberg et al. 2016), bistable architecture (Miyamoto 2018) or even ballistic barriers (Seymour et al. 2018), with some applications displayed in Fig 2.1.

Meanwhile, on a smaller scale, for example in robotics, rigid origami provides ideas for modular panel systems with electronic circuits inside plastic embeddings (Belke and Paik 2017), Fig. 2.1(e), or insect wing imitations (Saito et al. 2018). Such applications assume rigid panel kinematics to avoid damaging constituent elements. Moreover, material deformation and wrinkling are especially problematic, for example, in space applications due to performance decrease or failure. Therefore, inextensible rigid-origami ways of wrapping or deploying solar sails or panels (Guest and Pellegrino 1992) (Zirbel et al. 2013) (Xu et al. 2018), space-based telescopes (Irion 2010), or other reflective arrays (Wei and Pellegrino 2017), are actively researched, Fig. 2.1(f) and (g).

We must also note that origami crease patterns are developed for almost zero-thickness paper, while engineering materials and structures often require a finite non-zero thickness. Its introduction would significantly alter the patterns' kinematic models. For example, when the thickness is assumed to be zero, some folds in a crease pattern meet at one point, which allows modelling such vertices as particular mechanisms called spherical linkages. Using thick panels would cause crease misalignments resulting in multiple intersection points, and another mechanism type, called spatial linkages, would have to be used. They have different kinematic models and thus often a different number of the required control inputs.

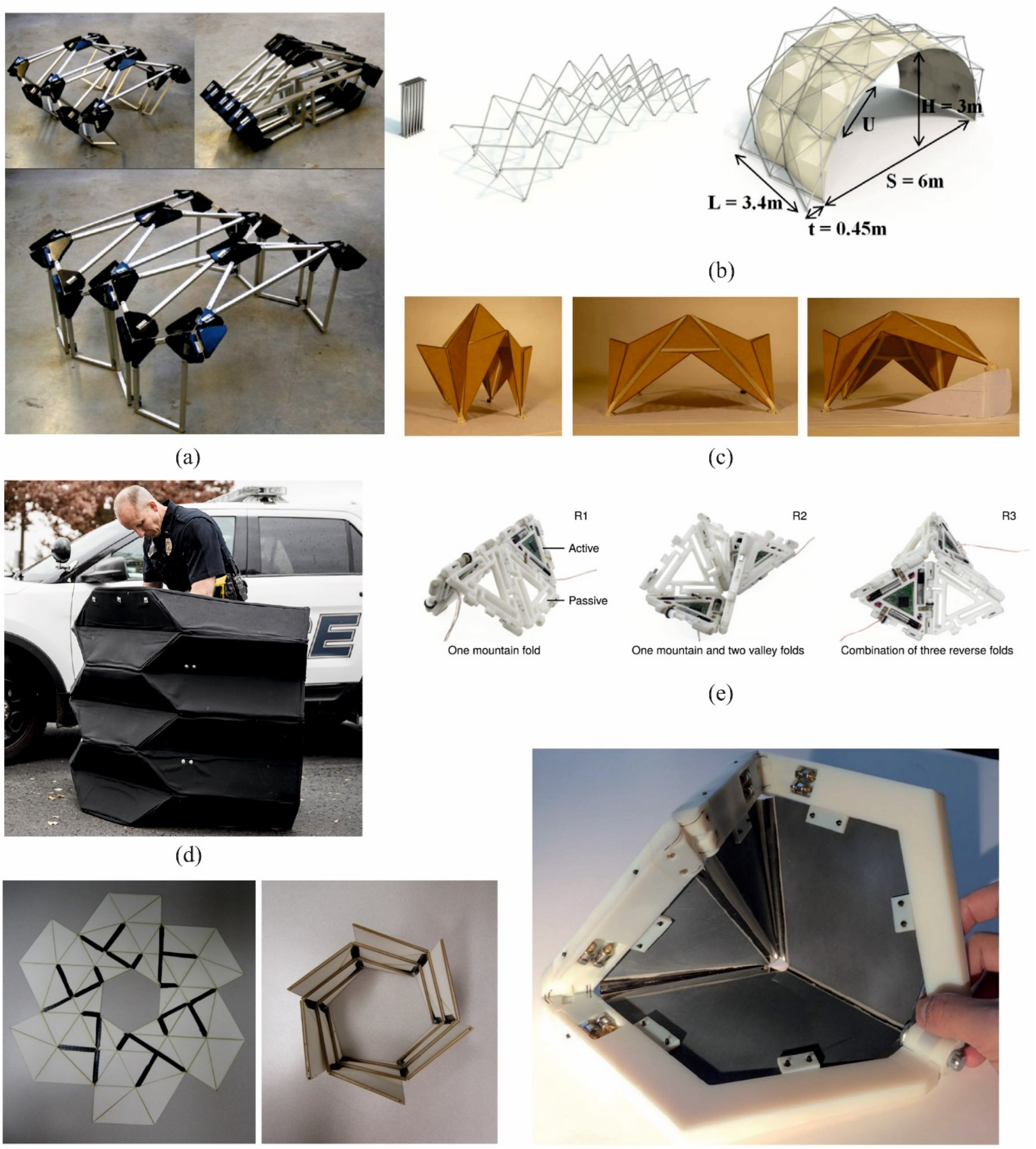

(b)

(a)

(c)

(e)

(d)

(f)

(g)

Fig. 2.1 Exemplary rigid-origami applications. (a) a prototype (De Temmerman et al. 2007) and (b) a conceptual design (Mira et al. 2014) of deployable aluminium bar shelters; (c) rigidly-foldable model of an adaptive pavilion (van Knippenberg et al. 2016); (d) rigidly-foldable ballistic-grade aramid fabric barrier (Seymour et al. 2018); (e) Three configurations of a modular rigid-panel origami robot (Belke and Paik 2017); (f) A rigidly-foldable array model based on six-sided flasher pattern (Zirbel et al. 2013); (e) A prototype of a deployable surface array module with rigid spatial mechanism (Wei and Pellegrino 2017).

Moreover, as the Miura-ori will be the representative origami on which we will conduct investigations, it must be mentioned that the challenge of introducing the panel thickness even to the unmodified version of this pattern has not been fully solved yet. Its characteristic geometry, including some panels overlapping the previous ones, makes the thickness accommodation especially troublesome, and the solutions found so far in the literature involve altering or constraining the kinematic behaviour.

Therefore, while under rigid origami assumptions, the assemblies investigated in this thesis will remain in the domain of zero-thickness surfaces. To stay as close as possible to the traditional patterns' kinematics and investigate the impact of the slit introduction, i.e. the kirigami modifications, we will assume geometries unaffected by panel thickness. Suppose bigger, scaled-up versions of the patterns, for example, meter-size, are to be explored. In that case, it is important to keep the thickness negligible to other dimensions to stay as true to the original kinematics as possible. Moreover, using cuts not to obtain reconfigurability but more efficient thickness accommodation is an intriguing research question for a separate project.

Kirigami is an extension of origami that, apart from only folding a sheet of paper, allows cutting it beforehand (Callens and Zadpoor 2017). It makes many more unique 2D and 3D shapes possible to obtain from flat surfaces. Kirigami became a source of inspiration for applications in various engineering fields (Ning et al. 2018) (Park et al. 2019). For example, periodic geometries possible thanks to slit introduction inspire new variants of metamaterials and metastructures (Eidini and Paulino 2015) (Sun et al. 2021), allow engineering of materials’ elasticity (Callens and Zadpoor 2017), or provide structures with impressive load-to-weight ratios (Wang et al. 2020), Fig. 2.2(a), (b) and (c). The versatility of slit

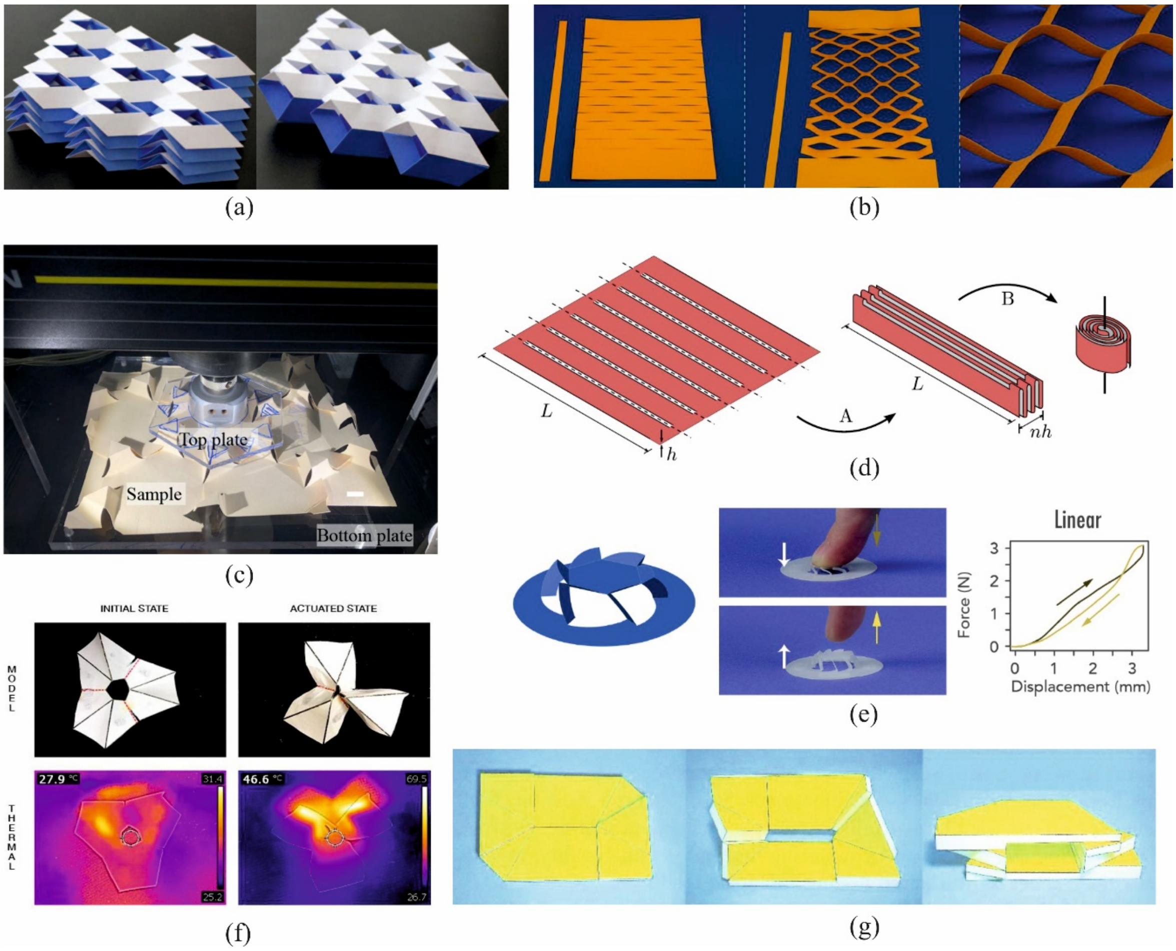

Fig. 2.2 Exemplary kirigami applications. (a) multi-layer cellular metamaterials (Eidini and Paulino 2015); (b) models of kirigami-engineered elasticity (Callens and Zadpoor 2017); (c) interleaved kirigami extension assemblies with significant load-to-weight ratios under test (Wang et al. 2020); (d) Packaging concept of a membrane with parallel slits (Arya et al. 2017); (e) Kirigami haptic swatch model and its experiment results (Chang et al. 2020); (f) kirigami folding using shape-memory polymers and thermal input (Liu et al. 2018); (g) folding of a thick-panel assembly enabled via slit introduction (Wang et al. 2018).

modifications is highlighted by applications using diverse materials, e.g. woven Kevlar fabric morphing wingboxes (Saito et al. 2011), kirigami glue-laminated bamboo structures (Yamada et al. 2018) or inflatables with programmable shapes (Melancon et al. 2021).

Moreover, in the space industry, introducing openings or slits in the material has been suggested to obtain deformation-free or -reduced ways of wrapping flexible solar sails or membranes (Arya et al. 2016, 2017, 2019), Fig. 2.2(d), or rigid solar panel arrays (Xu et al.

2018). Liu et al. (2018) also suggested kirigami-inspired applications with folding mechanisms triggered by various environmental inputs, e.g. microscale DNA-hydrogel hinges or heat-light responsive macroscale structures, Fig. 2.2(f). Chang et al. (2020) and Giraud et al. (2021) also employed the cuts to propose new types of haptic devices, Fig. 2.2(e). Kirigami has also been found to facilitate the use of thick panels (Wang et al. 2018). By making an inner slit and cutting a hinge, they removed a kinematic constraint, which allowed a gap to emerge during the folding process that facilitated the panel thickness accommodation, Fig. 2.2(g).

When it comes to cutting origami crease patterns to turn them into kirigami, we can distinguish a particular type of slit we can make. This work will resort to cuts only along origami's original folds, keeping its rigid panels intact. From the kinematic perspective, our slits will equal removing the fold-associated revolutes, along which we will introduce the slits. However, before we start making such modifications, a few origami rules and characteristics must be mentioned first.

One of the most straightforward is the requirement that the sum of the sector angles at a single vertex, i.e. the angles between the creases meeting at a point, must equal 2π. For an origami pattern, it means that it can have a fully deployed flat form, i.e. is developable (Hull 1994). All the patterns investigated in this thesis, except for the Eggbox pattern, satisfy this requirement. Also, It means they can be readily manufactured using planar crease patterns.

There are also particular rules known as the Maekawa's and Kawasaki's theorems. The first states that at any vertex, the numbers of the valley and mountain folds always differ by two. The second informs that at a vertex, alternatingly adding and subtracting consecutive sector angles returns zero. These two rules identify an origami pattern that can fold compactly into a flat form, i.e. is flat-foldable (Hull 1994, 2002). All the patterns in this thesis satisfy the flat foldability conditions above, as we investigate only the geometries that allow compact folding.

Moreover, researchers have also identified a set of methods that help recognize rigidly-foldable patterns, i.e. the ones that can exhibit continuous folding under rigid origami assumptions. For example, some approaches include diagram (Watanabe and Kawaguchi 2009) or Jacobian matrix analyses (Tachi 2010a). Others focus on particular origami subsets, e.g. the investigations into rigid foldability of twists by Evans et al. (2015a, 2015b).

Researchers have also specified theorems and requirements based on different mountain-valley (MV) crease assignments. They introduced particular arrangements, named ‘tripods’, ‘crosses’, or ‘bird’s feet’ that help identify rigidly-foldable origami. (Abel et al. 2016). Even though such concepts allow a swift judgement about a single vertex, we will not employ these frameworks. Instead, we will use detailed kinematic analyses, which return precise results about the motion, beyond only informing about the rigid foldability. Moreover, the precise techniques are more suitable for analysing multi-vertex origami. The remaining part of this chapter provides insight into such methods.

2.2 Linkages, mobility and overconstrained mechanisms

In mechanical terms, rigid origami is an assembly of rigid bodies capable of motion during the pattern’s folding and deployment. Hence, such motion can be modelled using the mechanism theory (Hunt 1978) (Philips 1984) (You and Chen 2012). As rigid origami assumes folds to be hinges, we deal with an assembly of rigid bodies connected by kinematic joints, i.e. a mechanism, also called a kinematic chain. Moreover, rigid origami's hinges are ideal revolutes, which belong to a group of kinematic joints known as lower pairs (Reuleaux 1876). Such joints include contact at every point of one or more surface segments between two rigid bodies. This case applies to all the origami patterns examined in this thesis. As a result, the mechanisms can be referred to as linkages.

While investigating linkages' kinematics, one of the key concepts is mobility, i.e. the number of DOFs, which are the inputs required to define an assembly's shape (Hunt 1978) (Philips 1984) (You and Chen 2012). The more DOFs it has, the more alternative manipulations are possible. Unfortunately, with many inputs required, the complexity of the kinematics increases, and the control of the assembly becomes troublesome. The mobility value can be determined out of the detailed kinematic analysis, but it is often helpful to use formulas allowing initially estimating the value. Even though such ready-to-use equations sometimes turn out to be inaccurate due to their simplistic forms (Philips 1984) (You and Chen 2012), they are a straightforward to apply tool that can bring valuable insight.

In this thesis, we are going to use a formula, commonly known as the Kutzbach criterion, that allows calculating the mobility M of a rigid body assembly (Hunt 1978) (Philips 1984) (You and Chen 2012). It is

$$M = d(n-1-j)+\sum_{i=1}^{j} f_i \, , \tag{2.1}$$

where d is the number of DOFs each rigid body is entitled to in free space, having no constraints (we will also refer to it as the *DOFs potential*). It is $d = 6$ for a 3D object, which reduces to $d = 3$ in a 2D case. Also, n is the number of rigid bodies, j is the number of joints, and f_i is an ith joint's freedom number, equal to DOFs not constrained by this joint. Equation (2.1) also assumes subtracting DOFs of one rigid body (the '-1') that is fixed in space.

As indicated above, we can distinguish between two alternative versions of (2.1), with the DOFs potential d equal to six or three. However, we must first introduce the definitions of spherical and spatial linkages. The spherical one is a particular type of linkage with all its joints' (in our case, revolutes') axes meeting at one point. As a result, the trajectories of the linkage's links stay on concentric spheres (Hunt 1978) (Chiang 1988), hence the name. In other words, the assembly's rigid bodies are constrained to rotate around the same fixed point in space, i.e. each has by default only three DOFs to move. In the origami context, spherical linkages describe single vertices of rigid zero-thickness patterns.

A spherical linkage is also a more general term to a planar linkage, which has rigid bodies located on a plane and the revolute axes pointing in the normal direction. In a planar linkage, the revolutes meet at a point in infinity, while the revolutes of a spherical linkage intersect at any single point (Hunt 1978) (You and Chen 2012). As a result, for both planar and spherical types, the DOF potential is equal to three. In spherical linkages, this represents three rotations around the intersection point. Therefore, (2.1) for both spherical and planar types becomes

$$M = 3(n-1-j) + \sum_{i=1}^{j} f_i \, . \tag{2.2}$$

Moreover, as we deal with ideal revolutes, each joint's freedom number f_i equals one (a single rotation around a revolute's axis). As a result, the sum of all the joints' freedoms is j. Therefore, the final form of the Kutzbach formula for spherical linkages, which we will use in this thesis, is

$$M = 3(n-1-j)+j\,. \tag{2.3}$$

Alternatively, linkages may have revolutes intersecting at more than one point. We refer to them as spatial linkages (Hunt 1978) (You and Chen 2012). In such cases, the linkages will have much less constrained geometry, and their kinematics will involve motions in 3D space, not only restricted to 2D or spherical domains. As a result, we will use the value of six for each rigid body's DOF potential, and the formula (3.1) will become

$$M = 6(n-1-j)+\sum_{i=1}^{j} f_i\,. \tag{2.4}$$

As our spatial linkages will also consist of only revolutes, (2.4) similarly simplifies to

$$M = 6(n-1-j)+j\,. \tag{2.5}$$

Such formulas allowing initial assessment of mobility are often used during kinematic investigations. However, they have some drawbacks. Equations (2.1) to (2.5) do not consider geometry characteristics. They are purely a numerical approach that depends on counting the constituting elements without considering intricacies about their spatial alignment. As a result, in some cases, they may be inaccurate. They may even return values equal to zero or negative, informing that an assembly has no freedom to move. However, at the same time, due to special geometric conditions fulfilled, some rigid motions may occur.

If the assembly has a mobility value equal to zero or less, yet it still moves, it is called an overconstrained mechanism (Hunt 1978) (Philips 1984) (You and Chen 2012). Such mechanisms often have a single hidden DOF that allows them to exhibit motion, which results from geometric specialities and is undetected by numeric formulas. In such cases, the actual mobility of the assembly must be determined by the detailed kinematic analysis. The following section explains the one employed in this thesis.

In general, it can be considered that the Kutzbach formulas work for the majority of cases but become inaccurate when linkage parts, i.e. bars and revolutes, are specially aligned. Under such unusual geometric arrangements, so-called geometric specialities happen, and hidden DOFs emerge (Philips 1984), unfortunately, undetected by the numeric formulas. As a result, some extra motions become available only when these specific geometric requirements are satisfied. In reality, even minor imperfections make satisfying them challenging. However, when dealing with origami, the paper's deformability compensates for the inherent manufacturing imperfections, and these motions can be exercised. Therefore, when building origami out of rigid panels and when cannot rely on deformations, i.e. creating overconstrained mechanisms, attention must be drawn to the precise manufacturing and assembly process.

Even though the Kutzbach criterion is often inaccurate when applied to origami, as explained above, it usually provides an initial prediction of an assembly's mobility. It is the most accurate simple formula for DOF approximation we use. Moreover, later we will employ it as a guidance to build patterns with the desired finite DOF number. For that, we will take a specific approach. We will carry out the calculations in a step-wise manner while building the origami patterns. Even though still sometimes inaccurate, such an approach returns correct mobility predictions more often than applying the criterion only to a finished pattern. This is because it allows evaluating the freedom that the constituent bodies are entitled to much more clearly, after each step, which allows avoiding mistakes in assigning DOFs. A short explanation of this approach is presented in chapter 3.

2.3 Kinematic analysis using the matrix method, D-H notation

This section describes the main method that we will use to investigate rigid origami's kinematics in detail. It assumes representing the analysed fragment of a pattern as a mechanical linkage described under what is known as Denavit and Hartenberg's (D-H) notation (1955). Then, the approach, known as the matrix method of analysis (Beggs 1966) (You and Chen 2012), is used on a closed kinematic chain to find its so-called closure equations. These are symbolic trigonometric formulas that precisely describe the assembly's kinematics. When analysed, they can reveal details about the motion's nature, like bifurcations points or mobility variations, i.e. DOF changes. First, this section describes how D-H notation looks like for a generic linkage part.

A repeatable fragment of a mechanical linkage under D-H notation is presented in Fig. 2.1 (Beggs 1966). It has only revolutes as joints, each one consecutively numbered as i-1, i, i+1... The so-called links of the linkage, i.e. the rigid bodies of the assembly, are described by the adjacent joints, having numbers $(i\text{-}1)i$ or $i(i+1)$. Each revolute has its axis of rotation Z_i and each link, assumed to be perpendicular to the rotational axes of the joints it connects, e.g. joints i-1 and i, has a length marked as $a_{(i-1)i}$. In other words, $a_{(i-1)i}$ is the distance between the axes Z_{i-1} and Z_i. Along the link $a_{(i-1)i}$, in the joint i direction, there is an axis X_i of that joint. Having both axes Z_i and X_i, and knowing that the right-handed Cartesian coordinate system rules apply for the joints' axes, we can determine Y_i if needed. With the "right-hand screw" rotations, a twist angle $\alpha_{(i-1)i}$ between consecutive revolute axes Z_{i-1} and Z_i can be found, measured about X_i. As a result, the two parameters describing each link are the distance $a_{(i-1)i}$ and the twist angle $\alpha_{(i-1)i}$.

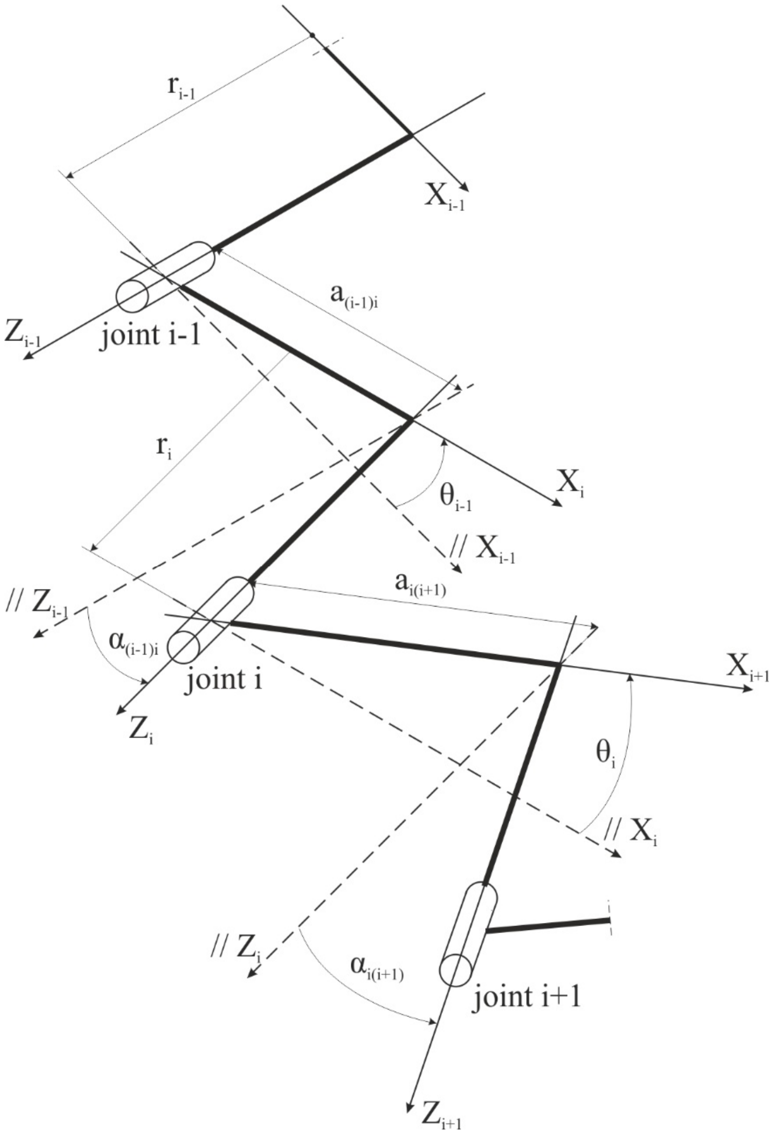

Fig. 2.3 A generic part of a mechanical linkage with revolute joints.

In a more general case, i.e. when as the joints sliding cylindrical pairs are chosen, not revolutes, the distance between axes X_i and X_{i+1}, here marked as r_i, is considered a variable at the joint *i*, which is a slide along axis Z_i. In our case, when representing origami, cylindrical pairs are replaced by revolute pairs, and r_i becomes a constant and can be considered a parameter of the joint *i*, a so-called offset at that joint. The second variable at this joint, an angle between X_i and X_{i+1} measured along Z_i, is denoted as θ_i. In our case, θ_i will indeed be a variable at a linkage's joint, which will describe the progressing motion.

Once a model of a mechanical linkage is decided, the matrix method can be applied, and particular transfer matrices be written for it. A transfer matrix $[T_{i(i+1)}]$ transforms coordinates of an arbitrary point P in a coordinate system i to its coordinates in a system $i+1$ and is

$$\left[T_{i(i+1)}\right]=\begin{bmatrix} 1 & 0 & 0 & 0 \\ -a_{i(i+1)} & C\theta_i & S\theta_i & 0 \\ -r_i S\alpha_{i(i+1)} & -C\alpha_{i(i+1)}S\theta_i & C\alpha_{i(i+1)}C\theta_i & S\alpha_{i(i+1)} \\ -r_i C\alpha_{i(i+1)} & S\alpha_{i(i+1)}S\theta_i & -S\alpha_{i(i+1)}C\theta_i & C\alpha_{i(i+1)} \end{bmatrix} \text{ where } P=\begin{bmatrix} 1 \\ X_{Pi} \\ Y_{Pi} \\ Z_{Pi} \end{bmatrix} \qquad (2.6)$$

Note that point P's coordinates are a 4×1 vector. This is due to an additional matrix column being responsible for the translation between the coordinate systems compared with the typical 3×3 rotational matrices. S and C in (2.6) are sine and cosine, respectively.

The method assumes continuous transformations between the consecutive joints' coordinate systems around a closed path defined by the mechanism's n rigid bodies. In other words, we complete a loop of such transformations between the joints connecting rigid links until we return to the initial coordinate system, yielding no change to point P's coordinates. Therefore, the product of such transformations, i.e. all the transfer matrices between the consecutive joints multiplied, is a unity matrix, which is represented by

$$[T_{n1}]\ldots[T_{34}][T_{23}][T_{12}]=\mathbf{I}\,. \qquad (2.7)$$

In (2.7), $\mathbf{I}$ is a 4×4 unit matrix. Equation (2.7) is known as the closure equation of a linkage in the matrix form. Both sides are 4×4 matrices, and equating their coefficients can provide as many as sixteen equations that describe the geometric relationships between the linkage's constituent elements, known as the linkage's individual closure equations. These exact symbolic equations allow describing the assembly's motion in detail and provide a platform for carrying out in-depth analyses of the linkage's kinematics. However, the equations together often constitute a complex system of non-linear trigonometric formulas, which may require extensive calculations to solve and may return complex final forms.

It has already been shown in the literature that single origami vertices with four, five or six creases meeting at a point can be described as spherical 4*R,* 5*R* or 6*R* linkages, i.e. spherical linkages comprising four, five or six revolute joints, respectively (Chen et al. 2015). For these cases, a set of parameter requirements and closure equations describing such linkages' motions have been identified using the method outlined above. In the next section, we will show how such generic results prove to be helpful when describing the kinematics of a rigid zero-thickness traditional Miura-ori.

2.4 Kinematics of a rigid zero-thickness Miura-ori

One of the most famous origami, known as Miura-ori and presented in Fig. 2.2, will be the main pattern on which we will test introducing slits, i.e. the kirigami approach. It was first introduced by Miura (1980) as a solution to an elastic problem of folding a zero-thick membrane in space. Since then, this folding has found applications in numerous deployable structures, e.g. mimicking biological structures or used in space (Miura 2009). It is now widely regarded as one of the most popular rigidly-foldable patterns (Tachi 2010a, 2010b). Kinematically, it has a one-DOF in-plane motion under rigid origami assumptions (Schenk and Guest 2013). Moreover, if deformation of panels is allowed, the pattern can also be bent or twisted out of its traditional plane, allowing it to approximate various curved surfaces from the macro-scale perspective (Liu and Paulino 2017) (Nassar et al. 2018). Examples of such deformed forms are presented in Fig. 2.5.

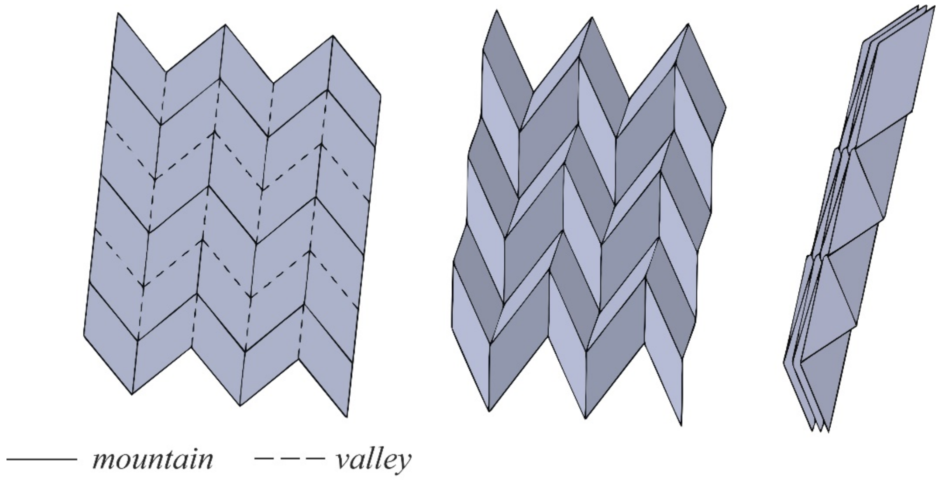

(a) (b) (c)

Fig. 2.4 Miura-ori in the (a) flat, (b) partially folded, and (c) fully folded* forms.

*In the thesis, while presenting folded forms, we will show slightly open configurations, with minimal non-zero dihedral angles to show how the panels stack.

(a) (b) (c)

Fig. 2.5 (a) Miura-ori in a traditional rigidly-foldable configuration; exemplary (b) bent and (c) twisted forms requiring panel deformations.

Miura-ori's geometry makes it a potent source of inspiration for engineering applications at various scales. For example, Silverberg et al. (2014) showed that Miura-ori's bistability could provide reprogrammable mechanical metamaterials at micro and nano scales. Another creative nanoscale application inspired by Miura-ori's geometry, reported by Hong et al. (2018), is a generator turning solar energy into steam. Metamaterials consisting of Miura-ori layers have also been found to exhibit intriguing energy-absorbing characteristics under compressive tests (Karagiozova et al. 2019) (Zhang et al. 2019). At bigger scales, the pattern's geometry also provides ideas for novel folded cores for sandwich structures with innovative properties like blast resistance (Schenk et al. 2014) or the ability to morph (Gattas and You 2015).

As this pattern is a fundamental element of the thesis, we will make an exemplary kinematic analysis of its uncut rigid origami version in this section. This will explain how the matrix method can be a valuable source of insight and how closure equations can allow estimating origami's DOFs. We will arrive at Miura-ori's specific formulas using the results reported for a general spherical 4R linkage (Chiang 1988) (Chen et al. 2015) and then adjusting them for the analysed case. However, in the remaining part of the thesis, we will perform the complete matrix method calculations, as the generic solutions for the linkages that result from the slit introductions have not been identified. The detailed closure equation derivations will be provided in attachments.

Figure 2.3 shows a repetitive part of a rigid zero-thick uncut Miura-ori. It consists of four non-deformable parallelograms connected by four hinges (Z_1 to Z_4). They form a loop of four rigid links connected by revolute joints, whose axes meet at the fragment's central vertex. Therefore, the repetitive part can be modelled as a spherical 4R linkage (Chiang 1988). The fragment satisfies the general flat foldability conditions of a single-vertex origami, i.e. the Maekawa's and Kawasaki's theorems from section 2.1, which for the analysed case become

$$\text{No. of mountain folds} - \text{No. of valley folds} = 3 - 1 = 2 \,, \tag{2.8}$$

$$\alpha_{12} + \alpha_{34} = \alpha_{23} + \alpha_{41} = \pi \,. \tag{2.9}$$

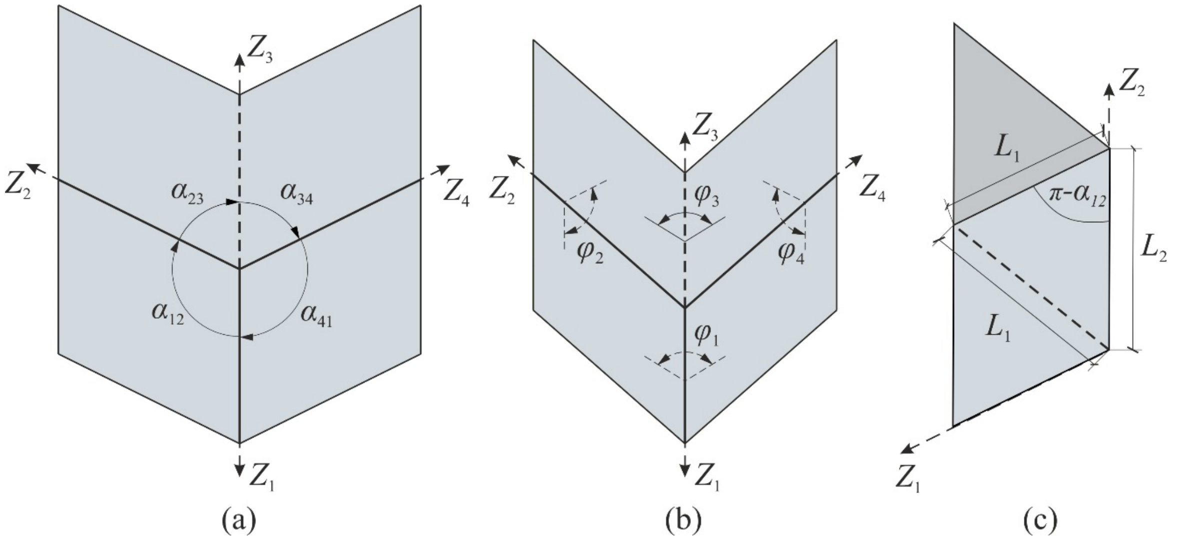

Fig. 2.6 A repetitive part of Miura-ori in (a) the flat, (b) a partially folded, and (c) the fully folded state.

For Miura-ori, though, there is an additional angle relationship that supplements the flat foldability conditions. For the parallelograms' sector angles, there is

$$\alpha_{12}+\alpha_{23}=\alpha_{34}+\alpha_{41}=\pi\,. \tag{2.10}$$

If the characteristic for Miura-ori relationship (2.10) is substituted into the closure equations reported for a general single-vertex four-crease rigid origami (Chiang 1988), (Chen et al. 2015), which for the sector and dihedral angles marked as in Fig. 2.3 are

$$\varphi_1=\varphi_3,\quad \varphi_2=\varphi_4 \quad \text{and} \quad \frac{\tan\left(\dfrac{\varphi_2}{2}\right)}{\tan\left(\dfrac{\varphi_1}{2}\right)}=\frac{\sin\left(\dfrac{\alpha_{12}-\alpha_{23}}{2}\right)}{\sin\left(\dfrac{\alpha_{12}+\alpha_{23}}{2}\right)}, \tag{2.11}$$

then (2.11) simplifies into closure equations specifically for the Miura-ori from Fig. 2.3, i.e.

$$\varphi_1=\varphi_3,\quad \varphi_2=\varphi_4 \quad \text{and} \quad \frac{\tan\left(\dfrac{\varphi_2}{2}\right)}{\tan\left(\dfrac{\varphi_1}{2}\right)}=-\cos\left(\alpha_{12}\right). \tag{2.12}$$

Equations (2.12) are the kinematic relationships of the repetitive Miura-ori piece, which provide insights into its motion. They include a variable type that uses the symbol φ and represents dihedral angles between panels. This will be the preferred way of describing kinematics, with φ's having values usually between 0° and 180° for typical mountain and valley folds. However, if an MV assignment changes at a particular crease, i.e. a fold turns from a mountain to a valley, or vice-versa, this will be noted by variable φ having a value higher than 180°.

If we closely inspect relationships (2.12), we notice they include four variables and three equations. If we specify one of the dihedral angles, e.g. φ_1, the other three will result from these equations. In other words, one input variable defines the Miura-ori fragment's shape. This confirms that the four-panel piece has mobility equal to one. Moreover, as Miura-ori has repetitive units arranged so that they share folds, Fig. 2.2, the dihedral angles' values and the resulting shape propagate throughout the entire pattern. This proves that a global version of a rigid origami Miura-ori is a one-DOF system. It indeed has a single continuous motion connecting the boundary flat and folded states.

At this point, it is worth mentioning that the approach we take to investigate mechanisms' kinematics yields equations that precisely describe the motion but cannot detect panel collisions. The closure equations describe the kinematics from the theoretical point of view, which allows rigid bodies to penetrate each other virtually. Such reconfigurations are impossible physically due to panel collisions happening beforehand, and the kinematic puzzle turns into an engineering problem of contact between rigid facets.

Some of the panel collisions can be easily identified by measuring dihedral angles. A point when a variable φ reaches 0° or 360° describes a state when two panels joined by a revolute fold fully, closing the dihedral angle between them. At such a configuration, panels become coplanar, and contact is initiated. Motions beyond such configurations, when dihedral angles become negative or higher than 360°, are forbidden, as theoretically the adjacent panels continue the reconfiguration while penetrating each other, which is impossible physically. We will perceive such shapes when at least one angle folds fully to be reconfiguration's boundary stages. Beyond them, the motion is impossible as physical models lock due to two rigid facets colliding. Such shapes will therefore be discouraged for structural applications to avoid the contact phenomenon.

The second type of collision is more problematic to identify. It happens between panels not connected by a hinge, i.e. not belonging to a single dihedral angle we can measure. Instead, they emerge on a macro scale when a pattern reconfigures so that any two panels hit each other, not due to a single-hinge-folding coplanarity. In such cases, we will take a visual approach to identifying such stages using digital models. We will also confirm the physical interference using manufactured versions of the patterns. Then, we will approximate the angle values leading to such problematic configurations and highlight them so they can be avoided during reconfigurations.

Notice that we also do not discuss the trivial motions that can happen when origami is flat and some creases align, as in Fig. 2.2(a). Also, as in Fig. 2.3(c), we assume that Miura-ori's panels overlap neatly in the folded shape and form triangles that satisfy

$$L_2 = -2L_1 \cos\left(\alpha_{12}\right). \tag{2.13}$$

Equation (2.13) means that the length of vertical creases L_1 and the characteristic sector angle α_{12} define the length of diagonal creases L_2 and thus the parallelograms' shape.

This research aims to change the kinematics of rigid zero-thick patterns with single DOF by using slits. Starting from Miura-ori introduced in this chapter, we will create new linkages whose equations will indicate more than one motion possibility. We expect that the extra inputs will lead to alternative configurations and folded forms. Moreover, the assemblies will ideally increase their DOF number only by one to keep the pattern manipulation handy.

Chapter 3

Introduction to slit types and mobility calculations

The previous chapter described the tools we will use to determine an assembly's mobility, namely the Kutzbach criterion and the matrix method of analysis. Throughout this work, we will use the Kutzbach formulas as an initial mobility estimator before we model a linkage and perform a detailed analysis that includes solving closure equations symbolically. This is because the Kutzbach equations are straightforward and quick to use, even though, as mentioned earlier, they are only numeric formulas that do not consider geometric specialities. Unfortunately, this means they may sometimes fail to recognise kinematic details and return incorrect values, e.g. not detecting some hidden DOFs. Nevertheless, they are a handy tool for the initial geometry analysis, which helps figure out the minimal number of DOFs an assembly has.

Before we attempt to build multi-DOF versions of rigid Miura-ori and other single-DOF patterns and analyse them using the matrix method, it is crucial to clarify how we will perform the initial assessments of their mobility. Therefore, this chapter introduces a particular approach we will take when using the Kutzbach formulas. It is a step-wise calculation, in which instead of counting the constituent elements of only the final form and using a formula to calculate the DOF number, we assume building an assembly linkage by linkage and updating the mobility result by calculations after each step.

This chapter consists of three separate sections with examples that clarify the approach to the Kutzbach criterion and simultaneously introduce various types and shapes of slits that we can make. Such insight will be helpful in the following chapters.

3.1 Mobility calculation of a rigid uncut Miura-ori

Before we introduce slits, let us first examine the use of Kutzbach formulas on an uncut Miura-ori with rigid panels. In this way, we can explain the step-wise approach and see if the equations indeed show that this pattern is a one-DOF assembly. Figure 3.1 presents stages in which we will build a Miura-ori fragment. We will perform calculations to update the mobility's estimated value after each step.

Figure 3.1(a) shows a two-by-two-panel piece of Miura-ori, a repetitive unit (or a so-called cell) of the pattern. Having analysed it in chapter 2 using closure equations, we know it is a spherical 4R linkage with one DOF. To calculate its mobility correctly using the Kutzbach criterion, we must realise that all its revolute axes met at one vertex, and it is a linkage of a spherical type. Then, we should use the appropriate version of the formula (2.3),

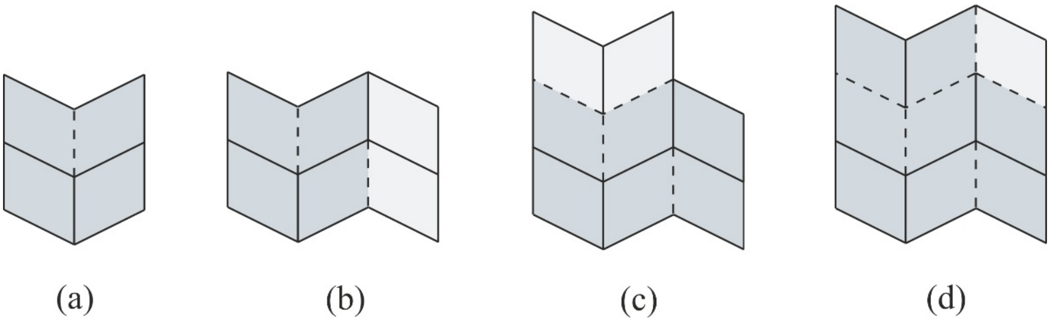

Fig. 3.1 Building a Miura-ori fragment by consecutive panel additions.

in which each panel has potential for three DOFs, before the kinematic constraints, i.e. joints, are added. As we apply the spherical variant of the formula, we will use the '*sph*' subscript. So, we have $N_{sph}=4$ panels and $j_{sph}=4$ revolutes, which return

$$M=3\left(N_{sph}-1-j_{sph}\right)+j_{sph}=3\left(4-1-4\right)+4=1. \tag{3.1}$$

Equation (3.1) shows the Kutzbach criterion returning the correct value. Miura-ori's unit cell indeed has a single DOF, i.e. one angle input defines its shape.

Next, we investigate what happens once we make the pattern larger by adding more panels. Figure 3.1(b) shows the next stage when we add two more panels from the right-hand side to grow Miura-ori in the horizontal direction (marked by the lighter shade of grey). At this stage, first, we make a note of the assembly's mobility before the panel addition, $M_{old}=1$. Next, we realise that the two new panels, along with two panels from the original unit, will form another spherical 4R linkage. As the new panels will be a part of a spherical linkage, we continue using the spherical variant of the formula. Finally, we count the new elements, i.e. $N_{sph}=2$ panels and $j_{sph}=3$ revolutes between them and the old unit, and calculate that

$$M=M_{old}+3\left(N_{sph}-j_{sph}\right)+j_{sph}=1+3\left(2-3\right)+3=1+0=1. \tag{3.2}$$

Notice that we do not fix one panel and remove its all DOFs, i.e. there is no '-1' between N_{sph} and j_{sph} in (3.2) this time. Instead, (3.2) represents adding two panels with three revolutes to the 'old' assembly in such a way that they form a new spherical linkage. The Kutzbach criterion continues to yield the correct DOF number, as the assembly remains a fragment of a typical one-DOF Miura-ori.

Figure 3.1(c) presents an analogous panel addition but this time in the vertical direction. The result is the same, as the old assembly has mobility $M_{old}=1$ and we add $N_{sph}=2$ panels and $j_{sph}=3$ revolutes to form yet another spherical linkage. Again, the formula is as in (3.2) and continues the correct prediction of the fragment's one DOF.

Things become challenging when we finish the rectangular pattern we are building, as in Fig. 3.1(d). Again, first, we denote the mobility before the panel addition, $M_{old}=1$. Then, we realise the light grey panel we are adding also becomes a part of a new spherical linkage formed in the top right corner. We use the spherical variant with the new elements $N_{sph}=1$ and $j_{sph}=2$. This time, it returns

$$M=M_{old}+3\left(N_{sph}-j_{sph}\right)+j_{sph}=1+3\left(1-2\right)+2=1-1=0. \tag{3.3}$$

A value equal to zero means that theoretically, the assembly does not have any freedom to move. However, we know this is a typical rigid-origami Miura-ori that has one DOF. Therefore, once a dihedral angle of any spherical linkage is defined, all its remaining angles adjust due to the linkage's one-DOF nature. Then, the values propagate throughout the pattern as the motion is transmitted to other spherical 4R linkages. This can be confirmed by calculating the dihedral angles using the closure equations obtained from the matrix method (2.12) and showing that all the values are consistent and that the spherical linkages are compatible from the kinematic perspective.

Moreover, the larger we grow the pattern, the more additions as in (3.3) we will have, and the mobility will decrease further, even to significantly negative values. Nevertheless, from the kinematic perspective, the assembly will remain a one-DOF cluster of spherical 4R linkages. This means the Kutzbach formulas start yielding inaccurate results at the stage depicted in Fig. 3.1(d) and continue doing so. This is because they are a numeric approach that does not recognise Miura-ori's geometric speciality. As a result, they fail to notice that all the spherical linkages are compatible in motion. It is not a surprising result, as Miura-ori is known as an overconstrained origami pattern. Due to geometric specialities, such assemblies retain the ability to move and usually have one DOF, while the traditional formulas suggest they have no freedom for any motion.

This example displayed the step-wise approach we will take to building the assemblies and estimating their mobility. Even though the Kutzbach formulas turned out to be inaccurate at some point for the rigid-origami version of Miura-ori without slits, the following examples show how we can use them efficiently to make initial kinematic estimations when slits are introduced.

3.2 Mobility of Miura-ori with different slit types

This section examines various types of cuts that we can make to Miura-ori and how they affect the kinematics. We will consider differently shaped slits of various lengths. This is to estimate the slits that we need to introduce to allow the pattern to exhibit new forms yet not increase its mobility too much, making the pattern's control problematic.

We start our investigations from simple slits along one fold. Exemplary Miura-ori fragments with such cuts are presented in Fig. 3.2(a). Such one-crease-long slits can be made either along a vertical or a diagonal fold. We construct such fragments by taking a six-panel piece of the pattern and then cutting it along the internal crease. We avoid cuts along the

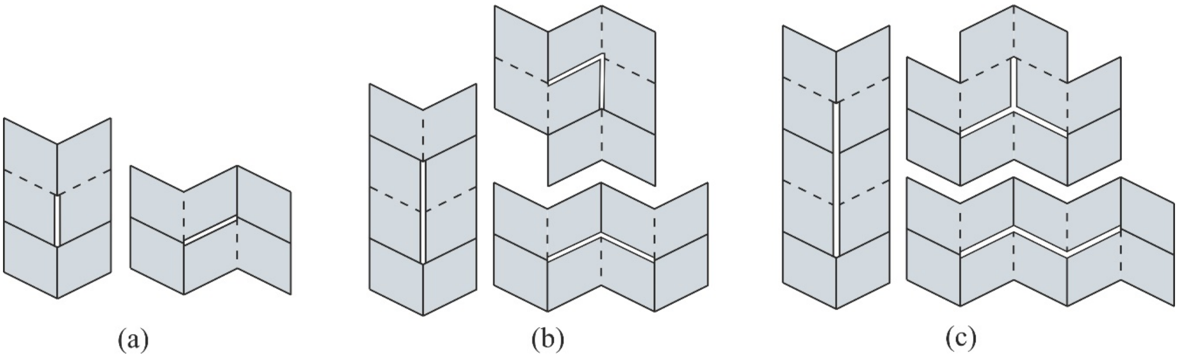

Fig. 3.2 Miura-ori fragments grouped according to the cut types. The pieces containing (a) single-crease-long, (b) two-crease-long (double), and (c) three-crease-long slits.

edge folds as they can result in some panels being connected to the other ones only via one revolute. That would introduce trivial motions like locally flapping panels.

If the assemblies in Fig. 3.2(a) are examined closely, we notice that the slits turn the Miura-ori fragments into closed loops of six rigid bodies connected by six revolute joints. We realise that they are mechanical linkages. This time, however, all revolutes do not meet at one point. This means we deal with spatial linkages comprised of six revolutes, i.e. spatial 6R linkages. Therefore, to initially estimate their mobility, we use the spatial version of the Kutzbach formula with $N = 6$ panels and $j = 6$ revolutes and calculate that

$$M = 6(N-1-j)+j = 6(6-1-6)+6 = -6+6 = 0. \tag{3.4}$$

The mobility formula suggests such assemblies have no freedom. However, we realise that the fragments in Fig. 3.2(a) can still move traditionally, i.e. have one DOF. We know that introducing a slit removes a joint, i.e. a kinematic constraint, which can only increase the assembly's freedom. As the pattern before the slit addition could already move in the Miura-ori way, we conclude that the Kutzbach formula is inaccurate again. We know it predicts only the minimal DOFs and is incapable of detecting some geometric specialities.

Moreover, we can realise that a single-crease-long slit does not change the kinematics. Even though it separates two panels, their edges adjacent to the slit are still defined by the two vertices at their ends. Because a single-crease cut does not destroy any vertex, the separated panels still share the same vertices at the slit's ends due to the connections to neighbouring panels. This means that whatever the assembly configuration, the two separate edges resulting from a slit always have the same end positions and are thus colinear, i.e. such slit cannot open. In other words, although a revolute joint is removed, the resulting edges cannot separate. As a result, the panels continue only rotating against each other, i.e. the assembly behaves as if a revolute was still there. This further reinforces that the kinematics of the fragments in Fig. 3.2(a) does not change and that they remain one-DOF assemblies.

This example shows that a slit inside a Miura-ori fragment can create a spatial linkage. However, a one-crease-long cut is not satisfactory, as it does not change the kinematics. The assembly becomes an overconstrained spatial 6R linkage that, thanks to Miura-ori's geometric specialities, maintains one DOF. A single DOF allows only the traditional folding and is not enough to trigger alternative configurations. Therefore, the subsequent attempts examine longer slits.

Figure 3.2(b) presents a few variants of Miura-ori fragments with two-crease-long slits. We construct such pieces by making a cut along two adjacent Miura-ori folds and keeping only the panels adjacent to the slit or its vertices. As a result, this time, the fragments are closed loops of eight rigid panels connected by revolutes, i.e. spatial 8R linkages. We update the parameters for $N = 8$ and $j = 8$ and use the spatial version of the mobility formula that returns

$$M = 6(N-1-j)+j = 6(8-1-8)+8 = -6+8 = 2. \tag{3.5}$$

The Kutzbach criterion suggests the minimal DOF number of such assemblies is two. This time, the formula returns an accurate result, and this is not only the minimal but the actual number of DOFs. We can confirm this by manufacturing physical models of such rigid-panel assemblies or constructing their digital versions. Two DOFs is a promising result, as they give extra freedom to manipulate an assembly and are still relatively easy to control.

We can notice that the Rubik's Magic mentioned in the thesis' introduction is an example of such an assembly in its starting configuration. It is built out of eight square rigid panels connected by hinges, with a double slit inside. As a result, the puzzle is also a closed kinematic chain of eight bodies and has two DOFs. Having mobility higher than one allows various manipulations, which result in the toy's many alternative shapes.

Moreover, we examine also variants of slits that are three-crease-long, with some examples presented in Fig. 3.2(c). Similarly, to construct such assemblies, we make cuts to Miura-ori along three neighbouring folds that share vertices and keep only the adjacent panels. This time, the closed loops consist of $N=10$ panels connected by $j=10$ revolutes. As they are spatial 10R linkages, the Kutzbach formula returns

$$M = 6(N-1-j)+j = 6(10-1-10)+10 = -6+10 = 4. \tag{3.6}$$

This is again an accurate DOF number result, which can be verified with physical or digital models. Even though four DOFs provide a lot of freedom, which can significantly improve Miura-ori's ability to obtain new forms, such a number makes the assembly problematic from the control perspective. Reconfiguring such patterns manually using hands is complex and requires dexterity. If the control were exercised mechanically, such a small

Miura-ori fragment would require not only one or two actuators, as in the previous examples, but as many as four.

This section showed that introducing slits inside Miura-ori can turn it locally into spatial linkages. Depending on the length of the slits, we can create linkages of a higher or lower degree, which consist of more or less revolute joints, respectively. The longer the slits and the more panels and revolutes the loop has, the higher the assembly's DOF number. While single-crease slits do not bring new DOFs and keep mobility equal to one, two- and three-crease-long cuts add extra DOFs, which is promising from the new configurations' perspective. Introducing a two-crease long slit, which we call a double slit, results in a local spatial 8R linkage with two DOFs. They represent a reasonable balance between the freedom to reconfigure the pattern and the complexity of such a procedure. On the other hand, longer cuts bring significantly more DOFs what makes the pattern's control problematic.

Therefore, Miura-ori fragments consisting of eight panels with double slits inside, i.e. Miura-derived spatial 8R linkages, will be the fundamental building blocks that we will use to construct a reconfigurable versions of the pattern. Research has shown that such two-DOF spatial 8R mechanisms can exhibit reconfigurability (Pfurner 2018) (Tang and Dai 2018) (Wang et al. 2021). Before we move to it, though, the last section of this chapter presents an example of using such a spatial 8R linkage in connection with a spherical 4R linkage to show how their kinematics can affect each other. This example also clarifies our step-wise approach to using Kutzbach formulas when dealing simultaneously with spatial and spherical linkages.

3.3 Mobility of a Miura-ori with a double slit and a spherical 4R linkage

In this section, we will analyse an assembly presented in Fig. 3.3(a). It is a three-by-three-panel Miura-ori piece with a two-crease-long slit in the upper part and a spherical linkage in the bottom-left corner. This means that this Miura-ori fragment includes a spatial 8R linkage, consisting of the panels around the slit, and a spherical 4R linkage, which shares three panels with the 8R loop. In order to clarify the kinematics and estimate the assembly's mobility, we take the step-wise approach as if we were building the fragment one linkage after another.

First, we assume there is only the spatial linkage, as in Fig. 3.3(b). We calculate such an assembly's DOFs using the spatial version of the formula, with $N = 8$ rigid panels and $j = 8$ revolutes. The result is mobility equal to two, as in (3.5). This means that the double slit turns an eight-panel Miura-ori piece into a two-DOF assembly.

However, in the next step, Fig. 3.3(c), we add the remaining panel in the bottom right corner to finish a rectangular assembly. As a result, we construct a spherical 4R linkage. We know that this is a one-DOF system, as calculated in (3.1). Once any of its dihedral angles

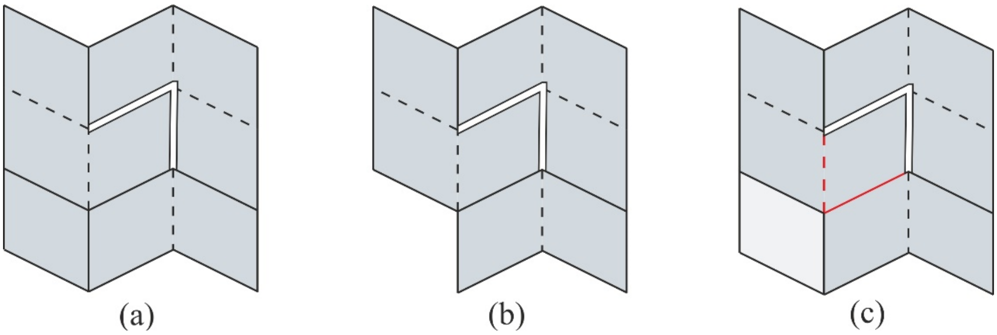

Fig. 3.3 (a) A Miura-ori piece consisting of a spatial 8R linkage merged with a spherical 4R linkage; (b) is the 8R loop before creating the spherical linkage; (c) is the final panel addition forming the spherical linkage that couples the 8R loop's two creases.

is defined, the other three adjust according to its closure equations (2.12). Simultaneously, the spherical linkage shares with the spatial 8R linkage three panels and two revolutes, with the joint creases marked in red in Fig. 3.3(c). If one of these two folds' angles is specified, the other adjusts according to the spherical linkage's kinematics. This means these two revolutes are coupled, and the spatial linkage now has seven, not eight, independent hinges. A loop like this, according to the Kutzbach Criterion, has only one DOF. The spherical linkage constrains the eight-panel loop and decreases overall freedom from two to one.

We verify that with the next step in our mobility calculation. We denote the mobility before adding the last panel to be $M_{old} = 2$. The last step brings $N_{sph} = 1$ rigid panel and $j_{sph} = 2$ revolute joints that form a spherical linkage, i.e. require the Kutzbach formula with the value '3'. Thus, the final mobility indeed equals

$$M = M_{old} + 3\left(N_{sph} - j_{sph}\right) + j_{sph} = 2 + 3\left(1-2\right) + 2 = 2 - 1 = 1. \qquad (3.7)$$

This example shows a situation that will often occur during our kinematic investigations – when the traditional spherical 4R linkages, typical for the uncut Miura-ori, share panels with the spatial linkages created after introducing slits. The presented case is not attractive from the perspective of new configurations. It shows a spherical linkage reducing spatial linkage's mobility from two to one, which means constraining the Miura-ori so it again can exhibit only the traditional folding. However, this analysis provides two significant insights.

First, while building a multi-DOF assembly, we must be careful about excessive spherical linkages, which may bring down the DOF number and enforce only the traditional motion. Simultaneously, though, such spherical 4R linkages can also be used throughout the pattern as a repetitive element that reduces the excessive mobility to simplify the control.

For example, such spherical linkages could be positioned in the pattern strategically to use their one-DOF kinematics. They would constrain the motion once the DOF number gets too big due to excessive cuts to make the assembly manipulation less troublesome.

In conclusion, this chapter explained the step-wise approach we take for initial DOF estimations using the Kutzbach formulas. The evaluation of mobility after each stage allows us to control the DOF number and construct origami patterns in a more kinematically-aware manner, out of the pieces whose freedom we can predict. Simultaneously, the chapter showed how different shapes and lengths of slits affect mobility locally and how kinematic linkages can constrain each other. Equipped with this insight, we move to the next chapter, in which we will attempt to build a reconfigurable version of a rigid-origami Miura-ori. We want it to experience shapes and folded forms beyond the ones resulting from the traditional one-DOF folding.

Chapter 4

Reconfigurable Miura-ori with vertical slits

Chapter 4 presents the first attempts of cutting traditional origami to find its new forms and folded shapes. It focuses on rigid-panel single-DOF Miura-ori, which we want to transform into a reconfigurable structure with alternative motions. Inspired by the Rubik's Magic toy and hoping to reproduce some of its kinematics, we will introduce similar two-crease-long slits along Miura-ori's inner edges.

We will work with repetitive sub-assemblies, which, similarly to the toy, consist of eight panels with a two-crease-long slit inside. Such new Miura-ori cells will belong to the linkage group from Fig. 3.2(b) and have the minimal mobility value of two. We will use them mainly due to two reasons. First, building block's freedom should be higher than one DOF. Extra inputs offer a choice for starting the motion and reconfiguring the assembly. A sub-assembly with a single DOF would have only the traditional motion possible. Instead, we prefer building blocks with more than one DOF, as we want to join them into a structure with increased mobility that promises alternative motions and new forms.

Simultaneously, though, while each extra DOF increases the freedom to manipulate the pattern and thus its chances to obtain alternative shapes, it makes the control problematic. Pattern manipulation becomes troublesome when more inputs are required. We showed that making slits longer by even one edge increases mobility substantially, e.g. from two to four, as in (3.6). Therefore, building blocks that are spatial 8R linkages with two DOFs represent a reasonable balance between available manipulations and the complexity of exercising them.

In this chapter, we will take a particular approach to joining such building blocks together. After we analyse a repetitive part with a slit that gives two DOFs, we will regularly multiply such elements in orthogonal directions and merge them to build a larger pattern. This is to ensure that the kirigami Miura-ori that we are building has a regular slit arrangement. Then, we will analyse the resulting assembly's mobility and kinematics to judge if the outcome is satisfactory.

The layout of the chapter is as follows. First, section 4.1 provides a kinematic analysis of a building block for the pattern, a repetitive Miura-ori cell with two DOFs. Then, section 4.2 explains how to multiply and join such cells together in the horizontal direction. Next, section 4.3 describes the new configurations such assemblies can have. Then, section 4.4 explains how to add cells in the vertical direction. Next, section 4.5 evaluates the kinematics of a finished global assembly and provides the final estimation of mobility and the number of alternative forms. Lastly, section 4.6 concludes the chapter.

4.1 Single Miura-ori cell with a double vertical slit

This section focuses on a cell with a two-crease-long (double) vertical slit inside. It is one of the most straightforward cuts that can alter the Miura-ori's kinematics. If we take a two-by-four piece of the pattern and cut it along the two inner folds, we obtain a new Miura-ori cell with a double slit inside. Figure 4.1 shows the cell as well as the equivalent mechanical linkage describing it. Similar to Rubik's Magic, it is a closed kinematic chain of eight rigid bodies connected by revolute joints. Applying the spatial version of the Kutzbach formula confirms it has at least two DOFs, (3.5).

To verify the kinematics of the linkage in Fig. 4.1(b), we perform symbolic calculations using the matrix method. As a result, we obtain a set of closure equations. They are relationships between the linkage's variables that describe its motion. However, instead of using θ, we can express the kinematics with dihedral angles φ. This type of variable makes

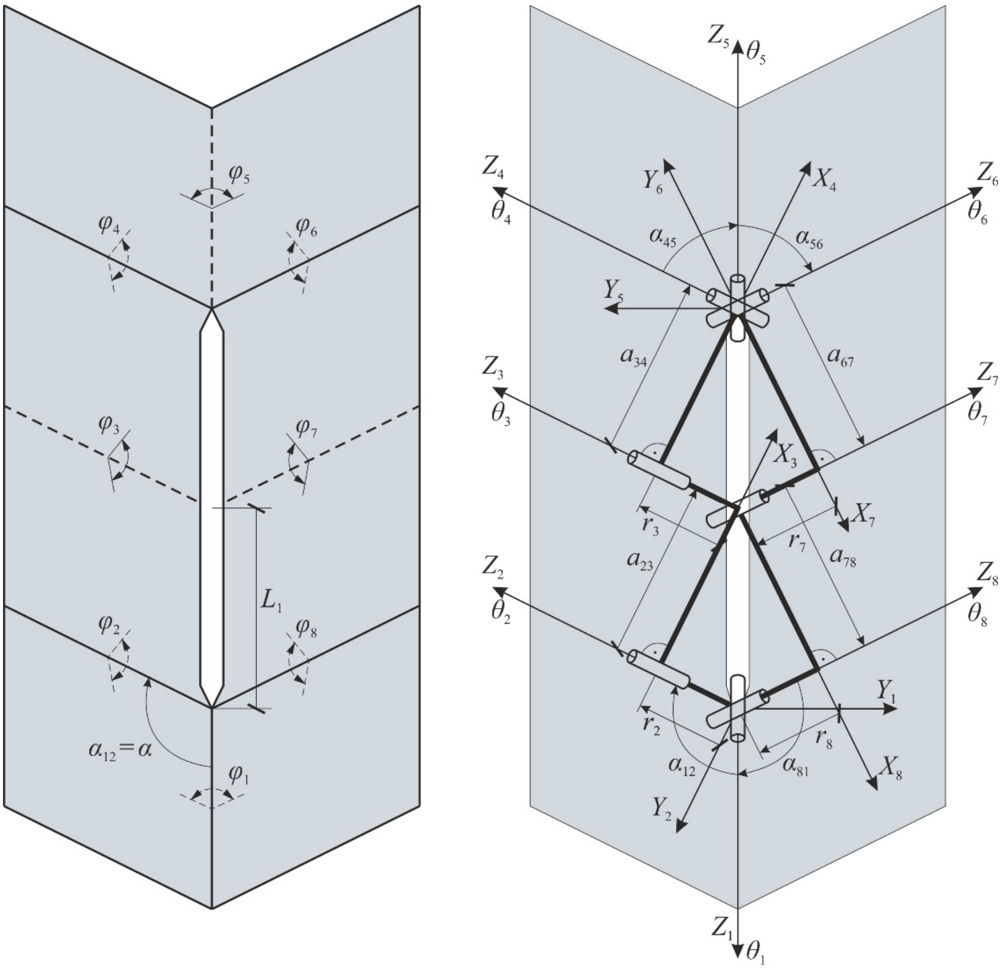

(a) (b)

Fig. 4.1 (a) A single cell with the double vertical slit, and (b) its equivalent mechanical linkage.

the formulas more intuitive as dihedral angles are easier to visualise and track. For the closure equation derivations, see appendix A.

First, we learn that for the linkage in Fig. 4.1(b), there is

$$\varphi_5 = \varphi_1 . \tag{4.1}$$

Equation (4.1) means that once we specify a dihedral angle at one of the vertical creases, the second one inherits the angle and unfolds equally. Additionally, we also find two relationships that connect φ's at vertical and diagonal creases, i.e.

$$\frac{\tan\left(\frac{\varphi_2 - \varphi_3 + \varphi_4}{2}\right)}{\tan\left(\frac{\varphi_1}{2}\right)} = -\cos(\alpha) \text{ and } \frac{\tan\left(\frac{\varphi_6 - \varphi_7 + \varphi_8}{2}\right)}{\tan\left(\frac{\varphi_5}{2}\right)} = -\cos(\alpha). \qquad \text{(4.2), (4.3)}$$

The linkage's remaining closure equations are

$$\begin{gathered}\sin(\varphi_4) + \sin(\varphi_3 - \varphi_4) + \cos(\varphi_1)\big(\sin(\varphi_6) - \sin(\varphi_6 - \varphi_7)\big) \\ + \cos(\alpha)\sin(\varphi_1)\big(2 + \cos(\varphi_6) - \cos(\varphi_6 - \varphi_7)\big) = 0\end{gathered} , \tag{4.4}$$

$$\begin{gathered}\sin(\varphi_1)\big(\sin(\varphi_6) - \sin(\varphi_6 - \varphi_7)\big) + \\ \cos(\alpha)\Big(2 + \cos(\varphi_4) - \cos(\varphi_3 - \varphi_4) - \cos(\varphi_1)\big(2 + \cos(\varphi_6) - \cos(\varphi_6 - \varphi_7)\big)\Big) = 0\end{gathered} \tag{4.5}$$

and

$$\cos(\varphi_4) - \cos(\varphi_3 - \varphi_4) - \cos(\varphi_6) + \cos(\varphi_6 - \varphi_7) = 0 \tag{4.6}$$

Notice that the six equations (4.1) to (4.6) contain eight variables φ. Therefore, we must assume at least two φ's, e.g. one from (4.1) and one of the remaining angles, so that the rest is defined by the formulas. This confirms that the linkage and thus the cell from Fig. 4.1 are a two-DOF system. In this chapter, we will choose φ_1 and φ_6 to express the remaining dihedral angles, and they become the two inputs that decide on the cell's shape.

To explain the two-DOF nature of the kinematics, we will constrain one DOF by freezing dihedral angle φ_1 at a specific value. As φ_1's value decides how much folded the cell is, this disables the standard Miura-ori motion. If we choose our first input φ_1 to have a specific value, e.g. 90°, we can use (4. 1) to (4.6) to express other angles as functions of the second input – φ_6. Figures 4.2 and 4.3 show plots of such relationships, when φ_1 is frozen at a value and φ_6 is used to alter the cell's shape being the only remaining active input. In the plots, a value of φ_i higher than 180° means that crease *i* changed its mountain-valley (MV) fold type assignment, i.e. a mountain fold turned into a valley or vice versa. The plots are generated for parameter α equal to 135°.

Figure 4.2 presents a 3D plot of the relationship between the input φ_6 and the output variables φ_4 and φ_7. It shows the cell's alternative motion paths, allowed by the second DOF. We will refer to the cell's typical Miura-ori configuration as state 0 (point *A* in Fig. 4.2). From this position, the upper part of the cell can move upwards, but this shape change includes panel intersections (point *B*). In physical models, the rigid parallelograms would start colliding beforehand what would prevent such a motion. However, our goal is to achieve seamless reconfigurations without any contact or collisions. Therefore, as this section of the path is unavailable physically due to panels hitting each other, we grey it out. When the assembly is in a state that neighbours such greyed-out curve fragments, which require panel intersections to continue the motion, such paths should be avoided. Therefore, *A*, the input angle controlling the assembly should be chosen to steer clear of the greyed-out part. Indeed, it is possible to increase φ_6's value instead and start an opposite downward movement (point *C*). It continues until we achieve what we call state 1 (point *D*).

This configuration allows us to change the MV assignment for creases 3 and 7 (where dihedral angles φ_3 and φ_7 are). If both folds become mountains, the intersections again

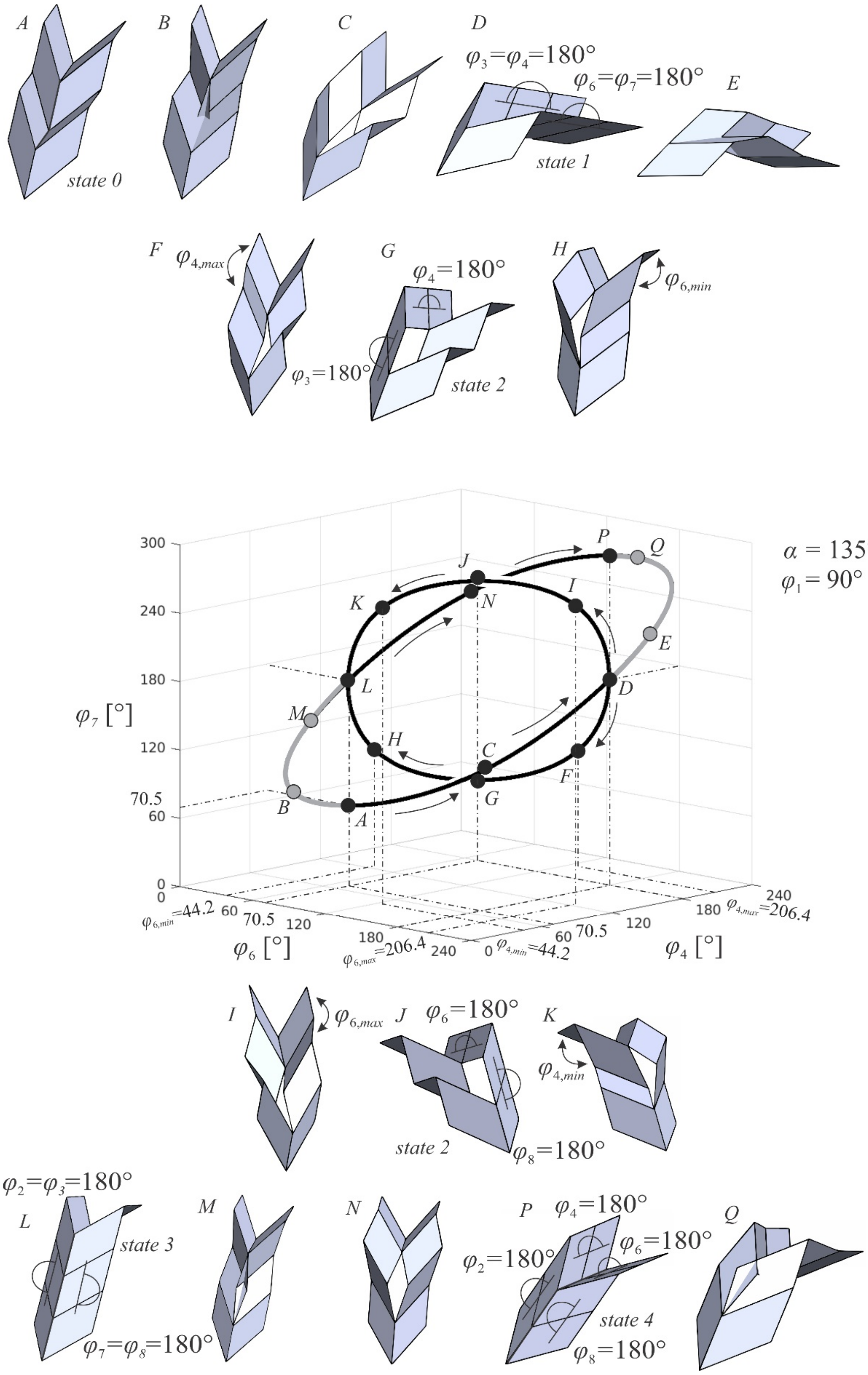

Fig. 4.2 The reconfiguration of a single cell with φ_1 frozen and φ_6 used to alter the shape. The relationship between output variables φ_4 and φ_7 and the input φ_6; *a* to *q* are different reconfiguration stages.

indicate a forbidden motion (point *E*) that should be avoided. If both stay as valleys, the cell returns to state 0. However, if one fold changes into a mountain and the second one stays as a valley, a further motion is possible, marked by points *F* or *I*. If continued, we reach an intermediate state 2, when one arm of the cell is in the natural Miura-ori arrangement, but the opposite one is in a new upward position. Points *G* and *J* show the two possible variants. From here, we can continue the motion upwards (*H* or *K*) and achieve the configuration *L*, which we will call state 3.

In this shape, creases 3 and 7 can change their MV assignment again. If both become valleys, the intersections occur with further motion, which is again physically impossible (point *M*). If the creases have different assignments, i.e. one is a valley and the second one a mountain, the cell returns to state 2. However, with the double mountain assignment, the upper part of the assembly moves downwards (point *N*) until the cell achieves state 4, marked by *P*. This configuration terminates the path, as the cell can only return to the previous states or experience a further motion with intersections (point *Q*), which in reality means a collision of panels if this grey section is not avoided.

The entire motion sequence, from state 0 to state 4, can be realised by the second DOF only, while the first one remains frozen. This means the cell can follow the paths without triggering the original Miura-ori motion. In order to activate the traditional folding, we need to change angle φ_1. Meanwhile, to switch between the new configurations described above, we should change one of the dihedral angles at the diagonal creases. In the example, we used φ_6, but we could also choose φ_2, φ_3, φ_4, φ_7 or φ_8. Notice φ_5 is not an option as it always takes φ_1's value (4.1) and is only an alternative to φ_1 to control the traditional folding.

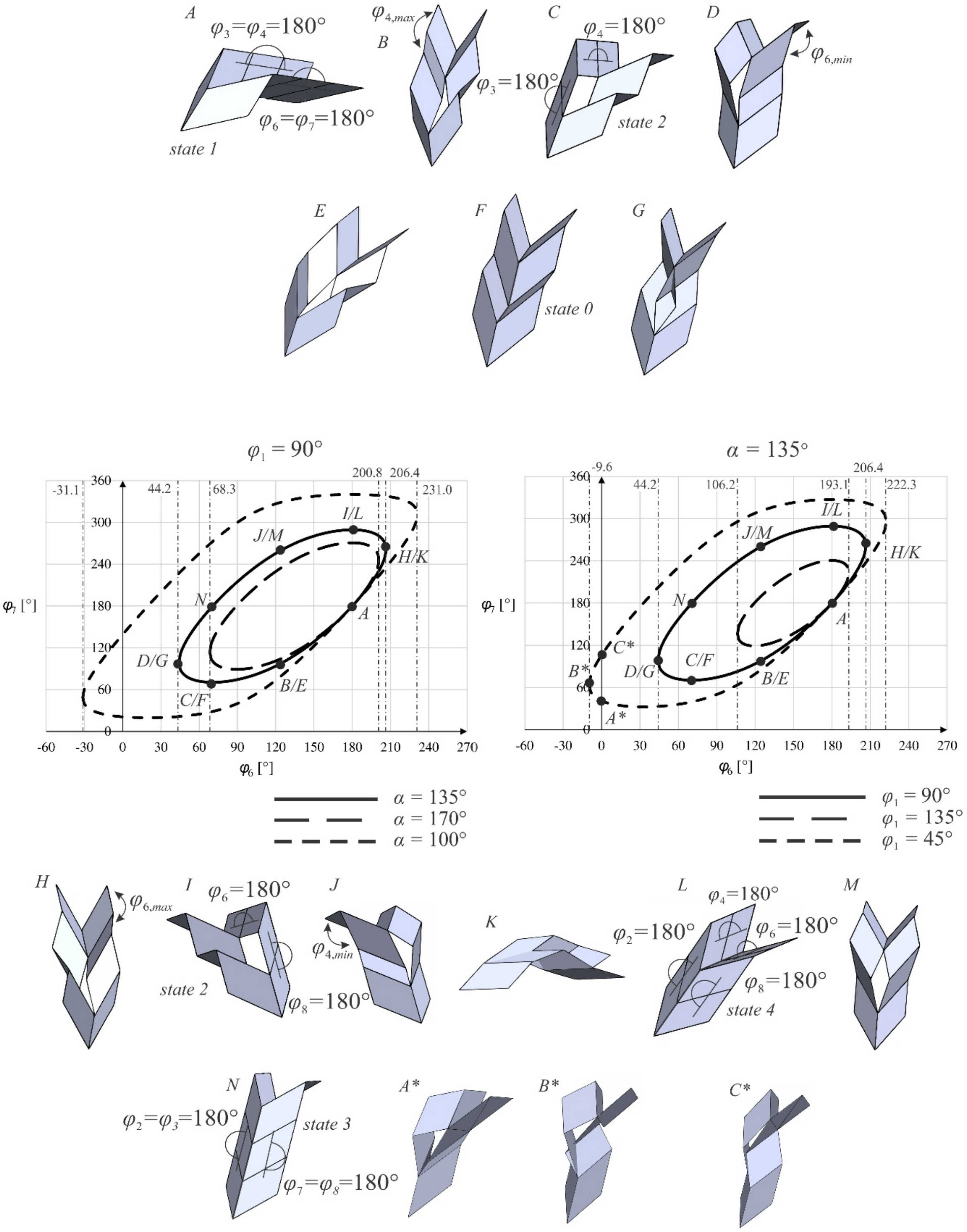

Fig. 4.3 The reconfiguration of a single cell with φ_1 frozen and φ_6 used to alter the shape. The relationship between φ_7 and φ_6 when different values of parameter α and frozen variable φ_1 are chosen; *a* to *c** are different reconfiguration stages.

To provide more insight, Fig. 4.3 shows the relationship between the output φ_7 and the input φ_6 variables in the form of a 2D plot. Two separate curves are leading from point *A* to *N*. They represent four alternative motions that allow the cell to reach state 3 from state 1. These are separate reconfigurations via points *B*-*C*-*D*, *E*-*F*-*G*, *H*-*I*-*J* and *K*-*L*-*M*. However, if we exclude the movements that exhibit intersections along the paths, it turns out two variants remain – via *B*-*C*-*D* and *H*-*I*-*J*. For the cell to experience a motion that represents a complete loop around the plot, it should reconfigure along both of them. It should first go from state 1 to state 3 via state 2, e.g. point *C*. Then, it should return to state 1 via the second variant of state 2, when the opposite parallelograms are in the upper position, e.g. point *I*.

Figure 4.3 also shows some modifications to the cell. We can change the crease pattern's geometry (different value of α) or how much unfolded the cell is when we decide to trigger new motions (different value of the frozen φ_1). Both the alterations have a similar effect on the plot. If we choose a bigger α *or* φ_1, the plot's size decreases. On the contrary, smaller values enlarge it. Figure 4.3 compares different loop sizes resulting from various inputs.

Notice that when either α or φ_1 are small enough, the plot enlarges so much that its part goes past a coordinate axis. Some values of φ_6 become equal and then lower than zero. This means that at some point, the dihedral angle folds fully (*A** or *C**) and then continues motion with interpenetrating panels (point *B**). Physically, such a motion would not be possible. Once φ_6 would become zero, its panels would cause blockage of the cell, in *A** or *C**. This example also highlights that we cannot assume too small α or φ_1 when designing the cell. Otherwise, we may cause self-collisions. Next, this chapter explains how to join multiple two-DOF cells into a bigger Miura-ori with slits.

4.2 Horizontal merging of the cells

Figure 4.4(a) presents a part of the Miura-ori crease pattern with two double vertical slits parallel to each other. It is two single cells merged so that they share four panels and three hinges in the middle. Therefore, we will refer to such assemblies with more than one slit as consisting of multiple cells. The fragment in Fig. 4.4(a) is created after adding extra four panels to a single Miura-ori cell with the double slit from the right-hand side and forming a second rigid-body loop. Figure 4.4(b) presents the assembly as two mechanical linkages.

First, we attempt to estimate the assembly's mobility by using the stepwise approach to Kutzbach formulas. We mark the mobility of the assembly before the panel addition, i.e. the

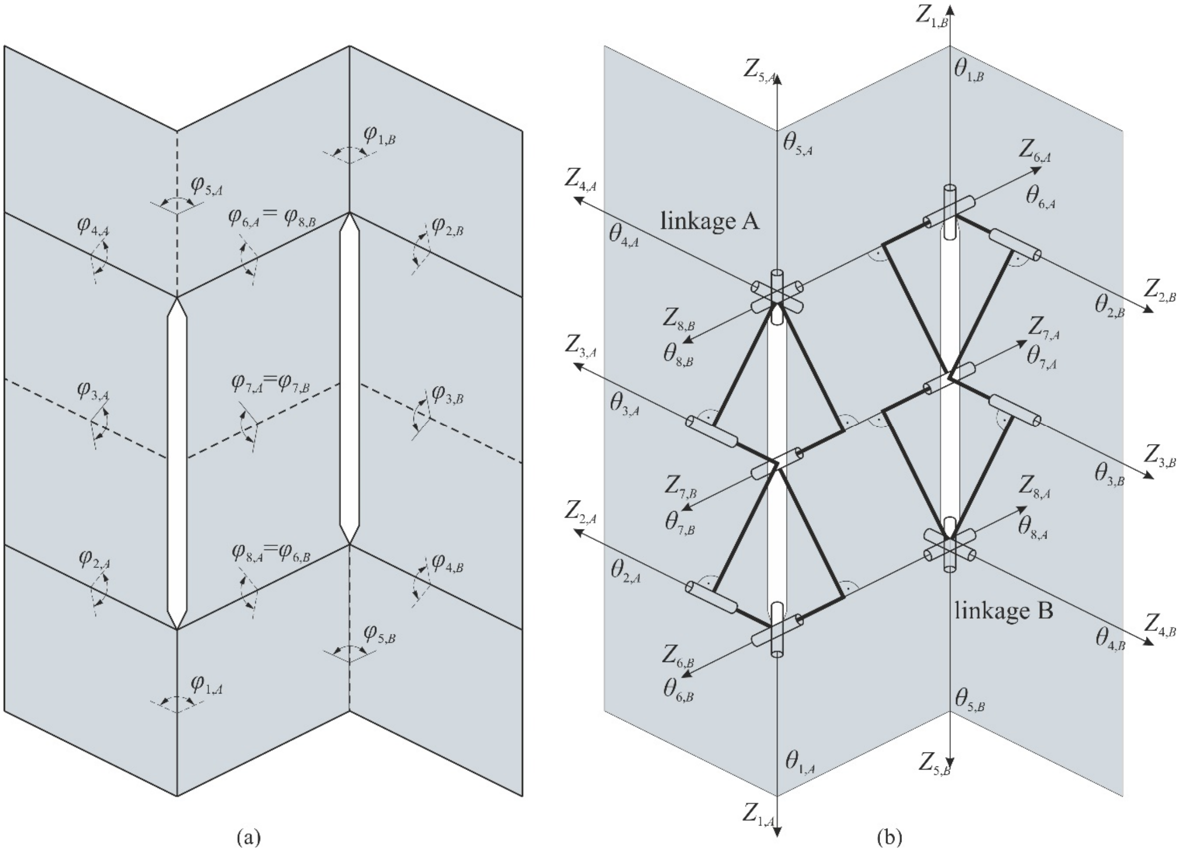

(a) (b)

Fig. 4.4 (a) A horizontal assembly of two cells with the double vertical slits, and (b) its equivalent mechanical-linkage version.

DOFs of a single cell as $M_{old} = 2$. Then, we count the new elements, i.e. $N = 4$ panels and $j = 5$ revolutes. We realise that the new loop is a spatial linkage and use the appropriate formula with the value ‘6’. The resulting mobility is

$$M = M_{old} + 6(N - j) + j = 2 + 6(4 - 5) + 5 = 2 - 1 = 1. \tag{4.7}$$

The above result suggests that such panel and hinge addition constraints the original single cell and reduces the assembly’s mobility to only a single DOF, i.e. to the traditional motion. However, the Kutzbach formulas being a numeric approach turn out to be again inaccurate and fail to recognise a geometric speciality that allows the assembly to maintain two DOFs, which we explain below. At this stage, we continue using the criterion to display its inaccuracies and maintain continuity, as later, in chapter 6, it will turn out to be a useful tool for DOF approximation while building a pattern with a finite mobility from scratch.

As linkage B is the same as linkage A but turned upside-down, it also needs two dihedral angles specified to express its remaining ones, using (4.1) to (4.6). Figure 4.4(a) shows that linkage A passes three dihedral angle values via the shared creases. This is enough to define the shape of linkage B. Moreover, the third angle passed proves to be redundant as linkage B needs only two inputs being a two-DOF system. After receiving them, the third angle already takes a value resulting from linkage B’s own closure equations. It turns out to be in agreement with the remaining input passed from linkage A. This can be proven by calculations carried out either symbolically or on arbitrarily assumed angles. However, due to the lengthy nature of these formulas, such proofs are not reported. Instead, they can both be reproduced by using the complete set of closure equations, (4.1) to (4.6).

Moreover, we see from Fig. 4.4(a) that

$$\varphi_{6,B} = \varphi_{8,A}\,,\ \ \varphi_{7,B} = \varphi_{7,A}\ \ \text{and}\ \ \varphi_{8,B} = \varphi_{6,A}\,. \tag{4.8}$$

We substitute (4.8) into (4.3) for linkage B, and compare the result with (4.3) for linkage A

$$\frac{\tan\left(\dfrac{\varphi_{8,A} - \varphi_{7,A} + \varphi_{6,A}}{2}\right)}{\tan\left(\dfrac{\varphi_{5,B}}{2}\right)} = -\cos(\alpha) = \frac{\tan\left(\dfrac{\varphi_{6,A} - \varphi_{7,A} + \varphi_{8,A}}{2}\right)}{\tan\left(\dfrac{\varphi_{5,A}}{2}\right)}. \tag{4.9}$$

We notice that

$$\tan\left(\frac{\varphi_{5,B}}{2}\right) = \tan\left(\frac{\varphi_{5,A}}{2}\right), \tag{4.10}$$

what for the MV assignment in this case gives

$$\varphi_{5,B} = \varphi_{5,A}\,. \tag{4.11}$$

The above means that the three inputs that linkage B inherits from linkage A result in both cells having eventually the same φ's at all vertical creases. In other words, the cells merged horizontally are always equally folded. Additionally, we know that the same equations describe the motions of both linkages. Thus, if the shared panels in the middle are moved in a particular way, the side branches respond analogously to each other. Thus, the second loop mimics the first one's behaviour, and the entire assembly maintains the two-DOF nature.

As a result, if the Miura-ori folding is forbidden, i.e. φ's at all vertical creases get frozen, the second DOF activates an alternative motion that propagates horizontally. Figure 4.5 presents a diagram of such a reconfiguration. However, it turns out that due to the assembly's specific geometry, the merged cells cannot follow the single linkage's entire reconfiguration sequence between state 0 and 4, as in Fig. 4.2, which is explained below.

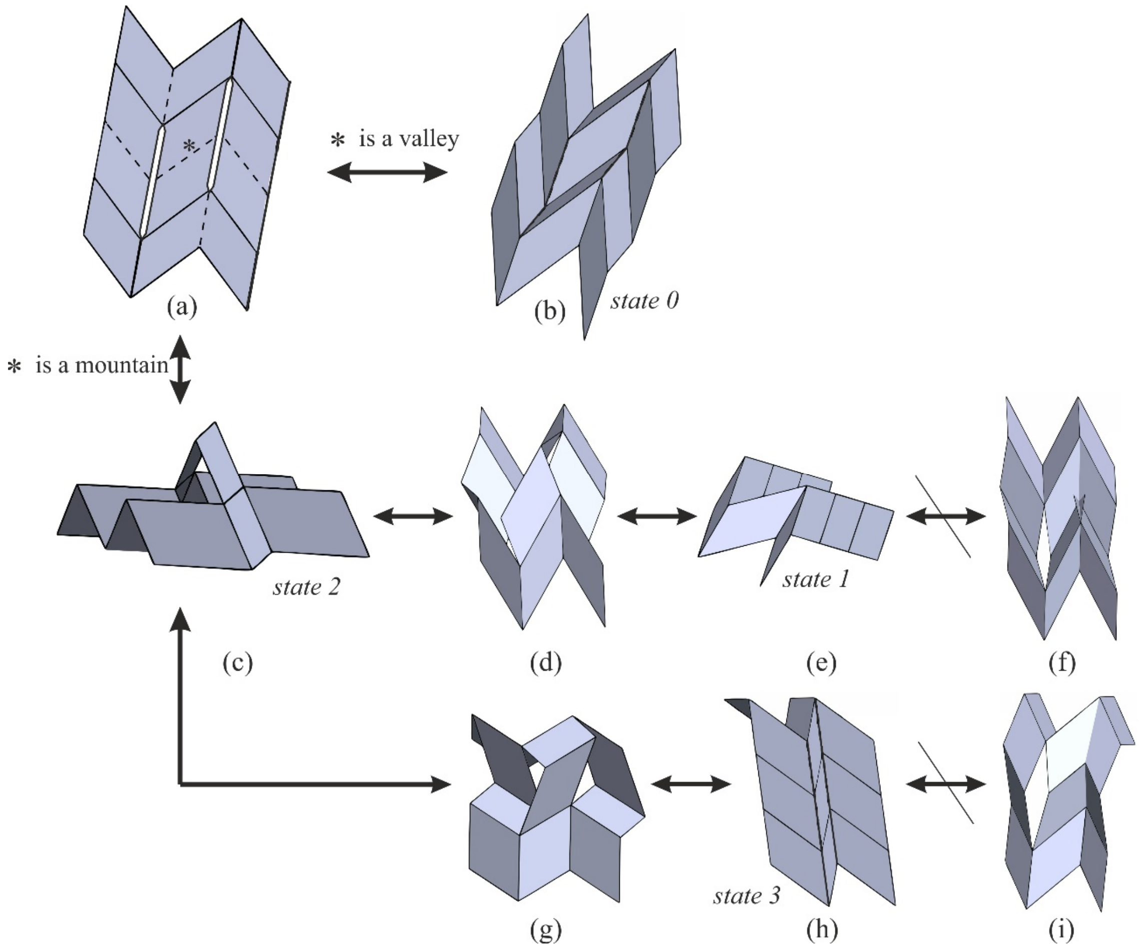

Fig. 4.5 A horizontal assembly of two cells with the double vertical slits in (a) the flat state, (b) state 0, (c) state 2, (d) the downward motion from state 2, (e) state 1, (f) the motion from state 1 to state 0 with intersections, (g) the upward motion from state 2, (h) state 3, and (i) the motion from state 3 to state 4 with intersections.

First, notice that from the flat state, Fig. 4.5(a), we can always fold the pattern in a standard way to take the traditional Miura-ori shape, Fig. 4.5(b). In this form, it is straightforward to exercise the typical one-DOF behaviour. However, to examine the new motion paths and report how they are limited, we must access the assembly's alternative state, equivalent to single cell's state 2, Fig. 4.5(c).

Thanks to the slits, this is possible starting from the same crease pattern. While in the flat state, we should reverse the MV assignment of crease 7,A (the middle diagonal one, marked by * in Fig. 4.5(a)). Then, if we decrease the value of φ_1 to start folding, it turns out the motion leads to a two-cell equivalent of state 2, Fig. 4.5(c). To activate the new motions in this configuration, we should freeze the input defining the vertical creases, i.e. φ_1. Now, using only the second DOF, i.e. changing φ at any diagonal crease, we can switch between states 1, 2 and 3 freely and without collisions, as illustrated in Fig. 4.5.

However, once we want to go to state 0 from state 1, we learn this motion is impossible, as intersections occur among the second cell's panels. Such shape, presented in Fig. 4.5(f), is impossible to reach physically, as contact between rigid panels would happen as soon as we start this reconfiguration when in state 1. Similar collisions prevent us from reaching state 4 from state 3, Fig. 4.5(i). This means a horizontal assembly of more than one cell can reproduce the single cell's motion sequence only partially, between states 1, 2 and 3.

If we continue adding panels to build new cells horizontally, we will create more similar linkages connected to the previous ones, which behave analogously. This means that no matter how many cells with the double vertical slits are merged in a row, the assembly maintains two DOFs and displays reduced but similar to the single cell's behaviour.

Notice that the two-DOF nature is maintained even though the Kutzbach formulas report that each new loop formed by the new panels should decrease mobility by one. As a result, a pattern consisting of many cells merged horizontally would be an example of an overconstrained assembly. According to theoretic formulas, it would have zero or negative mobility, i.e. should not move, but in reality, it would exhibit two DOFs that allow reconfiguration. The next section shows how the assembly's slit-enabled states lead to new folded forms.

4.3 New folded configurations

As the number of the slits, i.e. the 8R cells, in a row does not change the DOFs value, now we will combine four of them. Figure 4.6(a) shows such an assembly in its flat state. The option to fold it in the traditional Miura-ori way remains, as illustrated in Fig. 4.6(b) and (c). However, for the new configurations, we need to access the assembly's state 2. We do this in a way similar to the one in section 4.2. First, we reverse the MV assignment for the middle diagonal creases within every second vertical branch of the parallelograms (marked by * in Fig. 4.6(a)). Then, we use the first DOF and fold the pattern partially, as in Fig. 4.6(d).

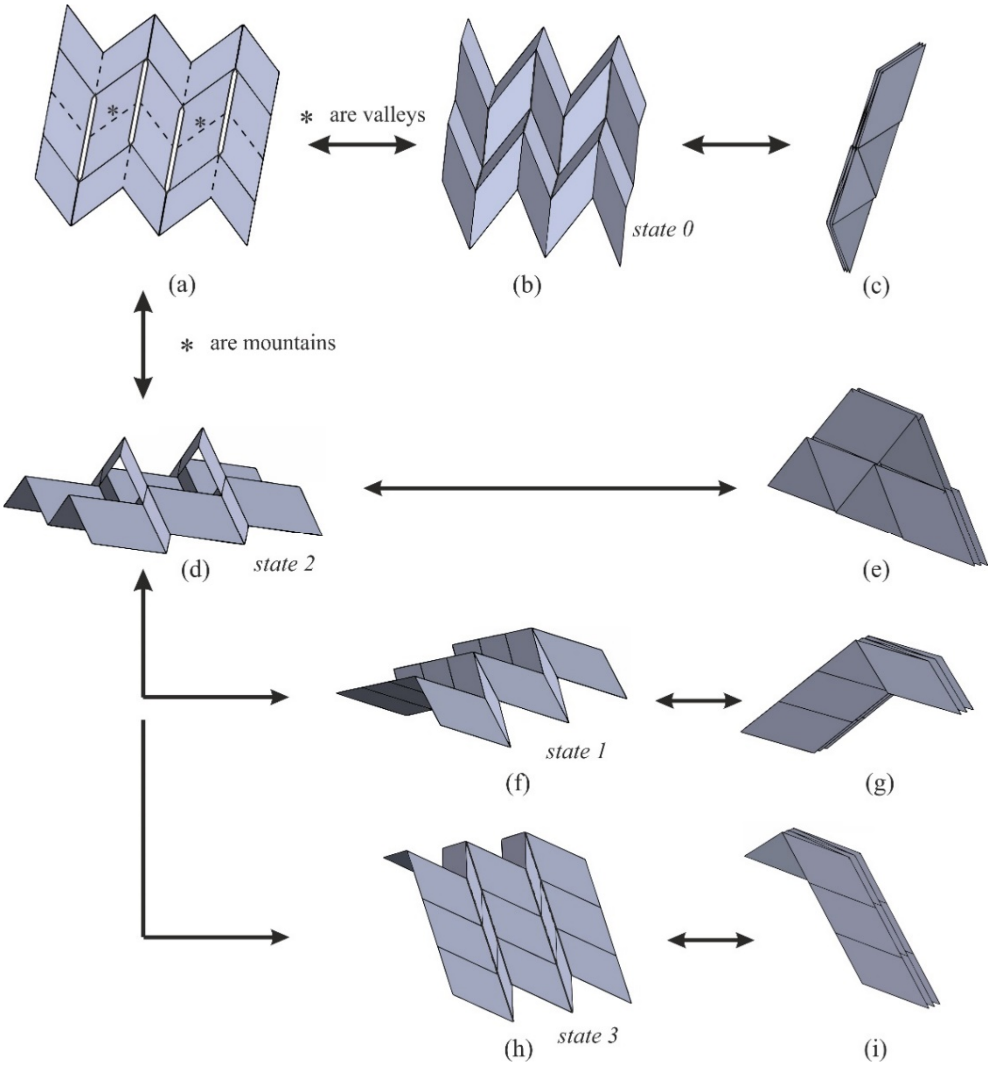

Fig. 4.6 A horizontal assembly of four cells in (a) the flat state; (b) and (c) show the traditional folding; (d) to (i) present the new configurations and their folded forms.

Next, if we use the first DOF to set any dihedral angle at the vertical creases to zero, we obtain a folded configuration of state 2 (Fig. 4.6(e)). Alternatively, we can treat state 2 as a starting point that leads to the remaining shapes. We should use the second DOF to access either state 1 or 3 (Fig. 4.6(f) and (h), respectively). In these configurations, we can fold the assembly using the first DOF to reach the other two compact forms (Fig. 4.6(g) and (i)).

To sum up, the first DOF related to vertical creases folds or deploys the pattern. Meanwhile, the second DOF activated with diagonal folds switches between the three new states. Also, state 2 has two variants, depending on if the MV assignment is changed for the creases on the slit's left- or right-hand side. This leads to configurations with the left- or right-hand side panels in the upper position, respectively. As a result, a horizontal assembly of the cells has four new folded configurations. With the Miura-ori's traditional compact form, when the MV assignment is unaltered, this gives five in total. This example showed that slits allow the Miura-ori to have more than one folded shape. The following section explains how to introduce additional rows of the cells and how this influences the kinematics.

4.4 Vertical merging of the cells and a global assembly

First, we will explain how mobility changes when a new cell with the double slit is merged with a single cell vertically. Figure 4.7 shows such an assembly and its equivalent mechanical linkages A, and C. Notice that linkage C has its axes numbered anticlockwise. This is because we choose the observer to look at it from the opposite direction, from behind the pattern. In this way, the creases with the same numbers have identical MV assignments in both linkages.

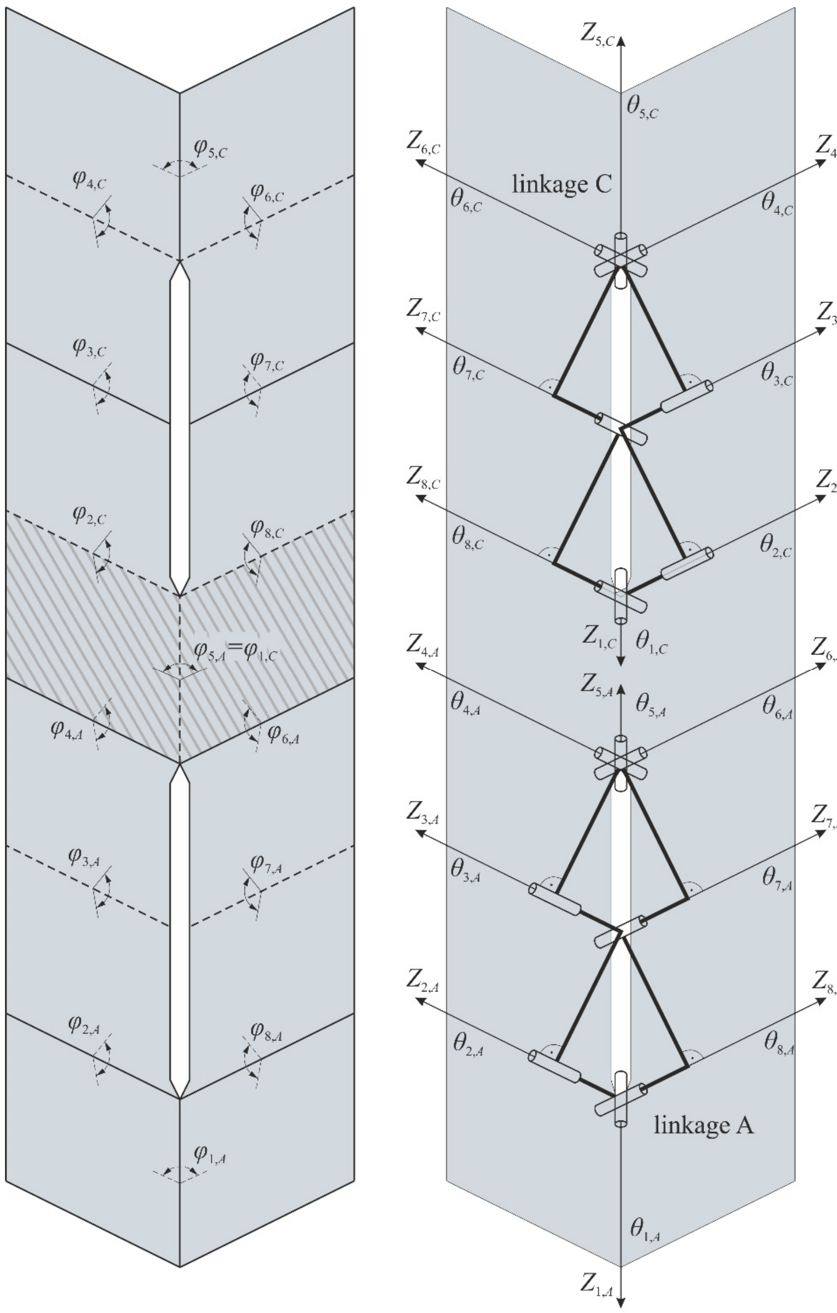

(a) (b)

Fig. 4.7 (a) A vertical assembly of two cells with the double vertical slits, and (b) its equivalent mechanical-linkage version.

Before we analyse the kinematics in detail, we again make initial estimations using Kutzbach formulas. Single cell's mobility is again marked as $M_{old}=2$. Building the next cell along the vertical direction means adding $N=6$ panels and $j=7$ revolutes this time. It is again forming a new spatial linkage, and the numeric estimation suggests mobility

$$M = M_{old} + 6(N - j) + j = 2 + 6(6 - 7) + 7 = 2 + 1 = 3 . \qquad (4.12)$$

As explained below, the formula is accurate this time, and the new cell adds an extra DOF.

The vertical merging of two cells means they share two panels (grey hatch in Fig. 4.7(a)). Thus, for the dihedral angles between them, there is

$$\varphi_{5,A} = \varphi_{1,C} . \qquad (4.13)$$

Substituting (4.13) into (4.1) for linkage A, we get

$$\varphi_{1,C} = \varphi_{1,A} . \qquad (4.14)$$

Equation (4.14) tells us that if we choose $\varphi_{1,A}$ as one of the control angles, it is also passed as an input to linkage C. As (4.1) remains valid for linkage C, all the assembly's vertical creases are equally folded. If we add additional linkages vertically, they will inherit the same dihedral angle at all vertical folds. Thus, it is the first DOF of the assembly, associated with vertical creases and deciding the degree to which all the cells are folded.

Simultaneously, there is no connection between the linkages' diagonal creases. As $\varphi_{1,C}$ does not change value when $\varphi_{1,A}$ is frozen, the changing shape of linkage A does not affect linkage B apart from causing overall translation. This means the second DOF of the lower cell, which results from the first slit and defines the shape of linkage A, is not passed to linkage C. Linkage C, however, remains a two-DOF mechanism. To define its form, we need to specify one of its dihedral angles at diagonal creases. In other words, the additional linkage requires a third input for the assembly, an extra DOF, which results from the upper slit and decides on the reconfiguration of linkage C. While the first DOF folds or deploys the entire assembly, the other two switch between the cells' alternative states independently. Also, we can notice that each next cell added vertically will further increase the DOFs number by one, which was accurately predicted by the Kutzbach formula.

Section 4.2 showed that the number of the cells horizontally does not change the DOFs. When multiplied horizontally, the cells are equally unfolded and inherit kinematics. They follow each other's motion automatically, without the need for extra inputs. We can use this characteristic and add the cells horizontally to an assembly of any number of cells merged vertically. In this way, we would produce a global version of the Miura-ori with multiple panels both horizontally and vertically and with the slits regularly multiplied in both orthogonal directions, as in Fig. 4.8.

As we have shown that the dihedral angle at vertical creases propagates in both horizontal and vertical directions, such structures will always have one DOF that controls how folded they are. It is the first DOF that originates from the Miura-ori geometry. We can activate it by manipulating any vertical crease of the pattern. Simultaneously, each row of the slits adds one DOF to the system, connected only with this particular row. By changing a dihedral angle at any diagonal crease within a chosen row, we will cause its reconfiguration. We can switch locally between its equivalent states 1, 2 and 3. These forms will be possible if we start from an equivalent state 2 accessed earlier. With such freedom to choose shapes, it is essential to count the global pattern's mobility and the number of possible folded variants.

4.5 Mobility and the number of folded configurations

From previous sections, we know the extra DOFs are connected only to the number of rows of the cells, *r*, as no new DOFs are introduced when growing the pattern horizontally.

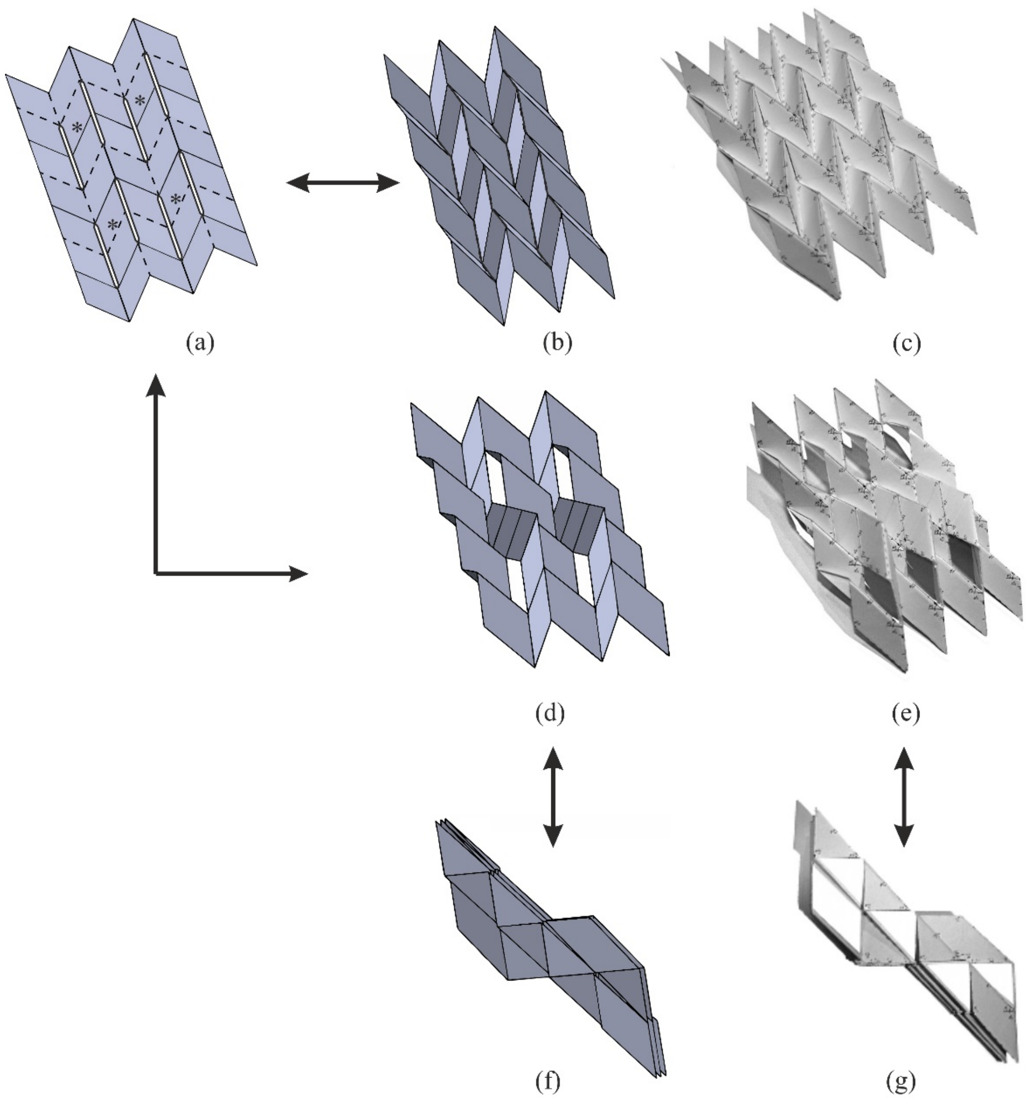

Fig. 4.8 A 2x4 assembly in (a) the flat state, (b) state 0, (d) state 2, and (f) the folded state 2; (c), (e) and (g) show a physical 2x6 model in the analogous configurations.

*The physical models presented in the thesis were manufactured out of 160gsm paper sheets. To ensure panel rigidity and distinguish between hinge and panel regions, all parallelograms were reinforced by attaching from the bottom much stiffer pasteboard.

Therefore, with the original Miura-ori DOF, the mobility M of a global assembly with the double vertical slits adds up to

$$M = r + 1\,. \tag{4.15}$$

This means that no matter how many cells constitute each row, the exact number of DOFs does not change if the number of rows stays the same.

According to (4.15), a two-row assembly should have three DOFs. Such a pattern, consisting of two rows of four slits each, is shown in Fig. 4.8. From the flat state, Fig. 4.8(a), we can always choose to reach the traditional form, as in Fig. 4.8(b) and fold it in a typical way if needed. Alternatively, we can change the MV assignment of selected diagonal creases (marked by * in Fig. 4.8(a)) to achieve a multicell equivalent of state 2, shown in Fig. 4.8(d). Then, it has a folded form, as in Fig. 4.8(f), which we obtain with the first DOF.

Alternatively, we can freeze the first DOF in state 2 and use the second or the third one. By manipulating any diagonal crease in the lower or upper row, we can reconfigure the rows independently into their equivalent states 1 or 3. Figure 4.9(b) shows an example where the downward motion for the lower row was activated by its DOF, which led to its state 1. Then,

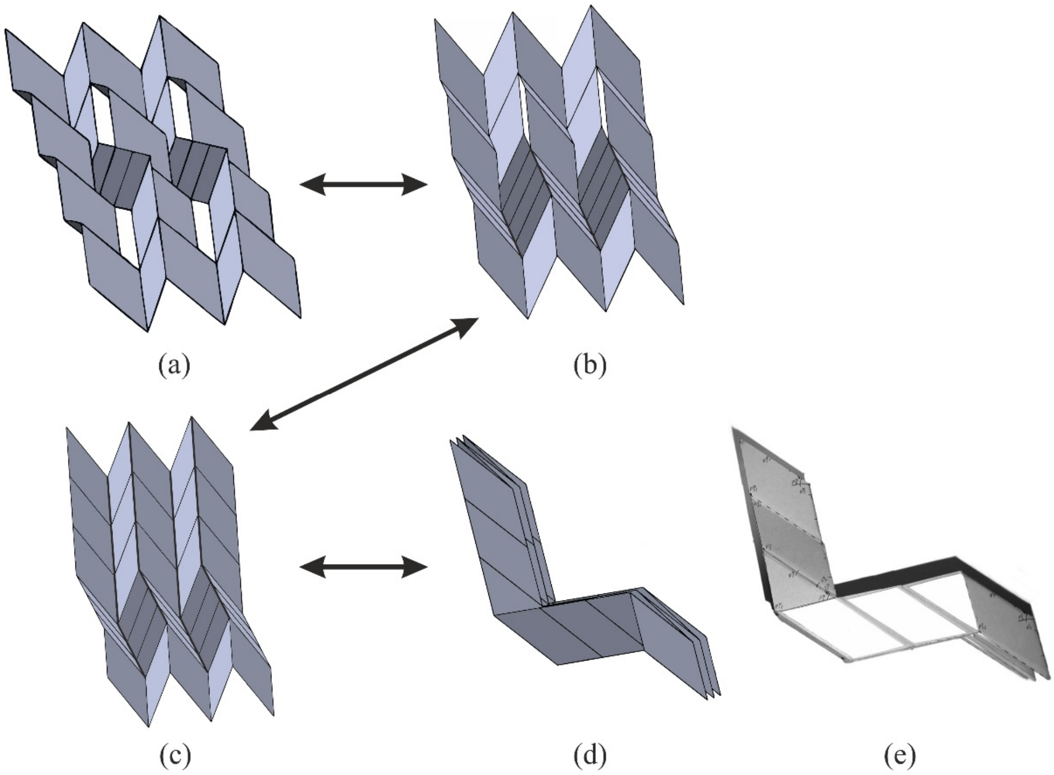

Fig. 4.9 A 2x4 assembly in (a) state 2, (b) when the first row moved downwards into its state 1, (c) when the first row remained in state 1 and the second one moved upwards; (d) the folded form of (c), and (e) a physical model of the assembly in form (d).

the upward movement for the upper row was achieved with its independent DOF (Fig. 4.9(c)). Finally, once a preferred shape of each row is decided, we can fold the pattern using the first DOF and obtain a compact form of the entire assembly. Figure 4.9(d) shows the one that results from the above reconfigurations.

This example confirms that the extra DOFs resulting from the rows of slits are separated, and we can reconfigure each row independently. We know from section 4.3 that the number of possible folded forms of each row adds up to five. It means the total number N of folded configurations of a global assembly with r rows equals

$$N = 5^r . \tag{4.16}$$

4.6 Summary

This chapter showed how the kirigami approach allows efficiently modifying Miura-ori's rigid origami version. The main goal was to allow new forms and folded shapes. Cuts along selected creases removed some of the revolute joints and relaxed the pattern kinematically. The eliminated constraints changed Miura-ori's kinematic model. As a result, a new version of the pattern was created with regular two-crease-long vertical slits. It no longer has only one motion that leads from the flat state to the single folded configuration. Instead, the slits increased the number of DOFs, and alternative motion paths are now available.

Apart from the traditional Miura-ori shape, a new configuration called state 2 is possible, starting from the same crease pattern. From this form, each row of the pattern's repetitive cells can switch between three different states. We do this by using specific new DOFs that are coupled only with the rows they reconfigure. Meanwhile, the original first DOF folds or deploys the entire pattern in a way similar to the traditional one.

The distribution of the DOFs allows many shapes and folded forms combinations. Moreover, the extra DOFs, when manipulated, have local effects within chosen rows of the cells. This feature makes the control of the multi-DOF assembly approachable, even though the mobility grows beyond the value of two for large patterns. The regular double vertical slits turn the Miura-ori into a structure that maintains the ability to fold compactly or deploy flat and additionally has a locally variable shape that is convenient to control. This could lead to novel engineering applications using varying geometries to achieve tunability. Figure 4.10 presents the strategy for manufacturing and controlling the Miura-ori variant with the regular double slits along its vertical creases.

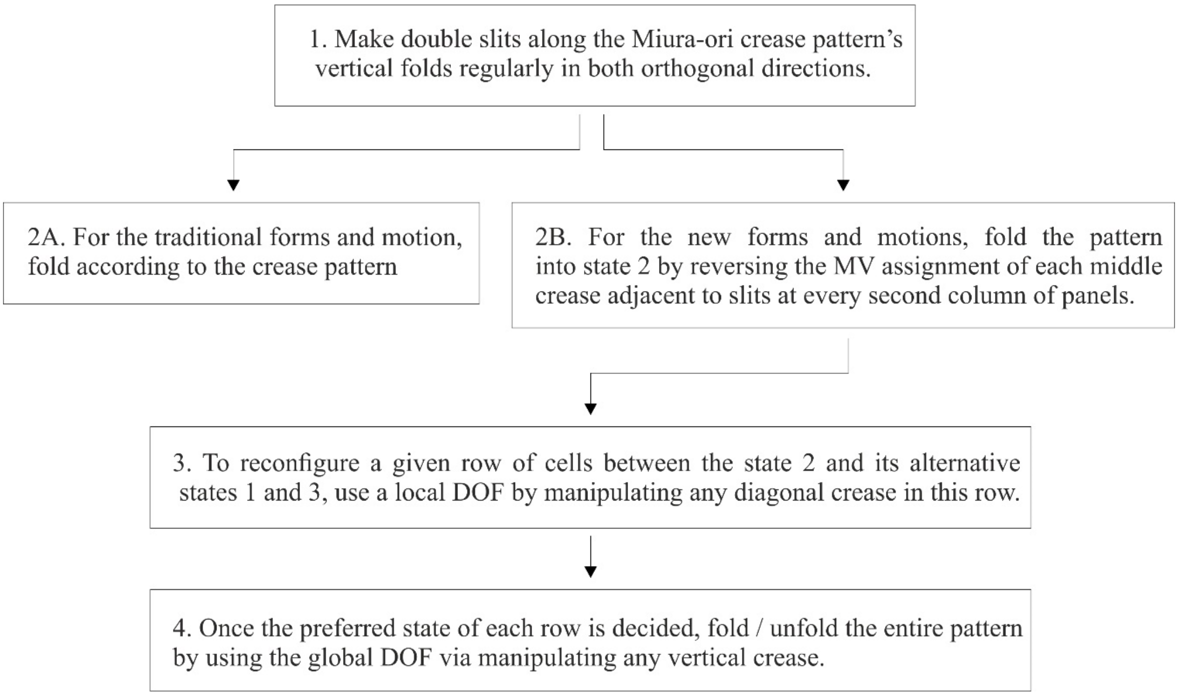

1. Make double slits along the Miura-ori crease pattern's vertical folds regularly in both orthogonal directions.

2A. For the traditional forms and motion, fold according to the crease pattern

2B. For the new forms and motions, fold the pattern into state 2 by reversing the MV assignment of each middle crease adjacent to slits at every second column of panels.

3. To reconfigure a given row of cells between the state 2 and its alternative states 1 and 3, use a local DOF by manipulating any diagonal crease in this row.

4. Once the preferred state of each row is decided, fold / unfold the entire pattern by using the global DOF via manipulating any vertical crease.

Fig. 4.10 A strategy for manufacturing and controlling the Miura-ori with the regular double vertical slits.

This chapter's findings confirm that an organised origami cutting can add DOFs to well-established patterns like Miura-ori and bring new unique configurations. Thanks to the kirigami approach, origami can turn from foldable structures into reconfigurable ones, which can morph between alternative shapes and folded forms. The main novelty introduced in this chapter is bringing extra DOFs to traditionally only one-DOF rigid-origami Miura-ori by means of slits. This allows new forms, i.e. reconfigurability of the pattern previously displaying only foldable behaviour.

As a result, we achieved one of the main objectives of the research – enabling alternative configurations via slit introduction. However, we accomplished it with the DOF number increasing as the pattern grows large, which is not ideal from the control perspective. Before tackling this problem, the next chapter examines another regular variant of slits, this time along the diagonal folds. This is to investigate how analogous cuts but in a different direction affect the kinematics and to discover even more new Miura-ori's forms.

Chapter 5

Reconfigurable Miura-ori with diagonal slits

In chapter 4, a rigid origami Miura-ori was cut along some vertical creases. The slits removed selected revolute joints and relaxed the pattern kinematically, increasing its mobility. As a result, two-DOF spatial 8R linkages were formed throughout the pattern. Regularly arranged, they altered the pattern's motion so that alternative configurations and folded forms became possible. This met one of the thesis's main objectives, i.e. allowing a one-DOF rigid origami to exhibit new motions and shapes.

Chapter 4 reported on only one slit type – double, along vertical folds. This chapter continues the kirigami modifications using two-crease-long cuts, but this time, along diagonal creases. Similarly to chapter 4, we will first build an assembly with a regular slit arrangement and then evaluate its mobility. Previously, such an approach brought many new forms, although the DOF number continued to increase as the pattern got large. Here, we want to investigate if this will repeat and what alternative shapes are possible with slits in the opposite direction. We hope that, for example, they will help fold the Miura-ori without panels enclosing each other. The elimination of such geometric limitations could allow designers to use the pattern more efficiently.

The layout of the chapter is as follows. First, section 5.1 analyses the kinematics of a single cell with a double slit along diagonal creases. Then, sections 5.2, 5.3 and 5.4 explain how to build a pattern with multiple regularly repeated slits and then evaluate its kinematic behaviour. Next, section 5.5 presents and discusses some of the new configurations. Finally, section 5.6 concludes the chapter.

5.1 Single Miura-ori cell with a double diagonal slit

First, we will examine a single cell with a double diagonal slit, as in Fig. 5.1(a). To obtain it, we need to take an eight-panel Miura-ori piece and make a two-crease-long cut along the inner diagonal folds. It is again a closed chain of eight rigid bodies connected by revolutes. It has at least two DOFs, according to (3.5), similarly to the cell with a double vertical slit from the previous chapter.

For the kinematic analysis, we again represent the origami with an equivalent mechanical linkage, as in Fig. 5.1(b). We continue using Denavit and Hartenberg's notation. Now, we use angle α_{23} as the geometric parameter α. Next, it is essential to find the relationships between the kinematic variables to explain how the linkage changes shape.

The matrix method continues providing closure equations that describe the kinematics. The product of the analysis is a set of six relationships between variables φ, which are

$$\varphi_7 = \varphi_3, \quad \cot\left(\frac{\varphi_3}{2}\right) = \frac{\cot\left(\frac{\varphi_1 - \varphi_2 - \varphi_8}{2}\right)}{\cos(\alpha)}, \qquad (5.1), (5.2)$$

$$\cot\left(\frac{\varphi_3}{2}\right) = \frac{-\cot\left(\frac{\varphi_4 - \varphi_5 + \varphi_6}{2}\right)}{\cos(\alpha)}, \quad \varphi_8 = \varphi_2, \qquad (5.3), (5.4)$$

$$\varphi_5 = \varphi_1 \text{ and } \varphi_6 = \varphi_2. \qquad (5.5), (5.6)$$

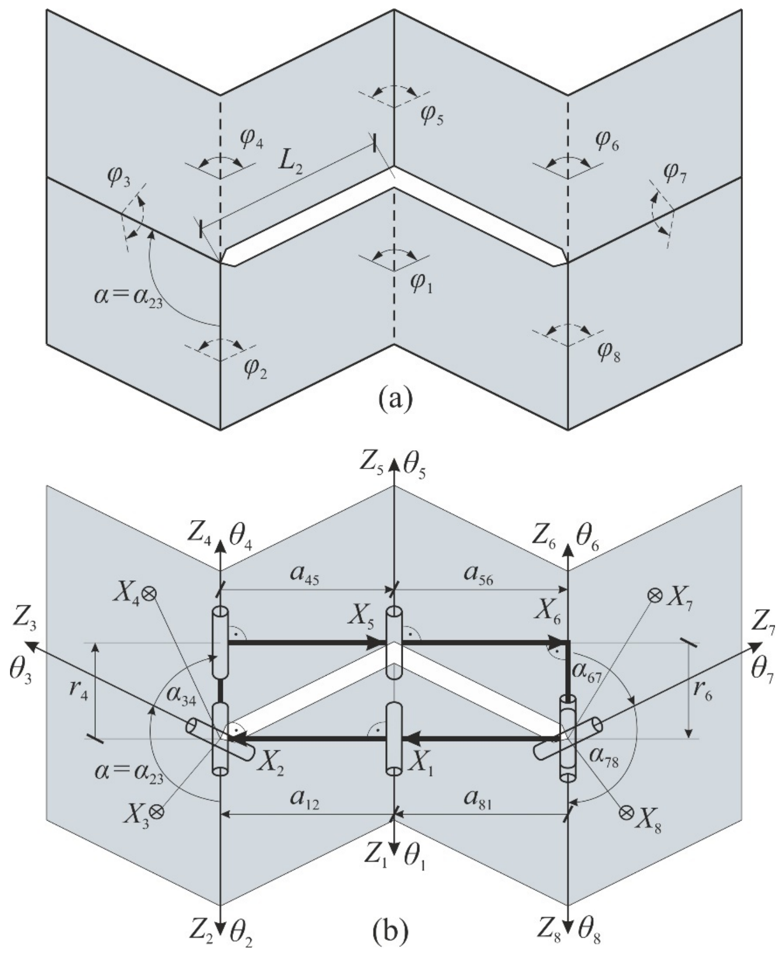

Fig. 5.1 (a) A single cell with the double diagonal slit, and
(b) its equivalent mechanical linkage.

In (5.1) to (5.6), we continue to use dihedral angles as our preferred variable type. Moreover, if we substitute some of the equations into the others, we can find two additional more straightforward relationships. They are

$$\varphi_4 = \varphi_2 \quad \text{and} \quad \varphi_6 = \varphi_4 . \qquad (5.7), (5.8)$$

As (5.7) and (5.8) result from (5.1) to (5.6), they are not independent but only clarify the motion. Therefore, we have six independent closure equations containing eight variables. We must assume at least two φ's so that the rest results from relationships (5.1) to (5.6). This proves that two inputs define the cell's shape, i.e. it has two DOFs at least. For the detailed derivations, see appendix B.

To inspect the kinematics, we first substitute (5.4) into (5.2) and get

$$\cot\left(\frac{\varphi_3}{2}\right)=\frac{\cot\left(\frac{\varphi_1}{2}-\varphi_2\right)}{\cos(\alpha)}. \tag{5.9}$$

Equation (5.9) shows that if we use φ_1 and φ_3 as the inputs, they will define φ_2. So, we choose them to be the two DOFs deciding on the cell's shape. We can freeze one, e.g. set φ_3 to 70.5°. It is the value of dihedral angles at diagonal creases corresponding to the angles at vertical folds set to 90° in the traditional Miura-ori, with no cuts and α equal to 135°. When disabled, we can treat φ_3 as a parameter and plot the relationship between φ_2 and the second DOF φ_1. In this chapter, we will continue presenting kinematics using 2D plots. In this way, we can keep the figures uncomplicated when investigating how different parameter values affect the motion paths.

Figure 5.2 presents the values of φ_2 when φ_3 is frozen and φ_1 used to change the cell's shape. Point *A* shows the starting configuration, which is the traditional Miura-ori shape. Without the slit, a disabled angle would immobilise the cell. However, thanks to the second DOF originating from the cut, we can trigger an alternative motion. If we decrease φ_1, the cell folds partially, as in *B*. If we continue, we get a configuration with φ_1 and φ_5 equal to zero, shown in *C*. A further decrease of φ_1 includes panel intersections, as in *D*. This motion is impossible with physical models due to the panel contact and the cell's blockage in state *C* instead.

Alternatively, we can increase φ_1 in *A*. If so, the motion continues as in *E* until the cell expands fully. In point *F*, φ_1 and φ_5 become 180°. This allows us to change these folds' MV assignment. For example, both creases 1 and 5 can become valleys. Then, if we decrease φ_1,

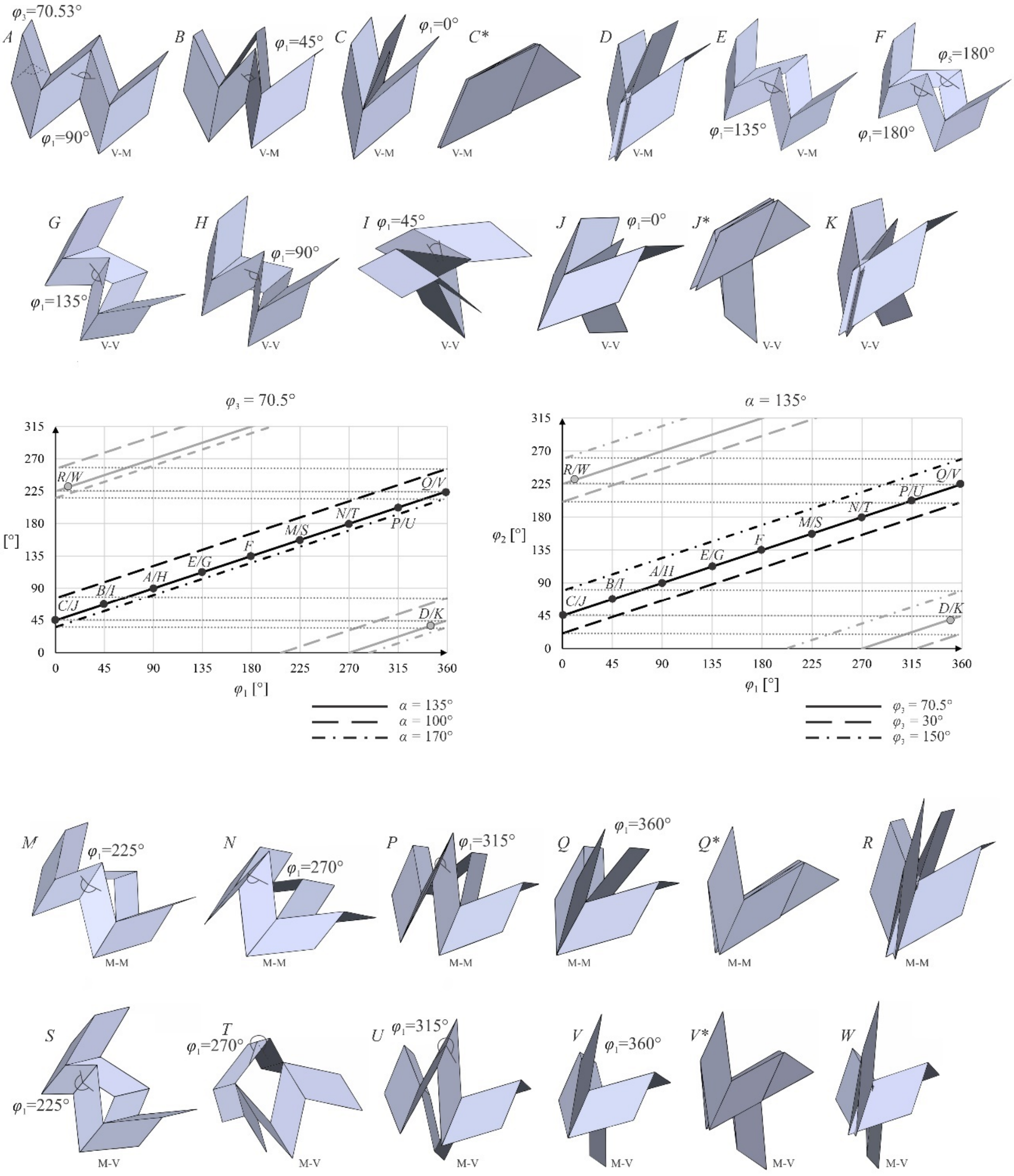

Fig. 5.2 The reconfiguration of a single cell when φ_3 is frozen, and φ_1 used to alter the shape. The plots show the relationship between φ_2 and φ_1; *A* to *W* are reconfiguration stages.

we start an alternative folding sequence, illustrated in *G*, *H*, *I* and *J*. Further motion, as in *K*, is again impossible due to panel intersections.

Moreover, in point *F*, crease 1 can turn into a mountain instead. According to our assumption, dihedral angles at folds changing the MV assignment take values bigger than 180˚. This means now we explore the plot's upper part. Simultaneously, crease 5 can stay a mountain or turn into a valley. As a result, we have two more folding variants. One, with crease 5 also a mountain, is indicated by points *M*, *N*, *P*, *Q* and forbidden *R*. On the other hand, points *S*, *T*, *U*, *V* and forbidden *W* show the variant with crease 5 as a valley.

These examples show that a single cell has four alternative configurations with their characteristic motion sequences. We will call them V-M, V-V, M-M and M-V, after the MV assignment for creases 1 and 5, respectively. Notice that in points *C, J, Q* and *V,* instead of changing φ_1 further and causing collisions, we can unfreeze φ_3 and decrease it, which folds the assembly fully. This means the cell has four folded forms, shown in *C*,J*, Q** and *V**.

Figure 5.2 also shows how different values of α and the disabled DOF influence the plot. If we choose smaller α or bigger φ_3, the plot moves up. Bigger α or smaller φ_3 translate the plot downwards. We will call the behaviour of the cell presented in Fig. 5.2 when we freeze φ_3 and use φ_1 to change the cell's shape, *motion type 1*. It is not the only one possible.

To depict the cell's other motion, we use (5.9) again. Now, however, we use φ_3 to drive the motion and freeze φ_1, e.g. at 90°. If we plot φ_2 in respect to φ_3, we obtain the curves in Fig. 5.3. Starting from point *A*, once φ_3 decreases, the cell changes its shape as in *B*. It continues until the diagonal creases fold fully, as in *C*. This configuration terminates the motion, as a further decrease of φ_3 includes the panel intersections shown in *D*. If we instead increase φ_3 in *A*, the cell moves in the opposite direction, as in *E*. It goes via point *F*, where φ_3 is 180°, and continues through *G, H* and *I*. Point *J* terminates the path from the other side due to further intersections shown in *K*.

Now, bigger φ_1 shifts the plot down, while smaller φ_1 moves it in the opposite direction.

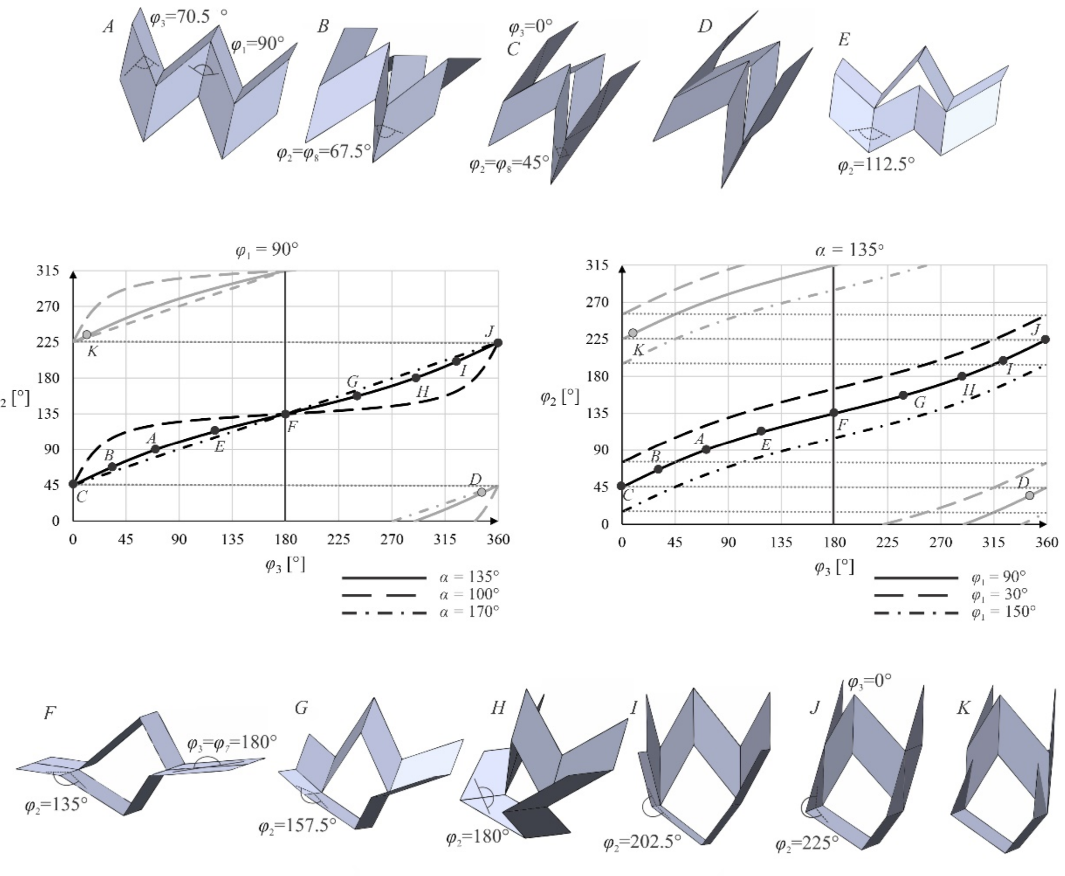

Fig. 5.3 The reconfiguration of a single cell when φ_1 is frozen, and φ_3 used to alter the shape. The plots show the relationship between φ_2 and φ_3; *A* to *K* are reconfiguration stages.

Additionally, this time, the bigger α is, the more the curve resembles a straight line. We will call the folding in Fig. 5.3 when we freeze φ_1 and use φ_3 to change the shape, *motion type 2*. Moreover, point *F* is particularly interesting from the kinematic perspective. We will refer to it as the *rhombic state*. Once φ_3 becomes 180˚, it enables an alternative solution for the closure equations. In other words, *F* is a bifurcation point at which the cell can change its kinematic behaviour. For the equation derivations, refer to appendix B.

For the linkage in the rhombic state, the matrix method returns an alternative set of relationships between φ's. First, we notice this configuration is characterised by

$$\varphi_3 = \varphi_7 = \pi \,. \qquad (5.10),\ (5.11)$$

Then, during the kinematic analysis, we find that the new closure equations are

$$1+\cot\left(\frac{\varphi_5}{2}\right)\cot\left(\frac{\varphi_6+\varphi_8}{2}\right)=0, \tag{5.12}$$

$$1+\cot\left(\frac{\varphi_5}{2}\right)\cot\left(\frac{\varphi_2+\varphi_4}{2}\right)=0 \quad \text{and} \quad \varphi_5=\varphi_1. \qquad (5.13), (5.14)$$

Notice that (5.10) to (5.14) still contain eight φ's. This time, however, there are only five equations. When φ_3 and φ_7 become 180°, we must assume at least three other φ's so that the rest variables result from equations (5.12) to (5.14). For example, the first input can be an angle from the pair φ_1 and φ_5. Then, (5.12) and (5.13) require us to specify two φ's more, each from a different pair of variables. We should choose one from φ_2 and φ_4, and one from φ_6 and φ_8. In chapter 5, we will use φ_1, φ_2 and φ_8 as the inputs that decide on the cell's reconfiguration in the rhombic state.

The above shows that once we set φ_3 to 180° and force the rhombic state, the two-DOF cell turns into a three-DOF assembly. It has now three distinct parts that can move independently – two arms consisting of two panels each and a four-panel middle part with a rhombic cross-section. This makes the cell an example of a particular linkage that is simultaneously metamorphic and kinematotropic. In such a mechanism, the effective number of links and joints, and the DOF value, respectively, change throughout the motion (Wohlhart 1996) (Dai and Rees Jones 1999) (Galletti and Fanghella 2001) (Song et al. 2019) (Wang et al. 2021). In our case, we can decide if we want to experience the metamorphosis and the DOF increase via manipulating φ_3 in *F*.

When point *F* in Fig. 5.3 is reached, we can choose to continue the two-DOF motion by further changing φ_3 and going along the original curve. Alternatively, we can decide to keep

φ_3 as 180° and explore the new motion path resulting from the DOF increase, depicted in Fig. 5.3 by the solid vertical lines. These motions are governed by (5.10) to (5.14) and illustrated in Fig. 5.4. In the rhombic state, when φ_3 stays 180°, we can decrease φ_1 to zero and fold the rhombus or keep it deployed. We can also rotate the cell's arms, i.e. use φ_2 and φ_8 to move them upwards, downwards or in opposite directions. This freedom gives many folding approaches.

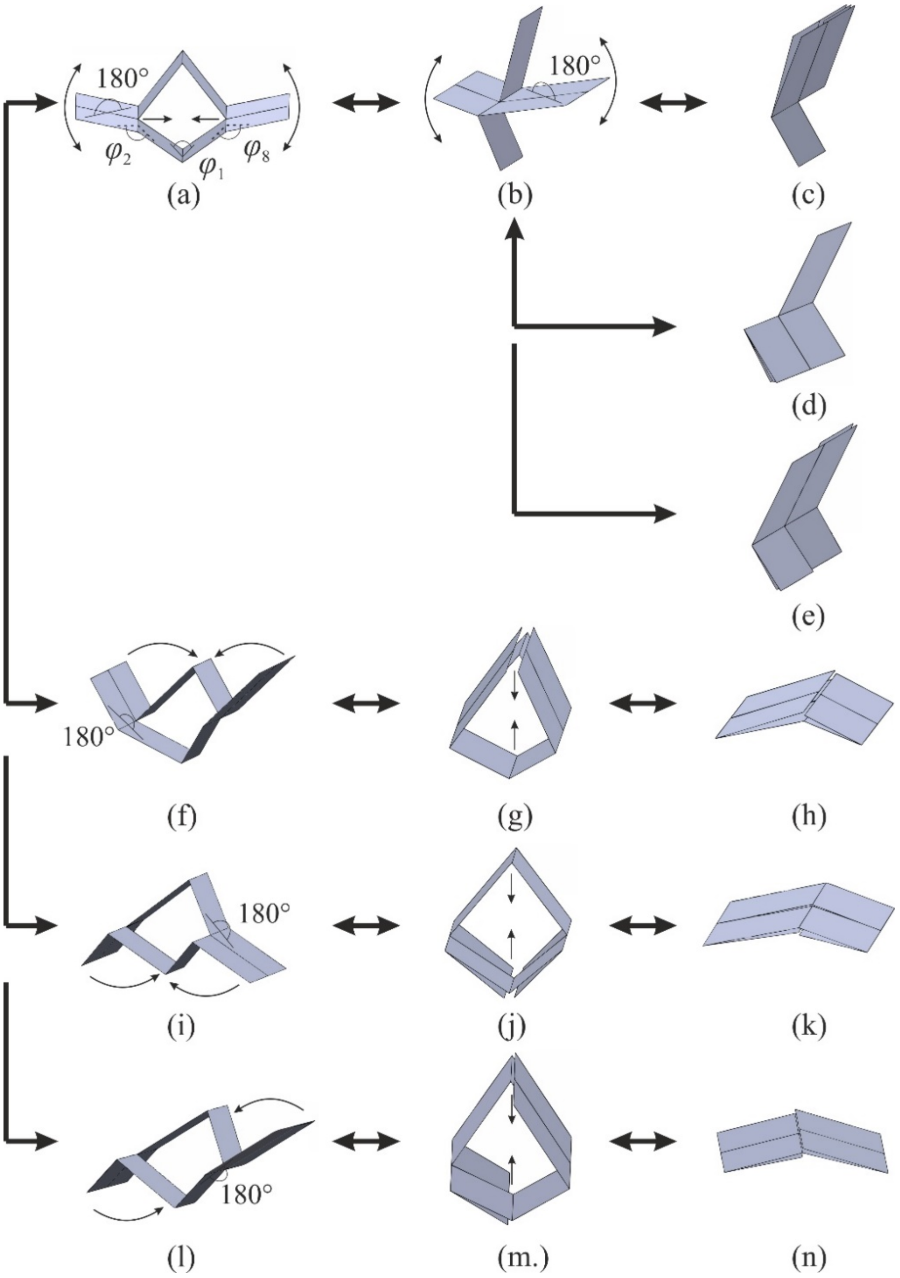

Fig. 5.4 Different folding variants of a single cell in the rhombic state.

To conclude, the cell behaves differently depending on the angles we freeze and use to reconfigure it. Additionally, along one of such two-DOF motion paths, a state in which the cell turns into a three-DOF assembly was identified. Unfortunately, the detailed analysis of this bifurcation point falls outside the scope of this project. Nevertheless, this feature allows a global Miura-ori with the slits to experience even more configurations and folded shapes. Next, we will discuss how to build an assembly consisting of multiple cells.

5.2 Vertical merging of the cells

First, we will merge two cells vertically so that they share four parallelograms. In other words, we will add four panels to a single cell from the top to form the second one in the vertical direction. Figure 5.5(a) presents such an assembly and (b) its equivalent mechanical linkage. Now, it is essential to figure out the number of DOFs.

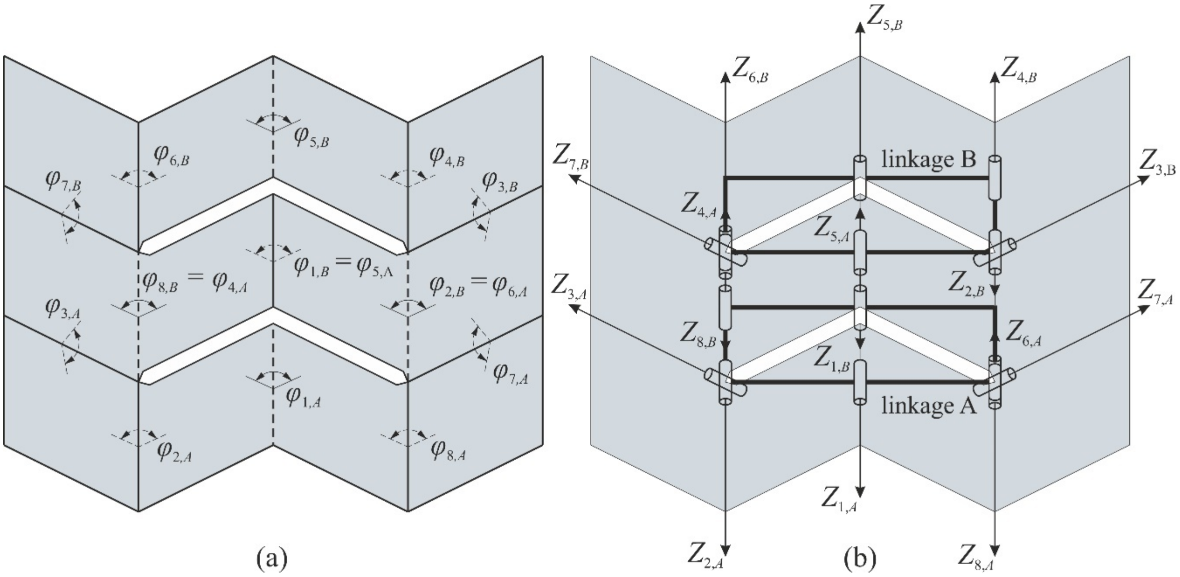

Fig. 5.5 (a) A vertical assembly of two cells with the double diagonal slits, and (b) its equivalent mechanical-linkage version.

Before we analyse the linkage's closure equations, we again use the Kutzbach formulas for the initial mobility estimation. We count the input parameters, which are $N = 4$ and $j = 5$. Knowing that before the panel addition there is $M_{old} = 2$, the spatial version of the formula returns

$$M = M_{old} + 6(N - j) + j = 2 + 6(4 - 5) + 5 = 2 - 1 = 1\,. \tag{5.15}$$

It again suggests that the mobility drops to a single DOF, and the assembly does not keep the ability to reconfigure but can move only in the traditional way. However, as the investigations below show, the Kutzbach calculations again fail to notice geometric specialities and provide inaccurate DOF estimation. This case is similar to an analogous assembly but with vertical slits, presented earlier in Fig. 4.4.

Before we prove that the assembly maintains the two-DOF nature after the panel addition, we should clarify that the upper linkage is the same as the lower one but has the axes numbered not clockwise but anticlockwise. If we look at linkage B from the same direction as linkage A, axis $Z_{1,B}$ is a mountain fold, while $Z_{1,A}$ is a valley. Axis $Z_{1,B}$ becomes a valley and the linkages are the same once the observer looks at linkage B from the opposite direction, from behind the pattern. To account for that, we numbered linkage B's axes anticlockwise.

To estimate the actual DOF number, we must notice that the same two-DOF linkage models the upper and lower cell. So, it needs two φ's to define its shape. As (5.5) applies to linkage A, from Fig. 5.5(a), we see

$$\varphi_{1,B} = \varphi_{5,A} = \varphi_{1,A}\,. \tag{5.16}$$

Equation (5.16) means linkage B receives $\varphi_{1,A}$ as one of its inputs.

From Fig. 5.5(a), with (5.7) determined earlier, we also have

$$\varphi_{8,B} = \varphi_{4,A} = \varphi_{2,A}\,. \tag{5.17}$$

Equation (5.17) tells us linkage A transfers the second input $\varphi_{2,A}$ to the upper linkage as well. As linkage B in the default form is a two-DOF assembly, two inputs are enough to define its shape. Therefore, it adjusts its geomtery to the linkage A's motion and the third angle shared between the linkages is a redundant input, which we prove below.

Knowing (5.6), we notice in Fig. 5.5(a) that the third input to linkage B is

$$\varphi_{2,B} = \varphi_{6,A} = \varphi_{2,A}\,. \tag{5.18}$$

However, (5.4) applies to linkage B too. Knowing already (5.17), we simultaneously have

$$\varphi_{2,B} = \varphi_{8,B} = \varphi_{2,A}\,. \tag{5.19}$$

Equation (5.19) tells us that the third input from (5.18) is already satisfied by the second one (5.17) and the upper linkage's geometry. This shows that the two inputs are enough to trigger linkage B's response that is compatible with the kinematics of linkage A. Thus, in this case, the two-DOF motion is passed to the upper linkage, and the shared third angle is compatible and, in fact, redundant.

To conclude, as the cells are two-DOF linkages, vertical merging passes enough inputs to linkage B to define its shape. As it imitates linkage A, the entire assembly keeps two DOFs. We illustrate this in Fig. 5.6. In the traditional Miura-ori shape, we can freeze $\varphi_{3,A}$ and use the second DOF to start motion type 1. The upper cell follows the lower one, as in Fig. 5.6(b), until they block simultaneously, Fig. 5.6(c).

If we go in the opposite direction, both cells expand until φ_1 and φ_5 in both cells become 180°, Fig. 5.6(d). For a single cell, this shape allows choosing between four possible MV assignments for creases 1 and 5. Now, with three rows of panels, the number of combinations and thus alternative configurations is eight. Two exemplary ones, which correspond to the MV assignments for the middle vertical creases M-M-M and M-V-M, are shown in Fig. 5.6(e) and (f), respectively.

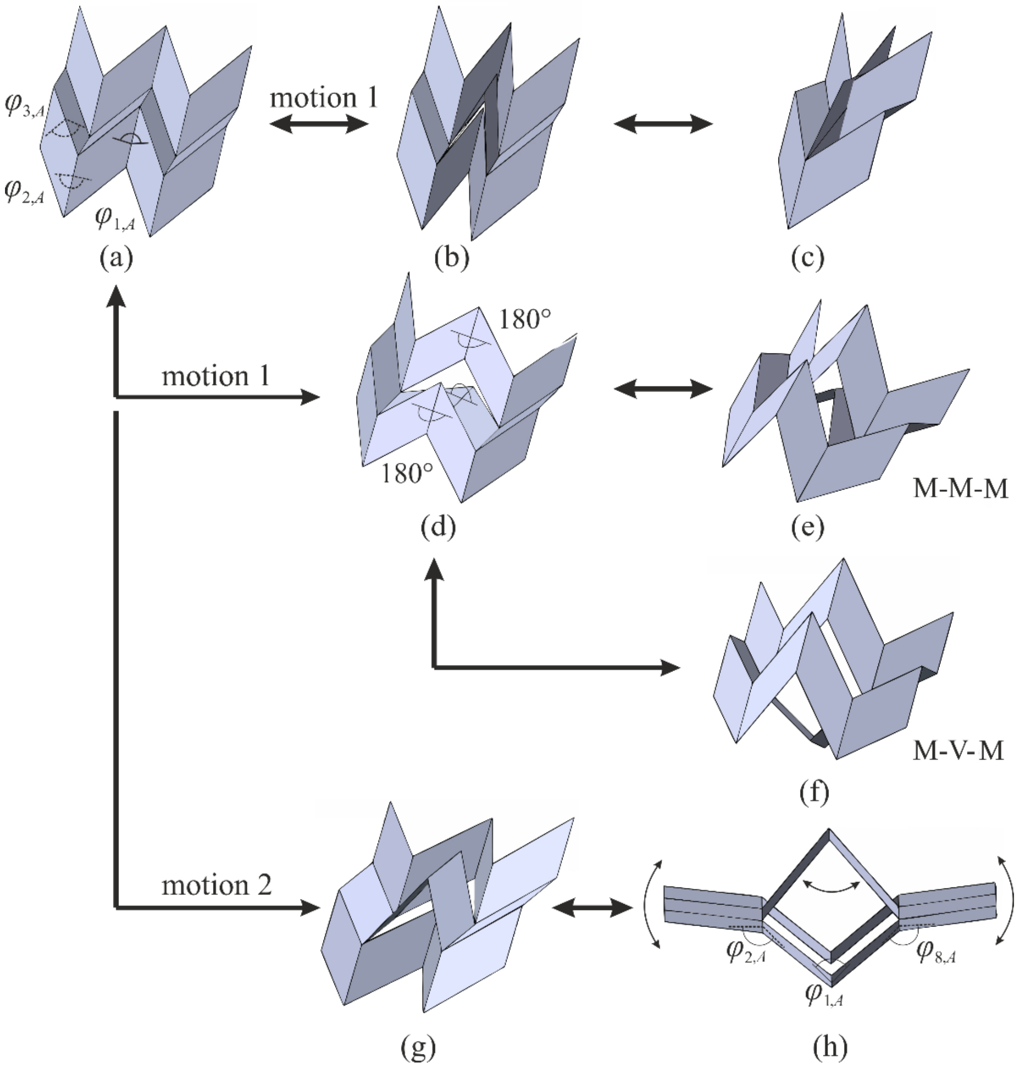

Fig. 5.6 Reconfiguration of a vertical assembly of two cells; (a) the assembly in the Miura-ori form; (b) to (f) are examples of the new shapes accessed via motion type 1; (g) and (h) are examples of the new shapes accessed via motion type 2.

If we merge additional cells vertically, we will create more of these linkages. They will all inherit enough inputs to follow the lower cell's motion and not change the assembly's mobility. Also, for r cells vertically, the number N_V of possible configurations with different MV assignments is

$$N_V = 2^{r+1}. \tag{5.20}$$

Things are different for motion type 2, for which we should freeze $\varphi_{1,A}$ instead and then use, for example, $\varphi_{3,A}$ to change the shape. Initially, the cells maintain the two-DOF motion, Fig. 5.6(g), and continue as long as $\varphi_{3,A}$ changes. However, when $\varphi_{3,A}$ becomes 180°, they reach the rhombic state, Fig. 5.6(h). Both linkages turn into three-DOF geometries, governed by kinematics as in (5.10) to (5.14). Now, all φ's shared between neighbouring linkages are needed to pass the required inputs – the third angle becomes not redundant in this state. We see this in Fig. 5.6(h). It shows we can use the three DOFs $\varphi_{1,A}$, $\varphi_{2,A}$ and $\varphi_{8,A}$ independently to change the shape. Moreover, further vertical merging adds more linkages. However, they maintain the assembly's three-DOF behaviour when in the rhombic state, no matter how many of them.

To conclude, the cells do not change mobility when merged vertically. A vertical assembly of several cells maintains two DOFs during both motions 1 and 2 and becomes a three-DOF structure in the rhombic state. Due to the additional rows of panels, the number of different MV assignments possible via motion type 1, i.e. the number of distinct configurations, becomes bigger. The next section examines what happens when joining the cells horizontally.

5.3 Horizontal merging of the cells

In this section, we will merge two cells in the horizontal direction. Figure 5.7 shows the assembly and its equivalent-linkage version. Notice that we look at the second cell upside down and number its axes accordingly. In this way, creases with the same numbers have identical MV assignments. This shows that the cells used are indeed the same.

Again, we use the spatial version of the Kutzbach formula to estimate DOFs before the detailed kinematic analysis. Horizontal panel addition means $N = 6$ new facets and $j = 7$ revolutes. Updating previous mobility $M_{old} = 2$ returns

$$M = M_{old} + 6(N - j) + j = 2 + 6(6 - 7) + 7 = 2 + 1 = 3 . \tag{5.21}$$

This is a case analogous to the one from Fig. 4.7. The formula predicts that new panels will result in more inputs required, and that the DOFs grow by one with each new horizontal cell.

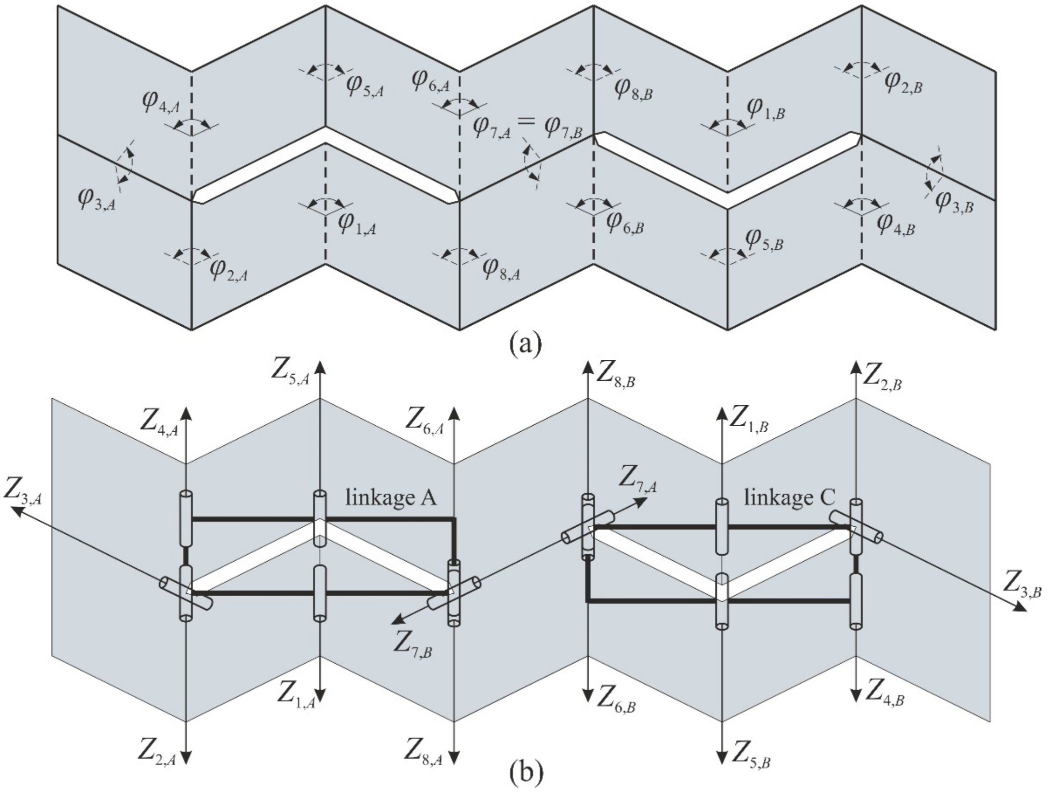

Fig. 5.7 (a) A horizontal assembly of two cells with the double diagonal slits, and (b) its equivalent mechanical-linkage version.

To understand what happens kinematically, notice that the equivalent linkages share one pair of panels. Once the shape of linkage A is decided, only angle $\varphi_{7,A}$ is passed. Linkage C receives one input, which is $\varphi_{7,C}$. Because of (5.1), the new cell behaves like a single one when φ_3 is fixed at a selected value – it can still move, in a way like in Fig. 5.2. Therefore, the right-hand side linkage needs one more input to define its shape. This tells us that the horizontal merging does not pass enough inputs and requires a new DOF to the assembly to define its shape. Now, the overall mobility equals three.

Figure 5.8 shows the cells' behaviour. In the Miura-ori form, Fig. 5.8(a), we can freeze $\varphi_{3,A}$. The angle at diagonal folds is the only one passed and the second cell's diagonal creases fold equally. It is the first DOF. Next, we can use the second one, e.g. change $\varphi_{1,A}$ and fold the first cell, as in Fig. 5.8(b). Notice that this action does not alter the second cell. This is because the extra DOFs act on separate cells. We reshape the second cell with the third DOF, e.g. by changing $\varphi_{1,C}$. We can either fold or expand the cell, as in Fig. 5.8(c) and (d).

Moreover, after we disable φ's at diagonal creases with the first DOF, we can use the second and the third one to expand the cells fully. In this configuration, Fig. 5.8(e), we can change the MV assignment for creases 1 and 5 in both cells. As each cell has four MV combinations, now there are 4^2 variants. The exemplary ones, corresponding to the MV assignments M-M/V-V and M-V/V-M, are shown in Fig. 5.8(f) and (g), respectively.

If we add more cells horizontally, they all inherit φ's at diagonal creases from the previous cells, i.e. the first DOF. Since the cells are two-DOF structures, each one adds a new DOF to the assembly. This allows us to fold or expand each cell individually. Therefore, the mobility M_H of a horizontal assembly of c cells is

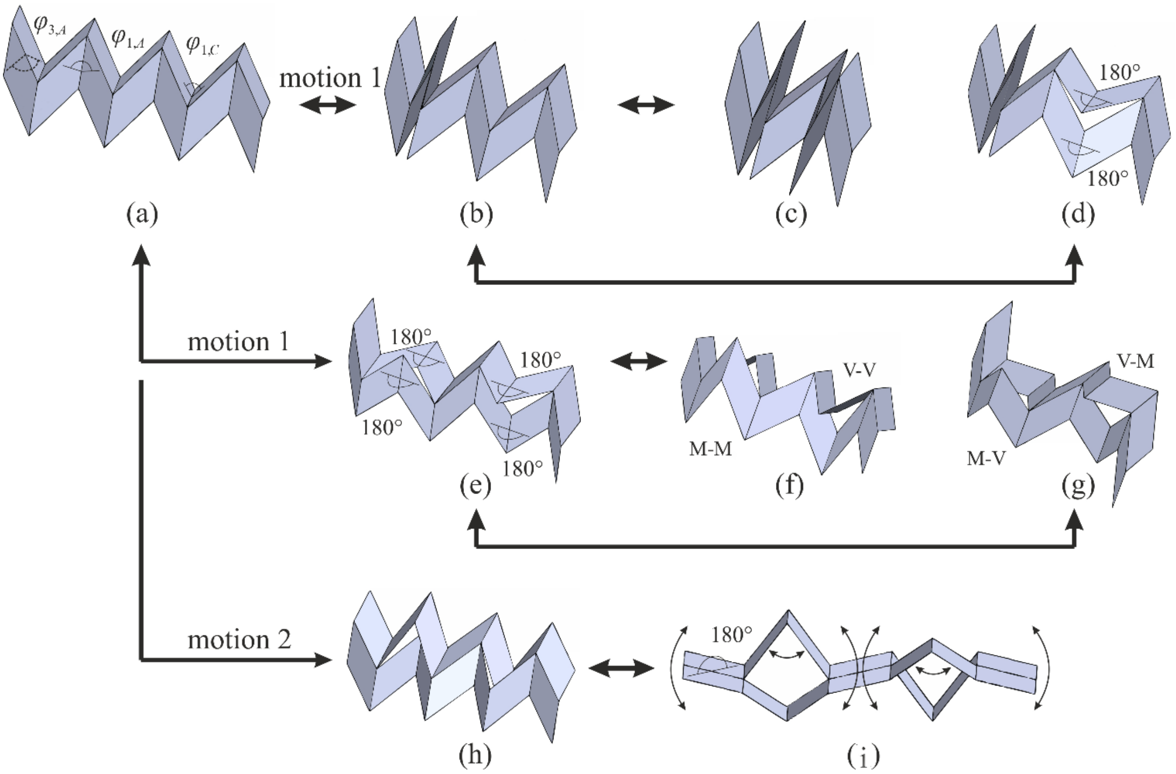

Fig. 5.8 Reconfiguration of a horizontal assembly of two cells; (a) the assembly in the Miura-ori form; (b) to (g) are examples of the new shapes accessed via motion type 1; (h) and (i) are examples of the new shapes accessed via motion type 2.

$$M_H = c + 1\,. \tag{5.22}$$

Additionally, the number N_H of alternative MV assignments for a horizontal assembly is

$$N_H = 4^c\,. \tag{5.23}$$

Moreover, in the Miura-ori configuration, we can freeze φ_1 in both cells, i.e. remove two of the three DOFs. Then, for example, using $\varphi_{3,A}$ we can start motion type 2. As the φ's at diagonal creases are passed along, the cells experience the motion simultaneously, as shown in Fig. 5.8(h). Once $\varphi_{3,A}$ is 180°, all diagonal folds become flat, and both cells enter the rhombic state at the exact moment, Fig. 5.8(i).

This configuration is less stable than the previous ones. This is because the second cell inherits only information that $\varphi_{3,C}$ equals 180°. As a result, both cells increase their individual

DOF count to three, in a way typical for a single cell in the rhombic state. Thus, the DOF number of the entire assembly jumps from three to six. This makes the control demanding but allows for more reconfigurations. All six DOFs, representing the arm rotations and closing-expanding the rhombuses inside, are illustrated schematically in Fig. 5.8(i) with arrows. We activate the three DOFs of each cell with its φ_1, φ_2 and φ_8, or, alternatively, φ_5, φ_4 and φ_6. Multiple cells in the horizontal direction still enter the rhombic state simultaneously. As each of c cells increases its DOFs to three, the assembly's overall mobility jumps from c+1 to 3c. This gives plenty of freedom to alter the shape.

To conclude, horizontal merging, unlike the vertical one, adds new DOFs. The assembly's mobility depends on the number of cells in a row – c. In the Miura-ori configuration and during motion types 1 and 2, the number of DOFs equals c+1. However, in the rhombic state, it increases to 3c. In terms of the alternative forms, motion type 1 allows for 4^c MV assignment variants. The following section combines both ways of merging to build a global pattern.

5.4 Global Miura-ori with diagonal slits

For a global Miura-ori with the slits, first, we merge a few cells horizontally, like in section 5.3. Then, we add panels from the top to build more cells. Section 5.2 showed that vertical cell addition does not increase mobility. Therefore, a global pattern should have kinematics similar to the horizontal assembly. The example in Fig. 5.9 confirms this.

According to (5.22), an assembly of three cells in a row should have mobility equal to four. We can use all the DOFs to fold the pattern into the traditional form, Fig. 5.9(b).

Alternatively, we can freeze φ at any diagonal crease. If so, the remaining three DOFs act on each cell of the lowest row independently. Meanwhile, in the vertical direction, the motion reproduces automatically, without new inputs needed. Figure 5.9(c) illustrates this. For example, we can fold the first cell and expand the third one fully while keeping the middle one in the Miura-ori shape. This displays that the mobility M of a global pattern of c cells in each row equals in general case

$$M = c + 1. \tag{5.24}$$

Moreover, we can use the DOFs to expand all the columns fully, as in Fig. 5.9(d). In this configuration, we can change the MV assignment independently for each crease with φ equal to 180°. For example, in Fig. 5.9(e), the MV assignment for creases 1 and 5 is M-M-M-M in the first column of the cells, V-V-V-V in the second, and M-V-M-V in the third. The number

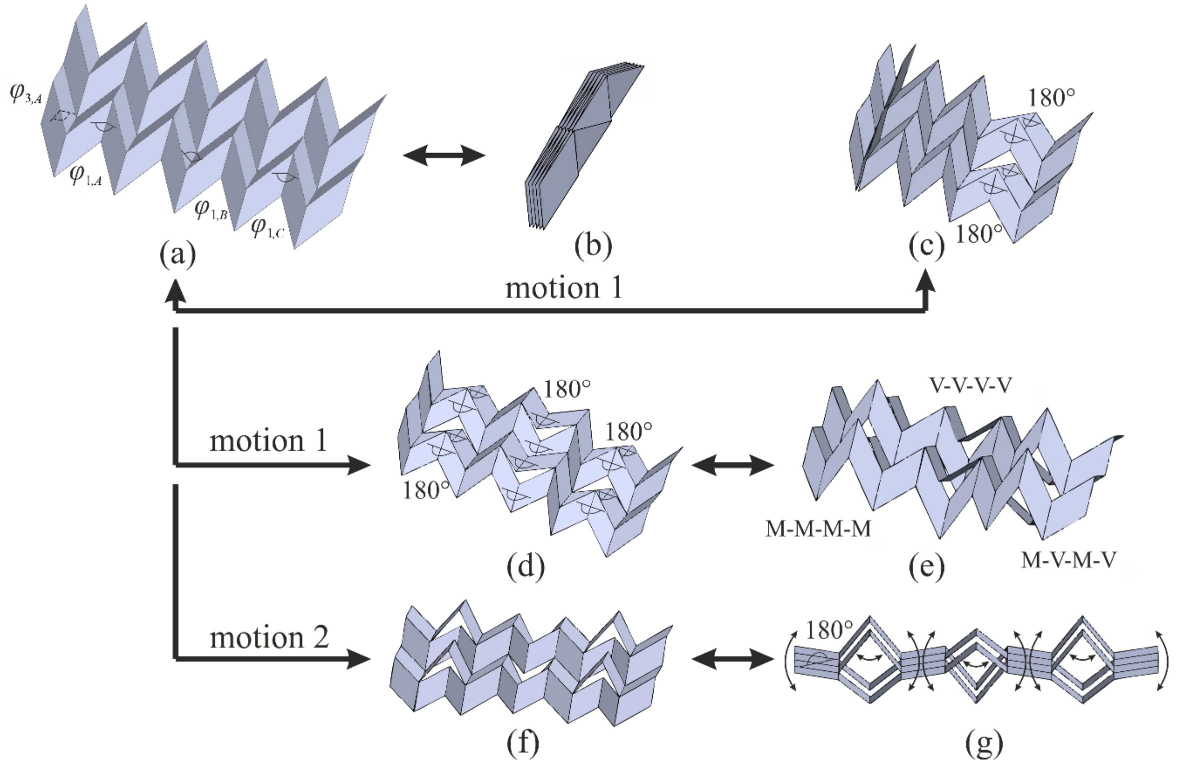

Fig. 5.9 Reconfiguration of a global 3x3 assembly; (a) the assembly in the Miura-ori form; (b) its standard folded shape; (c) to (e) are exemplary new shapes accessed via motion type 1; (f) and (g) are exemplary new shapes accessed via motion type 2.

of variants increases with more vertical cells, according to (5.20). Horizontal merging also adds combinations, as in (5.23). Thus, the total number of alternative forms and folded shapes accessed via motion type 1 of a pattern with r rows and c columns of the cells is

$$N = 2^{c(r+1)}. \tag{5.25}$$

Also, to start motion type 2, we should first freeze all individual DOFs belonging to separate cell columns, e.g. φ_1's in Fig. 5.9(a). Then, we should change one φ at any diagonal crease. We notice that the rest of φ's at diagonal folds follow, as in Fig. 5.9(f), and all the cells reach the rhombic state simultaneously, Fig. 5.9(g). In this configuration, each cell has three DOFs that rotate its arms and fold or expand the rhombus inside. As vertical creases align, each input affects all cells within the same column. Therefore, the example has nine independent DOFs in its rhombic state.

The above confirms that the mobility of a global pattern does not depend on how many rows of cells it has. Instead, it is columns of the cells that matter. Also, while the DOF number of an assembly with c columns is c+1 during motion types 1 and 2, as soon as it enters the rhombic state, its mobility M_{RS} jumps to

$$M_{RS} = 3c. \tag{5.26}$$

This significant increase in DOFs makes controlling a global pattern complicated, mainly if many cells constitute a row. However, the extra freedom provides us with even more configurations. Next, section 5.5 presents a few interesting examples.

5.5 Exemplary new configurations

5.5.1 *More folded shapes*

This section shows that the rhombic state is an intermediate configuration that lets us fold the Miura-ori into even more shapes. For example, we take a crease pattern with double diagonal slits, Fig. 5.10(a). It consists of two rows of four cells each. While the DOF number due to the cuts is five, the pattern can still fold into the Miura-ori forms, Fig. 5.10(b) and (c).

Next, in the form in Fig. 5.10(b), we can start motion type 2. We should set all φ_1's in the lowest row to the same preselected value. This freezes four DOFs. Then, once we change φ at any diagonal crease, the last DOF activates motion type 2. When φ's at diagonal folds reach 180°, all the cells enter the rhombic state simultaneously, as in Fig. 5.10(e). The assembly's mobility jumps to 12 what is in agreement with (5.26).

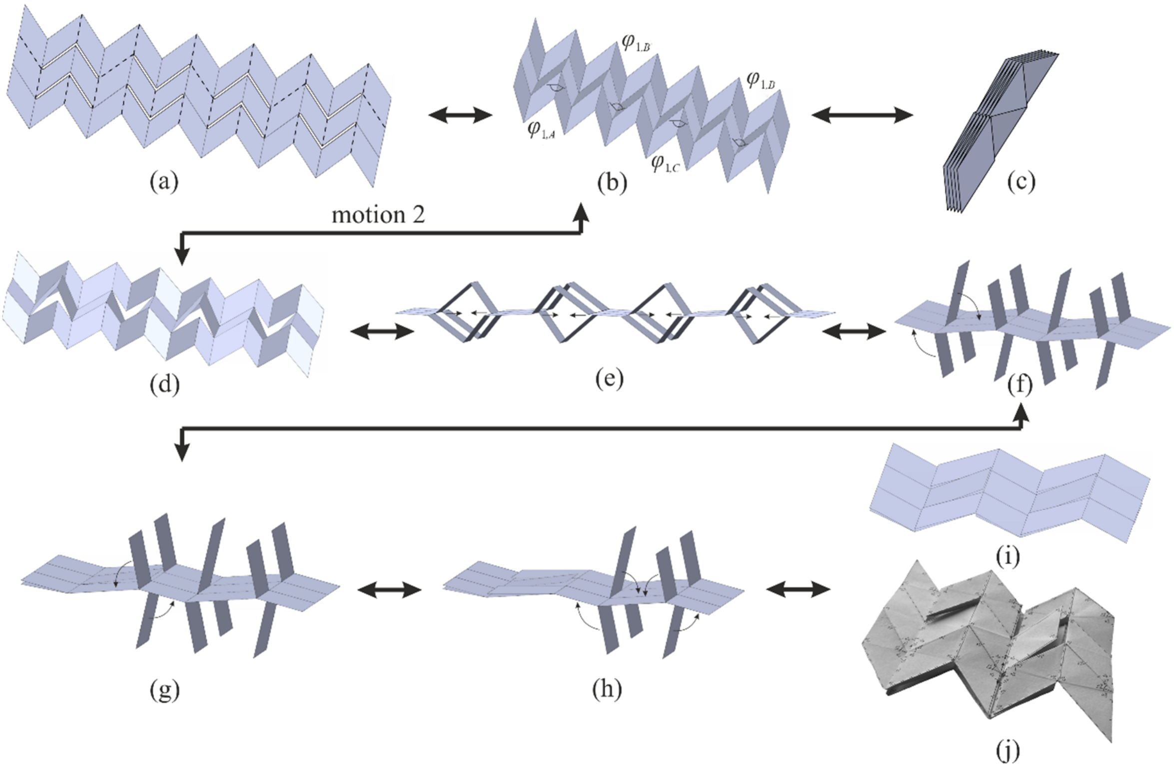

Fig. 5.10 (a) A 2x4 assembly in the flat state; (b) and (c) show its traditional folding; (d) to (i) is an alternative folding via motion type 2; (j) is a physical model in the alternative folded form.

To fold the pattern in a new way, we need to continue the reconfiguration of the rhombic state. First, we should change the value of all frozen φ_1's to zero, i.e. fold the rhombuses and disable four DOFs. Now, we can use the remaining eight inputs between the folded parts and their arms. The arms can move up, down or in opposite directions relative to the folded rhombuses. This gives many configurations we can pursue.

The example in Fig. 5.10 shows a particular folding with opposite arm rotations. We start by tilting the first folded part clockwise, as in Fig. 5.10(f), and we get the shape in Fig. 5.10(g). Then, we rotate the second folded rhombus anticlockwise and reach the form in Fig. 5.10(h). This reconfiguration continues for the third and the fourth folded parts. We rotate them clockwise and anticlockwise, respectively. As a result, we obtain a layered shape shown in Fig. 5.10(i).

This folded form is larger than the traditional one, Fig. 5.10(c). However, the panels arranged regularly in layers do not enclose each other from all sides anymore and can give smooth top and bottom surfaces. Also, we can freely increase the number of the assembly's cells. If we add them vertically, they follow the motion automatically. New horizontal cells add DOFs. We should fold their rhombuses too, and then continue the clockwise and anticlockwise rotations.

This example shows that the slits bring even more folded forms to the Miura-ori. This group is accessed via motion type 2 and the rhombic state and adds up to the folded shapes that result from motion type 1. These configurations can bring significant advantages to the Miura-ori. When in the traditional compact form, the pattern can now reshape into new folded stacks without going through the flat state. This may help with reconfiguration in limited space. Also, the folding initiated in the flat form may finish in various compact configurations. This wealth of possible forms may lead to more efficient packaging of structures and optimised use of storage or transportation volume. Additionally, thanks to the rhombic state, shapes with panels not enclosing each other are now possible. Such forms may be helpful to accommodate thick panels, which are often required in engineering applications.

5.5.2 *Metamaterial-like shapes*

Another way to use the rhombic state is to reconfigure it into structures resembling cellular folded metamaterials. For example, we can use a crease pattern as in Fig. 5.10(a), but with five rows of the cells, as in in Fig. 5.11(a). In the Miura-ori form, Fig. 5.11(b), we should freeze all φ_1's in the lowest row again. Now, we set them explicitly to 90°. One DOF remains, which we use to access the rhombic state. This time, we do not fold the rhombuses. We keep φ_1's as 90°, Fig. 5.11(c). Eight DOFs remain as our reconfiguration inputs, which move the cells' arms.

Next, we rotate the first cell's left arm anticlockwise until it aligns with the rhombus's panels. Then, we rotate the rhombus clockwise until its side aligns with the right arm. Figure 5.12(c) illustrates the motions schematically. Next, as in Fig. 5.11(d), we rotate the second rhombus anticlockwise and its right arm clockwise, again to the alignment point. Figure 5.12(e) shows the resulting shape and the subsequent motions, which should continue horizontally until all the parts rotate. Similar motion sequences can be applied to assemblies with more cells as well.

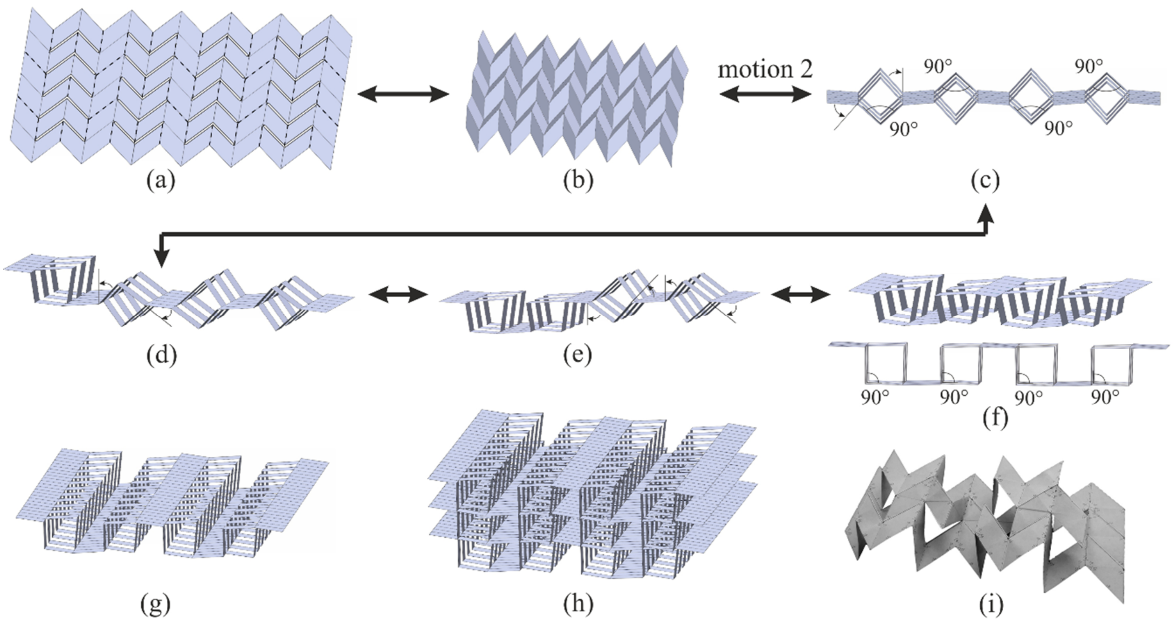

Fig. 5.11 (a) to (f) Reconfiguration of a 4x5 assembly into a metamaterial-like shape; (g) a similar assembly but with 23 cell rows in the final form; (h) three assemblies like in (g) stacked together; (i) a physical model of a 2x4 assembly in the final form.

As a result, we reconfigure the pattern into the structure in Fig. 5.11(f). It has a top and a bottom set of repeatable horizontal flanges and a system of open internal channels, square in cross-section. Moreover, the number of cells in the vertical direction does not change the mobility. Even if there are many, the motion sequence stays the same. Figure 5.11(g) shows the final configuration of a similar but much larger pattern, with 23 cells vertically. Also, the flanges allow stacking such structures on top of each other, in layers, like in Fig. 5.11(h).

Such reconfigurable shapes could suggest improved manufacturing methods in composite engineering or different folded cores of sandwich structures given extra load-bearing elements are introduced, so the final forms are no longer mechanisms but modified to meet the stiffness requirements of desirable cross-sections. Alternatively, these forms could inspire unique cellular folded mechanical metamaterials at a micro or a nanoscale. The geometries as in Fig. 5.11 have a cellular structure and remain mechanisms that can locally rotate and fold along revolutes that emerge when panels align, which would allow tuning their geometry and thus mechanical properties. Such shapes, along with the alternative configurations resulting from various MV assignments during motion 1, could also provide metamaterial layers that could be stacked and remain tunable. While worth investigating, this is a subject for another discussion.

5.5.3 *Tubular shapes*

We can also use the rhombic state to reconfigure Miura-ori into tube-like forms. For the first example, we should take an assembly with four cell columns. The number of rows is free to select. We choose 10, although even a much bigger number would not change the mobility. Figure 5.12(a) shows the crease pattern, which of course, can fold into the traditional Miura-ori shapes.

To obtain tubular forms, we use motion type 2. First, we freeze all φ_1's in the lowest row at 90° what disables four out of five DOFs. Next, we activate the last one to reach the rhombic state, Fig. 5.12(d). The DOF number jumps to 12, with four still blocked. The new DOFs allow us to rotate the first cell's arms upwards until they align with the rhombus' panels, as in Fig 12(e). Then, we tilt the next rhombus and its right arm anticlockwise to obtain a similar shape for the second cell. We continue as in Fig. 5.12(f) for the remaining cells until the motion returns the geometry in Fig. 5.12(g). It is a tube-like shape, square in cross-section. Figure 5.12(i) is the side view.

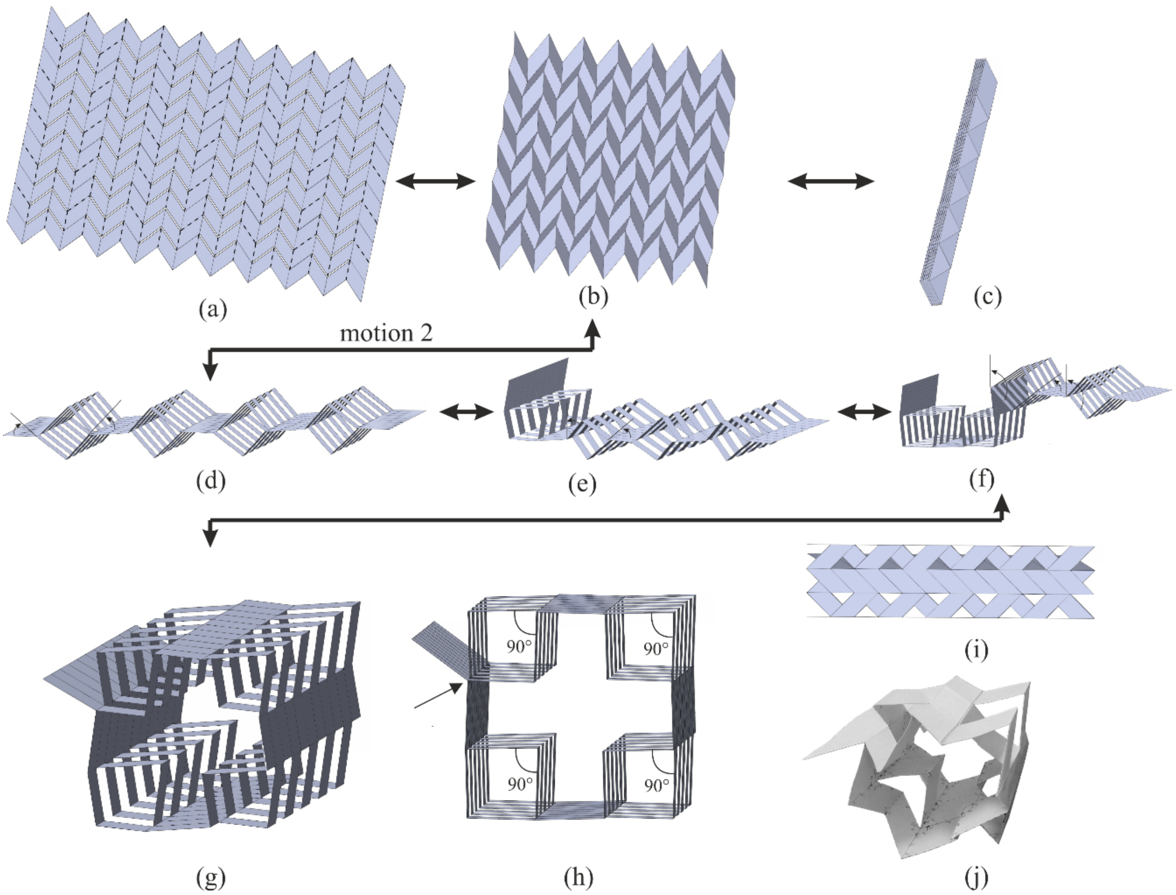

Fig. 5.12 (a) A 10x4 assembly in the flat state; (b) and (c) show the traditional folding; (d) to (g) illustrate a reconfiguration into a tube-like form; (h) and (i) show the front and the side of the final shape, respectively; (j) is a physical model of a 2x4 tube.

With φ_1's frozen at 90°, the rhombuses, now the tube's corners, behave as rigid bodies. The tube's cross-becomes an open chain of nine bodies. It has eight DOFs. We can close it in the place marked with an arrow in Fig. 5.12(g). If we join the panels using a hinge, the cross-section turns into a closed loop of eight rigid bodies. Its mobility drops to two. Notice we do not count the arm outside the tube, which is free to rotate trivially. Alternatively, if we make a rigid connection, we transform the cross-section into a closed chain of seven bodies with one DOF.

Figure 5.13 illustrates the reconfiguration of a second example. It is a pattern that has six cells in each row. This time, we freeze φ_1's at 120° and disable six DOFs. When the pattern

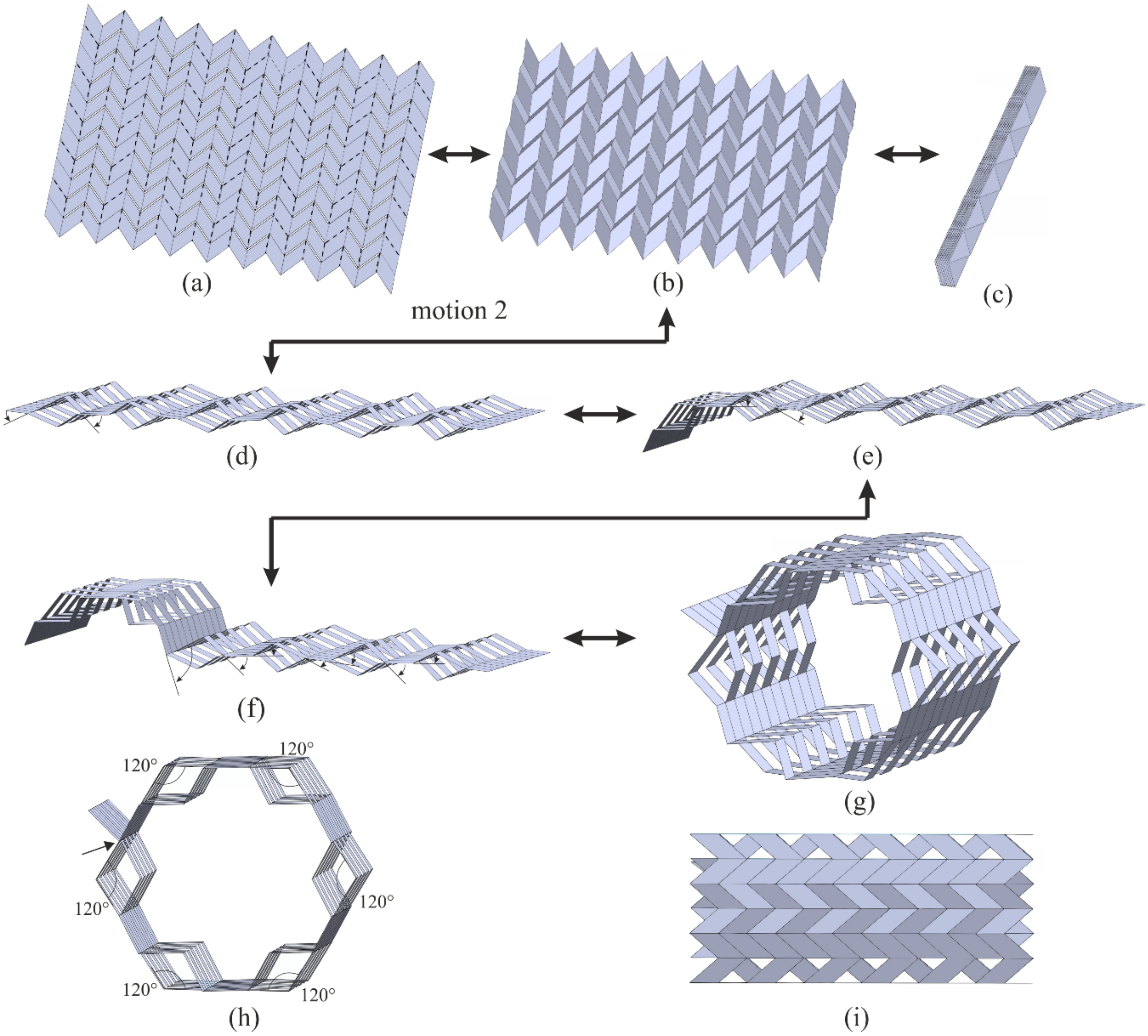

Fig. 5.13 (a) A 10x6 assembly in the flat state; (b) and (c) show the traditional folding; (d) to (g) illustrate a reconfiguration into a tube-like form; (h) and (i) show the front and the side of the final shape, respectively.

reaches the rhombic state, we have 12 out of 18 inputs to decide the shape. We again rotate the arms so that they align with the rhombuses. The reconfiguration gives another tubular shape, this time hexagonal, Fig. 5.13(g). If its cross-section is closed with a revolute joint, the mobility decreases to six (not counting the free-rotating arm). A rigid connection gives five DOFs.

Notice that the number of the cells in the vertical direction in both examples does not change the motion sequence. From the mechanical point of view, even infinitely long tubes will behave similarly and have the same number of DOFs. These examples show that slits can turn the Miura-ori into 3D tubes with reconfigurable cross-sections. They could find various applications at different scales. For example, they might inspire micro-medical devices or provide a structural framework for space habitats deployable in orbit.

5.6 Summary

This chapter continued the discussion on how regular two-crease-long cuts change the Miura-ori's kinematics. This time, the slits along diagonal creases were examined. They allowed Miura-ori to behave in even more exciting ways and brought unusual folded configurations, even without panels overlapping each other.

First, the chapter provided the kinematic analysis of a single cell with the slit and confirmed it is a two-DOF assembly capable of two new motion types. The choice between them depends on freezing specific dihedral angles. Also, an intermediate form along the second motion type called the rhombic state was identified. It involves a sudden increase in the cell's mobility, from two to three. This brings even more freedom to reconfigure the cell.

Next, chapter 5 explained how to build a global kirigami version of the Miura-ori using the cells. Such a pattern still can fold traditionally but also inherits the new motions. By freezing φ at any diagonal crease, we decide for motion type 1. If so, each column of the cells has its own DOF that allows for a local reconfiguration. Alternatively, if all φ_1's in the lowest row are disabled, we can use the remaining DOF for motion type 2.

Moreover, along motion 2's path, the pattern enters the rhombic state. It brings a significant increase in mobility, from $c+1$ to $3c$, where c is the number of cells in each row.

The extra DOFs provide even more alternative configurations and folded forms of the assembly. Some of them even without lower rows of panels enclosing the upper ones, which can be helpful when manufacturing physical applications. Additionally, the rhombic state's mobility allows it to rearrange the pattern into metamaterial- and tube-like forms. These shapes can be a source of ideas for structures in many disciplines. Figure 5.14 presents the strategy for manufacturing and controlling the Miura-ori variant with the regular double slits along its diagonal creases.

Both cutting variants from chapters 4 and 5 confirm that slits can bring unique reconfigurations to traditional single-DOF rigid origami. Such removal of joints can relax a pattern kinematically and add extra DOFs. However, keeping the slit arrangement regular

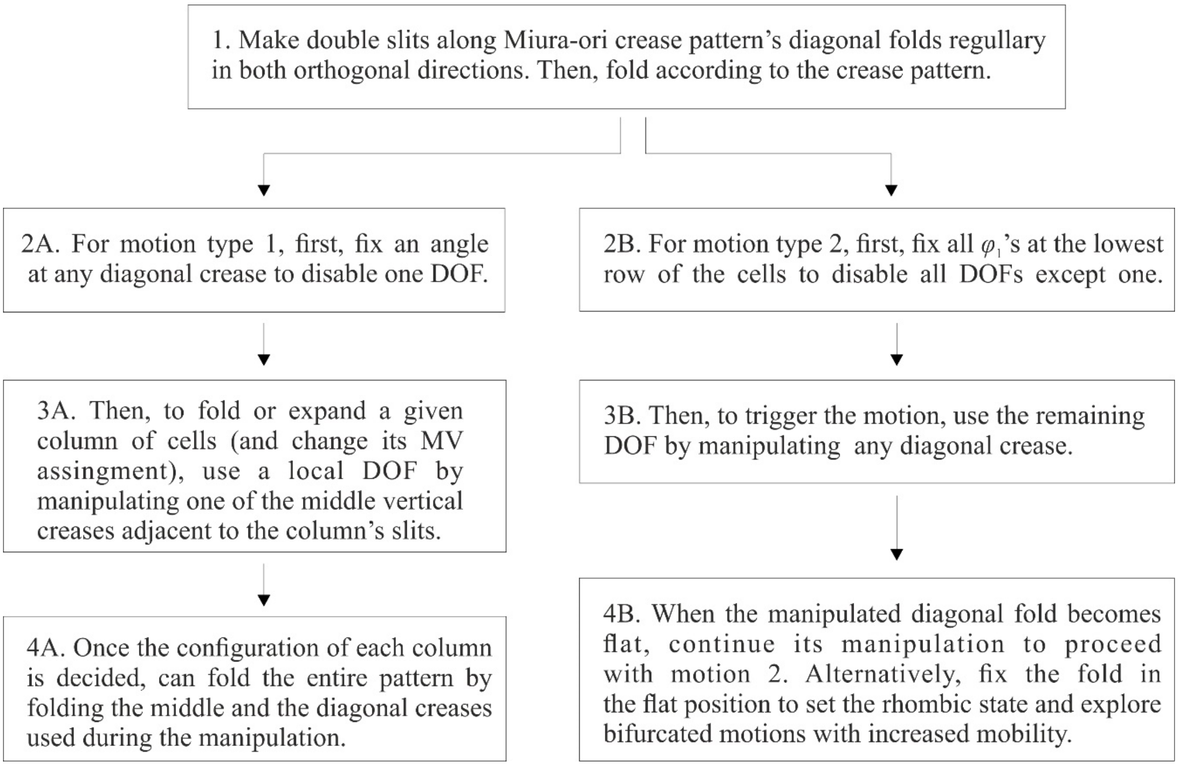

1. Make double slits along Miura-ori crease pattern's diagonal folds regullary in both orthogonal directions. Then, fold according to the crease pattern.

2A. For motion type 1, first, fix an angle at any diagonal crease to disable one DOF.

3A. Then, to fold or expand a given column of cells (and change its MV assingment), use a local DOF by manipulating one of the middle vertical creases adjacent to the column's slits.

4A. Once the configuration of each column is decided, can fold the entire pattern by folding the middle and the diagonal creases used during the manipulation.

2B. For motion type 2, first, fix all φ_1's at the lowest row of the cells to disable all DOFs except one.

3B. Then, to trigger the motion, use the remaining DOF by manipulating any diagonal crease.

4B. When the manipulated diagonal fold becomes flat, continue its manipulation to proceed with motion 2. Alternatively, fix the fold in the flat position to set the rhombic state and explore bifurcated motions with increased mobility.

Fig. 5.14 A strategy for manufacturing and controlling the Miura-ori with the regular double diagonal slits.

by the orderly multiplication of cuts in both orthogonal directions turned out to be at the expense of increasing mobility. For slits both along vertical and diagonal edges, we cannot keep the DOF number finite, as it gets bigger as the pattern grows larger.

Moreover, the elaborate shapes presented in Figs. 5.10-5.13, which are possible thanks to the mobility increase and multiple DOFs, are unfortunately unhandy and their control very complex. The number of the required inputs, reaching even double-digit values for larger patterns, makes manipulating physical models troublesome. For engineering applications, such structures would require designing special control devices.

The examples in this chapter highlight a point that a slit arrangement that provides reconfigurability while simultaneously maintaining a finite low DOF number would be desirable. Therefore, the thesis's following chapters will attempt to achieve the remaining research objectives. As the slit patterns that make new reconfigurations possible have been already identified, we will now try to assemble the spatial 8R linkages in a way that assigns priority to keeping the entire assembly's DOF number finite, equal to two.

Chapter 6

Two-DOF reconfigurable Miura-ori

The previous chapters showed that slits creating local 8R lops can give Miura-ori multiple new forms. However, the orderly way of multiplying cuts resulted in assemblies with numerous DOFs that are difficult to control when the pattern gets large. In this chapter, we will slit Miura-ori once again. This time, we will prioritise keeping the DOF number finite, ideally equal to two. In this way, the resulting pattern would stay relatively easy to control while still exhibiting some previously unavailable configurations.

This chapter aims to obtain a two-DOF reconfigurable structure out of the rigid-origami Miura-ori that would be significantly easier to control than the assemblies in chapters 4 and 5. First, the chapter develops a two-DOF assembly, then explains its kinematics, and finally simplifies the slit arrangement to make it more regular and easy to replicate.

6.1 Building a two-DOF Miura-ori

Figure 6.1 presents a process of assembling a cluster of 8R linkages in a step-wise manner that ensures the final DOF number is equal to two. We start from a single 8R Miura cell with the diagonal slit that we used in chapter 5, which we know has two DOFs (the dark grey panels in Fig. 6.1(a)). Being our linkage A, we can assume its inputs are $\varphi_{1,A}$ and $\varphi_{3,A}$.

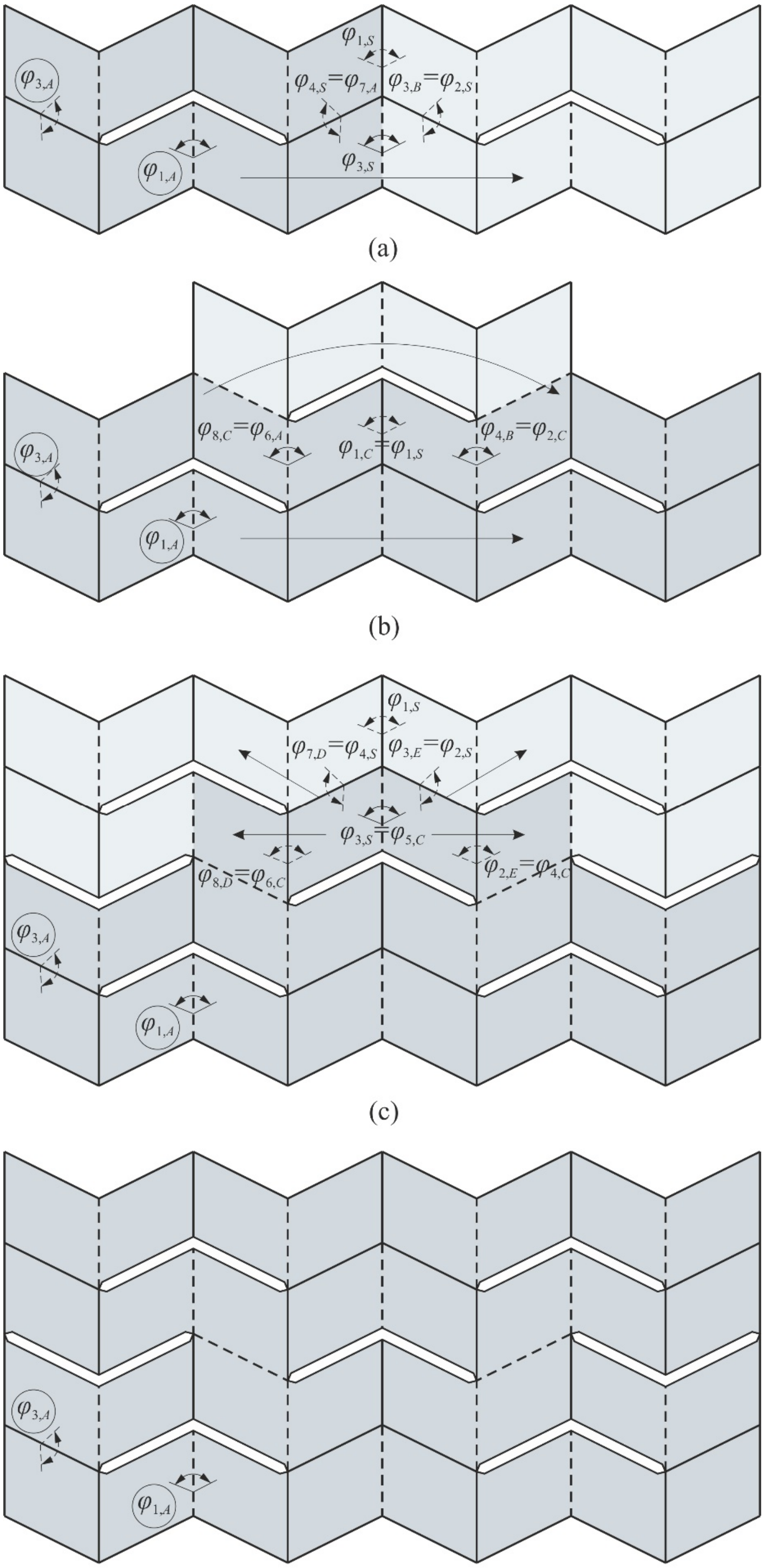

Fig. 6.1 A process of assembling a two-DOF cluster of 8R Miura-ori cells with the double diagonal slits. Arrows show the DOF transmission throughout the pattern.

The rest of its dihedral angels result from the geometry, according to (5.1) to (5.6). Next, we attach a second 8R loop to it so that the cells do not share any panels, but a spherical 4R linkage is formed between, with dihedral angles $\varphi_{1,S}$, $\varphi_{2,S}$, $\varphi_{3,S}$ and $\varphi_{4,S}$.

From Fig. 6.1(a), we see that the spherical linkage works as a link between the two cells, transmitting one input to the second 8R. From linkage A's closure equation (5.1), we know

$$\varphi_{7,A} = \varphi_{3,A} \tag{6.1}$$

Therefore, from Fig. 6.1(a) there is

$$\varphi_{4,S} = \varphi_{7,A} = \varphi_{3,A} \tag{6.2}$$

From the Miura-ori spherical 4R linkages' kinematics (2.12), we know that

$$\varphi_{2,S} = \varphi_{4,S} = \varphi_{3,A} \tag{6.3}$$

This means that input $\varphi_{3,A}$ is transmitted via 4R linkage to linkage B because

$$\varphi_{3,B} = \varphi_{2,S} = \varphi_{3,A} \tag{6.4}$$

The second input $\varphi_{1,A}$ is not transferred to the second cell. As linkage B inherits only one variable and requires us to specify another one, the horizontal assembly of two 8R linkages from Fig. 6.1(a) has three DOFs – two from linkage A and one from linkage B.

We can confirm the above with step-wise Kutzbach mobility calculations. We start from a single 8R loop with mobility $M_{old} = 2$. Next, going towards the right, we add $N_{sph} = 2$ panels with $j_{sph} = 3$ joints that are a part of the newly formed spherical linkage. Then, we add $N = 6$ panels with $j = 7$ revolutes more, which complete the second 8R loop. The panels forming spherical linkages are of the three-DOF potential and the rest of the six-DOF type. As a result, we have

$$M = M_{old} + 3(N_{sph} - j_{sph}) + j_{sph} + 6(N - j) + j = 2 + 0 + 1 = 3 \tag{6.5}$$

The next step, displayed in Fig. 6.1(b), is adding extra four panels vertically to complete a third 8R linkage in the middle. It does not add any new DOFs as it already inherits two inputs from linkage A and the spherical 4R linkage below, as follows.

$$\varphi_{8,C} = \varphi_{6,A} = f(\varphi_{1,A}, \varphi_{3,A}), \quad \varphi_{1,C} = \varphi_{1,S} = g(\varphi_{4,S}) = g(\varphi_{3,A}). \qquad (6.6),(6.7)$$

Functions *f* and g result from the closure equations for the 8R linkage, (5.1) to (5.6), and the Miura-ori spherical 4R linkage, (2.12), respectively. Linkage C's remaining dihedral angles adjust to the two inputs $\varphi_{8,C}$ and $\varphi_{1,C}$ i.e. are indirectly functions of $\varphi_{1,A}$ and $\varphi_{3,A}$.

Moreover, linkage C additionally constrains the two cells below (A and B) as it works as an additional link between them, transmitting the second missing input to linkage B according to

$$\varphi_{4,B} = \varphi_{2,C} = \varphi_{8,C} = f(\varphi_{1,A}, \varphi_{3,A}). \qquad (6.8)$$

As all the linkages inherit now two variables, no extra inputs are required to define their shapes, i.e. the overall mobility of the assembly decreases to two. We can confirm this again with Kutzbach calculations. In the step from Fig. 6.1(b), we added $N = 4$ panels and $j = 5$ joints to an assembly of two 8R cells with overall mobility $M_{old} = 3$. So,

$$M = M_{old} + 6(N - j) + j = 3 + 6(4 - 5) + 5 = 3 - 1 = 2. \qquad (6.9)$$

Next, what is presented in Fig. 6.1(c) can be divided into two sub-steps. First, we add $N_{sph} = 2$ panels and $j_{sph} = 3$ joints at the top of linkage C to create another spherical 4R linkage. It inherits a dihedral angle from linkage C,

$$\varphi_{3,S} = \varphi_{5,C} = \varphi_{1,C} = g(\varphi_{3,A}), \qquad (6.10)$$

and adjusts its shape to the single input it requires, without changing the overall mobility,

$$M = M_{old} + 3(N_{sph} - j_{sph}) + j_{sph} = 2 + 3(2 - 3) + 3 = 2 + 0 = 2. \qquad (6.11)$$

Then, on the left-hand side, we add five panels to finish the next 8R linkage D, in the top left corner. It also inherits two inputs from the previous linkages

$$\varphi_{8,D} = \varphi_{6,C} = \varphi_{8,C} = f(\varphi_{1,A}, \varphi_{3,A}), \quad \varphi_{7,D} = \varphi_{4,S} = g^{-1}(\varphi_{3,S}) = \varphi_{3,A}. \quad (6.12),(6.13)$$

This means it neither adds nor removes DOFs from the assembly with $M_{old} = 2$, which we confirm again with a formula with $N = 5$ and $j = 6$ that gives

$$M = M_{old} + 6(N - j) + j = 2 + 6(5 - 6) + 6 = 2 + 0 = 2. \quad (6.11)$$

We repeat the same for the top-right corner to form the final 8R linkage E, whose addition also does not change the overall mobility.

Figure 6.1(d) presents the eight-by-four-panel assembly in its finished form. It is a cluster of spatial 8R and spherical 4R linkages, which has precisely two DOFs. Therefore, we can control it with just the first cell's two inputs $\varphi_{1,A}$ and $\varphi_{3,A}$. Before we analyse its kinematics, we attempt to determine repeatable steps that will allow us to grow the pattern with such diagonal slits infinitely while keeping the mobility value equal to two.

Figure 6.2 presents how growing the assembly by maintaining a regular arrangement of 8R and 4R linkages does not allow keeping two DOFs. Figure 6.2(a) shows the two-DOF cluster of 8R and 4R linkages, which we developed earlier. The types of mechanical linkages that comprise the assembly and their regular geometric arrangement are highlighted in Figure 6.2(b) in a symbolic and coloured manner. Next, we present two attempts to grow the cluster while keeping the regular linkage layout.

Figures 6.2(c) and (d) display an attempt to close one of the two-crease-long slits on the edges of the cluster with two extra panels. As the original assembly in Fig. 6.2(a) has already two folds cut next to its edge, we provide the missing panels to complete a linkage loop and guarantee a familiar 8R linkage is formed. Again, this is to ensure that the assembly we are growing is regular, consisting of only 4R and 8R linkages.

However, this means adding $N=2$ panels and $j=3$ revolutes to an assembly with mobility $M_{old}=2$ to finish yet another spatial linkage. The new mobility becomes

$$M = M_{old} + 6(N - j) + j = 2 + 6(2-3) + 3 = -1 . \tag{6.12}$$

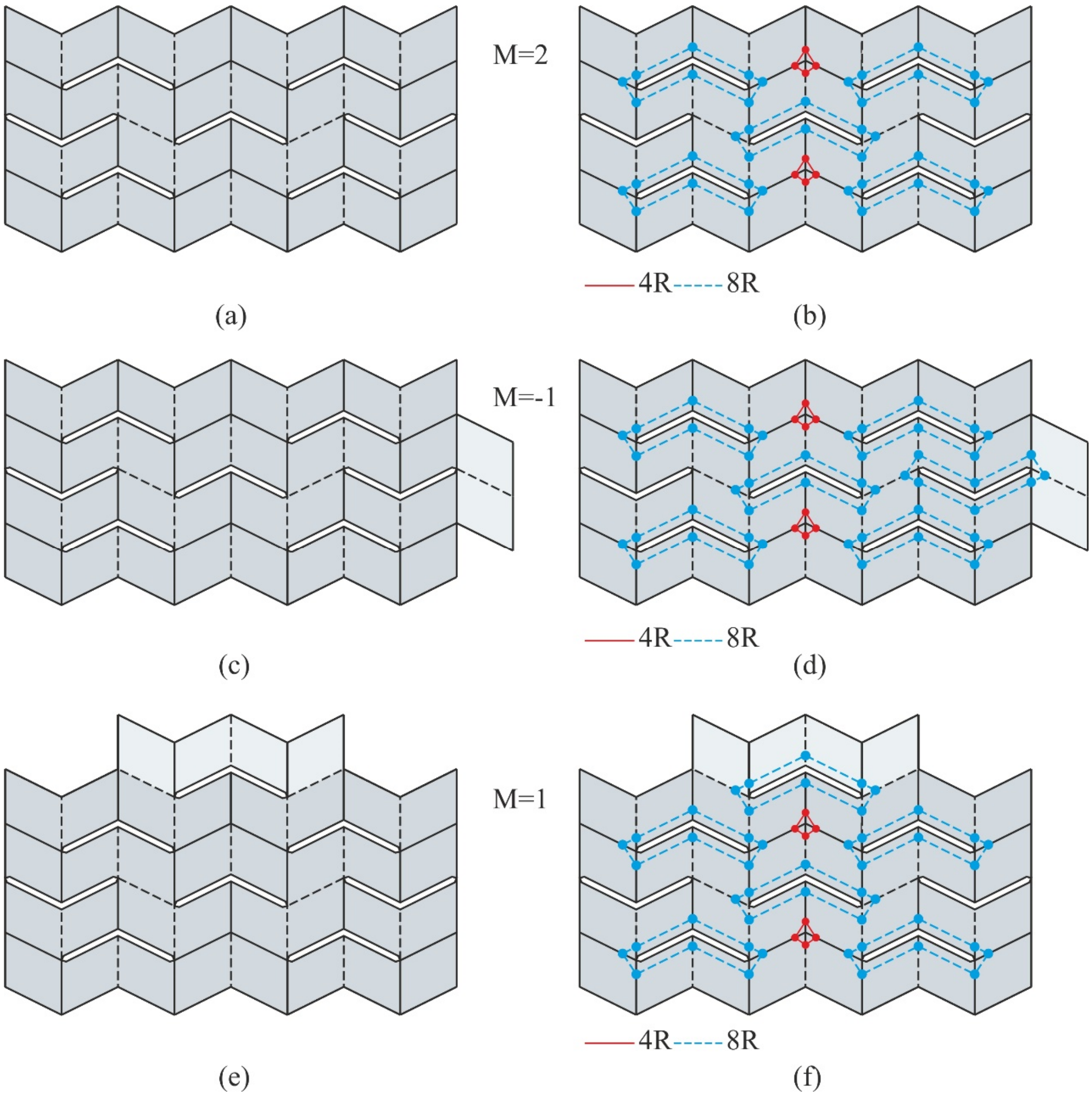

(a) (b)

(c) (d)

(e) (f)

Fig. 6.2 Unsuccessful attempts to grow a two-DOF assembly while keeping regular linkage arrangement; (a) and (b) is a regular two-DOF cluster of 4R and 8R cells; (c) and (d) is an attempt to continue the regular slit arrangement in the horizontal direction; (e) and (f) is a similar effort in the vertical direction.

Equation (6.12) returning -1 suggests the two extra panels constrain the assembly significantly. Indeed after verifying the assembly's kinematics, due to the overconstraint, it can only exhibit the traditional one-DOF folding. This shows that growing the assembly in the horizontal direction to ensure the regular layout of only 4R and 8R linkages does not support maintaining two DOFs.

Figures 6.2(e) and (f) show another attempt to grow the pattern regularly, this time in the vertical direction. To continue alternating 4R and 8R linkages, we provide $N = 4$ panels and $j = 5$ joints to the two-DOF cluster from the top. The step-wise calculation,

$$M = M_{old} + 6(N - j) + j = 2 + 6(4 - 5) + 5 = 1, \qquad (6.13)$$

returns now mobility equal to one. This shows that the regular linkage addition again constrains the assembly to only the original Miura-ori motion. Therefore, in the subsequent attempts, we decide to grow the pattern to ensure the overall mobility of two, even at the expense of the linkage arrangement becoming irregular.

Figure 6.3 presents an alternative approach to adding panels to build the assembly horizontally. It assumes adding panels in an arbitrary but systematic and kinematically-aware manner. While the majority of panel additions have alternatives, the panels are added in a way to control the final mobility value. As a result, the emerging assembly becomes irregular, but its two DOFs are maintained. Figures 6.3(a) to (f) present the subsequent steps. Each one adds extra panels forming either new loops around slits or new spherical linkages. We can evaluate the DOFs number after each step according to the following calculations.

Adding $N = 6$ new panels and $j = 7$ revolutes to form a new loop adds 1 DOF:

$$M = M_{old} + 6(N - j) + j = M_{old} + 6(6 - 7) + 7 = M_{old} + 1 \quad . \qquad (6.14a)$$

$N=5$ new panels and $j=6$ joints keep the assembly's previous mobility unchanged:

$$M = M_{old} + 6(N-j) + j = M_{old} + 6(5-6) + 6 = M_{old} + 0 \quad . \tag{6.14b}$$

$N=4$ new panels and $j=5$ revolutes constrain the assembly by removing 1 DOF:

$$M = M_{old} + 6(N-j) + j = M_{old} + 6(4-5) + 5 = M_{old} - 1 \quad . \tag{6.14c}$$

Additionally, extra $N_{sph}=2$ panels with $j_{sph}=3$ joints building a new spherical linkage also do not change the mobility:

$$M = M_{old} + 3(N_{sph} - j_{sph}) + j_{sph} = M_{old} + 3(2-3) + 3 = M_{old} + 0 \quad . \tag{6.14d}$$

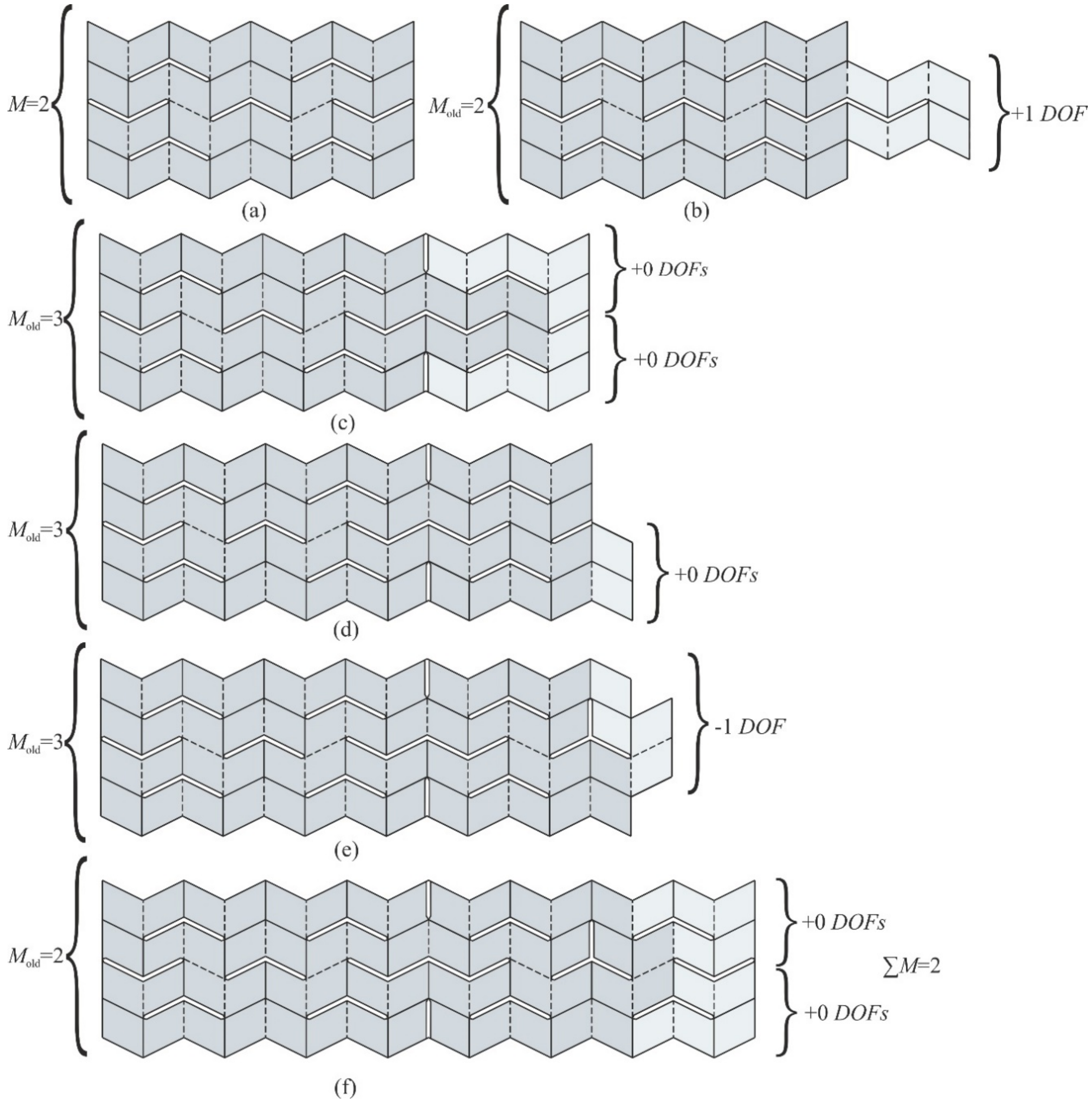

Fig. 6.3 A repeatable panel addition sequence to grow the pattern horizontally that sacrifices the regularity of slits but ensures the final mobility equals two.

Using the above estimations and making sure we add panels either by not changing mobility or by first increasing DOFs and then constraining them to return to the mobility of two, we grow the pattern horizontally. Figure 6.3(f) presents a finished assembly, now sixteen-by-four in size. The sequence of adding an extra eight-by-four-panel cluster horizontally presented in Fig.6.3 can be repeated infinitely.

Figure 6.4 presents an equivalent step-wise approach to growing the assembly in the vertical direction. We again build on the original eight-by-four cluster, ensuring the final mobility equals two by using the panel additions with mobility changes (6.14a) to (6.14d).

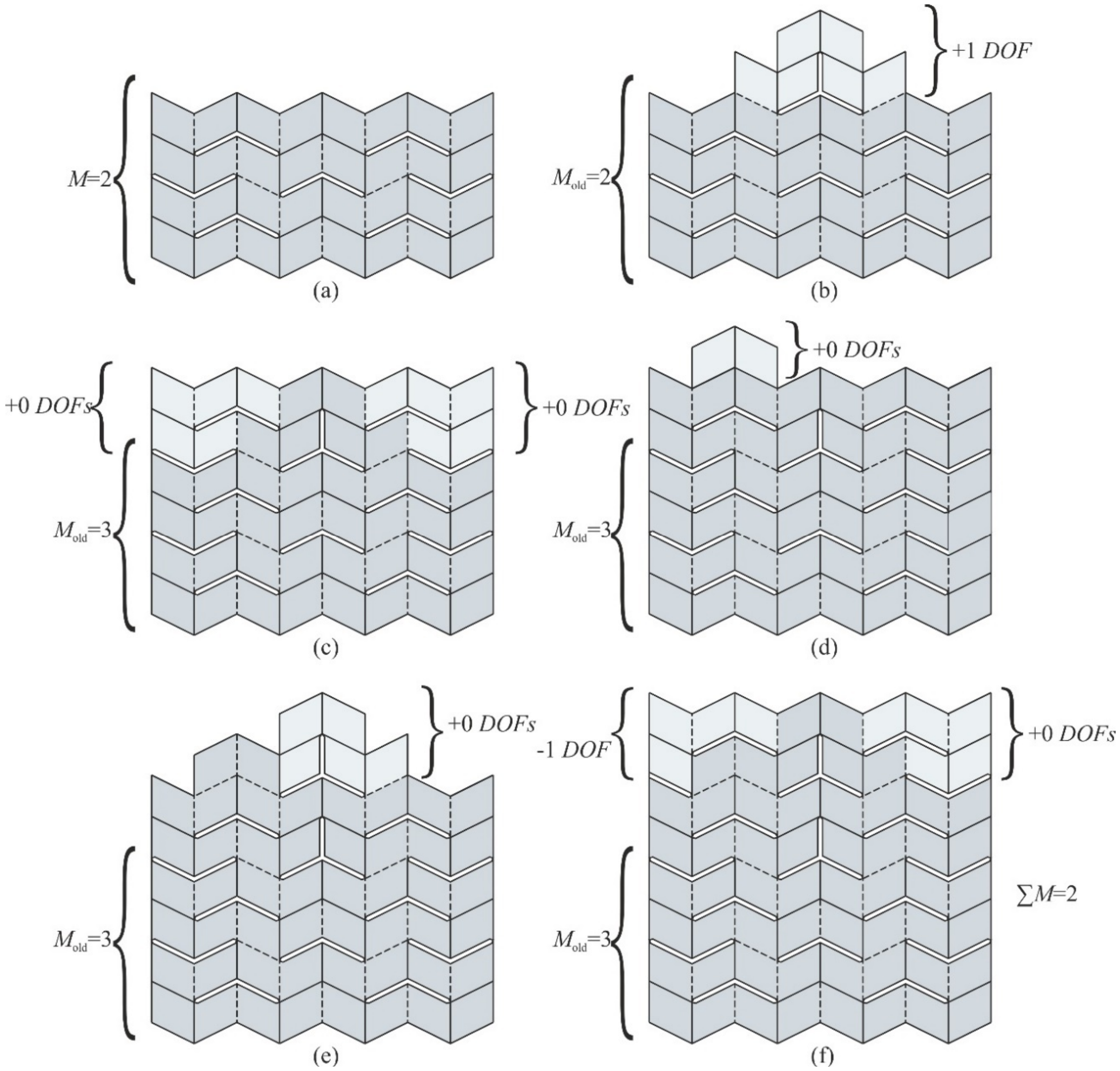

Fig. 6.4 A repeatable panel addition sequence to grow the pattern vertically that sacrifices the regularity of slits but ensures the final mobility equals two.

Again, an eight-by-four cluster is added but this time vertically, giving an eight-by-eight assembly. The steps (a) to (f) in Fig. 6.4 can be also repeated infinitelly.

We now have sequences to grow the pattern in both horizontal and vertical directions that keep two DOFs. The final step is to find a sequence that finishes a rectangular pattern. Figure 6.5 presents a step by step approach to fill the gap in the top-right corner, which forms after the assembly is grown both horizontally and vertically. We again use the same principles(6.14a) to (6.14d). Additionally, we notice that adding $N=3$ panels with $j=4$ revolutes to build a new loop removes two DOFs, adding $N=8$ and $j=9$ increases DOFs by three, and adding $N_{sph}=1$ and $j_{sph}=2$ to build a new spherical linkage removes one DOF. The sequence in Fig. 6.5 for an eight-by-four cluster surrounded by panels from the previous additions from the bottom and the left-hand side is also repeatable.

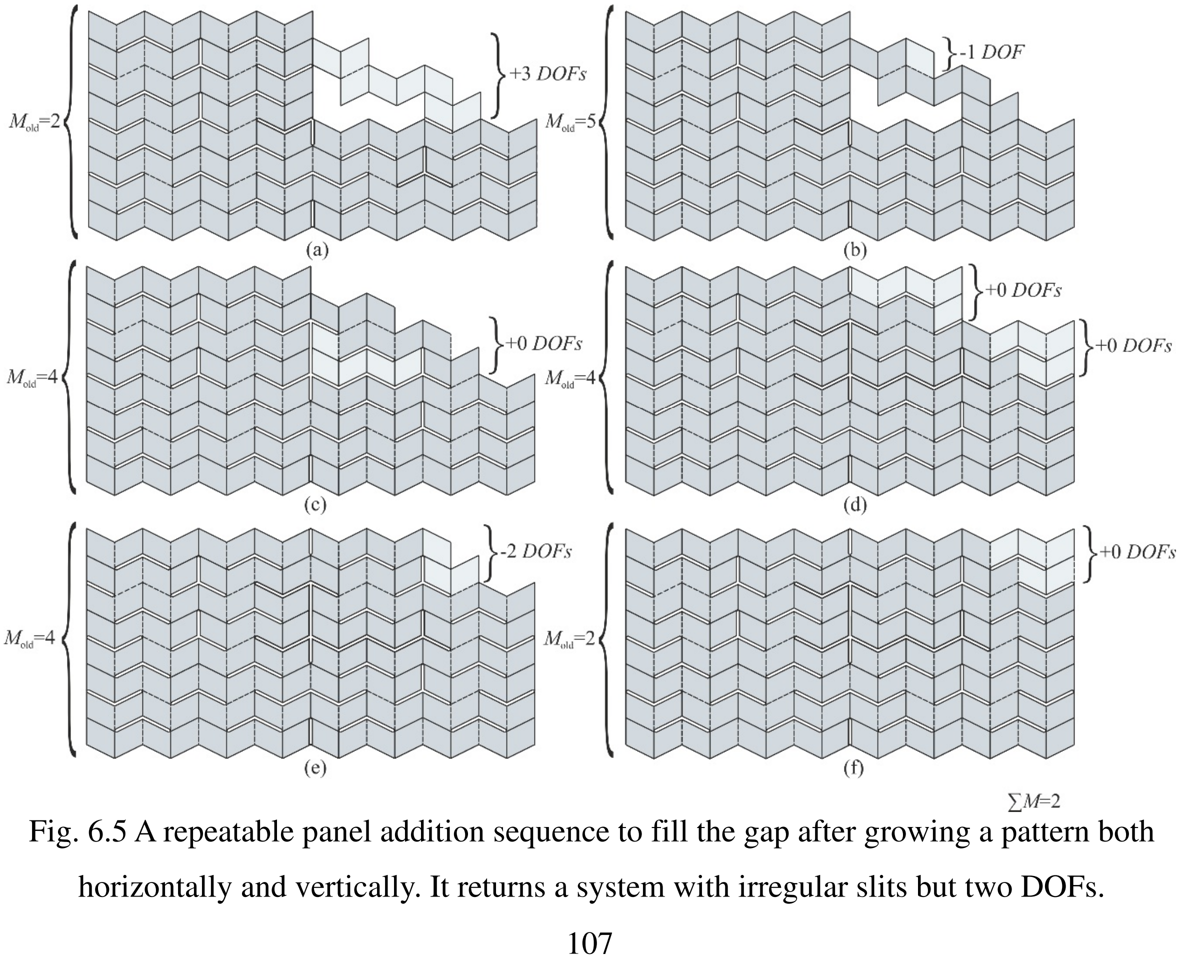

Fig. 6.5 A repeatable panel addition sequence to fill the gap after growing a pattern both horizontally and vertically. It returns a system with irregular slits but two DOFs.

We can now use the step-wise growth approach presented above to build infinitely large patterns, always keeping the mobility equal to two. The subsequent investigations will focus on a 16x16 assembly obtained in this way and presented in Fig. 6.6(a). Its slit arrangement is irregular but returns the pattern's finite mobility of two. Of course, it is not the only slit arrangement like this, as the choices we made when adding panels were at some points arbitrary. Figure 6.6(b) presents an alternative configuration obtained by slightly different panel addition sequences. There are more such alternatives possible, but they will all have irregular slit patterns yielding two DOFs. While the two patterns in Fig. 6.6 have different slit arrangements, they both have the same mobility and experience the same kinematic behaviour, which we shall discuss next.

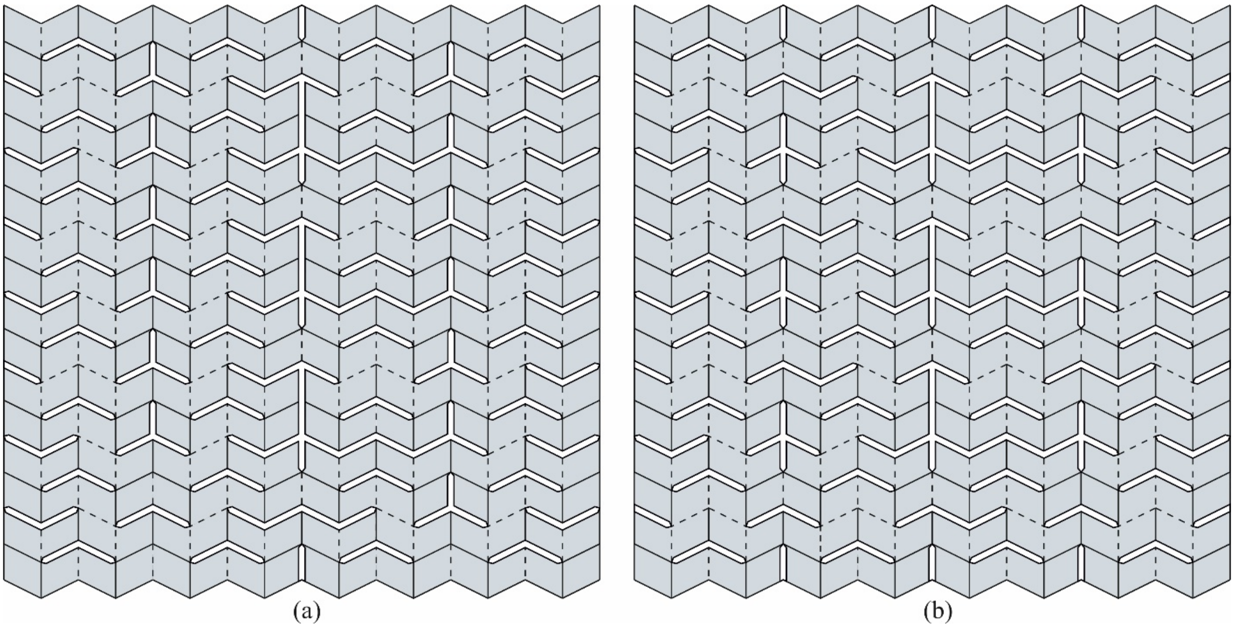

Fig. 6.6 Two alternative 16x16 Miura-ori with irregular slits resulting out of the step-wise panel additions that ensure the final mobility of two.

6.2 Kinematics of the two-DOF Miura-ori

As the assemblies from Fig. 6.6 built according to the step-wise approach have only two DOFs, we can use only one 8R cell, e.g. in the bottom left corner, to drive the entire pattern's motion. Figure 6.7 is a close-up of such a cell in a global pattern. To visualise the kinematics, we will use the circled dihedral angles φ_1 and φ_3 as the inputs and φ_2 resulting from the closure equations (5.1) to (5.6) as the output value. We continue using Miura-ori with the sector angle α equal to 135°.

We will explain the kinematics by creating and analysing 3D plots of the motion curves governed by the closure equations. Figure 6.8 presents the traditional Miura-ori motion path on the surface of all theoretically possible configurations of the new two-DOF pattern. As the assembly has mobility equal to two, it requires two inputs to define its shape. Therefore, we create a 3D plot by assigning the two inputs φ_1 and φ_3 to the horizontal axes and then marking the output variable φ_2 resulting from the motion equations on the vertical axis.

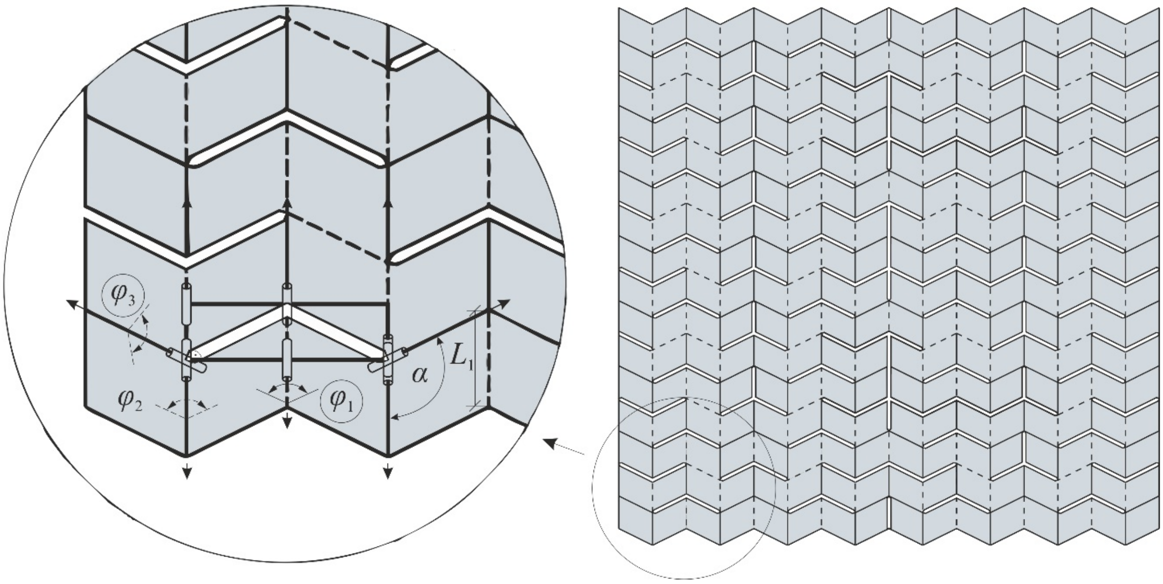

Fig. 6.7 A close-up of a single 8R cell that we use to reconfigure an entire two-DOF Miura-ori. Circled variables φ_1 and φ_3 are the inputs and φ_2 is a representative output.

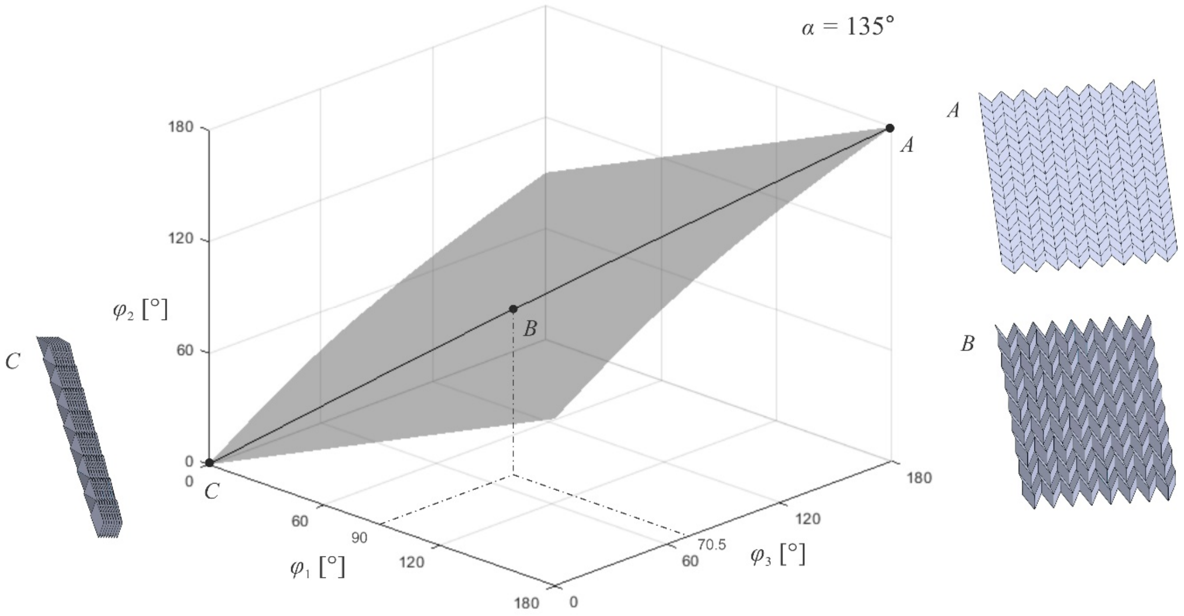

Fig. 6.8 A 3D plot of all theoretically possible configurations of the two-DOF Miura-ori, represented by a surface of the values φ_2 takes for the φ_1 and φ_3 input combinations. *A*, *B* and *C* are stages on the motion path representing the traditional folding.

There is a whole domain of the potential input combinations, with both φ_1 and φ_3 from 0° to 180°. As a result, φ_2 is represented as a surface of values for all the input combinations. Thus, it depicts all the pattern's theoretically viable configurations. Moreover, a single curve can be singled out on the surface, on which the pattern takes shapes the same as during the Miura-ori's traditional folding. In other words, all possible reconfigurations of the two-DOF pattern include the traditional Miura-ori motion path.

The two-DOF pattern requires synchronising its two inputs to follow this curve and realise the original motion imitating a standard Miura-ori. We do this by manipulating φ_1 and φ_3 so that they satisfy (2.12), i.e. simultaneously take the values resulting from the standard one-DOF equations. If we do so, the 8R closure equations (5.1 to 5.6) return the output variables (also φ_2) in agreement with the traditional Miura-ori motion. As a result, the two-DOF assembly reproduces the traditional single-DOF behaviour. Configurations *A*, *B* and *C* indicate such a motion path, along which the two-DOF pattern folds traditionally from a flat sheet, *A*, into a compact form, *C*.

Moreover, apart from imitating the traditional behaviour, the two-DOF pattern is capable of new reconfigurations. For example, Fig. 6.9 presents an alternative motion path that is available when at a given point, we decide to manipulate only one input instead of synchronising both to continue following the traditional curve. In other words, we decide to freeze one of the input angles, here φ_3, and keep changing only the second one, φ_1. In Fig. 6.9, in what we call alternative motion 1, we stop changing φ_3 at point *B*, at a value of 70.5°, which corresponds to dihedral angles at vertical creases being equal to 90°. Then, we can use φ_1 as the only input and explore the remaining regions of the surface of possible configurations.

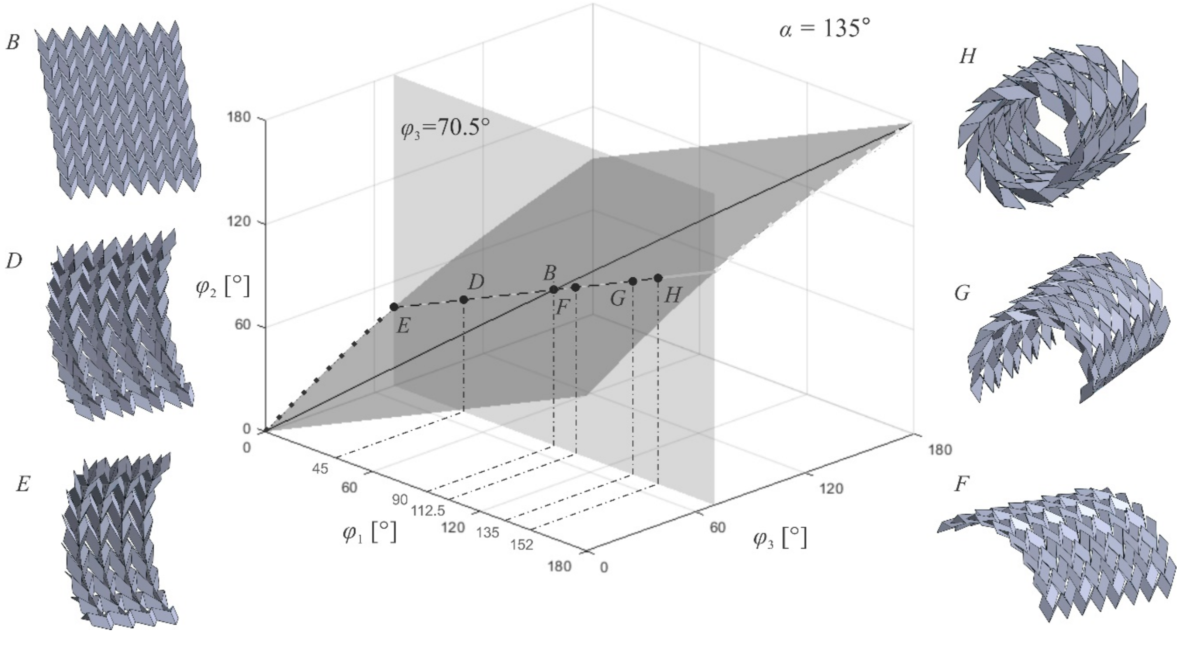

Fig. 6.9 An alternative motion 1 path started at point B, when input φ_3 is frozen and only φ_1 changes. *D, E, F, G* and *H* are the new arched and tubular forms.

We can either decrease or increase φ_1's value. If we make the dihedral angle smaller, we go along an alternative path marked by a dashed line via configurations *D* and *E*. Every second angle at vertical creases starts folding, *D*, until they close fully, *E*, while the rest of the angles remain unfolded. In other words, the pattern folds now only partially. On a macro scale, such reconfiguration causes the pattern to take a new shape with out-of-plane curvature along the vertical creases' direction. The assembly consisting of rigid panels and revolutes now can be reconfigured into a bent-like shape. It can imitate the bending of a typical paper Miura-ori while maintaining the panel's rigidity, i.e. without flexing them or introducing any strain to constituent elements. This was previously impossible with an unmodified pattern.

Point *E* is what we call a boundary state. In this configuration, some of the dihedral angles with similar kinematic behaviour to φ_1 close fully, i.e. take the vale of zero. It means that further motion is impossible due to panel coplanarity and collisions. If φ_3 is still disabled, the assembly locks in *E* or can reverse back to *D* and *B*. However, at this stage, we can keep φ_1 equal to zero and unfreeze φ_3. If we lower its value, we leave the motion 1 path and follow another one, marked with a dotted line at the boundary of the surface. It allows reconfiguring *E* into the standard compact form *C*. This manoeuvre also shows that thanks to two DOFs, the pattern can reach the traditional shapes, like the fully compact form *C*, both via the traditional path and by taking detours, i.e. using new alternative motions.

To fold Miura-ori in a way alternative to one smooth motion, we first go via point *E*, i.e. we close some of its vertical creases and obtain a partially folded form. Only after changing the inputs, we fold the remaining angles and finish the reconfiguration to the compact form.

This means we can decouple the folding process and execute it in two stages, using two separate inputs. The pattern's geometric Poisson's ratio (not related to material strain but to overall pattern shrinkage and expansion from the geometric, dimensional perspective) also gets decoupled during the folding. However, its analysis lies outside this project's scope.

At point *B*, we can also decide to increase φ_1's value. By doing so, we go along motion 1's path, but in the opposite direction, via *F*, *G*, *H*. Compared to previous reconfigurations, some of the dihedral angles now do not close but open up as they increase values. Thus, the assembly deploys partially and again takes configurations with an out-of-plane curvature, this time of an opposite value, as it bends downwards not upwards.

Due to its size, the assembly bends fully until configuration *H*. It is a tube-like shape. If we continue increasing φ_1's value, some panels start intersecting in the computational model, as shown in Fig. 6.10. It is a theoretical configuration further along the path, beyond point *H*. In reality, physical models lock when the intersections start, and such configurations are impossible due to panel collisions. Such forms are purely virtual, and this is why we grey out the rest of motion 1's path on the plot. In this way, we indicate regions with mathematically correct but only theoretically available shapes. Configuration *H* becomes the second boundary state defined by collisions.

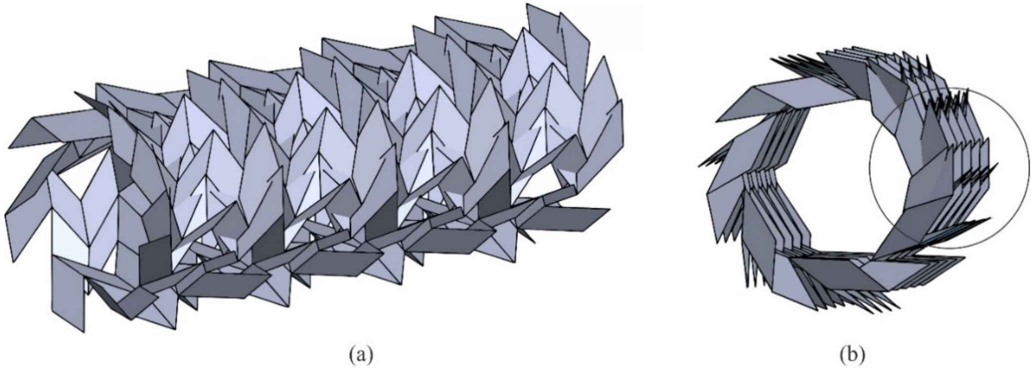

Fig. 6.10 (a) An exemplary configuration beyond point *H* from Fig.6.9, accessible only virtually due to panel collisions; (b) is a side view, with the intersections circled.

To sum up, the alternative motion 1 possible thanks to the second DOF allows us to reconfigure a Miura-ori with rigid panels into previously unavailable shapes that are curved along the vertical direction, out of the pattern's plane. Furthermore, this alternative path can be accessed via a simple manipulation of only one input starting at any of the traditional shapes. It is also defined by boundary states involving panel collisions from both sides.

That is not the only new motion possible. Figure 6.11 presents what we call alternative motion 2 of the two-DOF Miura. This time, at any point of the traditional path (here we again choose *B*) we freeze not φ_3 but φ_1. The second DOF, now φ_3, remains the only active input. The case is analogous. Decreasing φ_3's value causes every second parallelogram pair to fold, which leads to configurations with out-of-plane curvatures along the vertical direction, *D* and *E*. However, the pattern bends 'downwards' not 'upwards', as in motion 1. This side of the path again locks in a boundary state when some angles fold fully, *E*. This form can be reconfigured into the traditional compact form, *C*, too.

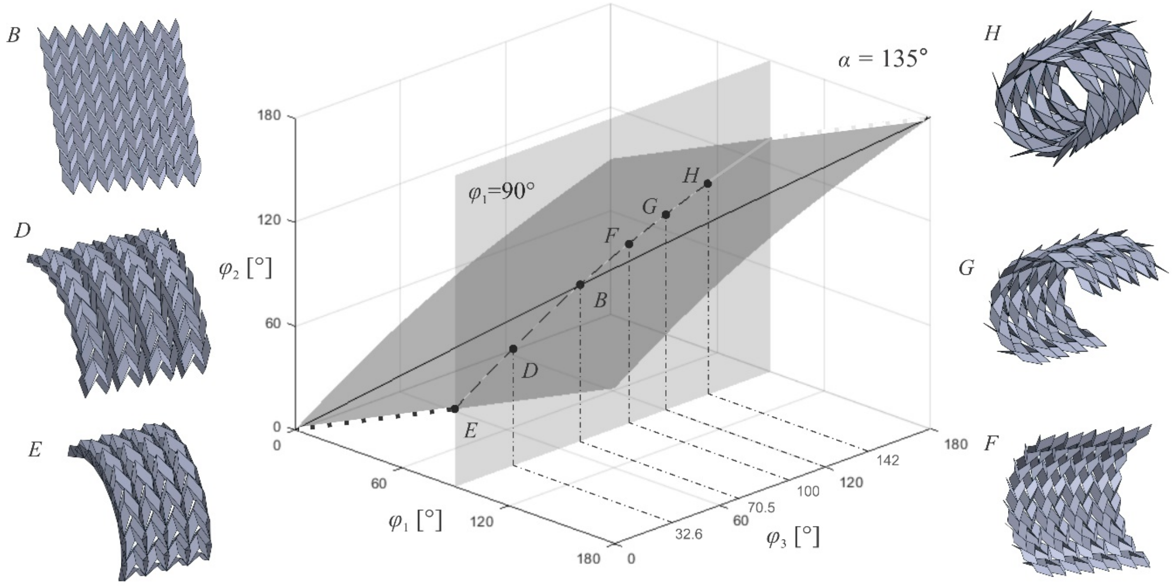

Fig. 6.11 An alternative motion 2 path started at point B, when input φ_1 is frozen and only φ_3 changes. *D, E, F, G* and *H* are the new arched and tubular forms.

Alternatively, increasing φ_3's value causes some dihedral angles to open up, giving curved shapes, but this time, bending upwards, not downwards. This side of the path is also limited by the assembly bending itself into a tubular shape. Further reconfigurations are only virtual and physically impossible due to panel collisions. Therefore, similarly to alternative motion 1, motion 2 reconfigures the pattern into curved shapes using only one input. The resulting shapes are slightly different but also limited by boundary states from both sides.

Handling the pattern to explore alternative motion paths 1 and 2 is especially easy as we do not change one of the inputs and manipulate only the second one. This means the reconfiguration is straightforward due to using only one DOF. Moreover, in engineering applications, it means that the change of the state of only one of the motion-driving actuators is required at a time. Compared to that, imitating the traditional Miura-ori folding by the two-DOF pattern is more challenging. As mentioned earlier, it requires synchronising two inputs to take specific values at an exact time, i.e. the actuators to work simultaneously, and realise a particular motion path. However, it turns out that for easier manipulation, we can use the alternative motions to approximate the Miura-ori behaviour, as shown in Fig. 6.12.

We focus on a fragment depicted by stages *A*, *B* and *C*. Starting from *A*, instead of following the standard curve, which requires the input synchronisation, we freeze φ_1 to trigger motion 2 and reconfigure the assembly into *D*. Here, we switch from motion 2 to motion 1 by disabling φ_3 and unfreezing φ_1 and decreasing its value to reach a point back on the traditional curve, *B*. We can repeat this and go via motion 2 to *E* and then return to the traditional form *C* via motion 1. In this way, we approximate the typical folding by reconfigurations using only one input at a time. The sizes of the steps can be adjusted, with the smaller ones approximating the Miura-ori motion more accurately.

Of course, we can approach the traditional curve from the other side by accessing configurations *F* and *G* instead of *D* and *E*. This requires an opposite order of reconfigurations, i.e. first using motion 1 and then correcting the path with motion 2. This alternate input approach assumes the physical assembly curving smoothly out of its plane via control of only two folds. It means that the traditional folding can be realised stepwise, changing one input, i.e. altering the state of only one of the actuators at a time.

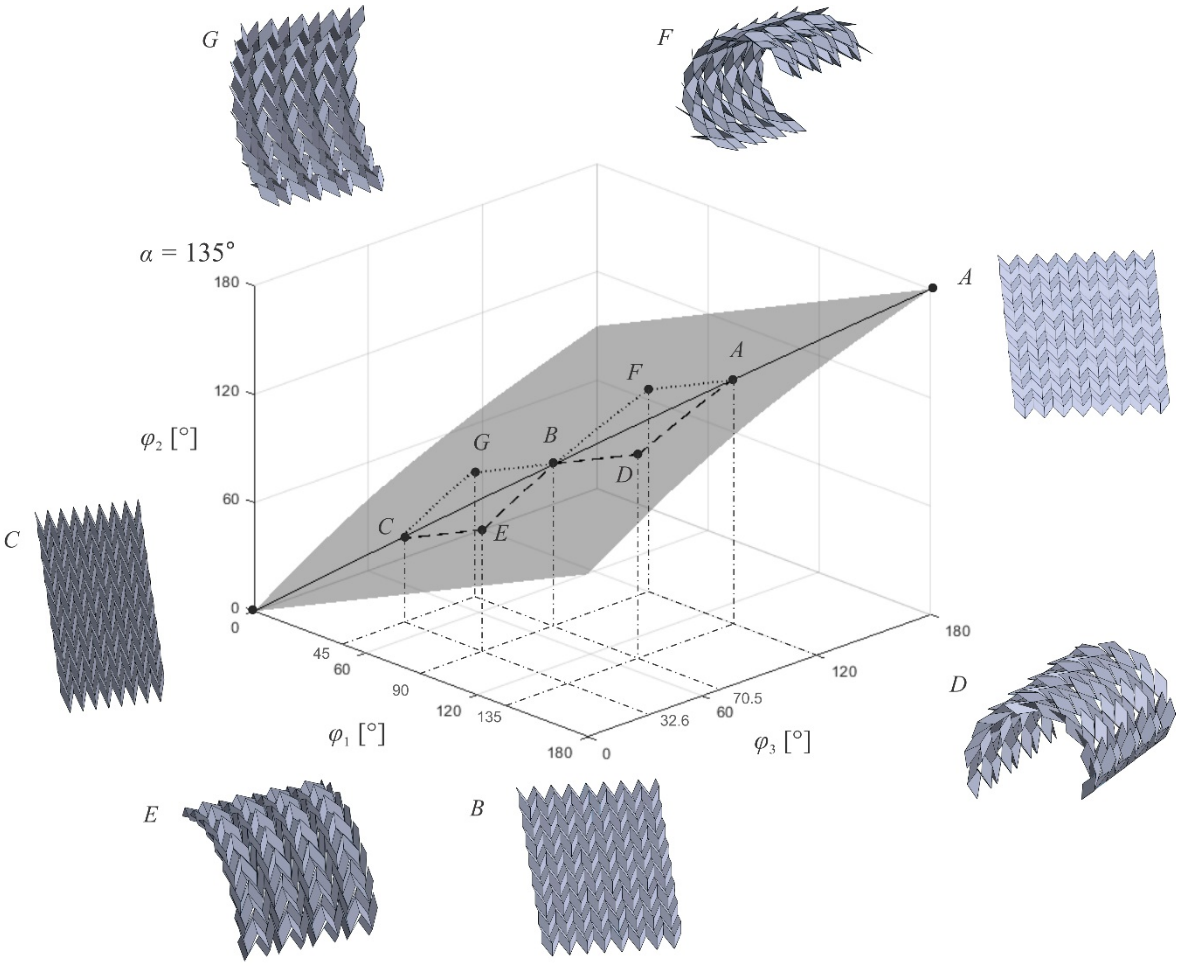

Fig. 6.12 An example of approximation of the traditional folding, using only a single input at a time. *D* and *E* are reconfigurations that allow obtaining the traditional forms *A*, *B* and *C*. *F* and *G* are alternatives to *D* and *E*.

In conclusion, adding a second DOF to a rigid Miura-ori by introducing particular slit arrangement allowed the pattern to exercise new specific motions. The traditional folding is still possible either by synchronising the two independent input angles or by approximation, using one input at a time, for simpler control. Moreover, as the two DOFs can be controlled independently, the motions by changing only one of the inputs lead to new shapes that allow the rigid-panel Miura-ori to have curvatures out of its original motion's plane. They can be used to reconfigure the pattern into arched or tubular forms or decouple the folding process into stages with different geometric Poisson's ratios. Such forms were impossible with an uncut Miura-ori when the panels were assumed rigid.

6.3 Making the two-DOF Miura-ori more regular

The above two-DOF behaviour that reproduces the traditional motion and reconfigures the pattern into new curved shapes is possible with the slit arrangements ensuring the final mobility of two, as in Fig. 6.6. Unfortunately, these layouts are highly irregular and lead to complex mechanical linkages, symbolically indicated in Fig. 6.13(a). There is, however, a possibility to simplify the slit arrangements and make the patterns more uniform while still retaining the two-DOF nature.

First, we must inspect closely the two-DOF kinematics presented in Figs. 6.8 to 6.12. It turns out that in all new configurations, some of the slits always open up, and the others never do. In other words, kinematically, the pattern uses some of the openings while others stay idle no matter the shape we want to achieve. Moreover, we can construct a digital or

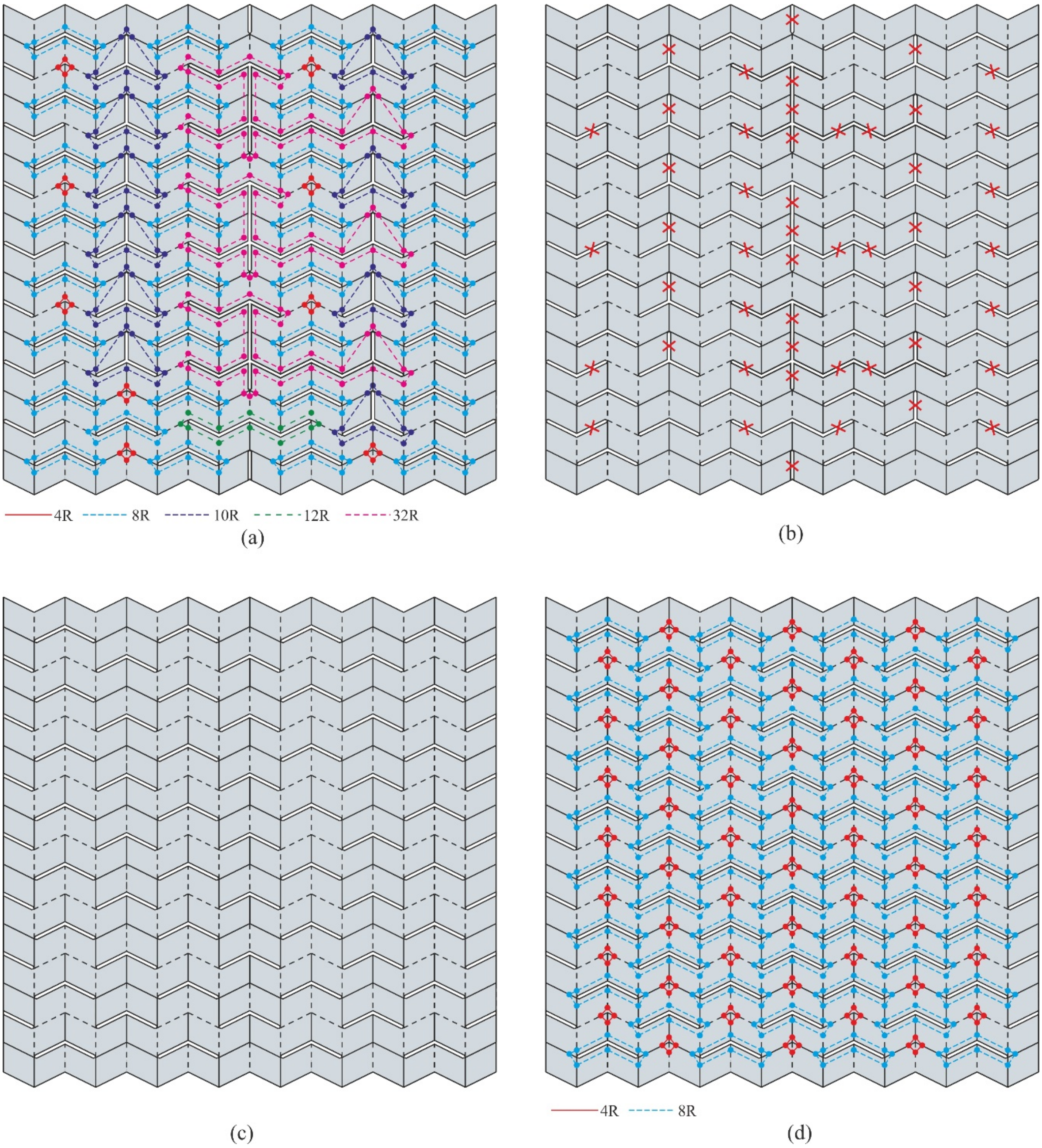

Fig. 6.13 (a) The two-DOF pattern from Fig. 6.6(a) with its complex linkage layout highlighted; (b) the same pattern with its inactive slits marked with red crosses; (c) the pattern with regular cuts after the inactive slits are removed; (d) the linkage layout of (c).

physical model. If we attempt to open some of the unused slits, the pattern's geometry and the panels' rigidity do not allow separating particular edges.

This means we can divide the slits into two types. One type is *active* slits that open up during the motions, i.e. are used kinematically. They are crucial for making the new motions possible. The second group are *inactive* slits that do not open up during the motion, i.e. are not fully utilised from the kinematic perspective. Even though such a slit removes a revolute from between adjacent panels, their edges stay colinear, and the assembly, due to the adjacent geometry, behaves as if the joint was still there. Therefore we can claim that the role of such slits that do not open up during the motion but discard redundant joints is only to decrease the assembly's overconstraint.

The patterns in Fig. 6.6 are examples of assemblies with both such slit types. Some of their cuts are active and open up during reconfigurations, while the others are inactive and only remove redundant hinges. By examining the new motions digitally or physically, we can identify the inactive slits. We recognise them by behaving as revolutes even after the hinge removal. Alternatively, for the identification, we can carry out calculations using the closure equations, as in appendix C. Figure 6.13(b) presents a pattern from Fig. 6.6(a) but with the inactive slits marked with red crosses.

We can now decide not to make the inactive slits. This brings back revolutes in their place. As a result, we obtain a pattern with only the active cuts, which is much more orderly, as presented in Fig.6.13(c). Also, the linkages constituting the pattern are now more regular. Only spherical 4R linkages and spatial 8R loops are used, as shown in Fig. 6.13(d). It is essential to highlight that by discarding inactive slits, whose role was to remove redundant hinges, we bring back some excessive kinematic joints, i.e. overconstrain the assembly.

By restoring the redundant joints, we decrease the mobility value significantly. After we count the markings in Fig. 6.13(b), it turns out we bring back 49 excessive hinges in the 16x16 pattern. Notice that these extra revolutes will form spherical linkages locally.

Therefore, we use the spherical version of the mobility formula (2.3). Adding no panels and a single revolute that becomes a part of a spherical linkage removes two DOFs,

$$M = M_{old} + 3(N_{sph} - j_{sph}) + j_{sph} = M_{old} + 3(0-1) + 1 = M_{old} - 2\,. \tag{6.15}$$

For the 16x16 assembly from Fig. 6.13(c) with 49 extra revolutes that has $M_{old} = 2$ we get

$$M = M_{old} + 3(N_{sph} - j_{sph}) + j_{sph} = 2 + 3(0-49) + 49 = 2 - 98 = -96\ . \tag{6.15}$$

The above can be verified by re-calculating the mobility while building the pattern from Fig. 6.13(c) in a step-wise manner as earlier, distinguishing between 8R and 4R linkages.

The negative mobility of -96 confirms the pattern becomes highly overconstraint after reversing inactive slits, and according to the formulas, should not have the freedom to move. However, the two-DOF motion described earlier is maintained. The removed slits were not used during the reconfigurations by any means, and the panels behaved as if the revolutes we just added were already there. Also, all the active slits that are required for the new motions were kept. Moreover, we can prove that such extra revolute addition does not affect the pattern’s motion but only contributes to its overconstraint by making calculations based on the closure equations. For the extra proof, see appendix to chapter 6.

If we examine the pattern in Fig. 6.13(c) digitally, or its physical model, even though the redundant hinges significantly overconstrain it from the kinematic perspective, it can still exercise all the motions presented in Figs. 6.8 to 6.12. The actual number of DOFs stays two. Moreover, such a pattern is now much more regular, with a repetitive linkage layout, Fig. 6.13(d), thanks to the orderly slit arrangement. Growing such a pattern becomes now straightforward. We can use symmetry or typical multiplication of units to create larger assemblies, as we only need to ensure that the regular slit pattern is continued.

In conclusion, a pattern with regular double slits along diagonal edges as in Fig. 6.13(c) retains all the reconfiguration possibilities of the irregular patterns from Fig. 6.6. Figure 6.14 presents its physical model both in the traditional Miura-ori form and the new configurations. It is a two-DOF version of Miura-ori that can experience the traditional in-plane motion and can be bent along the vertical direction and have an out-of-plane curvature without flexing any panels and introducing material strain. Moreover, the crease and slit pattern without inactive slits is regular and easy to replicate.

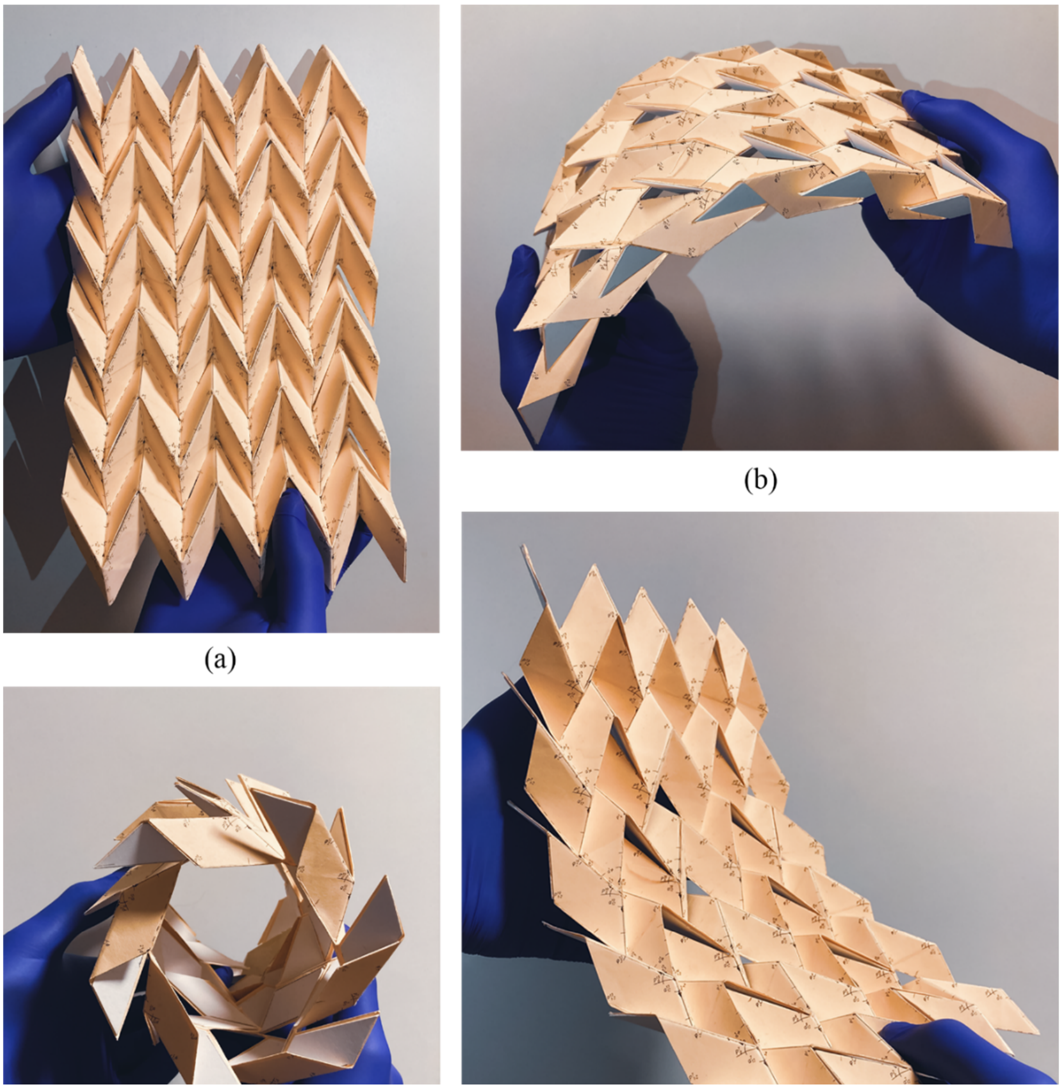
(b)

(a)

Fig. 6.14 A physical model of a two-DOF Miura-ori from Fig. 6.13(c) but having 9x12 panels; (a) is a traditional in-plane form; (b), (c), and (d) are exemplary new out-of-plane arched and tubular configurations.

6.4 Building a two-DOF Miura-ori with vertical slits

So far, we have succeeded in building a two-DOF version of rigid-panel Miura-ori capable of new configurations, for example, a macro-level bending along the vertical direction. We did this by starting from cuts along diagonal creases. Now, we attempt to build another two-DOF Miura-ori but with slits mainly along its vertical folds. We hope to achieve the out-of-plane bending in the perpendicular direction.

We take a similar step-wise approach when adding panels as in Figs 6.3 to 6.5, forming either spherical linkages or *N*-panel loops whose local DOFs we can predict. Our panel additions should either not change mobility or first increase and then constrain it to ensure the assembly maintains two DOFs. Figure 6.15(a) presents a 16x16 pattern resulting from the step-wise approach applied after starting from an 8R loop with the double vertical slit, as in Fig. 4.1. It is also a non-overconstrained assembly with the mobility of two. This time, the majority of slits are along Miura-ori's vertical creases.

Similarly, the cut arrangement from Fig. 6.15(a) includes both inactive and active slits. It is highly irregular, and its linkage layout consists of complex loops, Fig. 6.15(b). However, this time, we immediately examine the pattern and identify the inactive slits. Then, we remove them, bringing back some of the hinges, i.e. overconstraining the assembly. It turns out that such action again allows obtaining a much more regular two-DOF version, as in Fig.6.15(c). It consists of a mixture of two- and three-crease long vertical slits, and the whole pattern is built out of spherical 4R and spatial 8R and 10R linkages, Fig. 6.15(d). As earlier, the pattern maintains two DOFs even though it becomes overconstraint when turned into the regular-slit version.

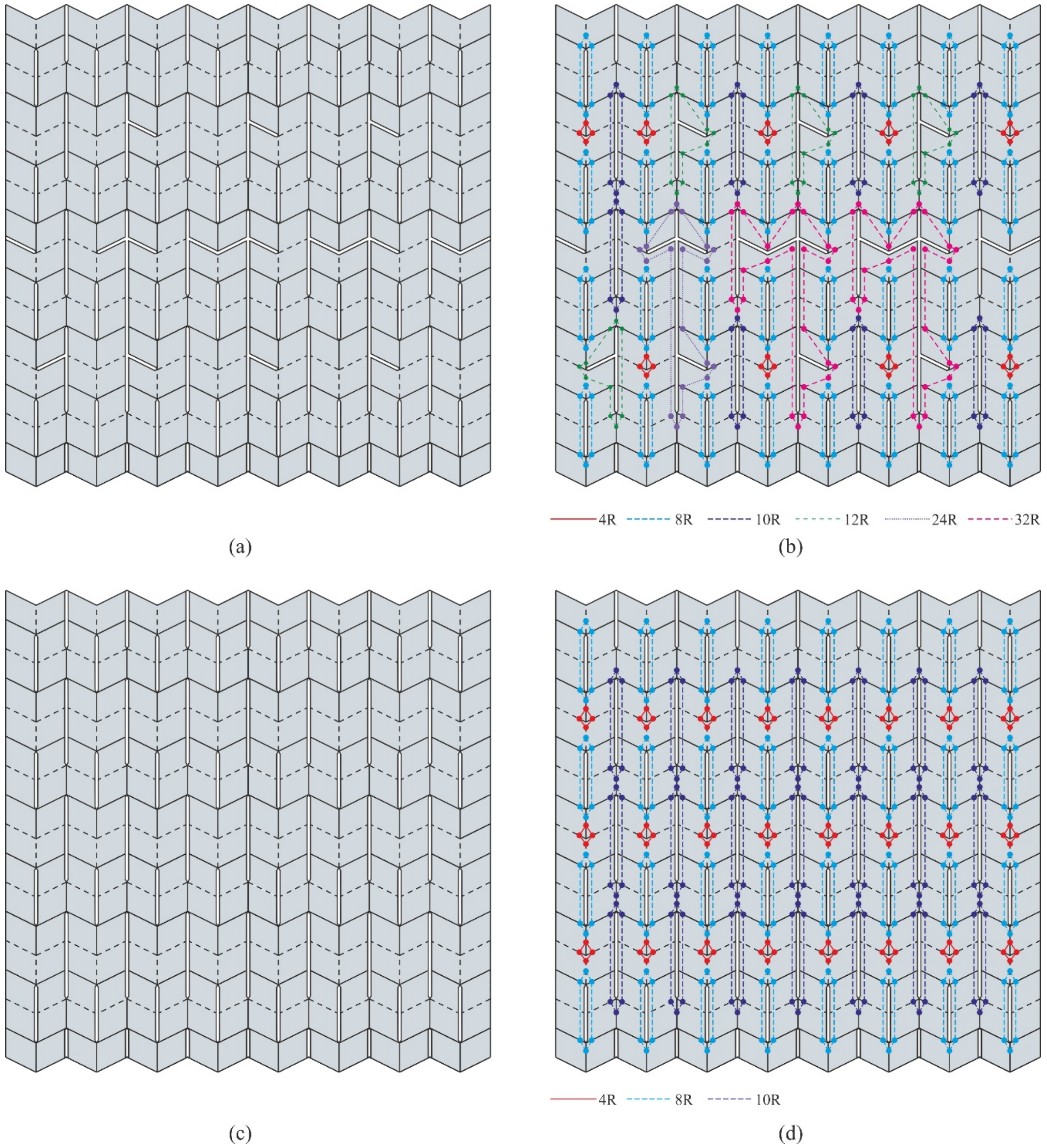

Fig. 6.15 (a) A two-DOF pattern obtained after starting from a cell with the vertical slit; (b) its complex linkage layout; (c) the regular pattern after the inactive slits are removed; (d) the regular linkage layout of (c).

6.5 Kinematics of the two-DOF Miura-ori with vertical slits

To explain the two-DOF motion of the pattern with the vertical slits, we use similar 3D plots of motion paths on a surface of possible configurations. Figure 6.16 is a close-up of a single cell in the bottom left corner, which we use to reconfigure the entire assembly.

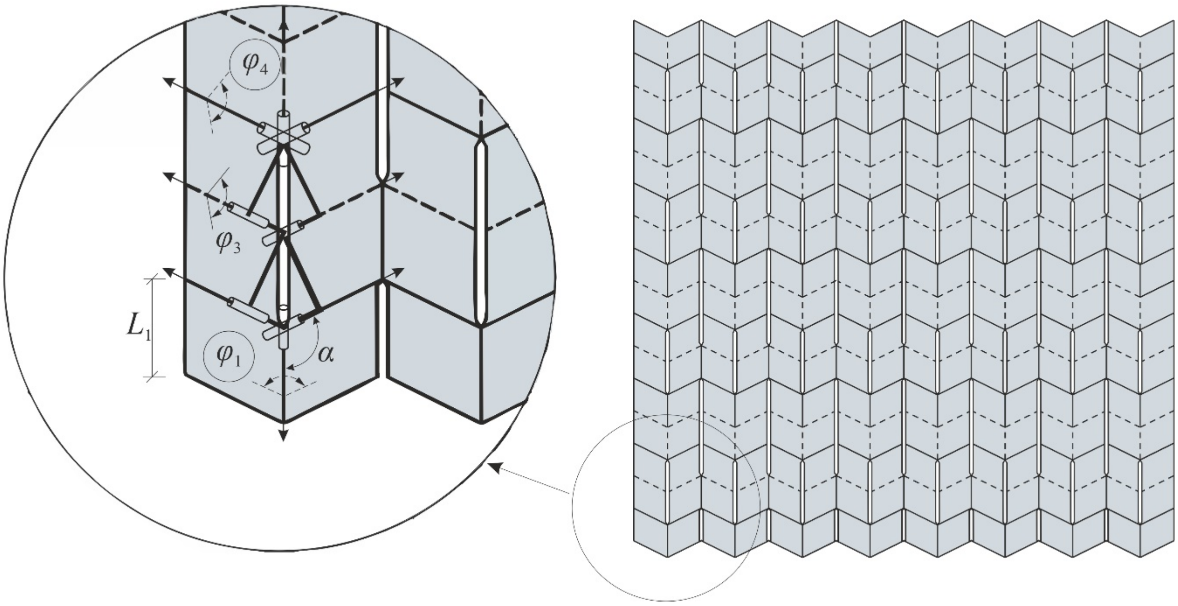

Fig. 6.16 A close-up of an 8R cell that we use to reconfigure an entire Miura-ori with vertical slits. Circled variables φ_1 and φ_4 are the inputs and φ_3 is a representative output.

The circled dihedral angles, φ_1 and φ_4, are the inputs. By changing their values, we control the pattern's reconfiguration. Angle φ_3 is a representative output variable, which adjusts to the inputs.

Using the closure equations of an 8R linkage with a double vertical slit (4.1) to (4.6), we create a plot with a surface representing all the possible configurations, Fig. 6.17. We also single out the traditional Miura-ori motion on it. The inputs φ_1 and φ_4 are plotted on the horizontal axes, while the output φ_3 is displayed vertically. Notice that this time, the surface significantly curls upwards. This is because some of the input combinations, especially with big φ_1 and small φ_4 values, are impossible due to the geometry. Therefore, the surface does not extend above this region. Moreover, as the surface bends above itself, it means that for some input combinations, φ_3 can take two different values, i.e. the cell has two alternative shapes, as described in chapter 4.

If we want the two-DOF assembly to exercise the traditional one-DOF motion, it again requires synchronising the two inputs to follow the original Miura-ori path. Figure 6.17 presents the traditional motion curve and its configurations, from *A* to *C*. Moreover, similarly to the Miura-ori with diagonal slits, we could also take the step-by-step approximation to the curve. Instead of synchronising two inputs and using them simultaneously to follow the path explicitly, we could diverge from the curve, correct the motion, and return to the curve making the operation easier to handle by one input at a time.

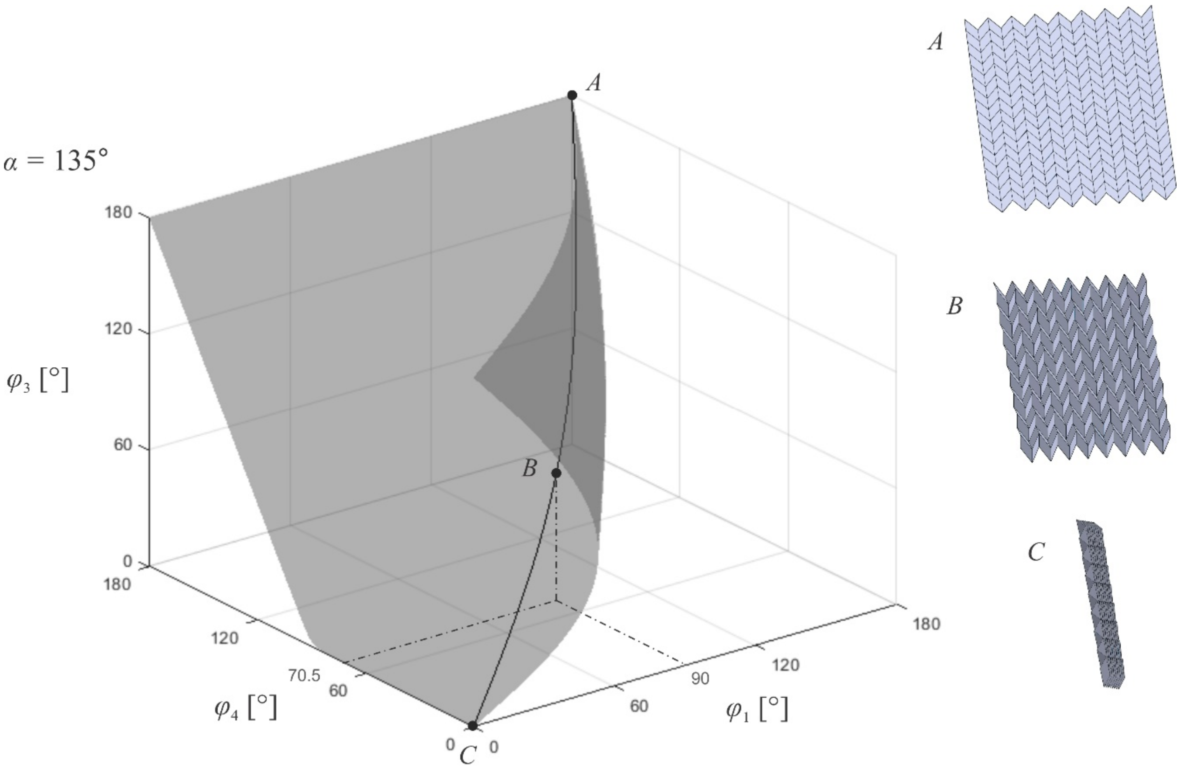

Fig. 6.17 A 3D plot of all theoretically possible configurations of the two-DOF Miura-ori with vertical slits, represented by a surface of the values φ_3 takes for the φ_1 and φ_4 input combinations. *A*, *B* and *C* are stages on the traditional one-DOF folding path.

Next, we explore this pattern's alternative motion by following a path on the surface outside the traditional curve, as in Fig. 6.18. To activate such a reconfiguration, we freeze the input angle φ_1 on the cell's vertical crease at an arbitrary value. In the example, we choose 90˚. Then, only φ_4 remains as an active DOF, whose value we change to put the assembly in motion. If we increase it, we start a new reconfiguration, via points *D* and *E*. The pattern again bends out of its plane, but this time, along the horizontal direction. Increasing the φ_4's value further causes the pattern to bend more and eventually close, forming a tube-like shape, *E*. It is a boundary state at which panels start hitting each other, and further reconfiguration is physically impossible. The rest of the path is theoretical and can be realised virtually, with interpenetrating panels. Thus, we grey-out the curve beyond point *E*.

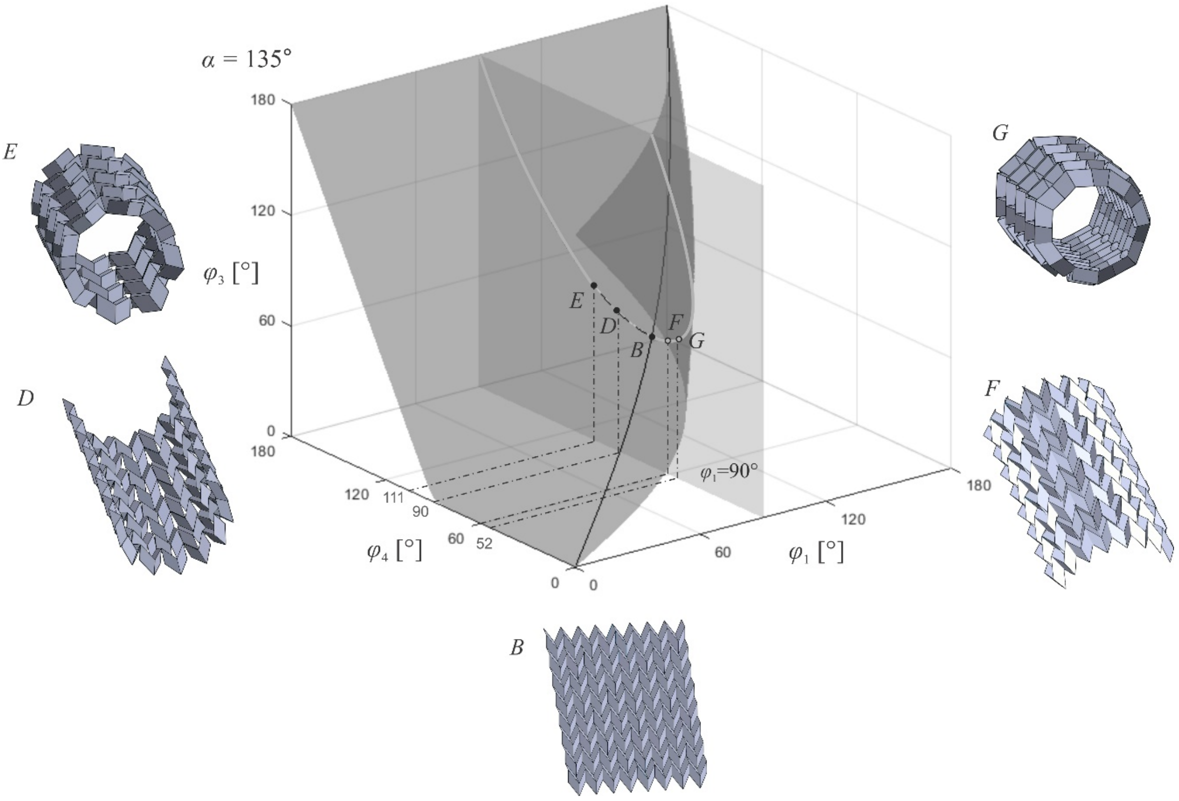

Fig. 6.18 An alternative motion path started at point B, when input φ_1 is frozen and only φ_4 changes. *D*, *E*, *F* and *G* are the new arched and tubular forms.

If we decrease φ_4 instead, we go along the new path via points *F* and *G*. This is also a reconfiguration that makes the pattern bend out of the plane. This time, the assembly bends ‘downwards’ not ‘upwards’, as shown in *F*. It continues until it forms a tubular shape, point *G*. However, we must realise that this path’s entire side is only virtual and thus greyed-out. If we closely inspect the shapes along the *B-F-G* section, we notice that, unfortunately, all of them involve small panel intersections that make this reconfiguration sequence impossible. A close-up of the configuration *F* is presented in Fig. 6.19. The *B-D-E* section of the alternative motion remains perfectly valid.

However, we can take advantage of such self-intersections and modify the pattern to realise the shapes from *B* via *F* to *G* physically and stop the motion automatically at a stage we choose. To achieve this, we first choose a shape on the *B-F-G* section that we want the assembly to reach and at which it should stop, e.g. the one in Fig. 6.19(a) and (b). As such downward-bent forms involve panels penetrating each other, we can simulate them using a digital model. We can now mark the intersections with red dash-dot lines, Fig. 6.19(c). This highlights the degree to which the panels interpenetrate until they realise the shape we chose.

Now, with that information, we can redesign our slits. This time, we do not cut rigid panels’ edges only to separate them. Instead, we cut out in the pattern openings of non-zero width, according to the shape dictated by our red-lined markings. Figure 6.19(d) presents a crease pattern with such slits. Now, the slits’ width is not drawn symbolically like earlier, but it is the actual size and shape of the openings. Such a pattern can be still folded to take the traditional Miura-ori configurations, which now, due to the slits’ non-zero width, have some gaps, as in Fig. 6.19(e). From such traditional shapes, we can still freely reconfigure

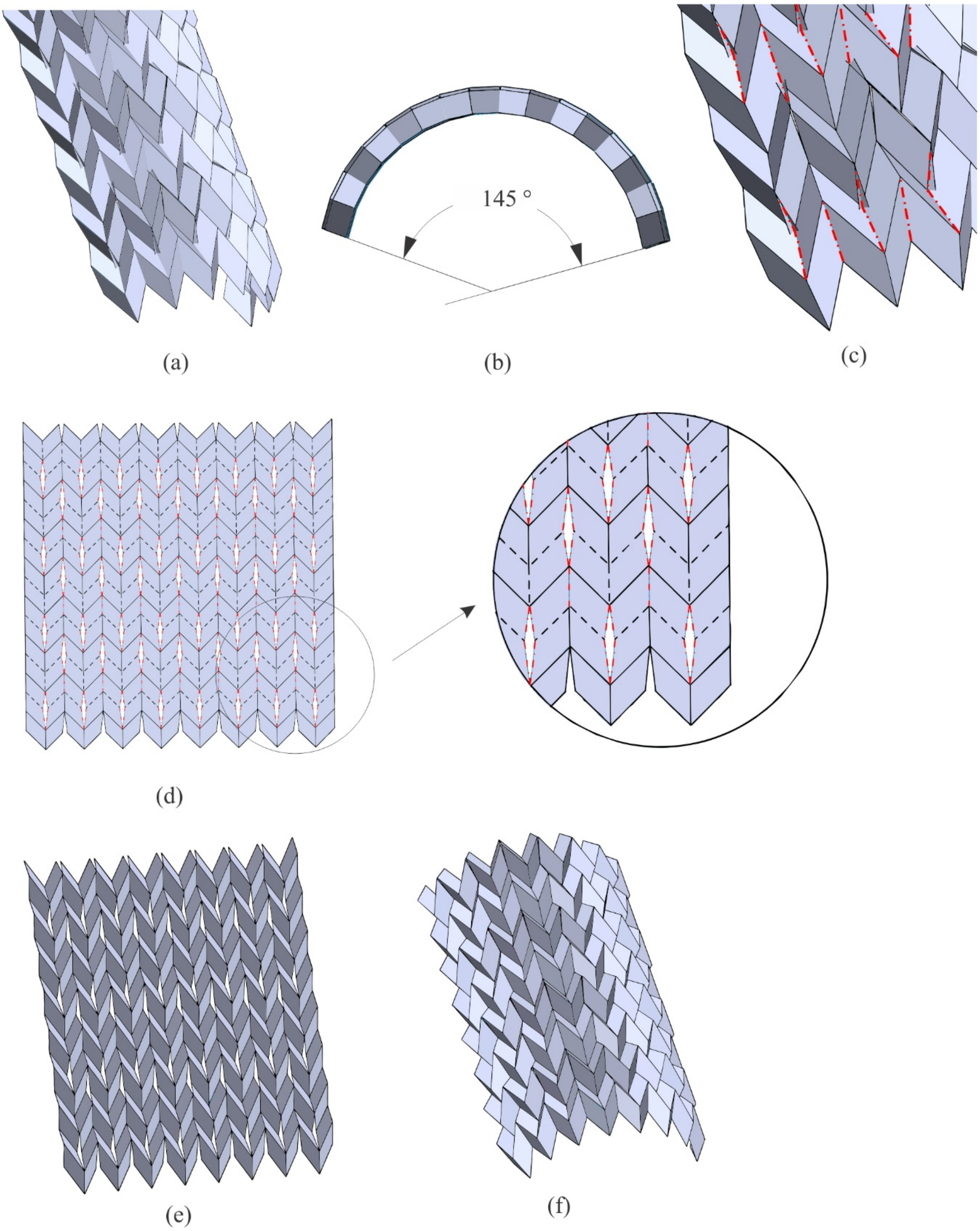

Fig. 6.19 (a) An exemplary shape from the *B*-*F*-*G* section, Fig. 6.18, with panel intersections; (b) is the front view; (c) dash-dotted lines that mark the degree to which the panels intersect; (d) is a modified crease pattern with non-zero-width slits, according to the markings in (c); (e) is (d) folded traditionally, now with gaps due to slits' width; (f) is a configuration in which the pattern locks, equivalent to (a) but now physically accessible thanks to the gaps between panels.

the pattern along the *B-D-E* section of the alternative path, where the panels did not experience intersections.

However, reconfiguration along the *B-F-G* fragment is now also possible, as the panels are trimmed and do not penetrate each other, but the gap gradually reduces. Then, we finally reach the curved shape we chose and for which we marked the slit penetration, Figs. 6.19(b) and (c). The gaps close, and the edges of the reshaped panels contact each other, locking the assembly in this form. As a result, the final shape presented in Fig. 6.19(f) cannot bend further but can return to other, less curved configurations or freely bend upwards.

Notice that in Fig. 6.19(c), we identified and marked an approximate slit shape on the panels at the desired and physically impossible configuration that was modelled digitally. For real, physical applications, for example, using the geometry in Fig. 6.19(f) as an architectural arch (after providing adequate support conditions), more accurate approach would be needed. It would be reasonable to estimate a precise formula for the slits' shape taking into account the patterns' geometry. For example, dihedral angles could be used as variables to calculate the slits' required width to allow a particular shape of the forbidden motion. The wider the gaps, the further the assembly could bend downwards. However, identifying such a formula for precise slit dimensions lies outside the scope of this work.

Above, we presented a slight modification to our patterns to make a particular reconfiguration segment possible. With it or not, we already showed that by changing the slit direction, we could find an alternative two-DOF Miura-ori. It also has a regular slit pattern, but this time along vertical edges. The assembly can similarly reproduce the traditional in-plane motion and obtain a set of new configurations with out-of-plane curvatures, which this time imitate bending along the opposite, horizontal direction. Such motions, alternative to the in-plane folding, were previously impossible under rigid origami assumptions. Figure 6.20 presents a model of the two-DOF Miura-ori with vertical slits that was manufactured physically.

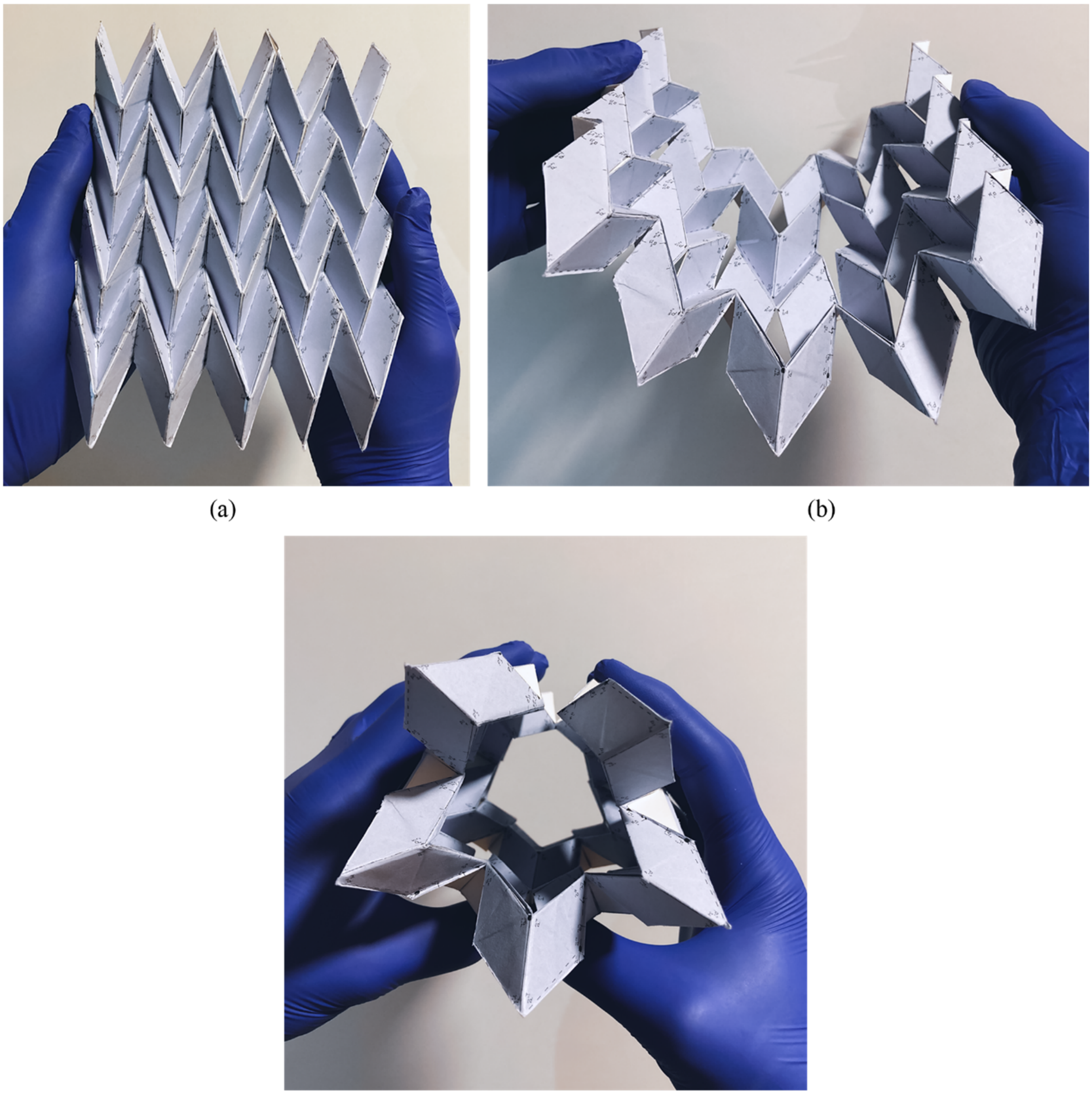

(a)

(b)

(c)

Fig. 6.20 A physical model of a two-DOF Miura-ori from Fig. 6.16 but having 10x8 panels; (a) is a traditional in-plane form; (b) and (c) are exemplary new out-of-plane arched and tubular configurations.

6.6 Summary

In this chapter, we accomplished the other main research objectives. The main achievement is that we successfully constructed reconfigurable rigid kirigami versions of an originally one-DOF pattern with precisely two DOFs. We found two regular slit layouts that allow Miura-ori to exhibit new motion types with out of plane curvatures, which are generally impossible without deforming the panels or redesigning the crease pattern. Now, rigid Miura-ori can bend upwards or downwards. Thanks to slits that open up during the reconfiguration, no strain is introduced as the panels do not need flexing. Simultaneously, the pattern has only two active DOFs that do not have to be used simultaneously to achieve all the forms, making its control easy. Figure 6.21 presents the strategy to design such reconfigurable kirigami crease patterns.

The only remaining two-crease-long slit type that we could analyse is a corner cut, made along one vertical and one diagonal slit, like the ones in Fig. 3.3(b). However, so far, such cuts have provided us with Miura-ori cells that exhibit unsymmetric motions and quickly experience panel collisions. Therefore, the thesis will not focus on investigating such slits further, even though they remain a potent research direction highlighted in the future works section of chapter 8. Instead, the thesis's next part investigates applying the successful findings to other four-crease-vertex origami tessellations.

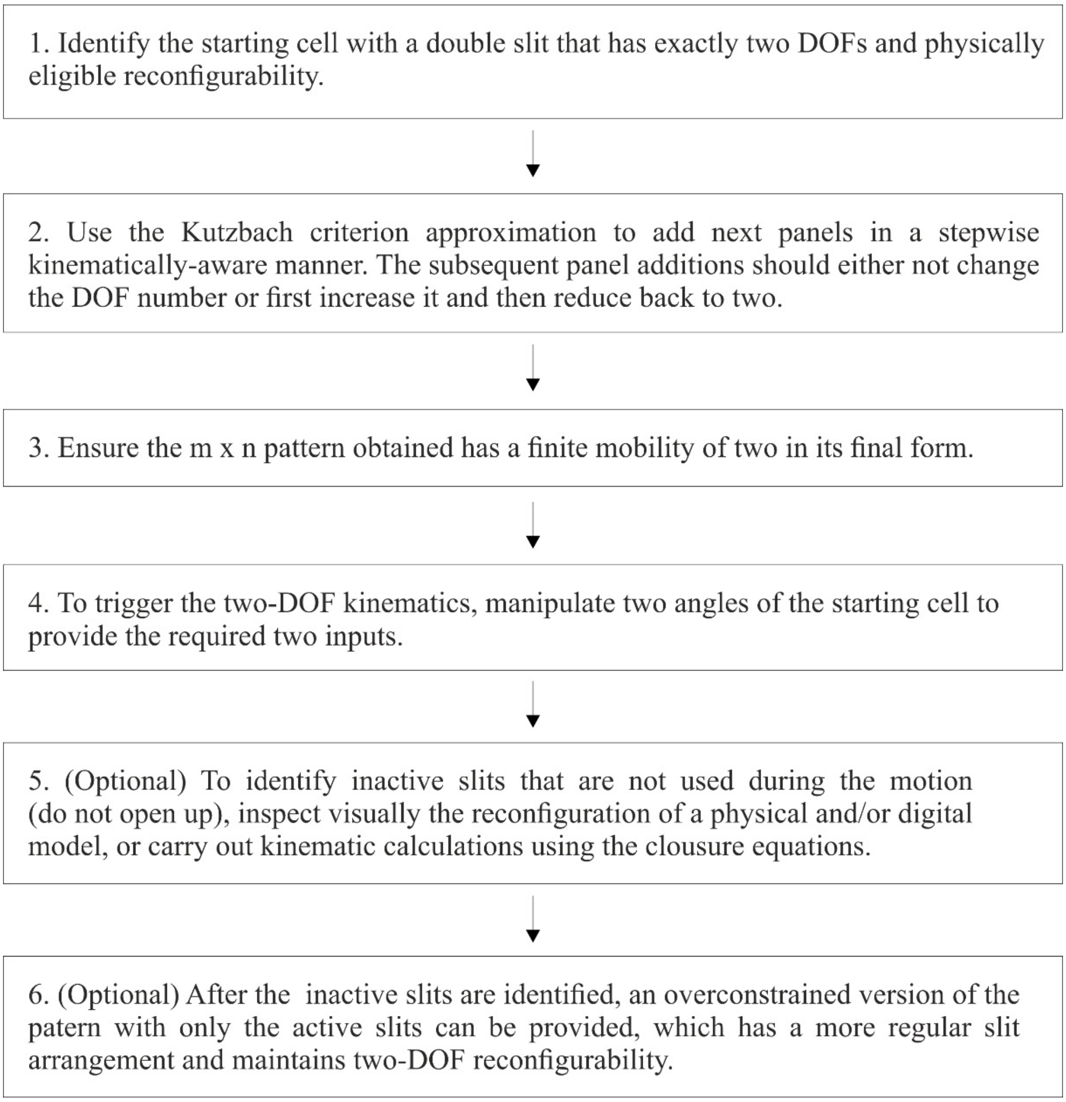

1. Identify the starting cell with a double slit that has exactly two DOFs and physically eligible reconfigurability.

2. Use the Kutzbach criterion approximation to add next panels in a stepwise kinematically-aware manner. The subsequent panel additions should either not change the DOF number or first increase it and then reduce back to two.

3. Ensure the m x n pattern obtained has a finite mobility of two in its final form.

4. To trigger the two-DOF kinematics, manipulate two angles of the starting cell to provide the required two inputs.

5. (Optional) To identify inactive slits that are not used during the motion (do not open up), inspect visually the reconfiguration of a physical and/or digital model, or carry out kinematic calculations using the clousure equations.

6. (Optional) After the inactive slits are identified, an overconstrained version of the patern with only the active slits can be provided, which has a more regular slit arrangement and maintains two-DOF reconfigurability.

Fig. 6.21 A strategy to design a reconfigurable two-DOF kirigami version of a traditionally single-DOF origami pattern.

Chapter 7

Two-DOF reconfigurable versions of other patterns

So far, the previous chapters showed how to obtain reconfigurable versions of Miura-ori, which not only fold in the traditional in-plane way but also can take new forms, e.g. with out-of-plane curvatures, bending upwards and downwards. They are all possible with panels remaining infinitely rigid, i.e. experiencing no deformations. Moreover, such patterns are designed to maintain two DOFs to keep the control easy while experiencing reconfigurations.

This chapter will apply the identified slit arrangements to other patterns to test the findings on assemblies different from Miura-ori. We will examine more origami tessellations composed of four-crease vertices. Similarly to Miura-ori, these patterns consist of interconnected spherical 4R linkages and have only one DOF allowing them to experience only one type of motion in their rigid origami versions. By applying the slit layouts identified in chapter 6, we expect to remove enough kinematic constraints to create a second DOF that will allow reconfiguration into unique and previously impossible shapes.

The objective is to identify a family of new reconfigurable rigid kirigami patterns whose control is as convenient as it is for the modified Miura-ori from chapter 6. This chapter introduces the slits subsequently to Eggbox, Anisotropic Miura, Arc-Miura and Arc patterns and reports on both the successful attempts and the encountered challenges.

7.1 Eggbox pattern

First, we modify Eggbox, which is another four-crease-vertex origami pattern. Its panels form repetitive concavities and convexities, like in egg boxes. When assuming the panels' rigidity, the pattern has only one DOF as it comprises only spherical 4R linkages. Similarly to Miura-ori, it has only one in-plane motion (Tachi 2010b) (Nassar et al. 2017). As the pattern's sector angles at each vertex do not add up to 2π (in the analysed example, all four angles at a vertex are $\alpha = 60^{\circ}$), Eggbox does not have a fully flat form. Therefore, we cannot present a flat crease pattern but only a partially-folded state. Figure 7.1 presents the pattern in such a configuration, with slits drawn symbolically along some of its edges. We use the double-slit arrangement along the horizontal direction, analogous to the one in Fig. 6.13(c).

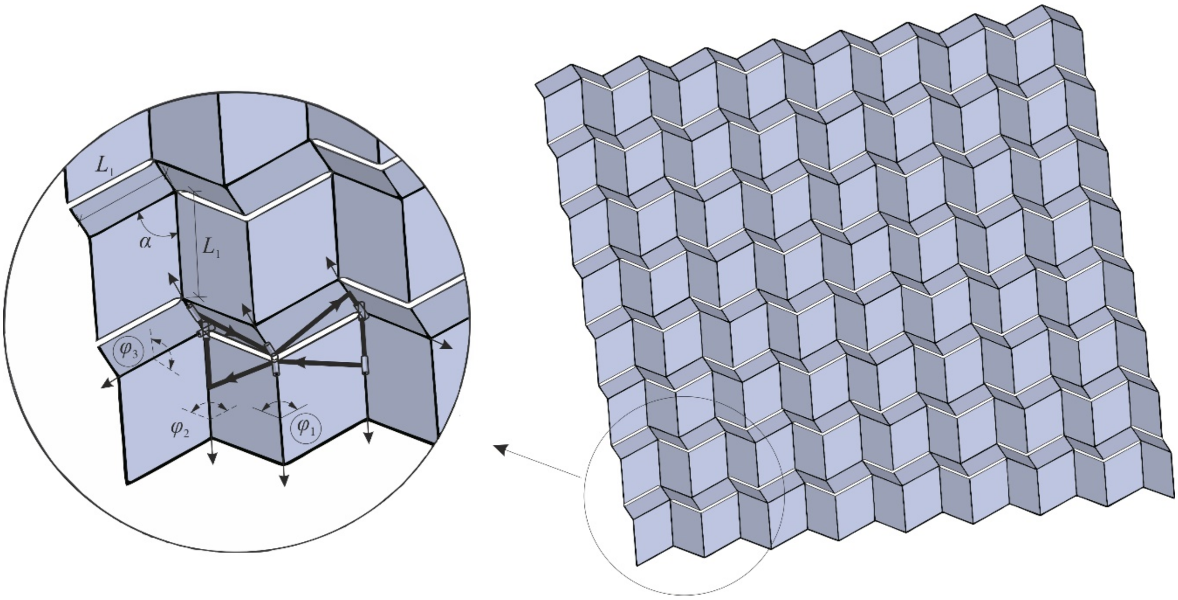

Fig. 7.1 A close-up of Eggbox's single 8R cell that we use to reconfigure the entire pattern. Circled variables φ_1 and φ_3 are the inputs and φ_2 is a representative output.

It is again enough to use one of the 8R cells to control the entire pattern's motion. Figure 7.1 also presents a close-up of the bottom-left cell, whose dihedral angles we will manipulate to reconfigure the entire pattern. Angles φ_1 and φ_3 again become our two input DOFs. We will be analogously disabling φ_3 and manipulating φ_1 to trigger alternative motion 1. The opposite approach, with φ_1 frozen and φ_3 changed, will lead to alternative motion 2. We will again plot the output variable φ_2 against the inputs to visualise the motion paths.

Due to different geometry, Eggbox's 8R cell is represented by a linkage different from the previously analysed Miura-ori's one from Fig. 5.1. The linkage equivalent to the Eggbox's geometry is presented in Fig 7.2. Using the matrix method, we can derive the closure equation that governs the kinematic relationship between φ_1, φ_2 and φ_3, i.e.

$$\cot\left(\frac{\varphi_3}{2}\right) = -\tan\left(\frac{\varphi_1}{2} - \varphi_2\right)\cos(\alpha). \tag{7.1}$$

We can compare it with the analogous equation derived from the Miura-ori's 8R linkage (5.9) to notice that the kinematic relationship is indeed different.

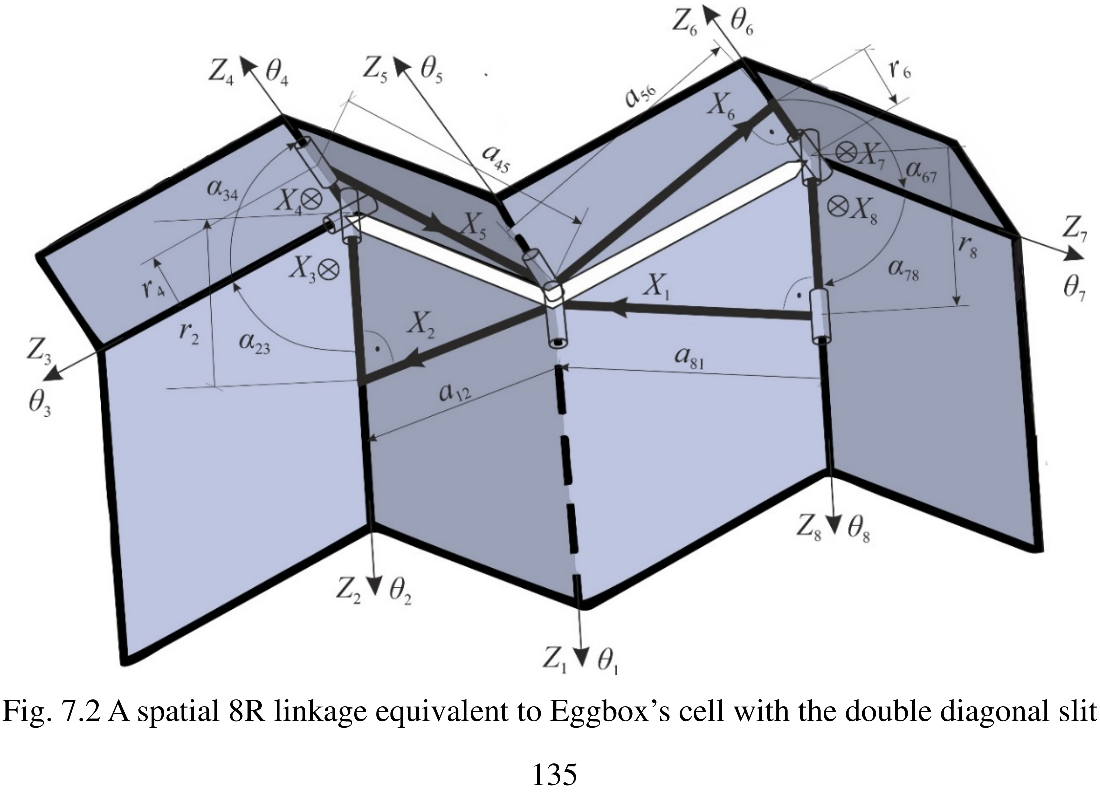

Fig. 7.2 A spatial 8R linkage equivalent to Eggbox's cell with the double diagonal slit.

We use Eggbox's closure equation (7.1) to visualise the kinematics by creating 3D plots similar to those used in chapter 6. As earlier, in Fig. 7.3, inputs φ_1 and φ_3 are plotted horizontally, and the variable φ_2 vertically. Due to φ_1 and φ_3 having values from 0° to 180°, we have an entire domain of possible input combinations. By calculating φ_2 for each combination, we again obtain a surface of all possible configurations of the pattern.

Moreover, by synchronising the inputs φ_1 and φ_3 so that they satisfy the kinematics of Eggbox's traditional spherical 4R linkages, we can single out a path on the surface representing the standard one-DOF motion of an uncut pattern. The required relationship between inputs φ_1 and φ_3 to reproduce the traditional folding is

$$\cot\left(\frac{\varphi_1}{2}\right)\cot\left(\frac{\varphi_3}{2}\right)=\cos\left(\alpha\right). \tag{7.2}$$

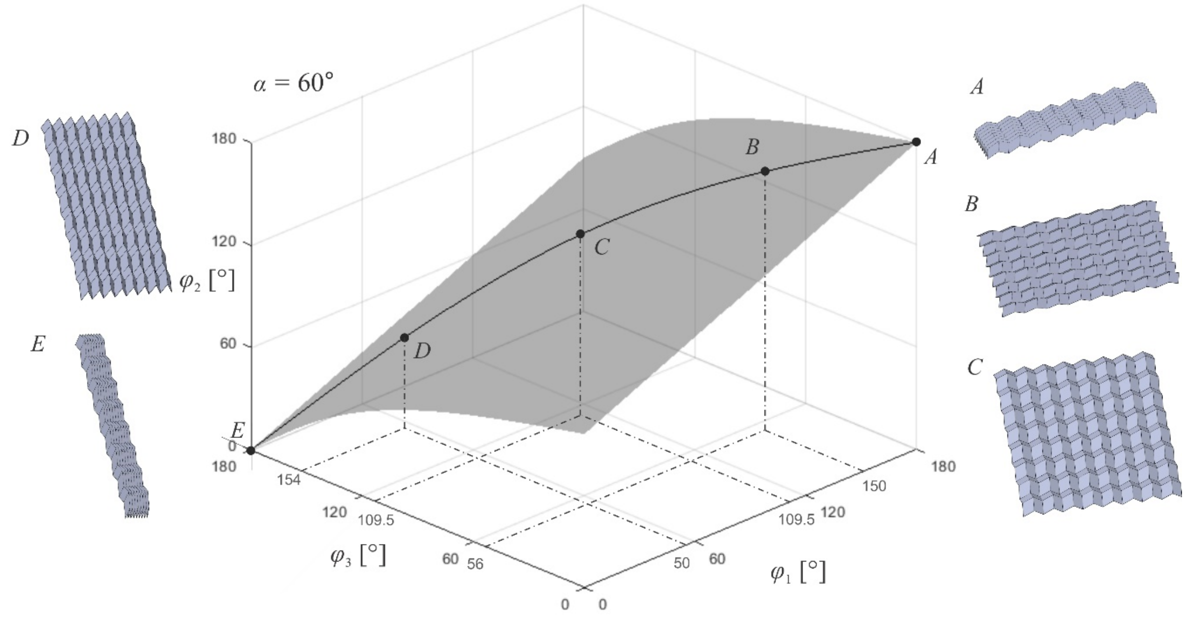

Fig. 7.3 A 3D plot of all theoretically possible configurations of the two-DOF Eggbox pattern, represented by a surface of the values φ_2 takes for the φ_1 and φ_3 input combinations. *A*, *B*, *C, D* and *E* are stages on the traditional one-DOF folding curve.

Such a curve representing the Eggbox's original one-DOF motion with corresponding shapes is presented in Fig. 7.3. As mentioned earlier, the pattern cannot deploy fully flat due to its geometry. From an intermediate shape, point *C*, it can go in two different directions. The first is via *B* to *A*, and the second via *D* to *E*. These are two alternative folding directions leading to different compact forms. They represent folding the pattern vertically and horizontally, respectively.

Point *C* is a configuration on the traditional path when φ_1 and φ_3 take the same value, around 109.5° in the analysed case. We use this point as a starting one for alternative motions. However, it is essential to highlight that reconfiguration can be triggered at any stage along the traditional curve. By freezing φ_3 at 109.5° and changing φ_1, we start alternative motion 1, shown in Fig. 7.4. Decreasing φ_1 allows reaching configurations *F* and *G*, which include folding every second pair of panels. Similarly to Miura-ori, it gives shapes with out of plane curvature, i.e. imitates pattern's bending even under the rigid panel assumption.

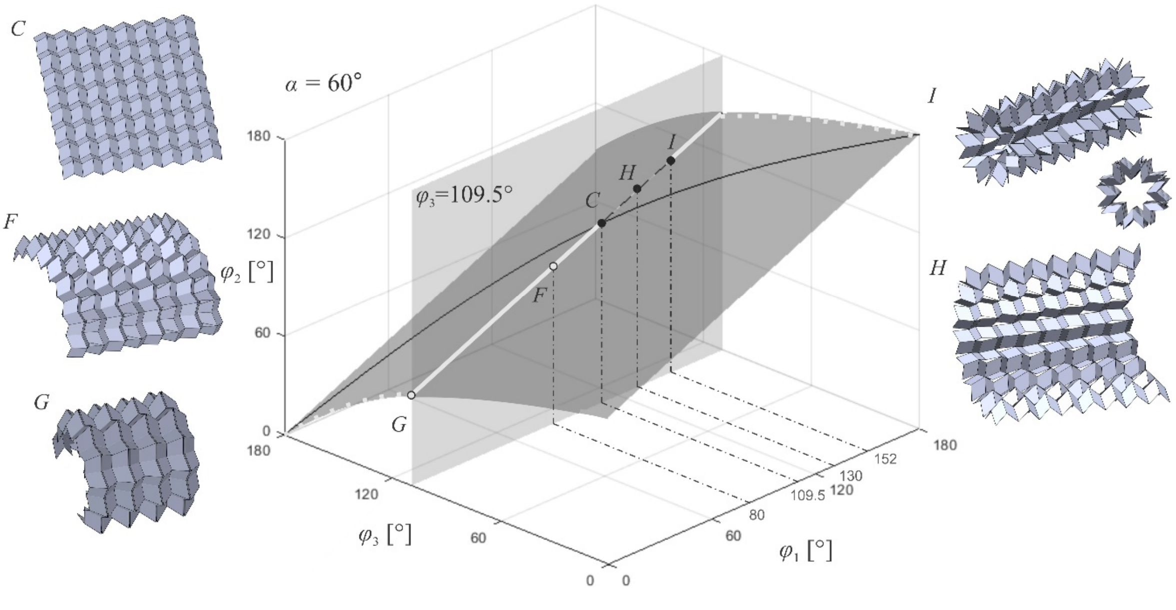

Fig. 7.4 An alternative motion 1 path started at point *C*, when input φ_3 is frozen at a value and only φ_1 changes. *F, G, H,* and *I* are Eggbox's new arched and tubular forms.

Notice that this section of the alternative path is greyed out. It is because even the slightest reconfiguration includes panel self-intersections. It means it is impossible to exercise these motions with physical models due to panel collisions. Therefore, section *C*-*F*-*G* is available only theoretically. However, it is valuable to remind that for such motion segments, we can again mark the panel intersections as in Fig. 6.19 and adjust the size of the openings. Such a redesigned Eggbox pattern with slits of non-zero width could follow the *C*-*F*-*G* path until the stage we would choose, at which the panels would finally collide.

An alternative to the *C*-*F*-*G* section is increasing φ_1 and going through configurations *H* and *I*. This time, the panels expand, and the pattern bends in the opposite direction, upwards. Moreover, this section is available as no collisions occur until configuration *I*. At this stage, the pattern folds into a tubular shape, and further reconfiguration includes macroscale collisions preventing us from going further. Therefore, *I* is a boundary state and the path beyond it is greyed out.

We can create an analogous plot to show alternative motion 2, Fig. 7.5. Freezing this time φ_1 at *C* and increasing the φ_3 allows accessing configurations *F* and *G*. Folding every second pair of panels causes the pattern to bend upwards, without collisions, until some of the panels close fully and the assembly locks in point *G*. This is a boundary state, as further reconfiguration is impossible due to panel contact. At point *G*, we can keep φ_3 equal to zero and unfreeze φ_1. If we fold it too, we reach the traditional compact form *E*. This shows that we can also use the *C*-*F*-*G* section to decouple the folding process.

Decreasing φ_3 at point *C* instead leads to shapes *H* and *I*. This section involves expanding panels and the assembly bending downwards until it reaches a tubular form.

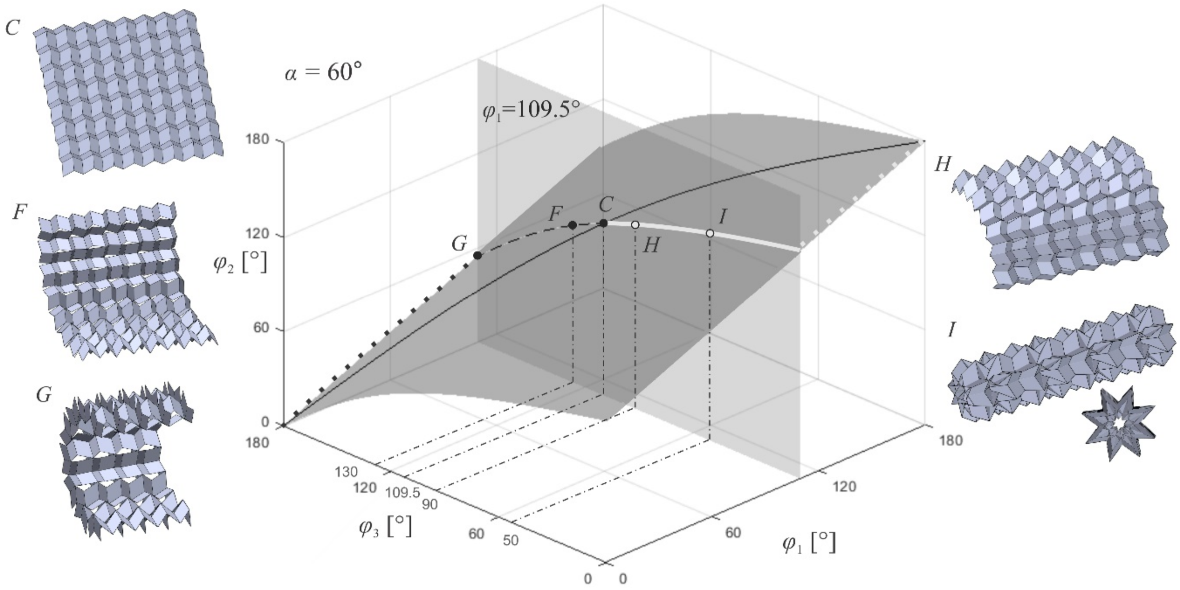

Fig. 7.5 An alternative motion 2 path started at point *C*, when input φ_1 is frozen at a value and only φ_3 changes. *F, G, H* and *I* are Eggbox's new arched and tubular forms.

However, analogously to the previous case, panel intersections occur from the motion's beginning, and this section is only theoretical. It can be again partially enabled by marking the degree of panel intersections and redesigning the pattern by widening the slits.

Above, we discussed the two-DOF kinematics of a rigid-panel Eggbox with slits along the horizontal direction. As a result, the pattern always bends vertically. However, making Eggbox reconfigure into shapes with a curvature horizontally is straightforward. The pattern is geometrically identical in both orthogonal directions and requires the same regular slit arrangement but along vertical edges. In other words, we only need to rotate the pattern in Fig. 7.1 by 90°.

In conclusion, by applying a familiar slit arrangement to a rigid Eggbox pattern, we successfully altered its DOFs number from one to two. Now, this classic tessellation not only exhibits the standard in-plane motion but, similarly to a two-DOF rigid Miura, can exhibit bent-like shapes with out-of-plane curvatures, as shown in Fig. 7.6. We can use this to provide unique, previously unavailable arched or tubular forms or decouple the traditional folding. Moreover, the Eggbox's geometry, identical in both orthogonal directions, makes it straightforward to choose between horizontal and vertical cuts what allows choosing the direction the pattern should bend.

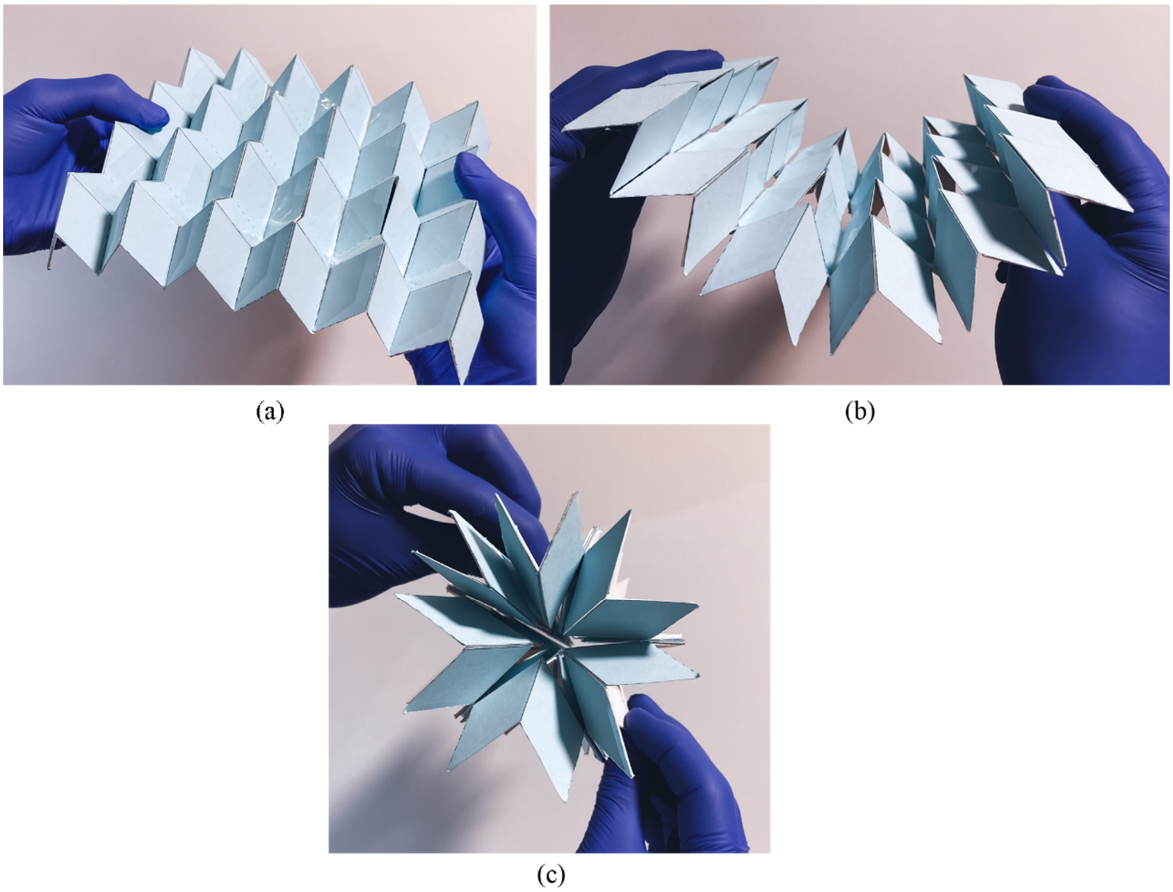
(a) (b) (c)

Fig. 7.6 A physical model of a two-DOF Eggbox pattern from Fig. 7.1 but having 12x8 panels; (a) is the traditional in-plane form; (b) and (c) are exemplary new out-of-plane arched and tubular configurations.

7.2 Anisotropic Miura

Next, we investigate another four-crease-vertex tessellation that in its rigid-origami version consists of spherical 4R linkages, has one DOF, and can move only in-plane. Known as Anisotropic Miura, it is inspired by Miura-ori. The anisotropic version reverses some creases' orientation and the MV assignment. This is to avoid the overlapping of consecutive panels, which is often problematic when introducing material thickness.

Figure 7.7 presents a 16x16-panel Anisotropic Miura's crease pattern with double slits along its diagonal creases. It also shows a close-up of the bottom left cell that we again use to steer the motion. Analogously, angles φ_1 and φ_2 are at vertical creases and φ_3 at a diagonal one. The circled φ_1 and φ_3 are the inputs, while φ_2 will depict one of the output values.

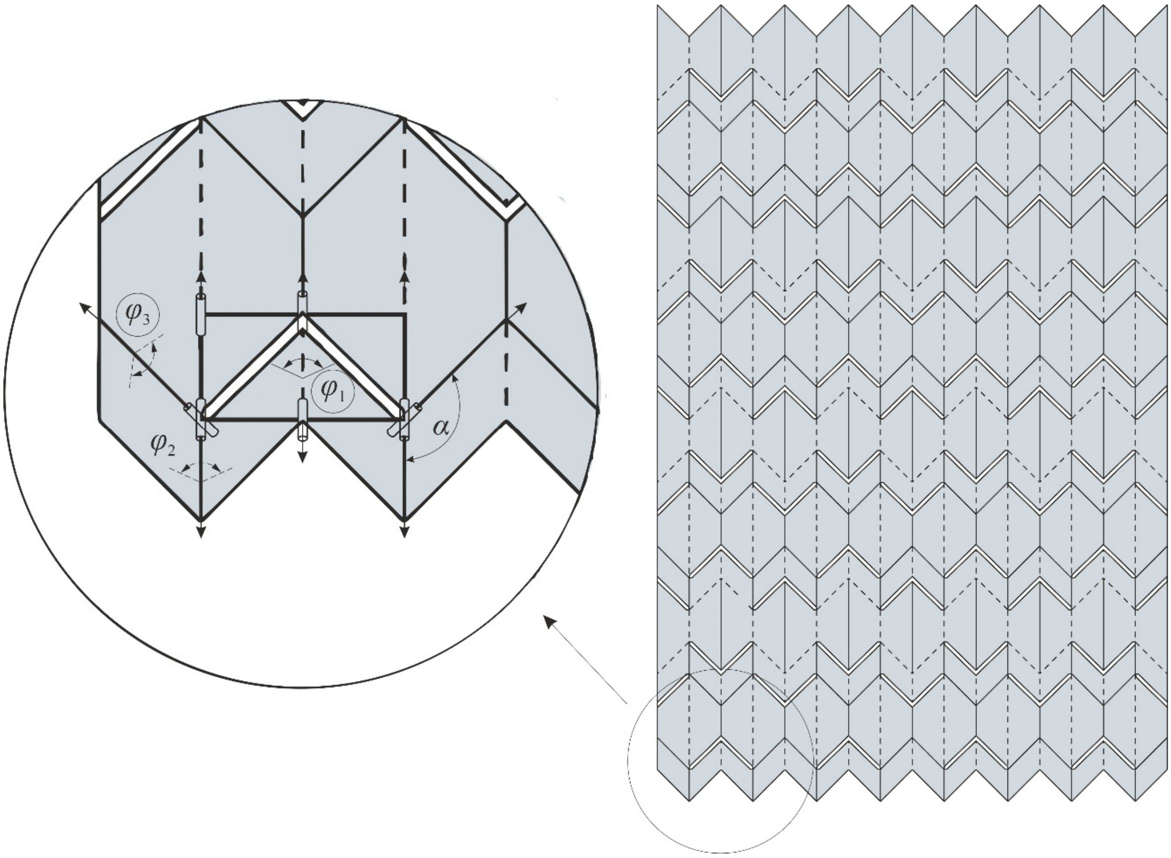

Fig. 7.7 A close-up of Anisotropic Miura's single 8R cell that we use to reconfigure the entire pattern. Circled φ_1 and φ_3 are the inputs and φ_2 is a representative output variable.

Notice that due to the pattern's and the slit's geometry, the cell's representative linkage is the same as the Miura-ori's one, Fig. 5.1. Moreover, we use similar sector angles for the parallelograms in the depicted model, i.e. $\alpha = 135^\circ$. Therefore, the relationships between variables are alike, and the surface of possible configurations and the traditional motion curve on the 3D plots have the same shape as in Fig. 6.8.

Figure 7.8 presents such a 3D kinematic plot, on which we locate Anisotropic Miura's typical configurations and examine alternative motion 1. We access it from any point at the traditional motion path, *A*-*B*-*C*. Again, we choose a point when vertical creases' dihedral angles are 90°, which corresponds to angles 70.5° at diagonal folds. Freezing φ_3 at 70.5° and increasing or decreasing φ_1 allow us to access the new path. Making φ_1 smaller folds every

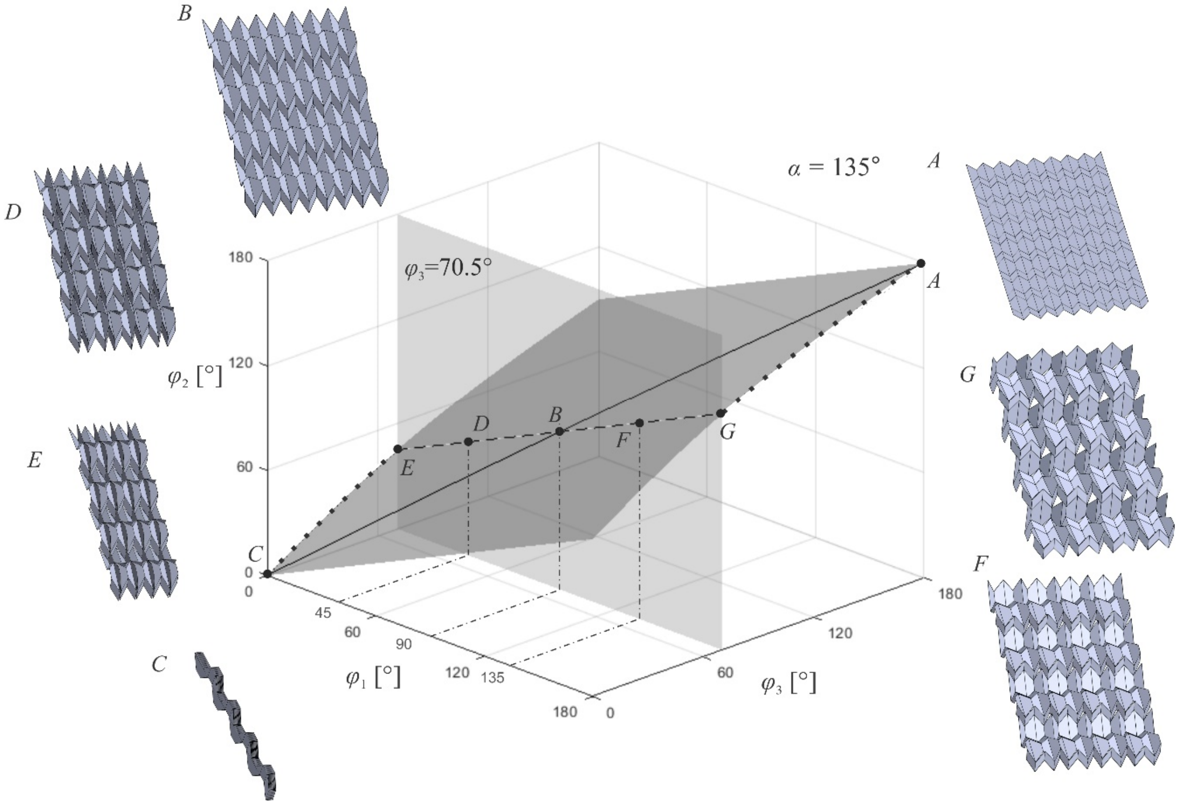

Fig. 7.8 A 3D plot of all theoretically possible configurations of the two-DOF Anisotropic Miura; *A*, *B* and *C* are stages on the traditional folding curve; *D*, *E*, *F* and *G* are new forms on alternative motion 1 path, activated by freezing φ_3 and changing φ_1.

second pair of panels, *D*, until a boundary state *E* is reached, at which they close fully. Alternatively, bigger φ_1 opens up every second pair, as in *F*, until another state is reached, *G*. In this form, some of the panels expand fully as the dihedral angles between them become 180°. Further expansion is geometrically impossible.

At both states *E* and *G*, we can freeze φ_1 and continue reconfiguration with φ_3 instead. This allows us to reach the traditional flat and compact forms, *A* and *C*, respectively, via new decoupled motions instead of following the traditional path. For previous patterns, it was impossible to reach both the flat and the compact form in this way, as one of the new paths leading to these configurations was usually invalid due to panel intersections.

Figure 7.9 presents an analogous 3D plot, but this time, showing alternative motion 2 when at point B we freeze φ_1 and manipulate φ_3 instead. Similarly, manipulating the input folds or deploys the pattern, *D* or *F*, until one of the edge states is reached, *E* or *G*. Motion 2 also does not include panel intersections, and both these states are accessible. They can also reconfigure into the traditional flat and compact forms, *A* and *C*, respectively.

Applying slits to Anisotropic Miura creates a two-DOF reconfigurable pattern successfully. However, this time, its reconfiguration does not return shapes with apparent out-of-plane curvatures. We suspect this is due to the varying orientation of the pattern's diagonal creases. On the crease pattern from Fig.7.7, the slits point not in one coherent direction, as in previous patterns, but in the alternating opposite ones. Some are directed towards the top of the pattern, others to the bottom. Each subsequent row with the opposite slit orientation cancels the out-of-plane motion triggered by the previous one. Such a geometry, as a result, prevents the pattern from coherently reshaping into a curved form.

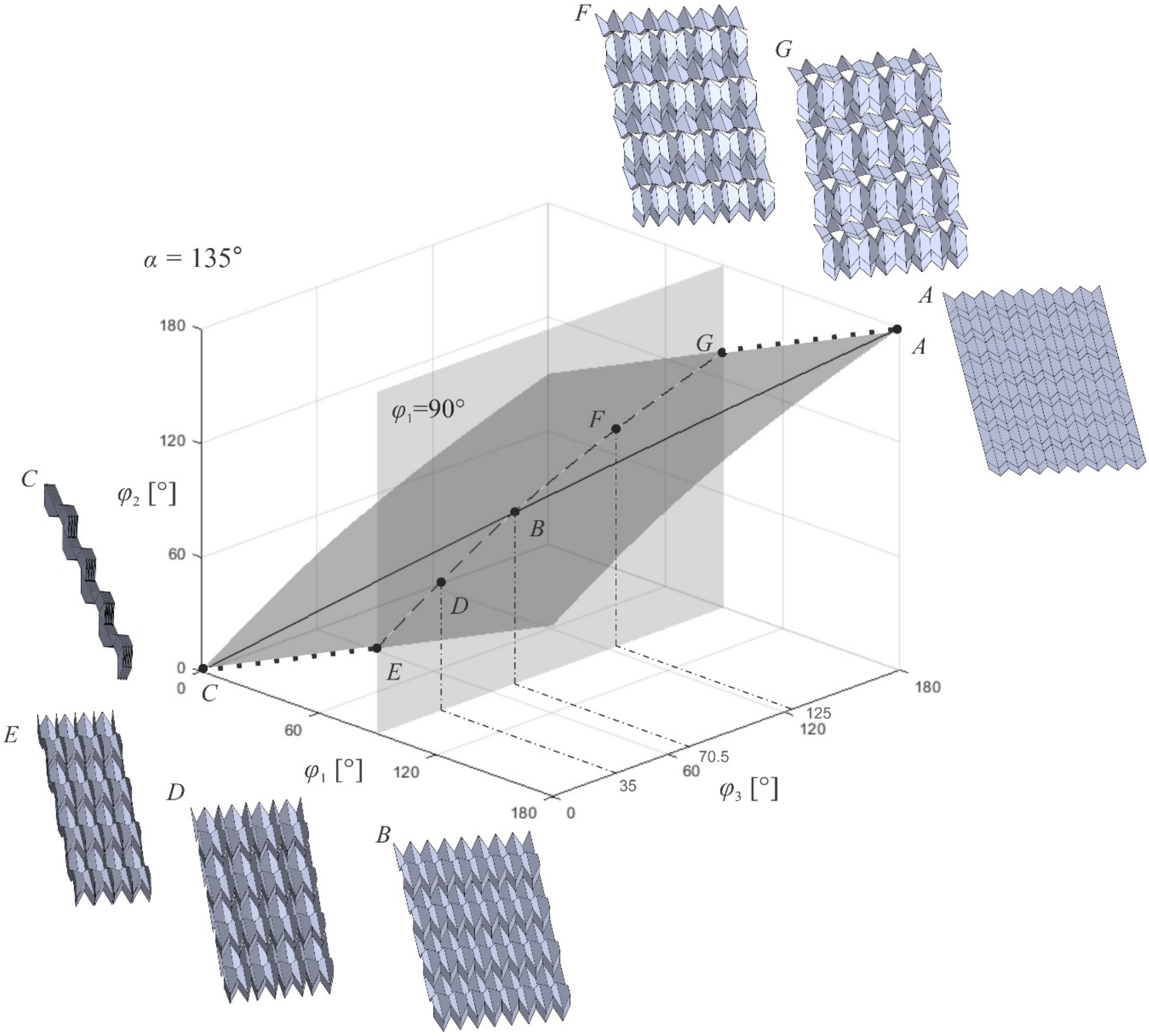

Fig. 7.9 A 3D plot of all theoretically possible configurations of the two-DOF Anisotropic Miura; *A*, *B* and *C* are stages on the traditional folding curve; *D*, *E*, *F* and *G* are new forms on alternative motion 2 path, activated by freezing φ_1 and changing φ_3.

The last modification to Anisotropic Miura we examine is applying slits along vertical creases to investigate if this is also a viable approach to achieving a two-DOF structure. Figure 7.10(a) presents an Anisotropic Miura's fragment with a slit arrangement analogous to Fig. 6.15(c). We know from previous calculations that such an assembly should have two DOFs. We similarly freeze one angle at any vertical crease, Fig. 7.10(b), and change one at the diagonal folds to trigger the new motion. This reconfigures the assembly as in Fig. 7.10(c). We notice that half of the panels rotate in respect to the other half. A particular geometric speciality happens, as all hinges in the middle of the assembly align and form a long revolute together. Mobility of such assembly is indeed two, but problems arise if we decide to enlarge the pattern.

Figure 7.10(d) presents two such sub-assemblies joined together into a larger pattern. Between every two-panel vertical strip, the uncut revolutes align and act on a macro scale as long hinges, marked with red axes in Fig. 7.10(e). Each panel strip can rotate along adjacent revolutes independently and reshape the assembly only locally, as in Fig. 7.10(f).

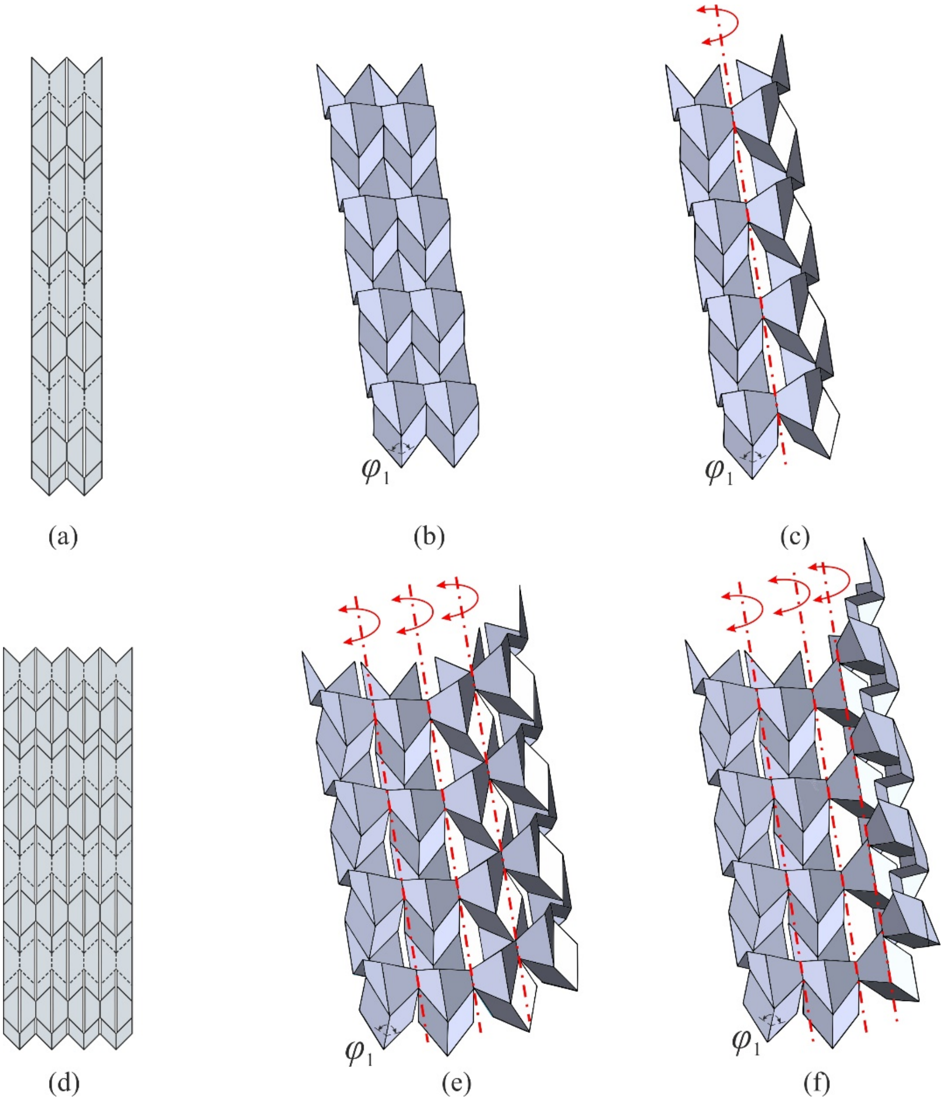

Fig. 7.10 An attempt of introducing vertical slits to Anisotropic Miura; (a) is a two-DOF fragment; (b) is (a) folded traditionally; (c) is (b) reconfigured, with a red axis showing a macro-scale revolute due to a geometric speciality; (d) is a fragment with more slits; (e) and (f) show an independent revolute rotation resulting from geometric specialities.

This means that a geometric speciality emerges due to the slit pattern leaving only particular creases uncut that align with each other. The pattern, instead of keeping two DOFs, increases their number as it grows larger. For example, it has $M = 4$ in Fig. 7.10(e) and (f) as each multi-crease revolute acts independently. This example displays how the slit patterns identified earlier have to be evaluated anew when applied to other origami. It is crucial to verify if no geometric specialities occur that may affect the kinematics surprisingly.

In conclusion, the arrangement of double slits along diagonal creases changed the Anisotropic Miura's kinematics by similarly adding an extra DOF. This allowed alternative kinematic paths, like for the Miura-ori with slits. This time, however, the new motions do not cause out-of-plane bending. Moreover, cuts along the vertical creases were so far unsuccessful. Even though a vertical-slit arrangement from chapter 6 allowed constructing a reconfigurable assembly, its DOF number does not stay finite, equal to two. It increases as the assembly grows larger due to a geometric speciality.

Nevertheless, the double diagonal slits successfully created a reconfigurable two-DOF structure out of a rigid one-DOF Anisotropic Miura. Compared to the uncut one, this version can decouple both the traditional folding and deployment motions. Moreover, it experiences no panel intersections along the presented motion paths. Every second pair of panels can be folded or deployed flat using the new DOF, without changing the other angles. Then, by switching the input we operate, we can finish the process and fold the pattern completely or deploy it to a fully flat form. This means that the traditional motion can now be realised under two different, sequential movements, with separate geometric Poisson's ratios. Figure 7.11 presents a manipulation of a physical model of the two-DOF Anisotropic Miura.

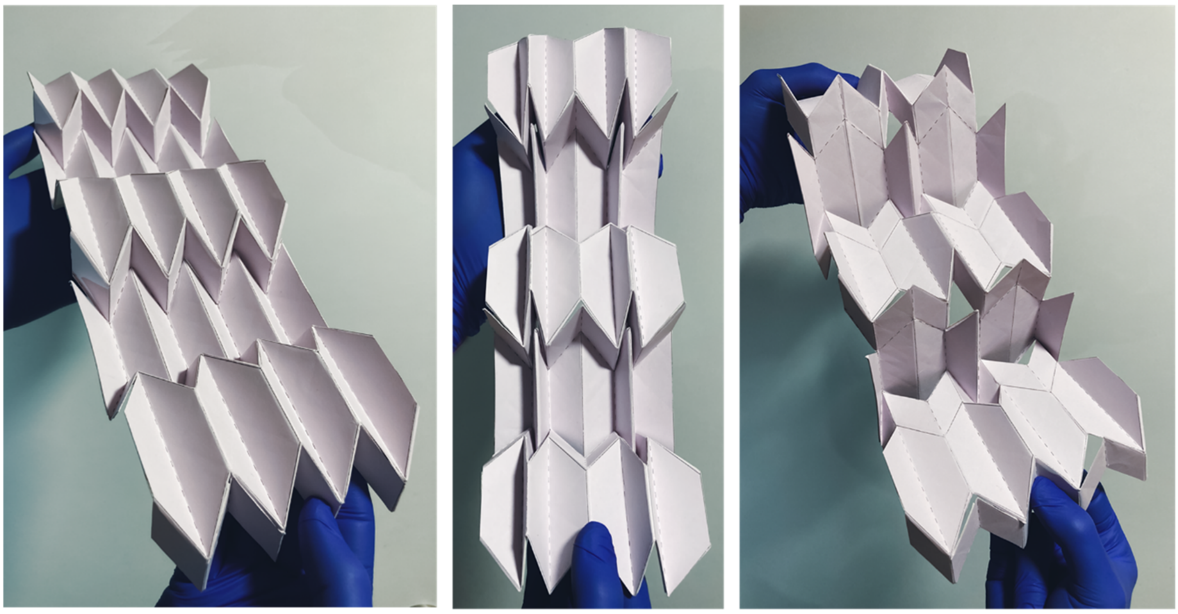
(a) (b) (c)

Fig. 7.11 A physical model of a two-DOF Anisotropic Miura from Fig. 7.7 but having 8x10 panels; (a) is a traditional in-plane form; (b) and (c) are exemplary new configurations.

7.3 Arc-Miura

Next, we apply the slit arrangements to a particular derivative of Miura-ori, called Arc-Miura. This tessellation also comprises spherical 4R linkages in its rigid form, and like Miura-ori, has only one folding motion. However, Arc-Miura varies the sector angle values what makes it fold naturally into a curved shape (Gattas et al. 2013). By making cuts as in chapter 6, we hope to gain the ability to manipulate the pattern's curvature or even straighten Arc-Miura.

Figure 7.12 presents a 16x16 crease pattern of Arc-Miura with double diagonal slits introduced. As mentioned above, Arc-Miura varies parallelograms' sector angles. We choose to alternate between $\alpha = 120^\circ$ and $\beta = 135^\circ$. Figure 7.12 also shows a close-up of the

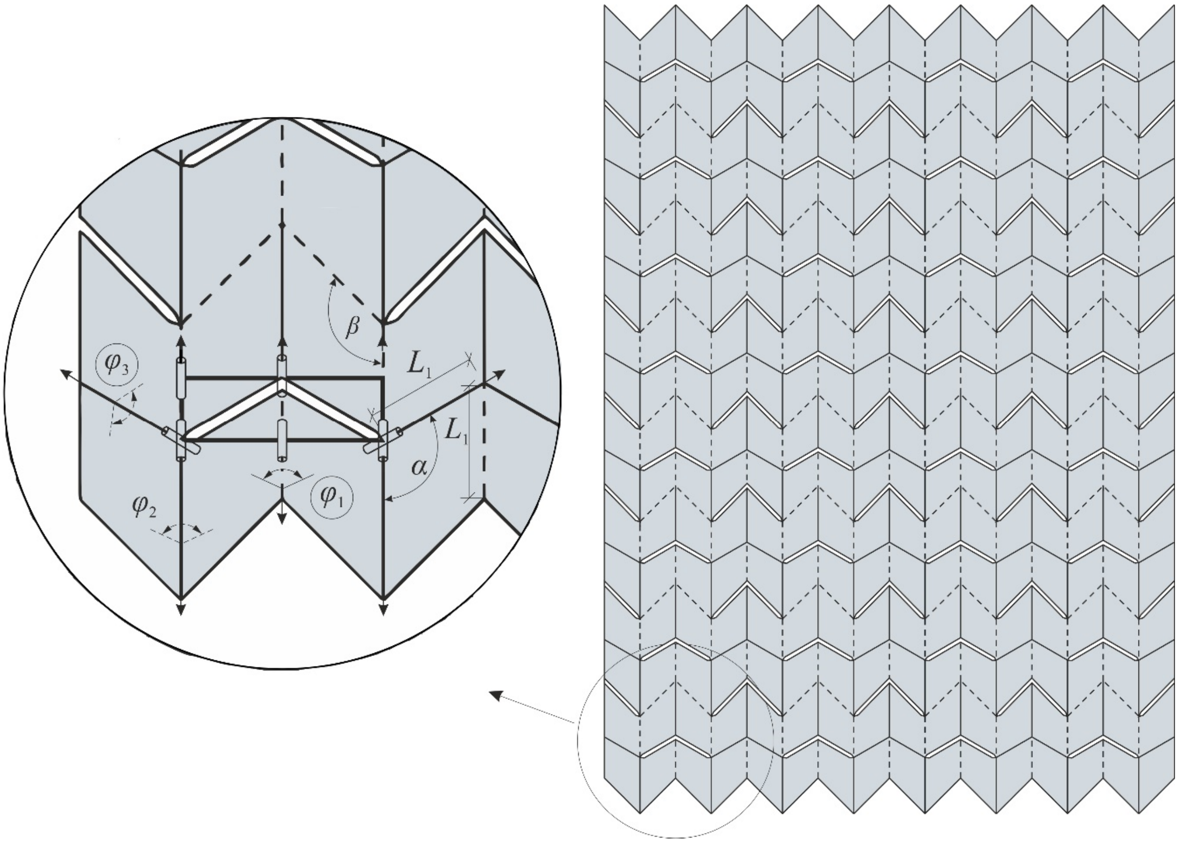

Fig. 7.12 A close-up of Arc-Miura's single 8R cell that we use to reconfigure the entire pattern. Circled φ_1 and φ_3 are the inputs and φ_2 is a representative output variable.

single motion-driving cell, with analogously marked φ_1, φ_2 and φ_3. The pattern and slit geometries again result in the same spatial 8R linkage from Fig. 5.1, which was used earlier to represent Miura-ori. Therefore, we can use its closure equations, noticing that the bottom cell's sector angle α is 120°.

Figure 7.13 presents an analogous 3D plot of the pattern's possible configurations represented as a surface of values that φ_2 takes for different combinations of inputs φ_1 and φ_3. Once more, synchronising both inputs to satisfy the traditional one-DOF equations (2.12) singles out a curve representing the typical folding. We see that Arc-Miura, similarly to Miura-ori, goes along the path *A*-*B*-*C* from a flat to a compact form. This time, however, the partially and fully folded shapes are curved along the vertical direction naturally.

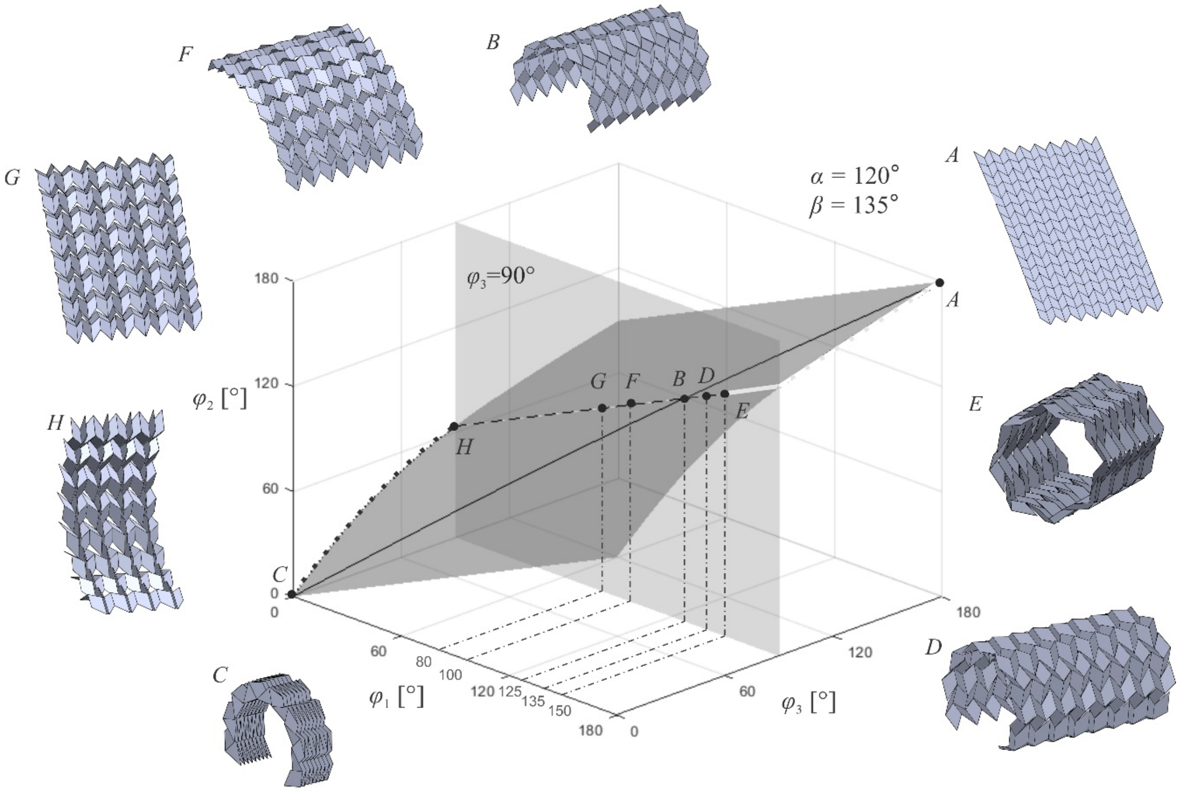

Fig. 7.13 A 3D plot of all theoretically possible configurations of the two-DOF Arc-Miura; *A*, *B* and *C* are stages on the traditional folding curve; *D*, *E*, *F*, *G* and *H* are new forms on alternative motion 1 path, activated by freezing φ_3 and changing φ_1.

We again select a point on the curve where we wish to start alternative motions. This time it is a configuration *B* with $\varphi_1 = 125^\circ$ and $\varphi_3 = 90^\circ$. By freezing φ_3 and increasing φ_1, we start alternative motion 1 that thanks to the slits, curves the pattern even more, as in *D*. This continues until it creates the shape as in *E*. The tubular form is again a boundary state, with further motion impossible due to panel collisions. The remaining part of the path is therefore virtual (greyed-out).

If we decrease φ_1 instead, we make the pattern curve less, as in *F*. Further motion decreases the curvature even more until the assembly reaches *G*, an unbent form with no out-of-plane curvature. Setting φ_1 even smaller bends pattern in the opposite direction, i.e. upwards. It continues until the pattern folds partially by closing every second pair of panels, as in *H*. It is the second boundary state that stops the reconfiguration. By switching input variables, we can go from point *H* to the traditional folded form *C*.

Alternatively, by freezing φ_1 at 125° and manipulating φ_3, we can activate motion 2, which allows slightly different configurations, Fig 7.14. Increasing φ_3 reduces the curvature and leads to unbent, in-plane configuration *D* or even bends the pattern in the opposite direction, *E*, until it reaches a tubular boundary shape *F*. Decreasing φ_3 increases the curvature until the pattern forms a second tube-like shape that limits the motion physically, *G*. The above shows that slits along Arc-Miura's diagonal creases again add extra freedom to manipulate curvature along the vertical direction. Next, we introduce vertical slits to see if we can create a pattern with curvatures in two directions.

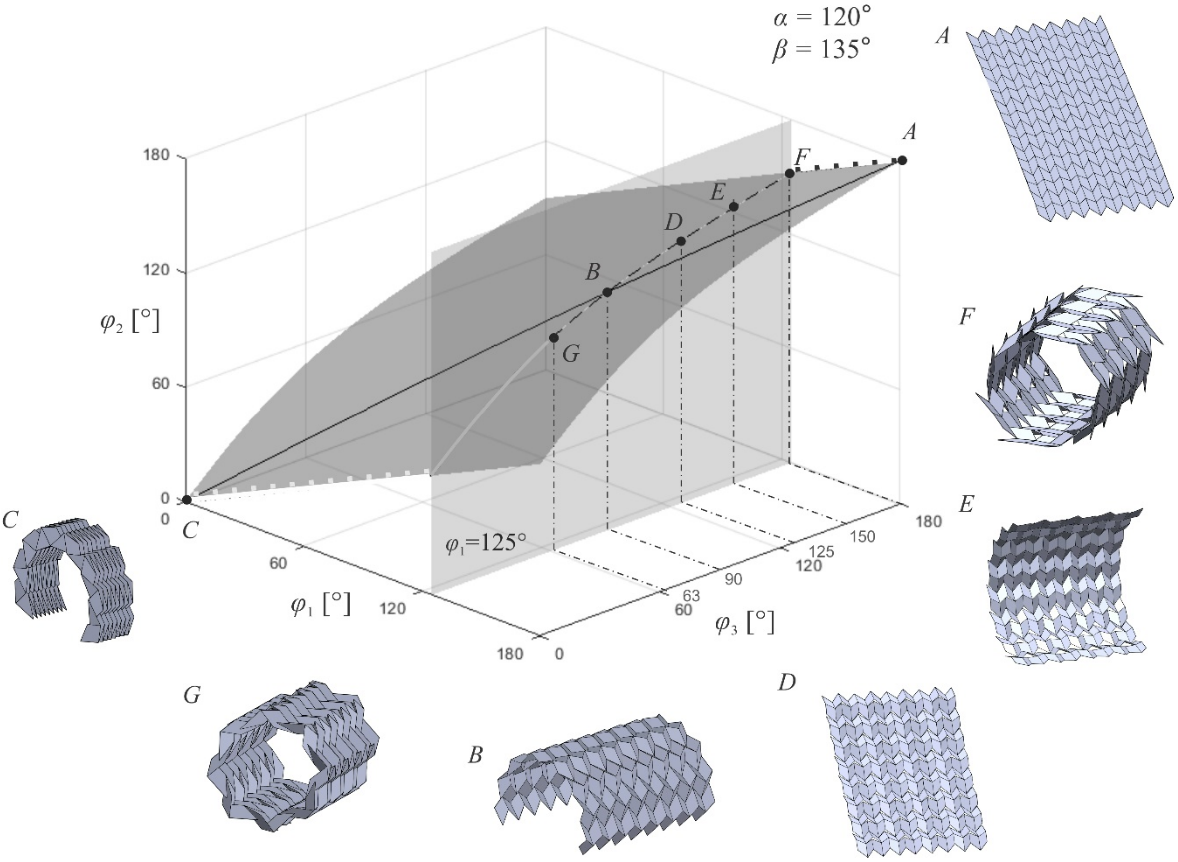

Fig. 7.14 A 3D plot of all theoretically possible configurations of the two-DOF Arc-Miura Miura; *A*, *B* and *C* are stages on the traditional folding curve; *D*, *E*, *F* and *G* are new forms on alternative motion 2 path, activated by freezing φ_1 and changing φ_3.

Figure 7.15(a) presents an Arc-Miura fragment but with vertical slits. Obtained by a similar step-wise cutting approach, the pattern maintains two DOFs after the inactive slit removal. If we reconfigure it into one of the traditional forms, we see it has a natural curvature in the vertical direction, Fig. 7.15(b). At this stage, we can freeze an angle at any vertical crease and use the second input to reconfigure the assembly into a new form. Such a reconfiguration adds another curvature in the perpendicular direction, as marked in Fig. 7.15(c). This shows that having curvatures in both orthogonal directions is possible with a fragmental pattern from Fig. 7.15(a).

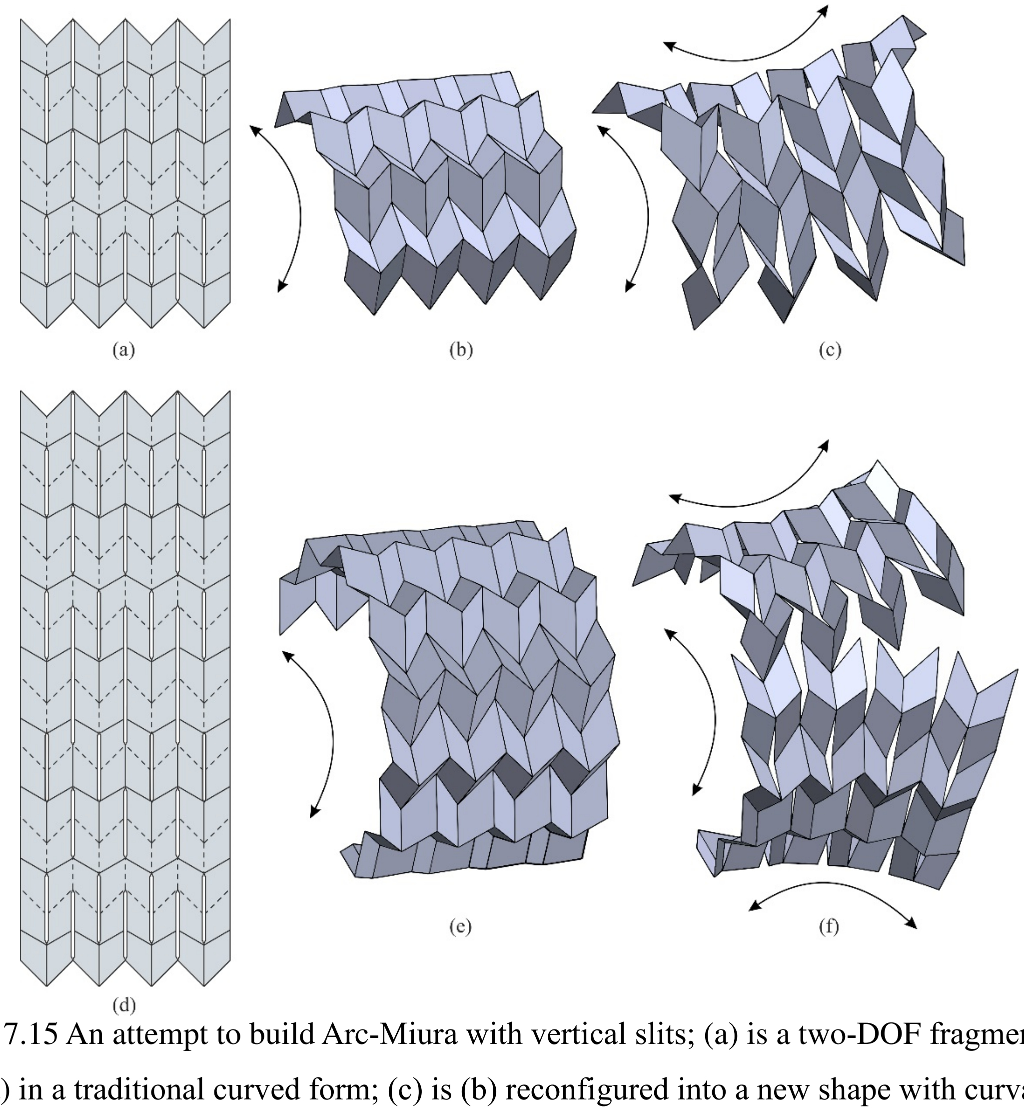

Fig. 7.15 An attempt to build Arc-Miura with vertical slits; (a) is a two-DOF fragment; (b) is (a) in a traditional curved form; (c) is (b) reconfigured into a new shape with curvatures in both directions; (d) are two fragments (a) joined together; (e) is (d) folded in the traditional shape; (f) is unsuccessful reconfiguration of (e) using the new DOF.

However, problems emerge when we multiply and join together such sub-assemblies to build a larger pattern. If we grow the pattern vertically by adding another fragment from Fig. 7.15(a) to the previous one to get assembly in Fig. 7.15(d), we learn that the alternative reconfiguration becomes impossible. When both fragments reshape from the traditionally folded form, Fig. 7.15(e), even if connected only partially, it turns out that due to their geometry, they reconfigure further apart, with ends moving in opposite directions, as in Fig. 7.15(f). Connecting the other ends is physically impossible with only two DOFs, and the fragments stay separate. This example shows that adding slits to a pattern with a natural curvature in one direction when folded in order to obtain configurations with curvatures simultaneously in both orthogonal directions is especially challenging for large patterns. Such a slit arrangement that could be freely repeated no matter how large the pattern is while keeping two DOFs has not been identified during this research project.

To conclude, slits along the diagonal creases successfully added an extra DOF to rigid Arc-Miura, which allows manipulating its out-of-plane curvature, similarly to Miura-ori. The kirigami version of the pattern is now a reconfigurable structure that can change the curvature without having to start the traditional folding. It can also reverse it by bending in the opposite direction or can obtain an in-plane zero-curvature shape. Unfortunately, adding slits along vertical creases was unsuccessful. Introducing an extra curvature horizontally to the natural one in the vertical direction proved to be especially challenging. Nevertheless, a reconfigurable two-DOF rigid kirigami version of Arc-Miura has been found. Figure 7.16 presents the manipulation of its physical model.

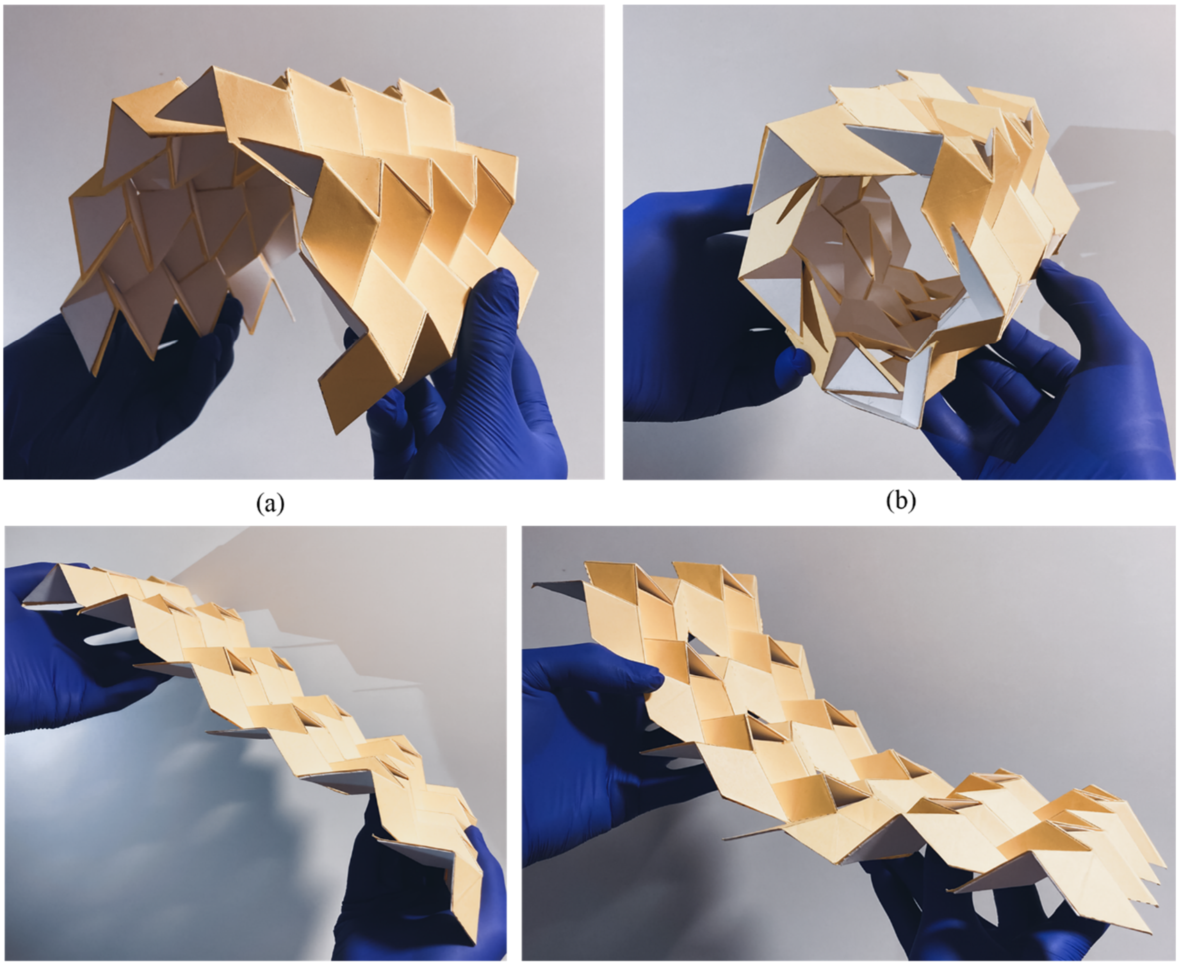

(a) (b) (c) (d)

Fig. 7.16 A physical model of a two-DOF Arc-Miura from Fig. 7.12 but having 8x12 panels; (a) is a traditionally folded form; (b), (c), and (d) are exemplary new configurations.

7.4 Arc pattern

The last origami that we modify with slits is the Arc pattern. It also consists of only four-crease vertices and is an assembly of spherical 4R linkages in its rigid panel form. Therefore, it exhibits only one motion, during which it folds from a flat sheet into arched forms until it reaches its final compact form (Gattas et al. 2013) (Evans et al. 2015b). Also, with a particular number of panel rows, the pattern can fold into a closed polygonal shape. We hope that regular slits will allow us to decouple the folding process and change the nature of the pattern's motion.

Figure 7.17 presents a crease pattern with regular double diagonal slits. As we use sector angles equal to 30° and 150°, we decide to have six rows of panels. This number will ensure that the Arc pattern, due to its geometry, will fold into a neat closed-loop form, with a hexagonal shape in the centre.

Figure 7.17 also presents a close-up od the bottom left 8R cell that we will use to control the entire assembly. Analogously, we choose angles φ_1 and φ_3 as inputs and φ_2 as the output. After examining the cell's geometry, we realise that we can use the linkage from Fig. 5.1 and refer to its closure equations once again. Notice that the slit positioning in different patterns that we analysed was usually alike and allowed us to use the same 8R linkage type in all the cases except for one. For the non-developable Eggbox pattern, we had to model a different linkage and calculate its closure equations separately.

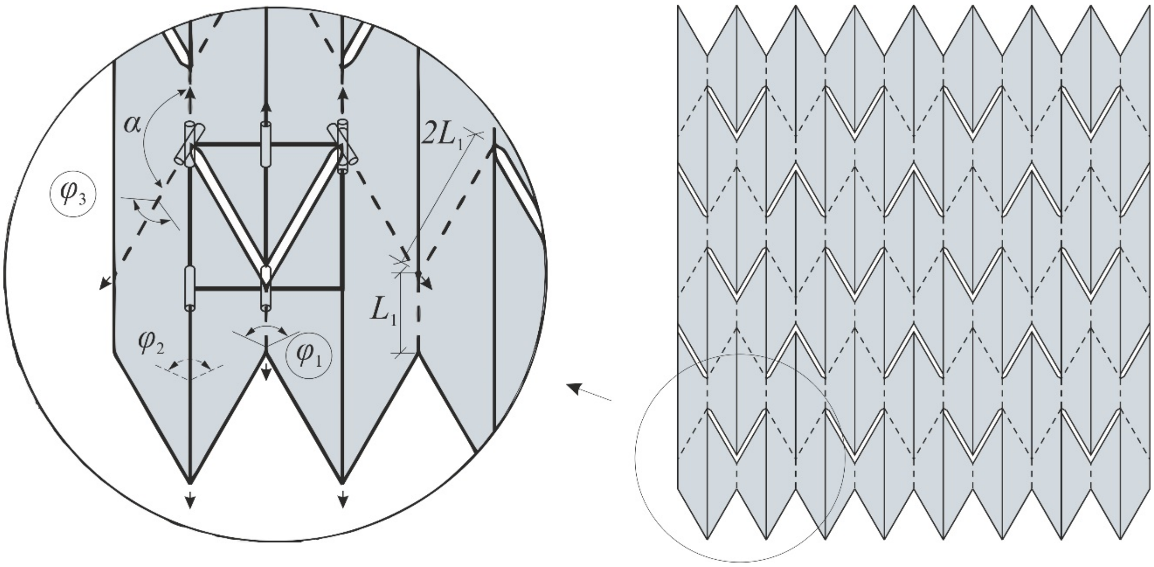

Fig. 7.17 A close-up of Arc pattern's single 8R cell that we use to reconfigure the entire pattern. Circled φ_1 and φ_3 are the inputs and φ_2 is a representative output variable.

Next, we use the closure equations and again plot φ_2 against inputs φ_1 and φ_3 to obtain the surface of the pattern's possible configurations, as in Figs 7.18 and 7.19. This time, however, we operate on angles from 0° to 360°. We show how the Arc pattern's motions allow handily switching the creases' MV assignment and exploring new shapes. For dihedral angles at creases that change from mountains to valleys and vice-versa, we use values greater than 180°. When investigating previous patterns, we limited plots to 180° as such MV changes were either impossible due to panel intersections, i.e. lied on the 'virtual' parts of motions, or were geometrically not interesting.

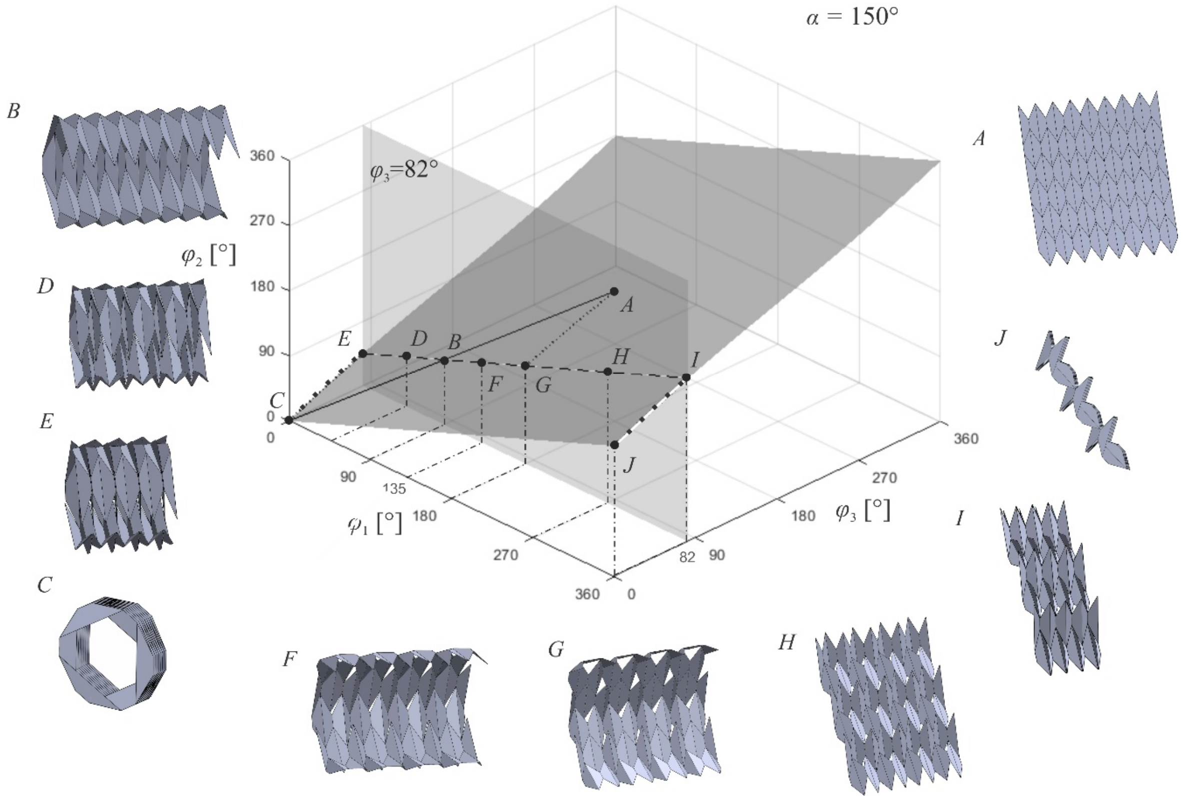

Fig. 7.18 A 3D plot of all theoretically possible configurations of the two-DOF Arc pattern; *A*, *B* and *C* are stages on the traditional folding curve; *D* to *J* are new forms on alternative motion 1 path, activated by freezing φ_3 and changing φ_1.

Again, by synchronising inputs φ_1 and φ_3 so that they satisfy the original spherical 4R linkages' kinematics, which can also be described by (2.12), we single out the traditional motion path, *A*-*B*-*C*. Notice that the pattern indeed folds from a flat sheet, via arched shapes, into a compact form with a hexagonal geometry in the centre.

Then, we again chose an intermediate point on the path from which we can activate alternative motions. Here, we choose *B*, at which φ_1 is 90° and φ_3 is 82°. By freezing φ_3 and decreasing φ_1, we trigger alternative motion 1, via *D* in Fig. 7.18. The pattern partially folds until it reaches a boundary state when some panels fold, *E*. By switching the input, we can go to the compact form *C*. This presents an alternative way of folding the assembly.

Alternatively, we can increase φ_1 and partially expand the pattern as in *F*, until we reach *G* when every second pair of panels expands fully and becomes colinear, i.e. their dihedral angles become 180°. This time, however, further motion does not include intersections, nor is it theoretical. Therefore, *G* is not a boundary state but a bifurcation point, at which the creases with angles equal to 180° can reverse their MV assignment.

If the motion continues, some mountains become valleys and vice-versa, and the assembly reaches new shapes *H* and *I*. At this stage, the pattern again partially folds, and *I* becomes a boundary state. Moreover, we can again switch our active input. By disabling φ_1 and decreasing φ_3, we can reconfigure the assembly into a new fully folded form, *J*. This shows how the alternative motion possible thanks to two DOFs can not only decouple the folding process but also reconfigure the pattern into an alternative folded form that was previously unavailable. As a result, the Arc pattern does not have to produce a curved loop-like shape, but its panels can arrange in the folded form along a straight line.

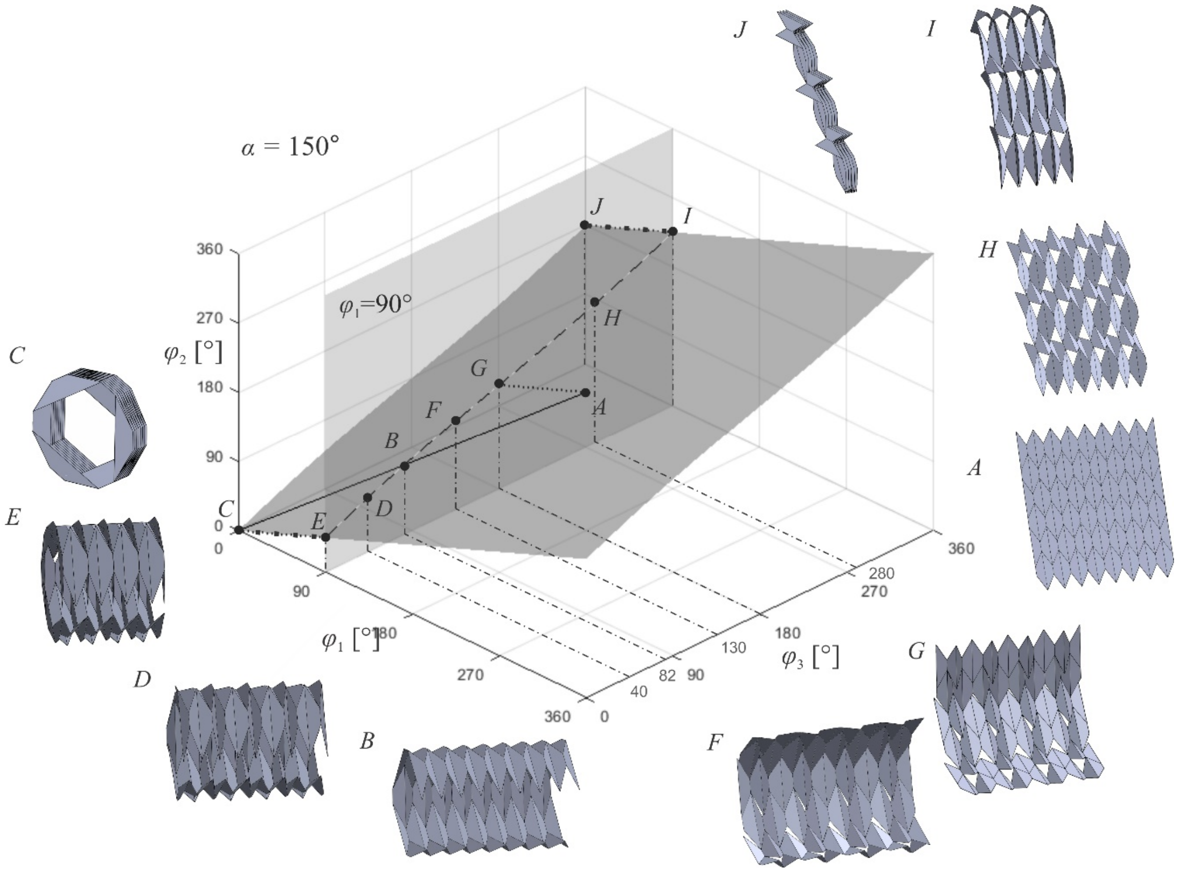

Fig. 7.19 A 3D plot of all theoretically possible configurations of the two-DOF Arc pattern; *A*, *B* and *C* are stages on the traditional folding curve; *D* to *J* are new forms on alternative motion 2 path, activated by freezing φ_1 and changing φ_3.

Similar reconfiguration can also be exercised with alternative motion 2, Fig. 7.19. The path is analogous, but the resulting configurations are slightly different. In point *B*, we freeze φ_1 and decrease φ_3 to again partially fold the pattern, *D*, until a boundary semi-folded form is achieved, *E*. Further motion includes negative dihedral angles, i.e. intersections. Here, we can switch inputs to go from *E* to *C*, bypassing the traditional folding.

Alternatively, we can increase φ_3 and go via *F*. At the same time, the pattern partially expands until some of the folds become flat, *G*. At this point, the MV assignment can be shifted again, and the motion continues via *H*, until *I* when partially folded assembly locks due to panel collisions. In this boundary state, we can again switch inputs to obtain an alternative folded form, *J*. The panels align in a straight line instead of forming a loop again.

Notice that similarly to Anisotropic Miura, the Arc pattern's slits also point in opposite directions due to its geometry, as we can see in Fig. 7.17. As a result, the alternative motions allowed by the new DOFs decouple the folding and cause the pattern to partially fold or expand but do not visibly alter the curvature along the vertical direction.

For this pattern, we do not report investigations of the version with slits along vertical creases. The pattern is too short, with a maximum of six rows of panels to ensure folding into a closed hexagonal form, as in *C*. More panels vertically would cause collisions while folding traditionally. Moreover, this pattern, similarly to Arc-Miura, has a natural curvature along the vertical direction. Adding vertical slits that cause a curvature horizontally would lead to similar problems that were encountered when reconfiguring large Arc-Miura with curvatures in both orthogonal directions.

As earlier, regular double slits along diagonal creases successfully added a new DOF and turned one-DOF assembly into a reconfigurable two-DOF kirigami. Even though the slits point in opposite directions and we cannot change curvature on a macro scale, we can successfully decouple the folding process and access new paths that give unfamiliar shapes, with some of them presented in Fig. 7.20 with a physical model.

Moreover, this time, we can switch some creases' MV assignment during the reconfiguration without collisions. That leads to a group of new shapes, ultimately folding the Arc pattern into alternative compact forms. In such shapes, the panels are arranged along a straight line, not in a loop. If we choose this folding, we avoid too many panel rows colliding during the process. As a result, the Arc pattern's size is not limited, and we could add many more panel rows as long as we avoid the traditional folded form, i.e. getting too close to point *C*. Instead, we should reverse the MV assignment and reconfigure for the alternative folded forms, *J*.

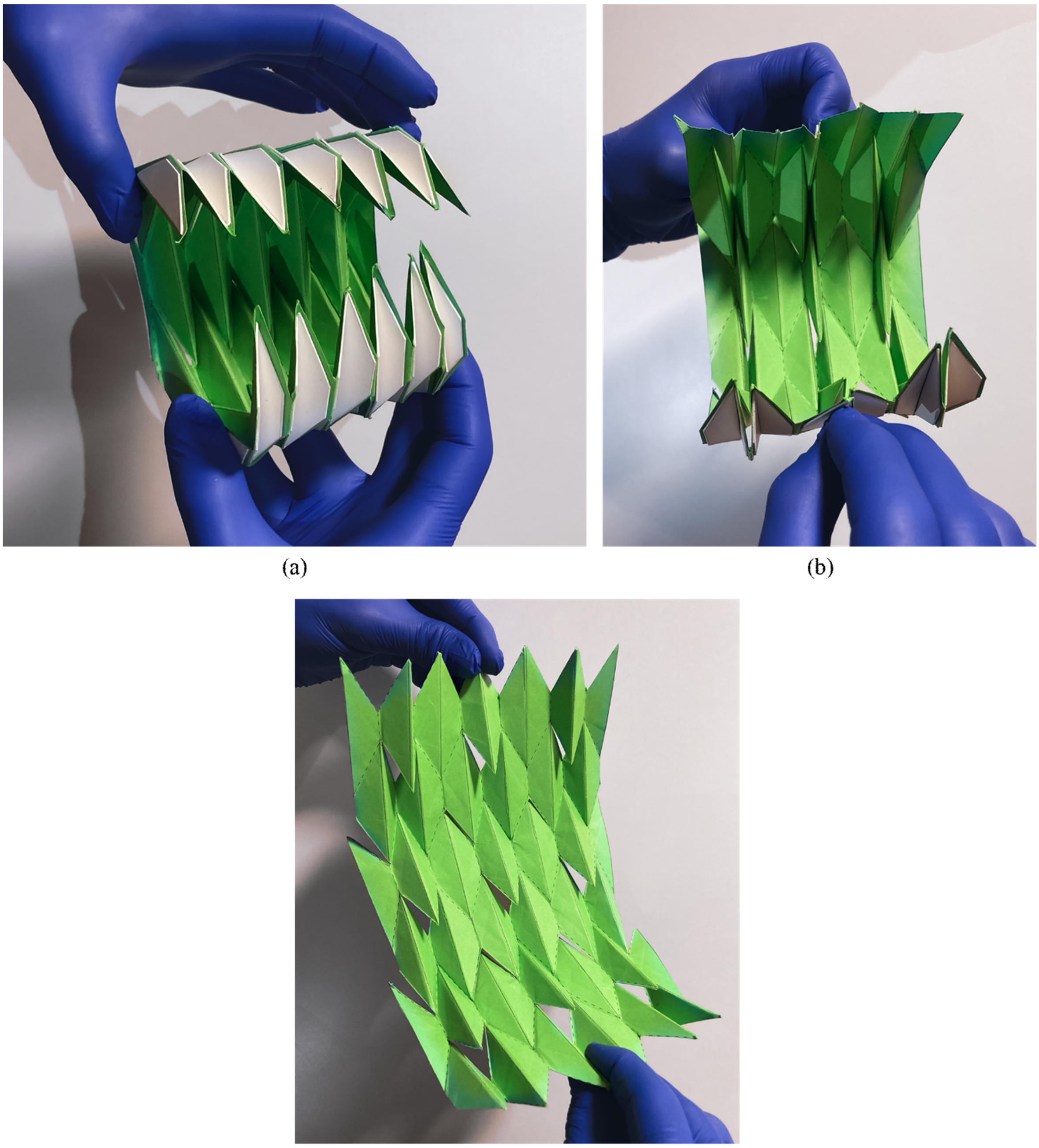
(a) (b)

(c)

Fig. 7.20 A physical model of a two-DOF Arc pattern from Fig. 7.17 but having 12x6 panels; (a) is a traditionally folded form; (b) and (c) are exemplary new configurations.

7.5 Summary

In this chapter, the slit arrangements identified for Miura-ori were successfully used on other tessellations, and new reconfigurable variants were found for each pattern. We showed that applying slits to various single-DOF rigid origami is an efficient way to add an extra DOF that changes a pattern's motion. Thus, tessellations that previously had only one folding method now have new motion paths leading to new forms. Moreover, they are relatively easy to achieve and control, thanks to keeping the DOFs number small, equal to two.

The examples in this chapter provided insights into the nature of these new reconfigurations. Moreover, we included some unsuccessful attempts to display limitations of the approach that often emerge from the patterns' specific geometries and kinematic specialities. This can be used as a reference point when judging what shapes to pursue or avoid while designing other reconfigurable kirigami patterns. This chapter's main novelty aspect is the successful modification of other single-DOF rigid-origami patterns, different from Miura-ori, and the subsequent identification of their two-DOF reconfigurable kirigami derivatives. Finally, the following chapter concludes the research and findings on the slit modifications of rigid origami presented in this thesis.

Chapter 8
Conclusions

8.1 Summary of the findings

The main objective of this project was to investigate if a kirigami approach of making cuts to rigid zero-thick traditional origami is an efficient way to increase DOFs and create new morphing structures that can exhibit unusual forms. Simultaneously, we were looking for particular slit arrangements that would ensure higher than one but small and finite DOF number, ideally equal to two. Having two inputs would keep the resulting structures' reconfiguration relatively straightforward. Below, we highlight the project's findings regarding these goals.

In the introductory chapter 3, we showed that a subassembly consisting of eight rigid panels and revolutes closed in a loop around a double slit is a spatial 8R linkage with two DOFs. As a result, it provided a promising building block for larger tessellations. Such elements derived from traditional Miura-ori pieces formed the basis of this research project. In chapter 3, we also examined how spherical 4R linkages can constrain higher-degree linkages and decrease DOFs. Therefore, they became a tool helping us control patterns' mobility when excessive DOFs needed removal to ensure that only two remain.

Next, in chapters 4 and 5, we used the 8R linkages derived from Miura-ori to build large patterns without the main emphasis on its final DOF number. Instead, regular layouts of two-crease-long slits were assumed to provide symmetrical and easy to replicate designs. Patterns obtained in this way turned out to be multi-DOF structures with locally variable shapes, controlled by separate inputs. This allowed the traditional rigid-origami version of Miura-ori to have numerous configuration and folded shape alternatives.

Such geometries, for example, could inspire new folded mechanical metamaterials that are tunable. A valuable feature of such architected materials is the ability to reconfigure them by different external inputs that lead to various functionalities (Overvelde et al. 2016, 2017) (Yang and You 2018). Origami has already inspired metamaterials at nano, micro or millimetre scale (Silverberg et al. 2014, 2015) (Yasuda and Yang 2015). Now, the kirigami approach opens a new branch for novel designs (Rafsanjani et al. 2019) (An et al. 2020) (Sun et al. 2021). For example, cutting zigzag (Eidini and Paulino 2015) or honeycomb (Neville et al. 2016) origami patterns has provided new cellular and morphing kirigami metamaterials. The reconfigurable Miura-ori variants from chapters 4 and 5 provide a family of novel foldable shapes potentially suggesting new variants of mechanical metamaterials.

Such reprogrammable structures could have various intriguing mechanical and physical properties. For example, variants with tunable positive and negative geometric (not strain-related) Poisson's ratios have been reported (Yasuda and Yang 2015) (Eidini and Paulino 2015). Geometries like this also allow compressive modulus programming (Silverberg et al. 2014) or, when many layers are stacked together, interesting dynamic responses, like energy absorption (Karagiozova et al. 2019) (Zhang et al. 2019) (Xiang et al. 2020, 2021). Moreover, they can even display tunable electromagnetic characteristics if resonant elements are incorporated (Nauroze et al. 2018). However, identifying and investigating such tunable properties that could potentially emerge from the reported reconfigurations fall outside this project's scope.

At a bigger scale, the new Miura-ori configurations could also provide unusual geometries for novel folded cores for sandwich-structured composites. Such origami-inspired cores can have distinct mechanical properties (Grzeschik et al. 2018). Often manufactured with rigid panels, they have displayed intriguing performance under quasi-static compression and impact load (Li et al. 2018a, 2018b) (Du et al. 2019) (Kshad et al. 2019). Some are even fabricated, for example, with shape-memory polymers to produce sandwich structures that are morphing (Kwon and Roh 2019). A foldcore based on a reconfigurable two-DOF pattern would have such morphing capabilities natural from the kinematic perspective. Moreover, additional DOFs provide significant optimisation flexibility when designing such composites (Muhs et al. 2018).

An exemplary shape with a potential for such applications is presented in Fig. 8.1. It was obtained using the slit arrangements from chapter 4. In this configuration, Miura-ori locks in a 3D structure with repeatable horizontal flanges. As a result, some of the panels align, and the body has a system of connected internal channels. Such new shapes may provide folded cores with all sorts of physical and structural properties. Similar kirigami-enabled geometries that self-lock in 3D structures have been found to have impressive load-to-weight ratios (Wang et al. 2020). However, the variety of forms possible to obtain with assemblies from chapters 4 and 5 is a topic for another discussion.


(a) (b) (c)

Fig. 8.1 (a) and (b) A physical model of a Miura-ori with one row of double vertical slits locked in an intermediate state resembling a folded core after the MV assignment of crease 5 is additionally reversed; (c) is a computational model but with two cell rows.

The reconfigurable Miura-ori could also be an inspiration for applications at bigger scales. For example, in civil engineering, reconfigurable origami designs have already been suggested for retractable and reconfigurable roofs (Filipov et al. 2019). Other ideas are kinetic architecture (Tachi 2011), which could shape-shift after the deployment thanks to extra DOFs, or smart origami façades. Their reconfigurability would allow changing building envelope's properties and thus environmental efficiency (ElGhazi and Mahmoud 2016) (Schultz and Katz 2018).

Moreover, in chapter 5, which assumed slits along the Miura-ori's diagonal creases, a kinematically interesting bifurcation point was identified. The pattern's building blocks could either continue their two-DOF motion or enter a new state with three-DOFs. For a multi-cell assembly, that meant a choice between the mobility of c+1 and 3c, where c is the number of 8R cells in a row. Such a significant DOF jump allowed Miura-ori to obtain a group of additional metamaterial- or tube-like shapes.

Increased reconfiguration choices like this are a valuable feature in novel robotic and material applications. Rigid surfaces with many DOFs, like the ones reported, could have enough freedom to adjust to variously-shaped geometries, which could be helpful in new haptic tool design (Chang et al. 2020) (Giraud et al. 2021). Also, many input and thus shape alternatives may expand robotic functionality, locomotion, or help with self-assembly (Gardiner 2009) (Felton et al. 2014) (Wu et al. 2021b). Multiple stable origami states are also appreciated in mechanical computing, where they help assign logic values (Yasuda et al. 2021). Having more alternative configurations could boost such machines' performance.

Moreover, the different tubular forms reported in the thesis could be valuable for particular applications. For example, origami tubes with reconfigurable cross-sections have been suggested for efficient structural elements in civil engineering (Filipov et al. 2016, 2019). Moreover, they often have unusual, yet to be discovered properties, which may suggest unique applications. For example, Yasuda et al. (2019) proposed a material made of tubular origami that could turn compression into tension under impact. Origami tubes have also been suggested in other disciplines, e.g. for minimally-invasive surgical devices (Kuribayashi et al. 2006) (You and Kuribayashi 2009), crawling robots (Okuya et al. 2018) or space habitation modules (Morgan et al. 2016). The reconfigurability from a flat Miura-ori into tubular forms could provide new exciting applications or develop the previous ones.

To conclude, we achieved one of the main research objectives in chapters 4 and 5. We confirmed that regular cuts made to a standard zero-thick rigid origami provided it with new forms and folded shapes that were previously impossible. However, while the available alternative configurations grew exponentially as the patterns got large, the resulting assemblies did not have finite DOFs. This made their control problematic, even though we confirmed that all the extra DOFs acted on the structures locally, which limited the manipulation complexity. The search for infinitely large kirigami patterns that could reconfigure into new forms but using only two DOFs continued.

Therefore, in chapter 6, we changed the approach to using the building blocks. This time, we focused on joining them together in a kinematically aware manner to ensure patterns with a final DOF number of two. This produced unsymmetric Miura-ori versions with irregular slits but finite mobility and without overconstraint. Moreover, we realised that cuts could be divided into two groups. Some actively contributed to new motions and opened up during the reconfiguration. Meanwhile, the geometry forced the others to stay inactive during the motion. As a result, they only removed redundant hinges. This means that two uses of slits along the creases of rigid zero-thickness overconstrained patterns were identified. One is to add new DOFs to enable new motions, and the second is to decrease overconstraint without changing the motion.

Having decided to keep only the active slits contributing to the motion, we brought back some of the hinges what overconstrained the assembly. As a result, its theoretically-calculated mobility turned negative. However, the active slits that remained now formed regular cutting patterns and were enough to maintain the two-DOF motion, even though mobility formulas stated otherwise. Moreover, the regular two-DOF slit arrangements could be easily repeated symmetrically to build infinitely large patterns. They would keep the new motions without increasing DOFs.

Patterns with regular two and three-crease-long slits found in chapter 6 allowed reconfigurations that were previously impossible under rigid origami assumptions. Thanks to slits, new rigid kirigami Miura-ori variants were possible, capable of two easily controlled motion types. One is the traditional in-plane folding from a flat sheet into the standard compact form. Second is a set of new out-of-plane motions producing curved shapes that were previously impossible with rigid panels, i.e. no facet deformation. Research states that obtaining such out-of-plane forms with the typical Miura-ori must involve flexible panels. High panel to fold stiffness ratio, i.e. the rigid origami assumptions, reduce Miura-ori's behaviour to the in-plane folding (Schenk and Guest 2011, 2013) (Liu and Paulino 2017).

Some researchers even looked into alternative ways to achieve Miura-ori's out-of-plane shapes. For example, Grey et al. (2021) suggested using networks of multiple actuators distributed on the pattern's surface to achieve its bending or twisting. However, such an approach confirmed that non-uniform angles, thus facet deformations, are required. Alternatively, to achieve the out-of-plane configurations, redesigning the original crease pattern and creating custom layouts have been suggested (Grey et al 2021) (Hayakawa et al. 2021). While not requiring panel bending, such derivative patterns, unfortunately, lose the crease collinearity and regularity, and ultimately the capacity to fold in the traditional way.

In our project, by using slits, we obtain curved shapes with Miura-ori without having to deform its panels or relying on crease patterns that produce curvature, e.g. Arc Miura. We do not have to change the crease pattern's geometry with our kirigami approach, and we can keep using the same panels. We achieve the deformation-free out-of-plane bending by using fewer joints but strategically placed. Moreover, we do not sacrifice the traditional in-plane folding.

Such bent-like forms without facet deformations could inspire new structural designs. Some of the ideas may revolve around applications that benefit from varying geometries while avoiding unwelcome material strain. For example, the reconfigurable two-DOF pattern as in Fig. 6.14 could provide a framework for deployable antennas or reflective arrays. A symbolic solution for such a structure is presented in Fig. 8.2. First, it could compactly fold for a launch, Fig. 8.2(a) and then deploy in orbit into the traditional form, Fig. 8.2(b). Then, the structure could be reconfigured into a curved shape, Fig. 8.2(c), i.e. achieve a particular serviceability mode, avoiding deformations to the underlying kirigami frame.

It has been shown that origami reconfiguration allows manipulating acoustic (Pratapa et al. 2018) (Zou and Harne 2019) and electromagnetic (Nauroze et al. 2018) waves, e.g. achieving a higher bandwidth. Moreover, Williams et al. (2020) suggested origami-inspired phased arrays that could have diverse radiation patterns thanks to reconfigurability.

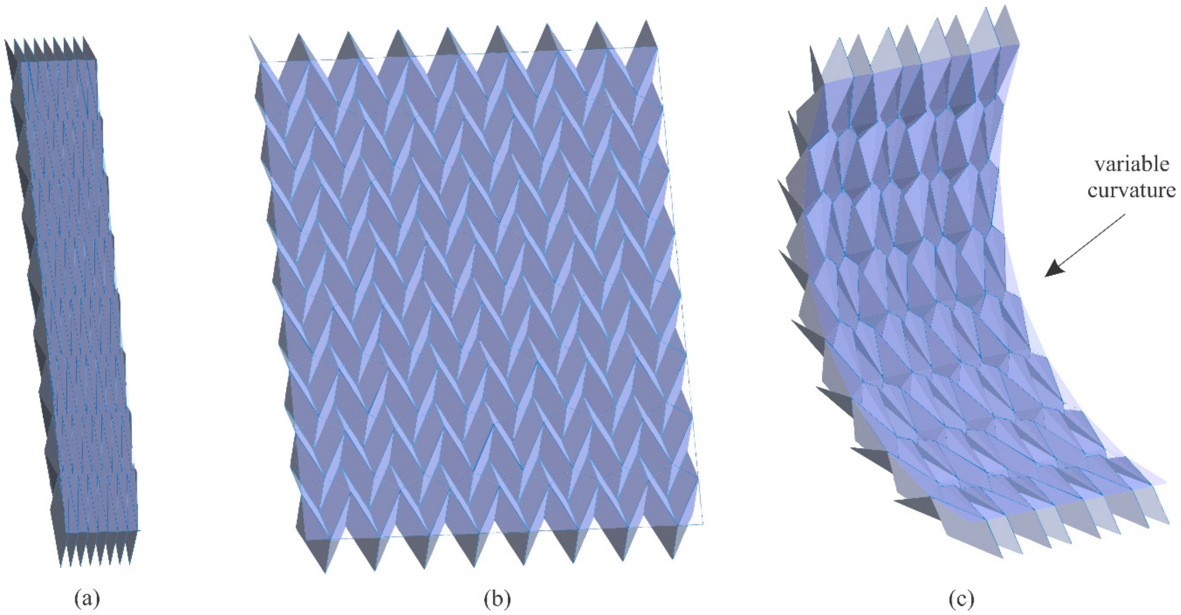

Fig. 8.2 A schematic design of a deployable and reconfigurable space antenna inspired by two-DOF rigid kirigami Miura-ori; (a) is the packaged form; (b) the deployed one; (c) is the antenna reconfigured into an arched shape with a variable curvature.

Compared with only deployable applications, the two-DOF kirigami could additionally reconfigure between forms with different curvatures. This would allow swiftly changing the spacecraft's operational mode once deployed, using only a single actuator.

The benefits of traditional patterns becoming rigidly-bendable could also be used during manufacturing processes. For example, research has shown that kirigami is an efficient tool to manufacture cellular- and meta-materials (Chen et al. 2014) (Neville et al. 2016) (Broccolo et al. 2017) (Calisch and Gershenfeld 2018), or fold cores (Hou et al. 2014) (Kwon and Roh 2019) out of flat sheets. Moreover, it is also used to fabricate nano and microscale 3D shapes (Chen et al. 2020), or structures with embedded electronics (Yamaoka et al. 2019).

For example, a rigid-panel pattern that can reconfigure out of plane could ease the production of stacks of single layers as in Fig. 8.3(a). So far, if engineers want to avoid deformations when manufacturing structures out of patterns that reconfigure only in-plane, they must ensure all connections between different layers at the same time, as some edges touch simultaneously. With an out-of-plane shape, a top layer could be bent away from the bottom one, Fig. 8.3(b), so that the connecting medium could be applied step-wise, only to

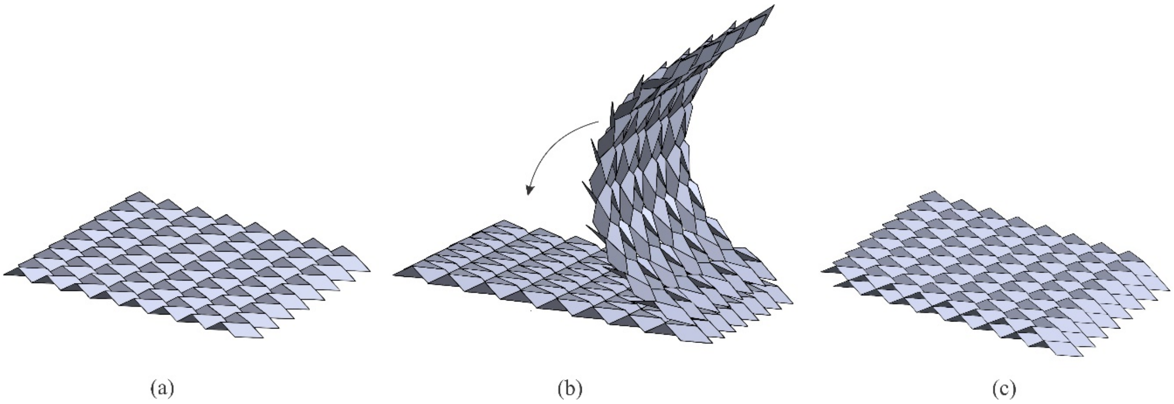

Fig. 8.3 An exemplary approach to manufacture multi-layer stacks of rigid-panel Miura-ori; (a) is a single layer; (b) are two layers being connected, with the upper one bent to obtain access to internal edges; (c) is the final two-layer stack.

a part that touches the bottom layer at a given time. Then, while the upper layer gradually goes from a curved form to a flat one, the other fragments could be joined until it produces the final stack as in Fig. 8.3(c).

To conclude, chapter 6 helped us achieve our other main research objectives. While the identified slit arrangements still allowed new unique shapes and turned Miura-ori into a reconfigurable structure, this time, the number of DOFs has been successfully kept low, at a finite value of two, no matter how large the pattern was. This made the control of such assemblies straightforward, even when assuming infinitely large Miura-ori pieces with slits. Therefore, in the final chapter, we tackled the remaining research question.

Chapter 7 investigated whether the determined slit arrangements could be used with other zero-thick rigid origami tessellations that traditionally also comprise only four-crease vertices. We applied the slit layouts producing two-DOF assemblies to four other patterns that exhibit only one-DOF motions in their rigid origami versions, similarly to Miura-ori. To represent the first group, whose rigid motion is also in-plane, we chose Anisotropic Miura, a four-crease-vertex tessellation derived from the Snake pattern, and a popular Eggbox pattern. The second group, whose traditional one-DOF folding includes curved shapes, was represented by Arc Miura and Arc patterns.

While the slit arrangements identified when working with Miura-ori yielded mixed results, at least one of the cut variants always turned out to be successful for each investigated pattern. Furthermore, all tested tessellations were successfully turned from rigidly foldable one-DOF assemblies into rigidly reconfigurable structures capable of new forms, which are easy to control with only two inputs.

8.2 Future work

While the project's objectives have been accomplished, many new questions emerged throughout the research. Possible future work can be already identified at this stage.

One group of challenges could focus on investigating other slit variants on Miura-ori. The cutting patterns determined so far allowed the pattern with rigid facets to fold in-plane and bend out of it. Further investigations could be done into imitating Miura-ori's twisting under the rigid origami assumptions, which we know is currently impossible (Schenk and Guest 2011, 2013). One way of achieving this could assume using corner or zigzag cuts, like the ones shown in Fig. 8.4(a), along both vertical and diagonal slits. Such slits indeed trigger motions that reconfigure Miura-ori into a twisted-like shape, as in Fig. 8.4(c). However, so far, a pattern doing this without panel intersections, with only a few DOFs to ensure easy control, has not been identified. The one in Fig. 8.4 has four DOFs, and its twisting motion would not be possible with a physical model due to panel collisions.

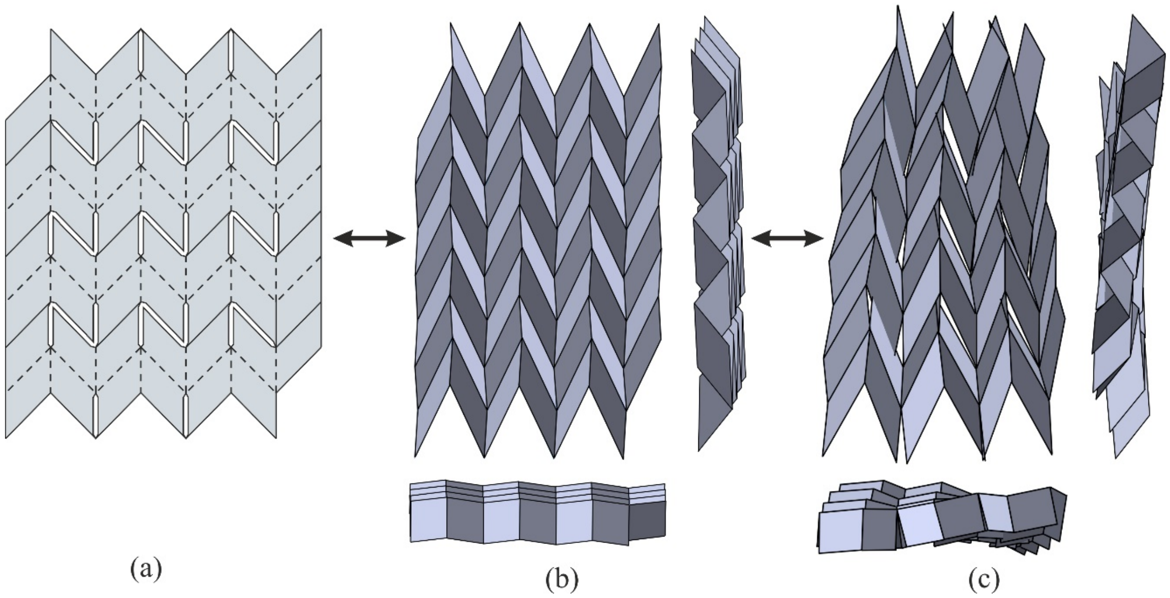

Fig. 8.4 A computational model of a rigid-panel zero-thick Miura-ori with corner and zigzag slits that allow twisting motions; (a) is the crease pattern; (b) is (a) folded into a conventional shape; (c) is (b) reconfigured into the twisted form.

More questions emerge when it comes to applying slits to other patterns. For example, the challenge of introducing motions that provide patterns with an extra curvature in the direction perpendicular to their traditional curvature, which was encountered in chapter 7 with Arc-Miura and Arc patterns, would be interesting to tackle. Also, many other four-crease vertex tessellations that we have not looked into remain.

For example, two out of four square twist pattern variants are reported to be rigidly foldable (Evans et al. 2015a) (Fang et al. 2020) and can be tessellated into larger assemblies that fold compactly, as shown in Fig. 8.5(a), (b), and (c). Slits could provide alternative folding approaches and compact forms, with an exemplary one presented in Fig. 8.5(d) and (e). So far, Fig. 8.5 shows only partially satisfactory results. We have performed the presented reconfiguration without panel collisions under rigid origami assumptions but with four or six DOFs, depending on the chosen slit arrangement. Such freedom makes the pattern's control unhandy. Reducing DOFs to two, unfortunately, brings panel intersections.

Another application of the kirigami approach would be to use slits not to allow new forms to patterns that are already rigidly foldable but experience a lack of alternatives, but to make folding possible for traditionally non-rigidly foldable geometries. For example, the two remaining non-rigidly foldable square twist types (Feng et al. 2020) or the square version of the Ron Resch pattern (van Knippenberg et al. 2016) (Callens and Zadpoor 2017) are known to have ineligible motions under rigid origami assumptions as due to their geometry, these patterns' folding sequences require deformations of panels.

To challenge this problem and make the unsuccessful square twist types fold rigidly, Feng et al. (2020) suggested making extra creases. Applying kirigami slits could similarly

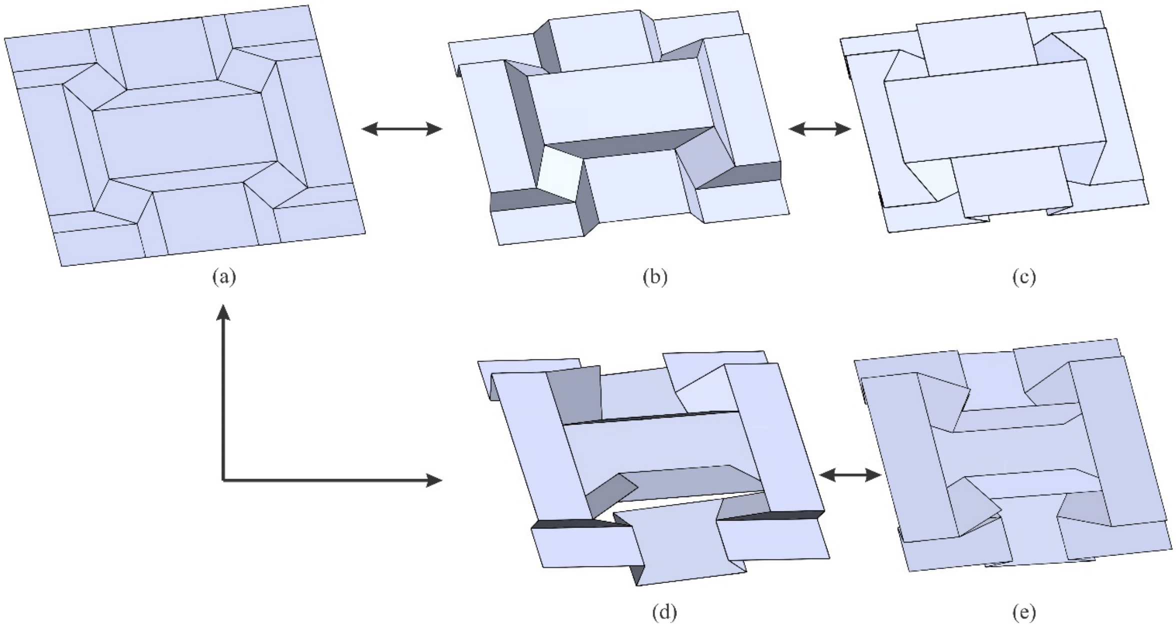

Fig. 8.5 (a) An exemplary tessellation of a rigidly foldable square twist type in its flat form; (b) and (c) present the standard one-DOF folding; (d) and (e) show an alternative folding possible thanks to slits.

add extra DOFs that would help overcome the kinematically challenging points and bridge the forbidden configurations, enabling rigid foldability. Simultaneously, Feng et al. (2020) have reported that MV alternations can make rigid-foldability possible. It is a promising research direction as this thesis showed that slits might allow MV assignment changes.

In conclusion, this research project successfully investigated the kirigami approach of modifying traditional origami patterns to obtain new reconfigurable structures. The identified assemblies continue complying with the rigid origami assumptions. Ensuring no facet deformation allows applications out of materials that are stiff or prone to strain-induced damage. Also, the specific geometric arrangement of revolutes results in assemblies with little DOFs, whose control is not complex.

Our investigations confirmed the research assumptions. We showed that slits are an efficient way to add extra DOFs to rigid origami, bringing new forms. Also, a cutting variant with a finite number of two DOFs is possible, ensuring simple manipulation between new configurations no matter the pattern's size. Moreover, this approach can be applied to different rigid-panel tessellations. It can increase their overall freedom by one DOF, avoiding too complex input requirements, and make previously unavailable motions and folded shapes possible.

The main finding of the research project and its novel input is the successful modification of traditionally only one-DOF rigid-panel origami into reconfigurable structures with precisely two DOFs, no matter the assembly size. Moreover, we hope the slit-modification process could be improved in the future. Currently, the variants with particular two-DOF kinematics are identified as they emerge naturally after the introduction of slits. For engineering applications, it would be desirable not only to enable but also to design the manner of reconfiguration and the final forms. However, the morphing structures reported already display exciting reconfiguration capabilities. Such novel forms may inspire new engineering applications, with a few suggestions mentioned in the dissertation.

A. Appendix to Chapter 4

Matrix method analysis of a cell with the double vertical slit.

In this appendix, we derive the kinematic equations of the linkage in Fig. A1, under Denavit-Hartenberg's notation.

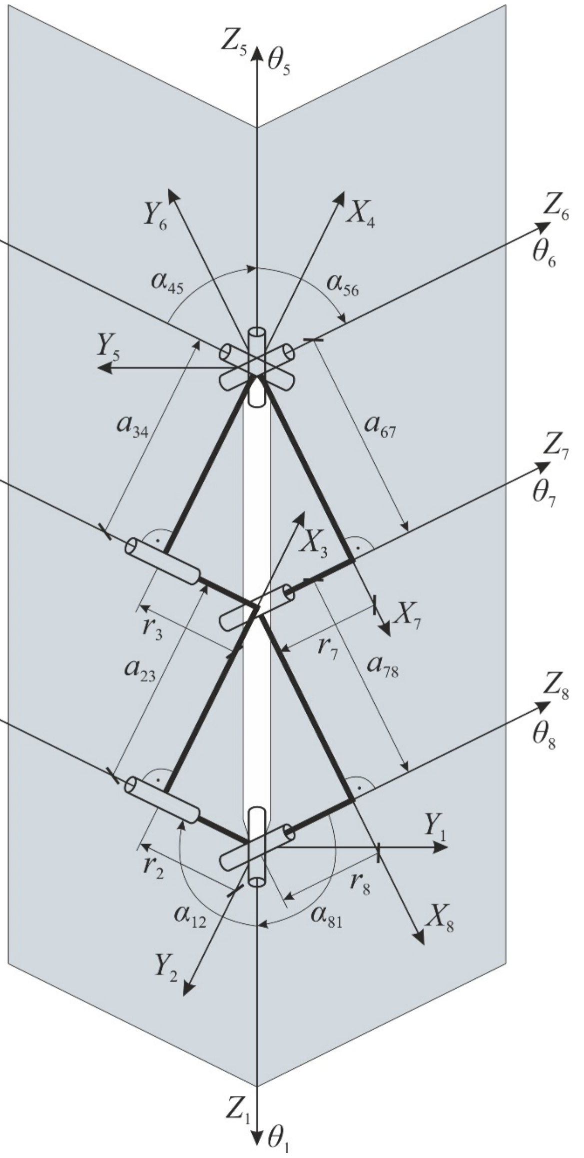

Fig. A1 A mechanical-linkage model of a single cell with the double vertical slit.

First, we list the linkage's constants, which satisfy

$$a_{12} = a_{45} = a_{56} = a_{81} = 0, \tag{A1}$$

$$a_{23} = a_{34} = a_{67} = a_{78} = L_1 \cdot \sin(\alpha), \tag{A2}$$

$$\alpha_{23} = \alpha_{34} = \alpha_{67} = \alpha_{78} = 0, \tag{A3}$$

$$\alpha_{45} = \alpha_{56} = \pi - \alpha, \;\; \alpha_{81} = \alpha_{12} = \alpha, \tag{A4}$$

$$r_1 = r_4 = r_5 = r_6 = 0, \tag{A5}$$

$$r_2 = r_3 = -L_1 \cdot \cos(\alpha) \text{ and } r_7 = r_8 = L_1 \cdot \cos(\alpha). \tag{A6}$$

Notice that parameter α that describes the twist angles is always bigger than 90°.

Then, we write transfer matrices for every pair of the consecutive revolute joints. A transfer matrix [T$_{i(i+1)}$] transforms coordinates of an arbitrary point P in the coordinate system of joint i to its coordinates in the system of joint $i+1$, and is

$$\left[T_{i(i+1)}\right] = \begin{bmatrix} 1 & 0 & 0 & 0 \\ -a_{i(i+1)} & C\theta_i & S\theta_i & 0 \\ -r_i S\alpha_{i(i+1)} & -C\alpha_{i(i+1)}S\theta_i & C\alpha_{i(i+1)}C\theta_i & S\alpha_{i(i+1)} \\ -r_i C\alpha_{i(i+1)} & S\alpha_{i(i+1)}S\theta_i & -S\alpha_{i(i+1)}C\theta_i & C\alpha_{i(i+1)} \end{bmatrix}, \text{ where } P = \begin{bmatrix} 1 \\ X_{Pi} \\ Y_{Pi} \\ Z_{Pi} \end{bmatrix}. \tag{A7}$$

Here, S and C are sine and cosine, respectively. We substitute (A1) to (A6) into (A7) to obtain transfer matrices relevant for the analysed linkage.

Next, we assume a coordinate transformation that continues between all the joints' coordinate systems and makes a complete loop around the linkage, returning to the starting point. The product of such transformation is a 4 × 4 unit matrix **I** –

$$[T_{81}][T_{78}][T_{67}][T_{56}][T_{45}][T_{34}][T_{23}][T_{12}] = \mathbf{I}. \tag{A8}$$

Relationship (A8) is the closure equation of the linkage in Fig. A1 in the matrix form. The left-hand side of (A8) is a 4 × 4 matrix with complex coefficients consisting of many trigonometric functions. Knowing that

$$\left[T_{i(i+1)}\right]=\left[T_{(i+1)i}\right]^{-1}, \tag{A9}$$

we multiply (A8) by inverse matrices of half of the left-hand side matrices to get

$$[T_{45}][T_{34}][T_{23}][T_{12}]=[T_{65}][T_{76}][T_{87}][T_{18}]. \tag{A10}$$

In this way, we turn an entire loop around the linkage into two paths in opposite directions, which are less problematic for calculations. They both start at joint 1 and meet at joint 5, but one goes along the left-hand side of the linkage, through joints 2, 3 and 4, and the second one along the right-hand side, via joints 8, 7, and 6.

Both sides of (A10) are 4 × 4 matrices, and we can start equating their coefficients to obtain individual closure equations. First, by comparing coefficients (4,4) we learn that the linkage's variables satisfy

$$\cos\left(\theta_2+\theta_3+\theta_4\right)=\cos\left(\theta_6+\theta_7+\theta_8\right). \tag{A11}$$

Then, from coefficients (4,3) we find that

$$\frac{\tan\left(\dfrac{\theta_1}{2}\right)}{\tan\left(\dfrac{\theta_2+\theta_3+\theta_4}{2}\right)}=-\cos(\alpha). \tag{A12}$$

Similarly, equating coefficients (3,4) gives

$$\frac{\tan\left(\dfrac{\theta_5}{2}\right)}{\tan\left(\dfrac{\theta_6+\theta_7+\theta_8}{2}\right)}=\cos(\alpha). \tag{A13}$$

Next, we compare (A12) with (A13). As we do this, we express tangents in the denominators as sines over cosines. Then, we take the square of both sides of the equation what gives

$$\frac{\tan^2\left(\dfrac{\theta_1}{2}\right)\cdot\cos^2\left(\dfrac{\theta_2+\theta_3+\theta_4}{2}\right)}{\sin^2\left(\dfrac{\theta_2+\theta_3+\theta_4}{2}\right)}=\frac{\tan^2\left(\dfrac{\theta_5}{2}\right)\cdot\cos^2\left(\dfrac{\theta_6+\theta_7+\theta_8}{2}\right)}{\sin^2\left(\dfrac{\theta_6+\theta_7+\theta_8}{2}\right)}. \tag{A14}$$

All squared sines and cosines of the sums of the halves of the angles in (A14) can be expressed, using trigonometric identities, as functions of cosines of the sums of full angles. Bearing in mind (A11), (A14) turns into a more straightforward equation, i.e.

$$\tan^2\left(\frac{\theta_1}{2}\right)=\tan^2\left(\frac{\theta_5}{2}\right). \tag{A15}$$

As θ's have values from $\langle 0,2\pi\rangle$, for the analysed geometry, the above gives

$$\theta_5=-\theta_1+2\pi\ . \tag{A16}$$

The second solution of (A15), which is

$$\theta_5=\theta_1, \tag{A17}$$

only applies when crease 5 is not a valley but also, like crease 1, a mountain fold. It is a case we do not analyse in chapter 4. Further calculations assume (A16), i.e. crease 5 having a different MV assignment from crease 1. If the creases are simultaneously mountains or valleys, (A17) should be used instead. To continue, we compare coefficients (3,3) and substitute (A16) into the equation to learn that

$$\sin\left(\theta_2+\theta_3+\theta_4\right)=\sin\left(\theta_6+\theta_7+\theta_8\right). \tag{A18}$$

At this stage of the analysis, we have three independent closure equations: (A12), (A13) and (A16). The remaining (A11) and (A18) can be derived from the above ones. Moreover, the matrix coefficients from columns 2, 3 and 4 do not provide any new relationships. We find the remaining three in the first column.

By equating coefficients (2,1), we find that

$$\begin{aligned}&\cos\left(\theta_4\right)+\cos\left(\theta_3+\theta_4\right)+\cos\left(\theta_1\right)\left(\cos\left(\theta_6\right)+\cos\left(\theta_6+\theta_7\right)\right)\\&-\cos\left(\alpha\right)\sin\left(\theta_1\right)\left(2+\sin\left(\theta_6\right)+\sin\left(\theta_6+\theta_7\right)\right)=0\end{aligned}\ . \tag{A19}$$

Coefficients (3,1) give

$$\begin{gathered}\sin(\theta_1)\left(\cos(\theta_6)+\cos(\theta_6+\theta_7)\right)+\\ \cos(\alpha)\left(2-\sin(\theta_4)-\sin(\theta_3+\theta_4)+\cos(\theta_1)\left(2+\sin(\theta_6)+\sin(\theta_6+\theta_7)\right)\right)=0\end{gathered}. \tag{A20}$$

And, from coefficients (4,1), we get

$$\sin(\theta_4)+\sin(\theta_3+\theta_4)+\sin(\theta_6)+\sin(\theta_6+\theta_7)=0. \tag{A21}$$

Both coefficients (1,1) are equal to 1.

To sum up, we have six independent closure equations that describe the kinematics of the Miura-ori cell with the double vertical slit. They contain eight variables, θ_1 to θ_8. If we choose two of them and specify their values, (A12), (A13), (A16), (A19), (A20) and (A21) can be solved for the remaining ones. This tells us the assembly has a shape defined by two inputs and proves the linkage has two DOFs. It is worth mentioning that the number of independent equations could be verified by Jacobian matrix ran analysis, but this falls outside the scope of this work. Notice that the equations contain only parameter α and are free from constant L_1. This means the results are scale-independent.

All the above closure equations are expressed by θ's. However, to make the results more intuitive, we can use φ's instead, i.e. the linkage's dihedral angles. For the analysed case, the relationships between these two types of kinematic variables are

$$\begin{gathered}\theta_1=\pi-\varphi_1,\ \theta_2=\frac{\pi}{2}-\varphi_2,\ \theta_3=\pi+\varphi_3,\ \theta_4=\frac{3}{2}\pi-\varphi_4,\\ \theta_5=\pi+\varphi_5,\ \theta_6=\frac{\pi}{2}-\varphi_6,\ \theta_7=\pi+\varphi_7\ \text{ and }\ \theta_8=\frac{3}{2}\pi-\varphi_8.\end{gathered} \tag{A22}$$

If we substitute (A22) into the previous relationships, we obtain a new set of six closure equations expressed with φ's. They can be used to investigate and depict the linkage's kinematics and are as follows.

$$\varphi_5=\varphi_1, \tag{A23}$$

$$\frac{\tan\left(\frac{\varphi_2-\varphi_3+\varphi_4}{2}\right)}{\tan\left(\frac{\varphi_1}{2}\right)}=-\cos(\alpha),\quad \frac{\tan\left(\frac{\varphi_6-\varphi_7+\varphi_8}{2}\right)}{\tan\left(\frac{\varphi_5}{2}\right)}=-\cos(\alpha),\qquad \text{(A24), (A25)}$$

$$\begin{aligned}&\sin(\varphi_4)+\sin(\varphi_3-\varphi_4)+\cos(\varphi_1)\big(\sin(\varphi_6)-\sin(\varphi_6-\varphi_7)\big)\\&+\cos(\alpha)\sin(\varphi_1)\big(2+\cos(\varphi_6)-\cos(\varphi_6-\varphi_7)\big)=0\end{aligned},\qquad \text{(A26)}$$

$$\begin{gathered}\sin(\varphi_1)\big(\sin(\varphi_6)-\sin(\varphi_6-\varphi_7)\big)+\\ \cos(\alpha)\Big(2+\cos(\varphi_4)-\cos(\varphi_3-\varphi_4)-\cos(\varphi_1)\big(2+\cos(\varphi_6)-\cos(\varphi_6-\varphi_7)\big)\Big)=0\end{gathered}\qquad \text{(A27)}$$

and $$\cos(\varphi_4)-\cos(\varphi_3-\varphi_4)-\cos(\varphi_6)+\cos(\varphi_6-\varphi_7)=0\,. \qquad \text{(A28)}$$

The remaining secondary relationships, which result from (A23), (A24) and (A25) become

$$\cos(\varphi_2-\varphi_3+\varphi_4)=\cos(\varphi_6-\varphi_7+\varphi_8) \qquad \text{(A29)}$$

and $$\sin(\varphi_2-\varphi_3+\varphi_4)=\sin(\varphi_6-\varphi_7+\varphi_8)\,. \qquad \text{(A30)}$$

B. Appendix to Chapter 5

Matrix method analysis of a cell with the double diagonal slit.

Figure B1 shows a mechanical linkage equivalent to the cell with the double diagonal slit under the Denavit and Hartenberg's notation. We use the matrix method to derive its kinematic equations. The characteristic parameters are

$$\alpha_{12} = \alpha_{45} = \alpha_{56} = \alpha_{81} = 0, \tag{B1}$$

$$\alpha_{23} = \alpha_{78} = \alpha, \;\; \alpha_{34} = \alpha_{67} = \pi - \alpha, \tag{B2}$$

$$a_{12} = a_{45} = a_{56} = a_{81} = L_2 \cdot \sin(\alpha), \tag{B3}$$

$$a_{23} = a_{34} = a_{67} = a_{78} = 0, \tag{B4}$$

$$r_1 = r_2 = r_3 = r_5 = r_7 = r_8 = 0, \tag{B5}$$

$$r_4 = -L_2 \cdot \cos(\alpha) \;\text{ and }\; r_6 = L_2 \cdot \cos(\alpha). \tag{B6}$$

Notice that α continues to be an angle bigger than 90°.

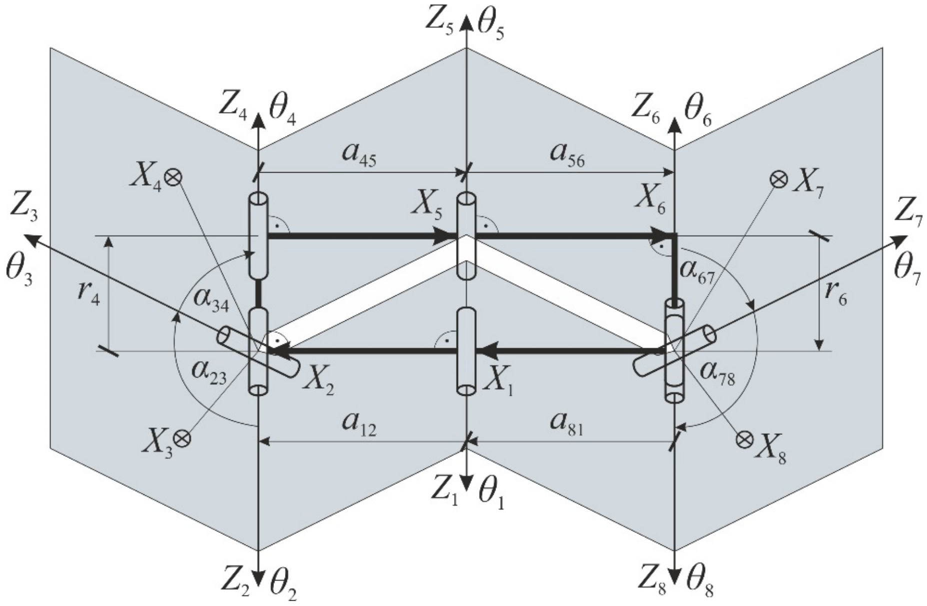

Fig. B1 A mechanical-linkage model of a single cell with the double diagonal slit.

Next, we write a transfer matrix for every consecutive pair of the revolute joints, i.e.

$$\left[T_{i(i+1)}\right]=\begin{bmatrix} 1 & 0 & 0 & 0 \\ -a_{i(i+1)} & C\theta_i & S\theta_i & 0 \\ -r_i S\alpha_{i(i+1)} & -C\alpha_{i(i+1)}S\theta_i & C\alpha_{i(i+1)}C\theta_i & S\alpha_{i(i+1)} \\ -r_i C\alpha_{i(i+1)} & S\alpha_{i(i+1)}S\theta_i & -S\alpha_{i(i+1)}C\theta_i & C\alpha_{i(i+1)} \end{bmatrix}, \text{ where } P=\begin{bmatrix} 1 \\ X_{Pi} \\ Y_{Pi} \\ Z_{Pi} \end{bmatrix}. \quad \text{(B7)}$$

If we substitute the parameters from (B1) to (B6) into (B7), we get eight matrices for our case. Then, we assume a continuous transformation that starts at joint 1, goes clockwise via joints 2, 3, 4, 5, 6, 7 and 8, and returns to joint 1. The product of such a looped operation is the same as the initial coordinates. Therefore, the transfer matrices, when multiplied, give

$$[T_{81}][T_{78}][T_{67}][T_{56}][T_{45}][T_{34}][T_{23}][T_{12}]=\mathbf{I}. \quad \text{(B8)}$$

Relationship (B8) is the linkage's closure equation in a matrix form. Since there is

$$\left[T_{i(i+1)}\right]=\left[T_{(i+1)i}\right]^{-1}, \quad \text{(B9)}$$

we decide to analyse the more approachable version of (B8), i.e.

$$[T_{45}][T_{34}][T_{23}][T_{12}]=[T_{65}][T_{76}][T_{87}][T_{18}]. \quad \text{(B10)}$$

Both sides of (B10) are 4 × 4 matrices. Next, we compare their coefficients to find the individual closure equations. We will repeat this for both general case and the linkage's special configuration, the rhombic state.

Part 1 – General Case

First, we equate both matrices' coefficients (4,4) and learn that

$$\cos(\theta_7)=\cos(\theta_3). \quad \text{(B11a)}$$

As creases 3 and 7 have the same MV assignment (in the analysed case, both are mountain fold types), (B11a) simplifies to

$$\theta_7=\theta_3. \quad \text{(B11b)}$$

Relationship (B11b) is the first individual closure equation. It tells us the angles at the diagonal creases are always equal. Next, we compare coefficients (4,3) and get

$$\cos(\alpha)\left(\cos(\theta_3)-1\right)\left(\cos(\theta_1+\theta_2)+\cos(\theta_8)\right)=\sin(\theta_3)\left(\sin(\theta_1+\theta_2)+\sin(\theta_8)\right). \qquad \text{(B12a)}$$

We use trigonometric identities to express sines and cosines above with tangents of halves of their arguments. After rearrangement, (B12a) becomes

$$\begin{gathered}\left[\tan\left(\frac{\theta_3}{2}\right)\right]\cdot\left[1+\tan\left(\frac{\theta_1+\theta_2}{2}\right)\tan\left(\frac{\theta_8}{2}\right)\right]\cdot\\ \left[-\tan\left(\frac{\theta_1+\theta_2}{2}\right)-\tan\left(\frac{\theta_8}{2}\right)+\tan\left(\frac{\theta_3}{2}\right)\cos(\alpha)\left(\tan\left(\frac{\theta_1+\theta_2}{2}\right)\tan\left(\frac{\theta_8}{2}\right)-1\right)\right]=0\end{gathered}. \qquad \text{(B12b)}$$

Three separate parts of (B12b) can satisfy the equation. The case when the first pair of the square brackets is zero is discussed in part 2 of appendix B. It describes the rhombic state. The second pair equal to zero also describes the cell's specific states, e.g. when θ_1 equals zero. Here, we focus on the third pair of the brackets. We assume it equals zero, rearrange it, and obtain the second closure equation. It expresses θ_3 with other variables and is

$$\tan\left(\frac{\theta_3}{2}\right)=\frac{-\tan\left(\frac{\theta_1+\theta_2+\theta_8}{2}\right)}{\cos(\alpha)}. \qquad \text{(B13)}$$

We repeat the steps for coefficients (3,4) and get similar equations:

$$\cos(\alpha)\left(\cos(\theta_3)-1\right)\left(\cos(\theta_5+\theta_6)+\cos(\theta_4)\right)=-\sin(\theta_3)\left(\sin(\theta_5+\theta_6)+\sin(\theta_4)\right), \qquad \text{(B14a)}$$

$$\begin{gathered}\left[\tan\left(\frac{\theta_3}{2}\right)\right]\cdot\left[1+\tan\left(\frac{\theta_5+\theta_6}{2}\right)\tan\left(\frac{\theta_4}{2}\right)\right]\cdot\\ \left[\tan\left(\frac{\theta_5+\theta_6}{2}\right)+\tan\left(\frac{\theta_4}{2}\right)+\tan\left(\frac{\theta_3}{2}\right)\cos(\alpha)\left(\tan\left(\frac{\theta_5+\theta_6}{2}\right)\tan\left(\frac{\theta_4}{2}\right)-1\right)\right]=0\end{gathered}. \qquad \text{(B14b)}$$

The third bracket from (B14b) gives the third closure equation, which is

$$\tan\left(\frac{\theta_3}{2}\right)=\frac{\tan\left(\frac{\theta_4+\theta_5+\theta_6}{2}\right)}{\cos(\alpha)}. \tag{B15}$$

Further comparison of coefficients from columns 2, 3, and 4 does not provide us with new relationships. However, we still have three equations from equating coefficients in columns number 1 (not four equations, as both coefficients (1,1) are equal to 1). First, we compare coefficients (4,1) and learn that

$$\cos(\alpha)\left(\cos(\theta_3)-1\right)\left(\sin(\theta_2)+\sin(\theta_8)\right)=-\sin(\theta_3)\left(\cos(\theta_2)+\cos(\theta_8)\right). \tag{B16a}$$

Trigonometric identities again let us find the tangent version of the equation, which is

$$\begin{gathered}\left[\tan\left(\frac{\theta_3}{2}\right)\right]\cdot\left[1+\tan\left(\frac{\theta_2}{2}\right)\tan\left(\frac{\theta_8}{2}\right)\right]\cdot\\ \left[\tan\left(\frac{\theta_2}{2}\right)\tan\left(\frac{\theta_8}{2}\right)-1+\tan\left(\frac{\theta_3}{2}\right)\cos(\alpha)\left(\tan\left(\frac{\theta_2}{2}\right)+\tan\left(\frac{\theta_8}{2}\right)\right)\right]=0\end{gathered}. \tag{B16b}$$

Again, the first pair of the square brackets equals zero when the assembly is in the rhombic state. This time, the third pair refers to a specific state, too. For example, if it is zero, it describes a configuration when θ_1 equals π. In (B16b), the second pair of the brackets describes a general case. We assume for further calculations that

$$1+\tan\left(\frac{\theta_2}{2}\right)\tan\left(\frac{\theta_8}{2}\right)=0, \tag{B17a}$$

Relationship (B17a) is the fourth closure equation. It can be rewritten into

$$\cos\left(\frac{\theta_2-\theta_8}{2}\right)\sec\left(\frac{\theta_2}{2}\right)\sec\left(\frac{\theta_8}{2}\right)=0. \tag{B17b}$$

As secants cannot be equal to zero, we have

$$\cos\left(\frac{\theta_2-\theta_8}{2}\right)=0. \tag{B17c}$$

If we solve (B17c), we obtain an alternative way to write the fourth closure equation, i.e.

$$\theta_8 = \begin{cases} \theta_2 + \pi & for \quad \theta_2 \le \pi \\ \theta_2 - \pi & for \quad \theta_2 \ge \pi \end{cases}. \tag{B17d}$$

We still have two more relationships that result from comparing coefficients (2,1) and (3,1). They are intricate and contain all variables. Due to the formatting limitations, they are not reported in this form. However, the already known equations can help us simplify them. First, we should compare coefficients (2,1) and find the equation's tangent form. This allows us to use (B11b), (B13), (B15) and (B17a), and substitute θ_3, θ_4, θ_7 and θ_8 out of the equation. We get a new relationship that contains only θ_1, θ_2, θ_5 and θ_6. We again use trigonometric identities, this time to return to the form with sines and cosines. We repeat the steps for the equation from coefficients (3,1). As a result, the last two relationships become

$$1+\cos\left(\theta_5\right)+\cos\left(\theta_2+\theta_5+\theta_6\right)+\cos\left(\theta_1+\theta_2+\theta_5+\theta_6\right)=0 \tag{B18}$$

and
$$\sin\left(\theta_5\right)+\sin\left(\theta_2+\theta_5+\theta_6\right)+\sin\left(\theta_1+\theta_2+\theta_5+\theta_6\right)=0\,. \tag{B19}$$

We can use them to express θ_5 and θ_6 with θ_1 and θ_2. We use Pythagorean trigonometric identity to substitute (B19) into (B18) to learn it is also true that

$$1+\cos\left(\theta_1\right)+\cos\left(\theta_2+\theta_5+\theta_6\right)+\cos\left(\theta_1+\theta_2+\theta_5+\theta_6\right)=0\,. \tag{B20}$$

We compare (B20) and (B18), and notice that to satisfy both equations there must be

$$\cos\left(\theta_5\right)=\cos\left(\theta_1\right). \tag{B21}$$

It is the fifth closure equation, which for our case gives

$$\theta_5 = 2\pi - \theta_1 \;\text{ or }\; \theta_5 = \theta_1 \qquad \text{(B22a), (B22b)}$$

Notice these results describe two alternative geometries. Equation (B22a) applies when creases 1 and 5 have opposite MV assignments. This is true, for example, if we analyse the cell starting from the typical Miura-ori shape when crease 1 is a valley and crease 5 a mountain. We continue the calculations assuming this. However, once the cell reconfigures and the MV assignment changes so that creases 1 and 5 are both valleys, or mountains, (B22b) should be used instead. The calculations that follow should be adjusted accordingly.

Having the relationship for θ_5, we can return to (B18) and (B19) and now define θ_6. Let us update both equations with (B22a). As a result, we get

$$1+\cos(\theta_1)+\cos(\theta_1-\theta_2-\theta_6)+\cos(\theta_2+\theta_6)=0 \tag{B23a}$$

and

$$\sin(\theta_1)+\sin(\theta_1-\theta_2-\theta_6)-\sin(\theta_2+\theta_6)=0. \tag{B23b}$$

We use trigonometric identities to find alternative forms, which are

$$4\cos\left(\frac{\theta_1}{2}\right)\cos\left(\frac{\theta_1-\theta_2-\theta_6}{2}\right)\cos\left(\frac{\theta_2+\theta_6}{2}\right)=0 \tag{B24a}$$

and

$$4\cos\left(\frac{\theta_1}{2}\right)\sin\left(\frac{\theta_1-\theta_2-\theta_6}{2}\right)\cos\left(\frac{\theta_2+\theta_6}{2}\right)=0. \tag{B24b}$$

There are only two relationships that satisfy both (B24a) and (B24b) simultaneously. The trigonometric functions in the middle, i.e. cosine and sine of $(\theta_1-\theta_2-\theta_6)/2$, cannot be equal to zero for the same arguments. Therefore, only two solutions remain. The first one, $\cos(\theta_1/2)$ equal to zero (θ_1 equal to π), is when the cell's middle part is folded. This is a specific, not a general configuration. Therefore, the second solution

$$\cos\left(\frac{\theta_2+\theta_6}{2}\right)=0 \tag{B25a}$$

is the sixth and the final closure equation. For our geometry, it solves into

$$\theta_6=\begin{cases}\pi-\theta_2 & for \quad \theta_2\le\pi \\ 3\pi-\theta_2 & for \quad \theta_2\ge\pi\end{cases}. \tag{B25b}$$

To sum up, the closure equations that describe the kinematics of the analysed linkage (when creases 1 and 5 have an opposite MV assignment) are

$$\theta_7 = \theta_3, \tag{B26a}$$

$$\tan\left(\frac{\theta_3}{2}\right) = \frac{-\tan\left(\frac{\theta_1+\theta_2+\theta_8}{2}\right)}{\cos(\alpha)}, \tag{B26b}$$

$$\tan\left(\frac{\theta_3}{2}\right) = \frac{\tan\left(\frac{\theta_4+\theta_5+\theta_6}{2}\right)}{\cos(\alpha)}, \tag{B26c}$$

$$\theta_8 = \begin{cases} \theta_2+\pi & for \quad \theta_2 \le \pi \\ \theta_2-\pi & for \quad \theta_2 \ge \pi \end{cases}, \tag{B26d}$$

$$\theta_5 = 2\pi - \theta_1 \tag{B26e}$$

and

$$\theta_6 = \begin{cases} \pi-\theta_2 & for \quad \theta_2 \le \pi \\ 3\pi-\theta_2 & for \quad \theta_2 \ge \pi \end{cases}. \tag{B26f}$$

There are eight variables θ_1 to θ_8 in six equations from (B26a) to (B26f). The values of at least two θ's must be assumed so that the remaining ones result from the closure equations. This confirms that the linkage has the mobility equal to two. Notice the relationships are independent of parameter L_2. This means the assembly, typically of origami, is scalable.

Moreover, we can find two supplementary relationships. They result from the closure equations and are not independent. However, they help us imagine the motion better, and are

$$\tan\left(\frac{\theta_2}{2}\right) + \tan\left(\frac{\theta_4}{2}\right) = 0 \quad \text{and} \quad \cos\left(\frac{\theta_4-\theta_6}{2}\right) = 0. \qquad \text{(B27a), (B27b)}$$

Or, when solved,

$$\theta_4 = 2\pi - \theta_2 \tag{B28a}$$

and

$$\theta_6 = \begin{cases} \theta_4+\pi & for \quad \theta_4 \le \pi \\ \theta_4-\pi & for \quad \theta_4 \ge \pi \end{cases}. \tag{B28b}$$

To get (B27a), we take (B26c) and substitute the information from (B26b), (B26d), (B26e) and (B26f). For (B27b), we substitute (B28a) into (B25a).

We again change the type of variables in the closure equations. Instead of θ's, we use φ's, i.e. dihedral angles between panels. The geometric relationships between θ's and φ's in the analysed case are

$$\theta_1 = \pi + \varphi_1,\ \theta_2 = \frac{3}{2}\pi - \varphi_2,\ \theta_3 = \pi - \varphi_3,\ \theta_4 = \frac{\pi}{2} + \varphi_4,\ \theta_5 = \pi - \varphi_5,$$

$$\theta_6 = \begin{cases} \varphi_6 - \frac{\pi}{2} & for\ \ \theta_6 \le \frac{3}{2}\pi \\ \frac{3}{2}\pi + \varphi_6 & for\ \ \theta_6 \ge \frac{3}{2}\pi \end{cases},\ \theta_7 = \pi - \varphi_7 \text{ and } \theta_8 = \begin{cases} \frac{\pi}{2} - \varphi_8 & for\ \ \theta_8 \le \frac{\pi}{2} \\ \frac{5}{2}\pi - \varphi_8 & for\ \ \theta_8 \ge \frac{\pi}{2} \end{cases}. \quad \text{(B29)}$$

We substitute (B29) into the six closure equations, i.e. (B26a) to (B26f). We obtain a new set of relationships that describe the kinematics. They are

$$\varphi_7 = \varphi_3. \quad \text{(B30a)}$$

$$\cot\left(\frac{\varphi_3}{2}\right) = \frac{\cot\left(\frac{\varphi_1 - \varphi_2 - \varphi_8}{2}\right)}{\cos(\alpha)}, \quad \text{(B30b)}$$

$$\cot\left(\frac{\varphi_3}{2}\right) = \frac{-\cot\left(\frac{\varphi_4 - \varphi_5 + \varphi_6}{2}\right)}{\cos(\alpha)}, \quad \text{(B30c)}$$

$$\varphi_8 = \varphi_2, \quad \text{(B30d)}$$

$$\varphi_5 = \varphi_1 \quad \text{(B30e)}$$

and

$$\varphi_6 = \varphi_2. \quad \text{(B30f)}$$

Equations (B29) can also be substituted into the secondary relationships (B28a) and (B28b) to learn the closure equations also mean that

$$\varphi_4 = \varphi_2 \text{ and } \varphi_6 = \varphi_4 \quad \text{(B31a), (B31b)}$$

Part 2 – Rhombic State

Now, we will examine the linkage's kinematics when it is in the rhombic state. The analysis starts like in Part 1. We equate both matrices' coefficients (4,4) and learn that (B11b) applies. Then, we move to coefficients (4,3) and get (B12b). This time, however, we assume the first pair of the square brackets satisfies the equation. There is

$$\tan\left(\frac{\theta_3}{2}\right)=0. \tag{B32}$$

We solve (B32) for our geometry. As (B11b) applies, we get

$$\theta_3=\theta_7=0. \qquad \text{(B33), (B34)}$$

Relationships (B33) and (B34) are the first two closure equations of the cell in the rhombic state. Both θ_3 and θ_7 equal to zero mean that diagonal folds are in the flat state.

Now, we can update both sides of (B10) with (B33) and (B34). They become

$$[T_{45}][T_{34}][T_{23}][T_{12}]=$$
$$=\begin{bmatrix} 1 & 0 & 0 & 0 \\ -L_2\sin(\alpha)\left(1+\cos(\theta_2-\theta_4)\right) & \cos(\theta_1+\theta_2-\theta_4) & \sin(\theta_1+\theta_2-\theta_4) & 0 \\ -L_2\sin(\alpha)\sin(\theta_2-\theta_4) & \sin(\theta_1+\theta_2-\theta_4) & -\cos(\theta_1+\theta_2-\theta_4) & 0 \\ L_2\cos(\alpha) & 0 & 0 & -1 \end{bmatrix} \tag{B35a}$$

$$[T_{65}][T_{76}][T_{87}][T_{18}]=$$
$$=\begin{bmatrix} 1 & 0 & 0 & 0 \\ L_2\sin(\alpha)\left(\cos(\theta_5)+\cos(\theta_5+\theta_6-\theta_8)\right) & \cos(\theta_5+\theta_6-\theta_8) & \sin(\theta_5+\theta_6-\theta_8) & 0 \\ L_2\sin(\alpha)\left(\sin(\theta_5)+\sin(\theta_5+\theta_6-\theta_8)\right) & \sin(\theta_5+\theta_6-\theta_8) & -\cos(\theta_5+\theta_6-\theta_8) & 0 \\ L_2\cos(\alpha) & 0 & 0 & -1 \end{bmatrix} \tag{B35b}$$

We find the rest of rhombic state's closure equations by comparing matrices (B35a) and (B35b). From equating coefficients in columns 2 and 3, we notice that

$$\cos\left(\theta_1+\theta_2-\theta_4\right)=\cos\left(\theta_5+\theta_6-\theta_8\right) \tag{B36a}$$

and
$$\sin\left(\theta_1+\theta_2-\theta_4\right)=\sin\left(\theta_5+\theta_6-\theta_8\right) \tag{B36b}$$

We use (B36a) and (B36b) to write an interim equation for θ_5, which is

$$\theta_5=\theta_1+\theta_2+\theta_8-\theta_4-\theta_6+2\pi k \text{ , where } k\in\mathbb{Z}\,. \tag{B37}$$

As columns 2 and 3 do not provide us with more information, we move to columns number 1. We compare coefficients (2,1) and obtain

$$1+\cos\left(\theta_2-\theta_4\right)+\cos\left(\theta_5\right)+\cos\left(\theta_5+\theta_6-\theta_8\right)=0\,. \tag{B38}$$

From coefficients (3,1) there is

$$\sin\left(\theta_2-\theta_4\right)+\sin\left(\theta_5\right)+\sin\left(\theta_5+\theta_6-\theta_8\right)=0\,. \tag{B39}$$

Now, we use Pythagorean trigonometric identity and combine (B38) with (B39) to eliminate functions of $\theta_2-\theta_4$. As a result, we get

$$1+\cos\left(\theta_5\right)+\cos\left(\theta_6-\theta_8\right)+\cos\left(\theta_5+\theta_6-\theta_8\right)=0\,. \tag{B40}$$

Then, using trigonometric identities, we separate θ_5 from $\theta_6-\theta_8$ and express sines and cosines with tangents of halves of the angles. This gives the third closure equation, which is

$$\tan\left(\frac{\theta_5}{2}\right)\tan\left(\frac{\theta_6-\theta_8}{2}\right)=1\,. \tag{B41}$$

We repeat the steps, but this time combine (B38) and (B39) to eliminate sine and cosine of $\theta_5+\theta_6-\theta_8$. We get a relationship similar to (B40), which is

$$1+\cos\left(\theta_5\right)+\cos\left(\theta_2-\theta_4\right)+\cos\left(\theta_2-\theta_4-\theta_5\right)=0\,. \tag{B42}$$

We separate $\theta_2-\theta_4$ from θ_5. The tangent version of (B42), the fourth closure equation, is

$$\tan\left(\frac{\theta_5}{2}\right)\tan\left(\frac{\theta_2-\theta_4}{2}\right)=-1\,. \tag{B43}$$

To continue, we take the closure equations (B41) and (B43) and find their alternative forms using trigonometric identities. They become

$$-\cos\left(\frac{\theta_5+\theta_6-\theta_8}{2}\right)\sec\left(\frac{\theta_5}{2}\right)\sec\left(\frac{\theta_6-\theta_8}{2}\right)=0 \tag{B44}$$

and
$$\cos\left(\frac{\theta_2-\theta_4-\theta_5}{2}\right)\sec\left(\frac{\theta_5}{2}\right)\sec\left(\frac{\theta_2-\theta_4}{2}\right)=0\,. \tag{B45}$$

In the above, only cosines can be equal to zero. If we solve (B44) and (B45), there is

$$\theta_8=\theta_5+\theta_6-\pi(4k_1-1) \text{ or } \theta_8=\theta_5+\theta_6-\pi(4k_1+1)\text{, where } k_1\in\mathbb{Z} \tag{B46}$$

and
$$\theta_2=\theta_4+\theta_5+\pi(4k_2-1) \text{ or } \theta_2=\theta_4+\theta_5+\pi(4k_2+1)\text{, where } k_2\in\mathbb{Z}. \tag{B47}$$

We can now substitute (B46) and (B47) into the interim equation (B37). It simplifies into the last closure equation. For our geometry, there is

$$\theta_5=2\pi-\theta_1 \tag{B48}$$

This completes the closure equations of the cell in the rhombic state. We rewrite them below:

$$\theta_3=\theta_7=0\,, \qquad \text{(B49a), (B49b)}$$

$$\tan\left(\frac{\theta_5}{2}\right)\tan\left(\frac{\theta_6-\theta_8}{2}\right)=1\,, \tag{B49c}$$

$$\tan\left(\frac{\theta_5}{2}\right)\tan\left(\frac{\theta_2-\theta_4}{2}\right)=-1\,, \tag{B49d}$$

and
$$\theta_5=2\pi-\theta_1\,. \tag{B49e}$$

Like earlier, the equations can be expressed with φ's instead of θ's. The relationships between these two types of variables remain as in (B29). We substitute them into (B49a) to (B49e) and get new closure equations that describe the kinematics with φ's, which are

$$\varphi_3=\varphi_7=\pi\,, \qquad \text{(B50a), (B50b)}$$

$$1+\cot\left(\frac{\varphi_5}{2}\right)\cot\left(\frac{\varphi_6+\varphi_8}{2}\right)=0\,, \tag{B50c}$$

$$1+\cot\left(\frac{\varphi_5}{2}\right)\cot\left(\frac{\varphi_2+\varphi_4}{2}\right)=0\,, \tag{B50d}$$

and $$\varphi_5 = \varphi_1 \tag{B50e}$$

There are still eight variables φ_1 to φ_8, but this time in five equations. This confirms that the cell in the rhombic state has three DOFs. We must input at least three angles so that the rest results from (B50a) to (B50e). For example, if we choose the value of φ_1, i.e. define the shape of the rhombus inside, this information, through (B50e), goes to (B50c) and (B50d). However, to fully define the cell's form, we need to add two more inputs, separately for (B50c) and (B50d). We should choose one angle from the pair φ_6 and φ_8, and one from φ_2 and φ_4. They specify the rotations of the cell's arms. Notice the equations remain independent of L_2. Additionally, (B50a) to (B50e) do not include geometric parameter α. This means the rhombic state's kinematics does not depend on the parallelograms' shape.

C. Appendix to Chapter 6

Removing inactive slits - motion compatibility calculations

The goal of the calculations in this appendix is to show how removing only inactive slits, i.e. bringing back redundant hinges, does not change a two-DOF pattern's kinematics.

First, Fig. C1(a) presents a part of the assembly from Fig. 6.6(a) without overconstraint and with both slit types, before removing the inactive ones, marked with (*). This time, to make calculations more straightforward, we assume two circled dihedral angles $\varphi_{1,A}$ and $\varphi_{2,A}$ to be our input variables defining the pattern's shape. The following analysis shows how subsequent angles adjust to the inputs and the motion transmits throughout the pattern. The goal is to estimate cell *B*'s output variable $\varphi_{7,B}$ marked in a box.

Using the cell's closure equations (5.1) to (5.6) we can express variable $\varphi_{7,A}$ with our inputs as below

$$\tan\left(\frac{\varphi_{7,A}}{2}\right)=\tan\left(\frac{\varphi_{3,A}}{2}\right)=\cos(\alpha)\cdot\tan\left(\frac{\varphi_{1,A}}{2}-\varphi_{2,A}\right) \tag{C1}$$

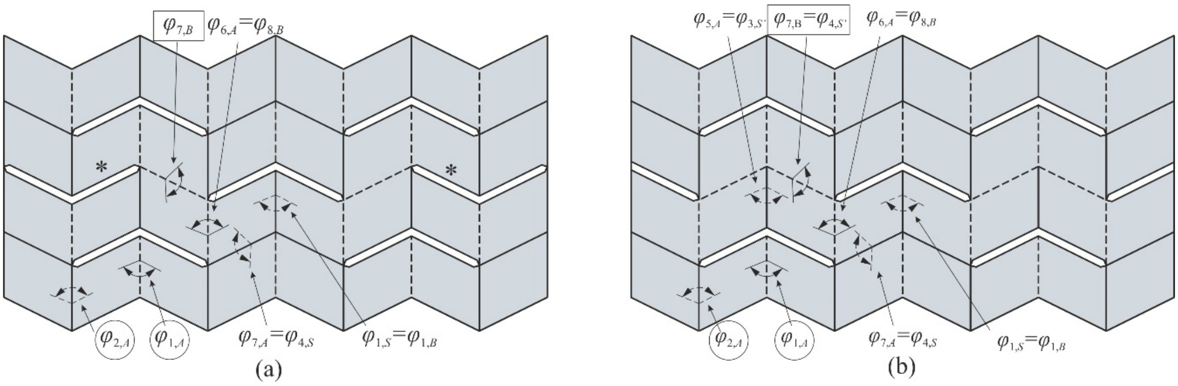

Fig. C1 (a) A fragment of a two-DOF Miura-ori with both active and inactive slits; (b) is (a) after the inactive slits (*) are removed and extra spherical 4R linkages created locally.

Angle $\varphi_{7,A}$ is simultaneously $\varphi_{4,S}$, a dihedral angle of a spherical 4R linkage adjacent to the cell from the right-hand side. Angle $\varphi_{4,S}$ becomes the spherical linkage's input that dictates its shape, due to its one-DOF nature, according to (2.12). Using these equations, we can express with our inputs spherical linkage's another angle $\varphi_{1,S}$, i.e.

$$\tan\left(\frac{\varphi_{1,S}}{2}\right)=-\frac{\tan\left(\frac{\varphi_{4,S}}{2}\right)}{\cos(\alpha)}=-\frac{\tan\left(\frac{\varphi_{7,A}}{2}\right)}{\cos(\alpha)}=-\tan\left(\frac{\varphi_{1,A}}{2}-\varphi_{2,A}\right). \tag{C2}$$

Angle $\varphi_{1,S}$ is simultaneously $\varphi_{1,B}$, one of the inputs to cell *B*, the eight-panel loop in the centre of the assembly. Cell *B*'s second required input comes directly from cell *A*. Out of the 8R linkage's closure equations, we know there is

$$\varphi_{8,B}=\varphi_{6,A}=\varphi_{2,A}\ . \tag{C3}$$

As both inputs to cell *B* $\varphi_{1,B}$ and $\varphi_{8,B}$ are expressed with $\varphi_{1,A}$ and $\varphi_{2,A}$, by using closure equations and trigonometric identities, we can also describe the value of our target angle $\varphi_{7,B}$ using the original inputs. It turns out the equation simplifies to

$$\tan\left(\frac{\varphi_{7,B}}{2}\right)=\tan\left(\frac{\varphi_{3,B}}{2}\right)=\cos(\alpha)\cdot\tan\left(\frac{\varphi_{1,B}}{2}-\varphi_{8,B}\right)=-\cos(\alpha)\tan\left(\frac{\varphi_{1,A}}{2}\right). \tag{C4}$$

In this way, we show how the input variables are transmitted throughout the pattern and define values of the subsequent dihedral angles until the entire pattern's shape is specified. In a larger assembly, this transfer of the angle values continues analogically.

However, removing inactive slits marked by * in Fig. C1(a) alters the kinematic model. Such action means bringing back two hinges that will create two additional spherical 4R linkages adjacent to cell *B*. Fig. C1(b) shows the same assembly but after removing the inactive slits.

If we analyse one of the new spherical linkages, e.g. the left-hand side one, we notice that it inherits its input directly from cell A.

$$\varphi_{3,S'} = \varphi_{5,A} = \varphi_{1,A}. \tag{C5}$$

As the spherical 4R linkage has one DOF, $\varphi_{3,S'}$ equal to $\varphi_{1,A}$ defines its other angles, also $\varphi_{4,S'}$. Moreover, $\varphi_{4,S'}$ is simultaneously our target $\varphi_{7,B}$. This means we can express it by $\varphi_{1,A}$. We estimate the value of $\varphi_{7,B}$ this time approaching the angle from the left-hand side via the newly formed spherical linkage, using equations (2.12). We obtain the result below, which is the same as in (C4).

$$\tan\left(\frac{\varphi_{7B}}{2}\right) = \tan\left(\frac{\varphi_{4,S'}}{2}\right) = -\cos(\alpha)\tan\left(\frac{\varphi_{3,S'}}{2}\right) = -\cos(\alpha)\tan\left(\frac{\varphi_{1,A}}{2}\right). \tag{C6}$$

Moreover, the angle transfer via cell B, described while analysing Fig. C1(a), still applies in Fig. C1(b). This shows that due to the extra hinge that forms a new spherical linkage, variable $\varphi_{7,B}$ can be estimated not via one but two independent paths, which yield the same result. In other words, the new spherical linkage's kinematics is compatible with the rest of the assembly, and the revolute restored via the slit removal only overdefines $\varphi_{7,B}$.

These calculations show how removing inactive slits, i.e. introducing redundant revolutes, creates excessive spherical linkages that over define some angles. Therefore, such redundant kinematic joints only overconstrain the assembly from the mobility point of view. However, the calculations showed also that the extra linkages are compatible with the motion already exercised by the pattern. It means they do not limit the assembly's two-DOF nature. In larger, e.g. 16x16 assemblies, removing inactive slits creates similar spherical linkages that do not change the DOF number. Thus, while the overall mobility calculated with the Kutzbach criterion drops due to extra constraints, the actual DOFs stay equal to two.

References

12Abel, Z., Cantarella, J., Demaine, E. D., Eppstein, D., Hull, T. C., Ku, J. S., Lang, R. J. and Tachi, T. (2016). “Rigid origami vertices: conditions and forcing sets.” *J Computational Geometry*, 7(1).

1An, N., Domel, A.G., Zhou, J., Rafsanjani, A. and Bertoldi, K. (2020). “Programmable Hierarchical Kirigami." *Adv. Funct. Mater.,* 30, 1906711.

1Arnouts, L.I.W., Massart, T.J., De Temmerman, N. and Berke, P.Z. (2018). “Computational modelling of the transformation of bistable scissor structures with geometrical imperfections." *Engineering Structures,* 177, 409–420.

1Arnouts, L.I.W., Massart, T.J., De Temmerman, N. and Berke, P.Z. (2020a). “Multi-objective optimisation of deployable bistable scissor structures." *Automation in Construction,* 114, 103154.

1Arnouts, L.I.W., De Temmerman, N., Massart, T.J. and Berke, P.Z. (2020b). “Geometric design of triangulated bistable scissor structures taking into account finite hub size." *Int J Solids Struct.* 206, 84-100.

2Arya, M., Lee, N. and Pellegrino, S. (2016). “Ultralight Structures for Space Solar Power Satellites." *3rd AIAA Spacecraft Structures Conference.* AIAA, Reston, VA, Art. No. 2016-1950.

2Arya, M., Lee, N. and Pellegrino, S. (2017). “Crease-free biaxial packaging of thick membranes with slipping folds." *Int J Solids Struct,* 108, 24-39.

12Arya, M., Sauder, J.F, Hodges, R. and Pellegrino, S. (2019). “Large-Area Deployable Reflectarray Antenna for CubeSats." *AIAA,* 2019-2257.

1Baek, S-M., Yim, S., Chae, S-H., Lee, D-Y. and Cho, K-J. (2020). “Ladybird beetle–inspired compliant origami." *Sci. Robot*., 5, eaaz6262.

2Beggs, J. S. (1966). *Advanced Mechanism*, The Macmillan Company, New York.

12Belke, C. H. and Paik, J. (2017). "Mori: A Modular Origami Robot." *IEEE/ASME Transactions On Mechatronics*, 22(5), 2153-2164.

8Broccolo, S.D., Laurenzi, S. and Scarpa, F. (2017). "AUXHEX – A Kirigami inspired zero Poisson's ratio cellular structure." *Composite Structures*, 176, 433–441.

8Calisch, S. and Gernshenfeld, N. (2018) "Kirigami fabrication of shaped, flat-foldable cellular materials based on the Tachi-Miura polyhedron" in *Origami 7: The Proceedings from the 7th International Meeting on Origami in Science, Mathematics, and Education*, Tarquin Publications, Volume 4: Engineering Two, 1357.

28Callens, S. J. P. and Zadpoor, A. A. (2018). "From flat sheets to curved geometries: Origami and kirigami approaches" *Materials Today*, 21 (3), 241-264.

2Chang, Z., Ta, T.D., Narumi, K., Kim, H., Okuya, F., Li, D., Kato, K., Qi, J., Miyamoto, Y., Saito, K. and Kawahara, Y. (2020). "Kirigami Haptic Swatches: Design Methods for Cut-and-Fold Haptic Feedback Mechanisms." *Proceedings of the 2020 CHI Conference on Human Factors in Computing Systems. Association for Computing Machinery*, New York, NY, USA, 1–12.

8Chen, S., Chen, J., Zhang, X., Li, Z-Y. and Li, J. (2020). "Kirigami/origami: unfolding the new regime of advanced 3D microfabrication/nanofabrication with "folding"." *Light Sci Appl*, 9, 75.

1x4Chen, Y., Feng, H., Ma, J., Peng, R. and You, Z. (2016). "Symmetric waterbomb origami." *Proc. R. Soc. A.,* 472: 20150846.

12x2Chen, Y., Peng, R. and You, Z. (2015). "Origami of Thick Panels." *Science*, 349(6246), 396-400.

1Chen, Y., Yang, F. and You, Z. (2018). "Transformation of Polyhedrons." *Int J Solids Struct*, 138, 193-204.

8Chen, Y., Scarpa, F., Remillat, C., Farrow, I., Liu, Y. and Leng, J. (2014). "Curved Kirigami SILICOMB cellular structures with zero Poisson's ratio for large deformations and morphing." *J Intell Mater Syst Struct*, 25(6), 731–743.

2x3Chiang, C. H. (1988) *Kinematics of spherical mechanism*, Cambridge University Press, Cambridge, UK.

1Choi, G. P. T, Dudte, L. H. and Mahadevan, L. (2021). "Compact reconfigurable kirigami." *Phys. Rev. Research*, 3, 043030.

1Chudoba, R. and Brakhage, K. H. (2018) "Rigid-facet Kinematics Coupled with Finite Bending Rotation along Crease Lines" in *Origami 7: The Proceedings from the 7th International Meeting on Origami in Science, Mathematics, and Education*, Tarquin Publications, Volume 4: Engineering Two, 1183-1199.

1Cui, J., Huang, T.-Y., Luo, Z., Testa, P., Gu, H., Chen. X.-Z., Nelson, B. J. and Heyderman, L. J. (2019). "Nanomagnetic encoding of shape-morphing micromachines." *Nature*, 575, 164–168.

5Dai, J.S. and Rees Jones, J. (1999). "Mobility in Metamorphic Mechanisms of Foldable/Erectable Kinds." *J. Mech. Des*, 121, 375-382.

2Denavit, J. and Hartenberg, R. S. (1955). "A kinematic notation for lower-pair mechanisms based on matrices." *J Appl Mech*, 22(2), 215-221.

2x2De Temmerman, N., Mollaert, M., Van Mele, T. and De Laet, L. (2007) "Design and Analysis of a Foldable Mobile Shelter System." *Int. J. Space Structures*, 22(3), 161-168.

8Du, Y., Song, C., Xiong, J. and Wu, L. (2019). "Fabrication and mechanical behaviors of carbon fiber reinforced composite foldcore based on curved-crease origami." *Composites Science and Technology*, 174, 94-105.

28x2Eidini, M. and Paulino, G. H. (2015). "Unraveling metamaterial properties in zigzag-base folded sheets." *Sci. Adv.*, 1, e1500224.

18Elghazi, Y.S. and Mahmoud, A.H. (2016). "Origami Explorations A Generative Parametric Technique For kinetic cellular façade to optimize Daylight Performance." *34th Annual eCAADe Conference,* Oulu, Finland, Vol.2, 399-408.

28Evans, T.A., Lang, R.J., Magleby, S.P. and Howell, L.L. (2015a). "Rigidly Foldable Origami Twists," *Origami 6, American Mathematical Society*, Vol. 1, 119-130.

27Evans, T.A., Lang, R.J., Magleby, S.P. and Howell, L.L. (2015b). "Rigidly foldable origami gadgets and tessellations," *R. Soc. open sci.* 2(9): 150067.

8Felton, F., Tolley, M., Demaine, E., Rus, D. and Wood, R. (2014). "A method for building self-folding machines." *Science*, 345(6197), 644-646.

8x3Feng H., Peng, R., Zang, S., Ma, J. and Chen, Y. (2020). "Rigid foldability and mountain-valley crease assignments of square-twist origami pattern". *Mech Mach Theory*, 152, 103947.

18Filipov, E. T., Paulino, G. H. and Tachi, T. (2016). "Origami tubes with reconfigurable polygonal cross-sections." *Proc. R. Soc. A.*, 472: 20150607.

18Filipov, E. T., Paulino, G. H. and Tachi, T. (2019). "Deployable Sandwich Surfaces with High Out-of-Plane Stiffness." *J. Struct. Eng.*, 145(2): 04018244.

5Galletti, C. and Fanghella, P. (2001). "Single-loop kinematotropic mechanisms." *Mech Mach Theory*, 36, 743-761.

8Gardiner, M. (2009). "A Brief History of Oribotics." in *Origami 4: Fourth International Meeting of Origami Science, Mathematics and Education*, A K Peters, 51-60.

7x2Gattas, J. M., Wu, W. and You, Z. (2013). "Miura-Base Rigid Origami: Parameterizations of First-Level Derivative and Piecewise Geometries." *J. Mech. Des.*, 135: 111011.

2Gattas, J. M. and You, Z. (2015). "Geometric assembly of rigid-foldable morphing sandwich structures." *Engineering Structures*, 94, 149-159.

2Giraud, F.H., Joshi, S. and Paik, J. (2021). "Haptigami: a fingertip haptic interface with vibrotactile and 3-DoF cutaneous force feedback." *IEEE Trans Haptics*. 11;PP.

8Grey S.W., Scarpa, F. and Schenk, M. (2021). "Embedded Actuation for Shape-Adaptive Origami". *J. Mech. Des.*, 143(8): 081703

8Grzeschik, M., Klett, Y. and Middendorf, P. (2018) "Reality Check – Mechanical Potential of Tessellation-based Foldcore Materials" in *Origami 7: The Proceedings from the 7th International Meeting on Origami in Science, Mathematics, and Education*, Tarquin Publications, Volume 4: Engineering Two, 1273-1284.

2Guest, S. D. and Pellegrino, S. (1992). “Inextensional wrapping of flat membranes.” *First International Seminar on Structural Morphology*, LMGC, Universite Montpellier-II, Montpellier, France, 203-215.

18Hayakawa, K. and Ohsaki, M. (2021). “Form generation of rigid origami for approximation of a curved surface based on mechanical property of partially rigid frames”. *Int J Solids Struct*, 216, 182-199.

2Hoberman, C. S. (1988). “Reversibly Expandable Three-Dimensional Structure”. U. S. Patent No. 4,780,344.

2Hong, S., Shi, Y., Li, R., Zhang, C., Jin, Y., and Wang, P. (2018). “Nature-Inspired, 3D Origami Solar Steam Generator toward Near Full Utilization of Solar Energy”. *ACS Appl. Mater. Interfaces*, 10, 28517–28524.

8Hou, Y., Neville, R., Scarpa, F., Remillat, C., Gu, B. and Ruzzene, M. (2014). “Graded conventional-auxetic Kirigami sandwich structures: Flatwise compression and edgewise loading”. *Composites: Part B*, 59, 33-42.

2x2Hull, T. (1994). "On the Mathematics of Flat Origamis." *Congr. Numer.*, 100, 215-224.

2Hull, T. C. (2002). "The Combinatorics of Flat Folds: a Survey." *The Proceedings of the Third International Meeting of Origami Science, Mathematics, and Education*, AK Peters.

2x7Hunt, K. H. (1978). *Kinematic geometry of mechanisms* Oxford: Clarendon Press, UK.

1x2Ikeya, K., Sakamoto, H., Nakanishi, H., Furuya, H., Tomura, T., Ide, R., Iijima, R., Iwasaki, Y., Ohno, K., Omoto, K., Furuya, T., Hayashi, T., Kato, M., Koide, S., Kurosaki, M., Nakatsuka, Y., Okuyama, S., Kashiyama, R., Nakamura, J., Nio, W., Tsunemitsu, T., Yamazaki, Y., Taga, K., Hohmann, B., Amamoto, T., Chubachi, T., Tamura, S., Okada, H., Watanabe, A., Kawabata, N., Hori, T., Ito, H., Kuratomi, T., Shimoda, Y., Hidaka, N., Watanabe, K., Torisaka, A., and Yamazaki, M. (2020). “Significance of 3U CubeSat OrigamiSat-1 for space demonstration of multifunctional deployable membrane.” *Acta Astronautica*, 173, 363-377.

2x2Irion, R. (2010). “Origami observatory: behind the scenes with the Webb space telescope.” *Scientific American*, Oct.

2Jasim, B. and Taheri, P. (2018). “An Origami-Based Portable Solar Panel System.” *2018 IEEE 9th Annual Information Technology, Electronics and Mobile Communication Conference (IEMCON)*, 199-203.

1Jin, L., Forte, A.E., Deng, B., Rafsanjani, A. and Bertoldi, K. (2020). “Kirigami-Inspired Inflatables with Programmable Shapes.” *Adv. Mater.,* 32, 2001863.

28Karagiozova, D., Zhang, J., Lu, G. and You, Z. (2019). “Dynamic in-plane compression of Miura-ori patterned metamaterials.” *Int. J. Impact Eng.*, 129, 80-100.

1Kim, S.Y., Baines, R., Booth, J., Vasios, N., Bertoldi, K. and Kramer-Bottiglio, R. (2019). “Reconfigurable soft body trajectories using unidirectionally stretchable composite laminae.” *Nat Commun* 10, 3464.

1Klett, Y., Middendorf, P., Sobek, W., Haase, W. and Heidingsfeld, M. (2017). “Potential of origami-based shell elements as next-generation envelope components.” *2017 IEEE International Conference on Advanced Intelligent Mechatronics (AIM)*, 916-920.

1Kotikian, A., McMahan, C., Davidson, E.C., Muhammad, J.M., Weeks, R.D., Daraio, C. and Lewis, J.A. (2019). “Untethered soft robotic matter with passive control of shape morphing and propulsion.” *Sci. Robot.,* 4, eaax7044.

8Kshad, M.A.E., Popinigis, C. and Naguib, H.E. (2019). “3D printing of Ron-Resch-like origami cores for compression and impact load damping.” *Smart Mater. Struct.*, 28, 015027

8x2Kuribayashi, K., Tsuchiya, K., You, Z., Tomus, D., Umemoto, M., Ito, T. and Sasaki, M. (2006). “Self-deployable origami stent grafts as a biomedical application of Ni-rich TiNi shape memory alloy foil.” *Mater. Sci. Eng. A*, 419, 131-137.

8x2Kwon, O-H. and Roh, J-H. (2019). “Origami-inspired shape memory dual-matrix composite structures.” *J Intell Mater Syst Struct*, 30(17) 2639–2647.

1Li, S., Deng, B., Grinthal, A., Schneider-Yamamura, A., Kang, J., Martens, R.S., Zhang, C.T., Li, J., Yu, S., Bertoldi, K. and Aizenberg, J. (2021). “Liquid-induced topological transformations of cellular microstructures.” *Nature*, 592, 386-391.

1Li, Y. and Pellegrino, S. (2020). “A Theory for the Design of Multi-Stable Morphing Structures.” *J Mech Phys Solids*, 136, 103772.

8Li, Z., Chen, W. and Hao, H. (2018a) “Quasi-static Crushing Behaviours of Folded Open-top Truncated Pyramid Structures with Interconnected Side Walls” in *Origami 7: The Proceedings from the 7th International Meeting on Origami in Science, Mathematics, and Education*, Tarquin Publications, Volume 4: Engineering Two, 1199-1212.

8Li, Z., Chen, W. and Hao, H. (2018b) “Blast Resistant Performance of Cladding With Folded Open-top Truncated Pyramid Structures as Core” in *Origami 7: The Proceedings from the 7th International Meeting on Origami in Science, Mathematics, and Education*, Tarquin Publications, Volume 4: Engineering Two, 1213-1226.

2Liu, J., Liu, C.-C., Eggers, M. and Sabin, J. E. (2018). “Responsive Kirigami: Context-Actuated Hinges in Folded Sheet Systems.” *SimAUD 2018,* Deft, the Netherlands.

12Liu, K. and Paulino, G.H. (2017). “Nonlinear mechanics of non-rigid origami: an efficient computational approach.” *Proc. R. Soc. A.,* 473: 20170348.

1Liu, K., Tachi, T. and Paulino, G.H. (2019). “Invariant and smooth limit of discrete geometry folded from bistable origami leading to multistable metasurfaces” *Nat Commun* 10, 4238.

1Liu, K., Tachi, T. and Paulino, G.H. (2021). “Bio-Inspired Origami Metamaterials With Metastable Phases Through Mechanical Phase Transitions” *J. Appl. Mech.,* 88(9): 091002.

1x3Liu, W. and Chen, Y. (2018). “A double spherical 6R linkage with spatial crank-rocker characteristics inspired by kirigami.” *Mech Mach Theory,* 153, 103995.

1McClintock, H.D., Doshi, N., Iniguez-Rabago, A., Weaver, J.C., Jafferis, N.T., Jayaram, K., Wood, R.J. and Overvelde, J.T.B. (2021). “A Fabrication Strategy for Reconfigurable Millimeter-Scale Metamaterials.” *Adv. Funct. Mater.,* 2103428.

12Melancon, D., Gorissen, B., Garcia-Mora, C. J., Hoberman, C. and Bertoldi, K. (2021). “Multistable inflatable origami structures at the metre scale.” *Nature,* 592, 545–550.

2Mira, L.A., Thrall, A.P. and De Temmerman, N. (2014). “Deployable scissor arch for transitional shelters.” *Automation in Construction* 43, 123–131.

2Miura, K. (1980). “Method of packaging and deployment of large membrane in space." *31st Congress of International Astronautical Federation,* New York, USA, Paper A 31, 1-10.

2Miura, K. (2009). “The science of Miura-ori: a review.” in *Origami 4: Fourth International Meeting of Origami Science, Mathematics and Education*, A K Peters, 87-99.

2Miyamoto Y. (2018) “Rigidly Foldable Rotational Erection System (RES)” in *Origami 7: The Proceedings from the 7th International Meeting on Origami in Science, Mathematics, and Education*, Tarquin Publications, Volume 3: Engineering One, 731-746.

18Morgan, J., Magleby, S. P. and Howell, L. L. (2016). “An Approach to Designing Origami-Adapted Aerospace Mechanisms.” *J. Mech. Des.*, 138(5): 052301.

8Muhs, F., Klett, Y. and Middendorf, P. (2018) “Automated Numerical Process Chain for the Design of Folded Sandwich Cores” in *Origami 7: The Proceedings from the 7th International Meeting on Origami in Science, Mathematics, and Education*, Tarquin Publications, Volume 4: Engineering Two, 1043-1058.

7Nassar, H., Lebee, A. and Monasse, L. (2017) “Curvature, metric and parametrization of origami tessellations: theory and application to the eggbox pattern” *Proc. R. Soc. A*,473(2197), 20160705.

2Nassar, H., Lebee, A. and Monasse, L. (2018) “Fitting Surfaces with the Miura Tessellation” in *Origami 7: The Proceedings from the 7th International Meeting on Origami in Science, Mathematics, and Education*, Tarquin Publications, Volume 3: Engineering One, 811-826.

8x2Nauroze, S. A., Novelino, L. S., Tentzeris, M. M. and Paulino G. H. (2018) “Continuous range tunable multilayer frequency-selective surfaces using origami and inkjet printing”. *PNAS,* 115 (52) 13210-13215.

8x2Neville, R., Scarpa, F. and Pirrera, A. (2016). “Shape morphing Kirigami mechanical metamaterials.” *Sci Rep,* 6, 31067.

2Ning, X., Wang, X., Zhang, Y., Yu, X., Choi, D., Zheng, N., Kim, D. S., Huang, Y., Zhang, Y. and Rogers, J. A. (2018) “Assembly of Advanced Materials into 3D Functional Structures by Methods Inspired by Origami and Kirigami: A Review”. *Adv. Mater. Interfaces*, 5, 1800284.

18Okuya, F., Umedachi, T., Saito, K. and Kawahara, Y. (2018) “Crawling Cylindrical Origami Robot Driven by Single Actuator” in *Origami 7: The Proceedings from the 7th International Meeting on Origami in Science, Mathematics, and Education*, Tarquin Publications, Volume 3: Engineering One, 949-963.

1Overvelde, J. T. B., Shan, S. and Bertoldi, K. (2012). “Compaction through buckling in 2D periodic, soft and porous structures: effect of pore shape.” *Advanced Materials*, 24, 2337–2342.

18Overvelde, J. T. B., de Jong, T. A., Shevchenko, Y., Becerra, S. A., Whitesides, G. M., Weaver, J. C., Hoberman, C. and Bertoldi, K. (2016). “A three-dimensional actuated origami-inspired transformable metamaterial with multiple degrees of freedom.” *Nat Commun,* 7, 10929.

18Overvelde, J. T. B., Weaver, J. C., Hoberman, C. and Bertoldi, K. (2017). “Rational design of reconfigurable prismatic architected materials.” *Nature*, 541, 347-352.

2Park, J. J., Won, P. and Ko S. H. (2019) “A Review on Hierarchical Origami and Kirigami Structure for Engineering Applications”. *Int. J. Precis. Eng. Manuf. - Green Technol.,* 6:147–161.

3Pfurner, M (2018) “Synthesis and Motion Analysis of a Single-Loop 8R-Chain”. *2018 International Conference on Reconfigurable Mechanisms and Robots (ReMAR),* 1-7

2x5Philips, J. (1984). *Freedom in Machinery*, vol. I, Cambridge Univ. Press, Cambridge, UK.

1Poon, R. and Hopkins, J.B. (2019). “Phase-Changing Metamaterial Capable of Variable Stiffness and Shape Morphing.” *Adv. Eng. Mater.,* 21, 1900802.

1x28Pratapa, P.P., Suryanarayana, P. and Paulino, G.H. (2018). "Bloch wave framework for structures with nonlocal interactions: Application to the design of origami acoustic metamaterials." *J Mech Phys Solids*, 118, 115-132.

1Pratapa, P.P., Liu, K., Vasudevan, S.P., and Paulino, G.H. (2021). "Reprogrammable Kinematic Branches in Tessellated Origami Structures." ASME. *J. Mechanisms Robotics.*, 13(3): 031004.

1Rafsanjani, A., Jin, L., Deng, B. and Bertoldi, K. (2019). "Propagation of pop ups in kirigami shells." *PNAS*, 116(17), 8200–8205.

2Reuleaux, F. (1876). *Kinematics of Machinery*, MacMillan and Co., London, UK.

2Saito, K., Agnese, F. and Scarpa, F. (2011). "A Cellular Kirigami Morphing Wingbox Concept" *J Intell Mater Syst Struct*, 22(9): 935-944.

12Saito, K., Tachi, T., Fujikawa, T., Niiyama, R. and Kawahara, Y. (2018) "Deployable Structures Inspired by Insect Wing Folding" in *Origami 7: The Proceedings from the 7th International Meeting on Origami in Science, Mathematics, and Education*, Tarquin Publications, Volume 3: Engineering One, 747-761.

8Schenk, M. and Guest, S. D. (2011). "Origami Folding: A Structural Engineering Approach." in *Origami 5: Fifth International Meeting of Origami Science, Mathematics and Education*, ed. P. Wang-Iverson, R. J. Lang and M. Yim, Eds. A K Peters/CRC Press, 293-305.

28Schenk, M. and Guest, S. D. (2013). "Geometry of Miura-folded metamaterials." *PNAS*, 110(9), 3276–3281.

2x2Schenk, M., Guest, S.D. and McShane, G. J. (2014). "Novel stacked folded cores for blast-resistant sandwich beams." *Int J Solids Struct*, 51(25-26), 4196-4214.

18Schultz, J. and Katz, N. (2018). "ORIGAMI-INSPIRED FAÇADE DESIGN: Parametric Studies for Architectural and Structural Efficiency." *Facade Tectonics 2018 World Congress.* Los Angeles, CA.

2x2Seymour, K., Burrow, D., Avila, A., Bateman, T., Morgan, D.C., Magleby, S.P., Howell, L.L. (2018) “Origami-Based Deployable Ballistic Barrier” in *Origami 7: The Proceedings from the 7th International Meeting on Origami in Science, Mathematics, and Education*, Tarquin Publications, Volume 3: Engineering One, 763-788.

1Shaw, L.A., Chizari, S., Dotson, M., Song, Y. and Hopkins, J.B. (2018). “Compliant rolling-contact architected materials for shape reconfigurability.” *Nat Commun,* 9, 4594.

128Silverberg, J. L., Evans, A. A., McLeod, L., Hayward, R. C., Hull, T., Santangelo, C.D. and Cohen, I. (2014). “Using origami design principles to fold reprogrammable mechanical metamaterials.” *Science*, 345(6197), 647-650.

18Silverberg, J. L., Na, J., Evans, A. A., Liu, B., Hull, T. C., Santangelo, C. D., Lang, R. J., Hayward, R. C. and Cohen, I. (2015). “Origami structures with a critical transition to bistability arising from hidden degrees of freedom.” *Nature Materials*, 14, 389–393

5Song, Y., Ma, X. and Dai, J.S. (2019). “A novel 6R metamorphic mechanism with eight motion branches and multiple furcation points” *Mech Mach Theory,* 142, 103598.

128Sun, Y., Ye, W., Chen, Y., Fan, W., Feng, J. and Sareh, P. (2021) “Geometric design classification of kirigami-inspired metastructures and metamaterials”. *Structures*, 33, 3633–3643.

12x2Tachi, T. (2010a). “Geometric Considerations for the Design of Rigid Origami Structures”. *Proceedings of the International Association for Shell and Spatial Structures (IASS) Symposium 2010*, Shanghai, China.

27Tachi, T. (2010b). “Freeform Rigid-Foldable Structure using Bidirectionally Flat-Foldable Planar Quadrilateral Mesh”. *Advances in Architectural Geometry*, Ceccato C., Hesselgren L., Pauly M., Pottmann H., Wallner J. (eds), Springer, Vienna.

18Tachi, T. (2011). “Rigid-Foldable Thick Origami.” in *Origami 5: Fifth International Meeting of Origami Science, Mathematics, and Education*, P. Wang-Iverson, R. J. Lang, M. YIM, eds. A K Peters/CRC Press, Chapter 20.

1Tachi, T. (2013). “Freeform Origami Tessellations by Generalizing Resch’s Patterns.” in *Proceedings of the ASME IDETC/CIE 2013,* Portland, Oregon, USA.

3Tang, Z. and Dai, J.S. (2018). “Bifurcated configurations and their variations of an 8-bar linkage derived from an 8-kaleidocycle” *Mech Mach Theory,* 121, 745–754.

1Udani, J.P. and Arrieta, A.F. (2021). “Programmable mechanical metastructures from locally bistable domes.” *Extreme Mech. Lett*, 42, 101081.

1Underwood, C., Viquerat, A., Schenk, M., Taylor, B., Massimiani, C., Duke, R., Stewart, B., Fellowes, S., Bridges, C., Aglietti, G., Sanders, B., Masutti, D. and Denis, A. (2019). “InflateSail de-orbit flight demonstration results and follow-on drag-sail applications.” *Acta Astronautica*, 162, 344-358.

28van Knippenberg, R., Habraken, A. and Teuffel, P. (2016). “Deployable structures using non-singular rigid foldable patterns.” *Procedia Engineering*, 155, 388 – 397.

12Wang, C., Li, J. L. and You, Z. (2018) “A Kirigami-inspired Foldable Model for Thick Panels” in *Origami 7: The Proceedings from the 7th International Meeting on Origami in Science, Mathematics, and Education*, Tarquin Publications, Volume 3: Engineering One, 715-730.

35Wang, R., Song, Y. and Dai, J.S. (2021). “Reconfigurability of the origami-inspired integrated 8R kinematotropic metamorphic mechanism and its evolved 6R and 4R mechanisms” *Mech Mach Theory,* 161, 104245.

2Wang, X., Guest, S. D. and Kamien, R. D. (2020) “Keeping It Together: Interleaved Kirigami Extension Assembly” *Phys. Rev. X*, 10, 011013.

2Watanabe, N. and Kawaguchi, K. (2009). “The Method for Judging Rigid Foldability.” in *Origami 4: Fourth International Meeting of Origami Science, Mathematics and Education*, R. J. Lang, ed. A K Peters, 165-174.

12Wei, Y. and Pellegrino, S. (2017). “Modular Foldable Surfaces: a Novel Approach based on Spatial Mechanisms and Thin Shells” *AIAA 2017-1345. 4th AIAA Spacecraft Structures Conference*.

8Williams, D. E., Dorn, C., Pellegrino, S. and Hajimiri, A. (2021). “Origami-Inspired Shape-Changing Phased Array”. *2020 50th European Microwave Conference (EuMC),* Utrecht Netherlands, 344-347.

5Wohlhart, K. (1996). “Kinematotropic Linkages.” *Recent Advances in Robot Kinematics*, Lenarčič J., Parenti-Castelli V. (eds), Springer, Dordrecht, 359-368.

1Wu, R., Roberts, P.C.E., Lyu, S., Zheng, F., Soutis, C., Diver, C., Zhou, D., Li, L. and Deng, Z. (2021a) “Lightweight Self-Forming Super-Elastic Mechanical Metamaterials with Adaptive Stiffness” *Adv. Funct. Mater.,* 31, 2008252.

1Wu, S., Ze, Q., Dai, J., Udipi, N., Paulino, G.H. and Zhao, R.. (2021b) “Stretchable origami robotic arm with omnidirectional bending and twisting” *PNAS*, 118 (36), e2110023118.

8Xiang, X.M., Lu, G. and You, Z.. (2020) “Energy absorption of origami inspired structures and materials” *Thin–Walled Structures,* 157,107130.

8Xiang, X.M., Fu, Z., Zhang, S., Lu, G., San Ha, N., Liang, Y. and Zhang, X. (2021) “The mechanical characteristics of graded Miura-ori metamaterials” *Materials & Design,* 211, 110173.

2x2Xu, R., Zhang, X., Ma, J., Chen, Y., Chao, Y. and You, Z. (2018). “Folding a rigid flat surface around a square hub.” *Proceedings of the ASME IDETC/CIE 2018,* Quebec City, Canada.

2Yamada, T. R. U., do Nascimento, R. A. and dos R. Pereira, M. A. (2018) “Flat foldable structure in Glued Laminated Bamboo based on origami and kirigami design” in *Origami 7: The Proceedings from the 7th International Meeting on Origami in Science, Mathematics, and Education*, Tarquin Publications, Volume 1: Design, Education, History, and Science, 285-298.

18Yang, Y. and You, Z. (2018). “Geometry of Transformable Metamaterials Inspired by Modular Origami.” *J. Mechanisms Robotics.*, 10(2), 021001.

1Yang, Z., Chen, D., Levine, D.J. and Sung, C. (2021). “Origami-Inspired Robot That Swims via Jet Propulsion.” in *IEEE Robotics and Automation Letters,* 6(4), 7145-7152.

18Yasuda, H., Buskohl, P.R., Gillman, A., Murphey, T.D., Stepney, S., Vaia, R.A. and Raney, J.R. (2021). "Mechanical computing". *Nature,* 598, 39–48.

8Yasuda, H., Miyazawa, Y., Charalampidis, E.G., Chong, C., Kevrekidis, P.G.. and Yang, J. (2019). "Origami-based impact mitigation via rarefaction solitary wave creation". *Sci. Adv.,* 5: eaau2835.

18x2Yasuda, H. and Yang, J. (2015). "Reentrant origami-based metamaterials with negative Poisson's ratio and bistability." *Physics Review Letters*, 114, 185502.

2x8You, Z. and Chen, Y. (2012). "Motion structures: deployable structural assemblies of mechanisms." *Spon Press*.

8You, Z. and Kuribayashi K. (2009). "Expandable Tubes with Negative Poisson's Ratio and Their Application in Medicine." in *Origami 4: Fourth International Meeting of Origami Science, Mathematics and Education*, A K Peters, 117-128.

128Zhang, J., Karagiozova, D., You, Z., Chen, Y. and Guoxing, L. (2019). "Quasi-static large deformation compressive behaviour of origami-based metamaterials." *Int. J. Mech. Sci.*, 153-154, 194-207

1Zhang, X. and Chen, Y. (2019). "Vertex-Splitting on a Diamond Origami Pattern." *J. Mechanisms Robotics.*, 11(3): 031014

1Zhu, Y., Birla, M., Oldham, K.R., and Filipov, E.T. (2020). "Elastically and Plastically Foldable Electrothermal Micro-Origami for Controllable and Rapid Shape Morphing." *Adv. Funct. Mater.,* 2003741.

2Zirbel, S. A., Lang, R. J., Thomson, M. W., Sigel, D. A., Walkemeyer, P. E., Trease, B. P., Magleby, S. P. and Howell, L. L. (2013). "Accommodating Thickness in Origami-Based Deployable Arrays." *J. Mech. Des.*, 135(11): 111005

8Zou, C. and Harne, R. L. (2019). "Tailoring reflected and diffracted wave fields from tessellated acoustic arrays by origami folding." *Wave Motion*, 89, 193–206.